RADIOMETRIC CHARACTERISATION OF VINEYARD SOILS, WESTERN CAPE, SOUTH AFRICA

Nolasco Anton Mlwilo

Thesis presented in fulfillment of the requirements for the degree of Doctor of Philosophiae in the Department of Physics at the University of the Western Cape.

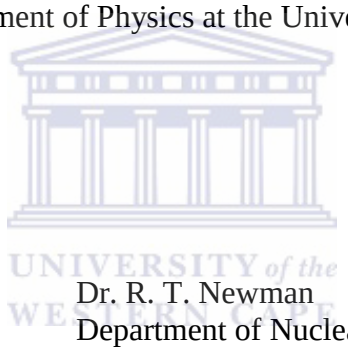

Supervisors:

Dr. R. T. Newman
Department of Nuclear Physics
iThemba LABS

Prof. R. Lindsay
Department of Physics
University of the Western Cape

June 2010

DECLARATION

I, Nolasco Anton Mlwilo hereby declare that the work contained in this thesis is my own original work and that I have not previously in its entirely or in part submitted it at any university for a degree.

Signature:……..

Date:……..

Radiometric characterisation of vineyard soils, Western Cape, South Africa.

Nolasco Anton Mlwilo

KEYWORDS

Gamma-ray spectroscopy
In-situ measurements
MEDUSA detector
Hyperpure Germanium detector
Sediment characterisation
Physico-chemical soil properties
Detector efficiency
Vineyards
Full spectrum analysis
Radiometric mapping

Radiometric characterisation of vineyard soils, Western Cape, South Africa.

Nolasco Anton Mlwilo

Department of Physics, University of the Western Cape, Private Bag X 17, Bellville, South Africa.

ABSTRACT

This study is aimed at investigating the feasibility of using the radiometric technique as an alternative to traditional methods for determining soil physico-chemical parameters which are important for *terroir* characterization. *In-situ* and *ex-situ* radiometric analyses of soil from three vineyard blocks of Simonsig Wine Estate in the Stellenbosch district (Western Cape, South Africa) were studied. A mobile MEDUSA gamma-ray detection system comprising a CsI(Na) crystal (length 15 cm, diameter 7 cm) and associated electronics mounted on a portable trolley were used for partial *terroir* characterisation. Thereafter activity concentrations of ^{40}K, ^{232}Th series and ^{238}U series in soil (top ~30 cm) from the measured MEDUSA spectra (0 – 3 MeV) were extracted by means of the full-spectrum analysis (FSA) method. A lead-shielded HPGe detector was used for analyzing collected soil samples while soil physico-chemical parameters were analysed using standard methods at research and commercial laboratories.

The activity concentrations (AC), number of decays per mass measured in Bq/kg of ^{40}K, ^{232}Th series and ^{238}U series for samples in three blocks were determined. The AC values of ^{40}K, ^{232}Th series and ^{238}U series range from 127 to 227, 28 to 111 and 28 to 68 for Block 2, respectively. For the Pomphuis block, the values range from 29 to 288, 11 to 55 and 11 to 68, for ^{40}K, ^{232}Th series and ^{238}U series, respectively. As for the Nuweland block, the values range from 62 to 315, 14 to 57 and 17 to 47 for ^{40}K, ^{232}Th series and ^{238}U series, respectively. An analysis of the radiometric results led to the identification of two sediment groups (Pomphuis/Nuweland and Block 2), which showed clear differences when characterized. Correlation analyses suggested that it was possible to reduce the radiometric and physico-chemical data of relevance to new eigenvectors, *W*. In addition, the correlation fit parameters obtained from radiometric and chemical-sample data were used in projecting *in-situ* radiometric MEDUSA data onto chemical data.

The large data set that was obtained from the *in-situ* measurements, shows large variations in the activity concentrations. These variations have been further investigated by studying smaller sections of the vineyard blocks that were chosen to reflect high and low activity concentrations of Th and K. A study of the ACs in these areas showed that a new vector can be defined that characterises the soil and that can be compared to soil physico-chemical parameters. This led to the confirmation that the soil on the three blocks consists of primarily two types. The analysis of the radiometric data allows for a comparison with the physico-chemical parameters of the soil. Good correlations for some, but not all major elements and trace elements, were found.

The radiometric technique has been shown to be useful in studying vineyard soils. It is shown how the technique can be used to characterise soils within a specific vineyard block, and to differentiate between soils from different blocks. The approach presented can therefore be used to assist with the management of vineyard soils and to characterise the *terroir* of specific vineyard blocks.

ACKNOWLEDGEMENTS

I am sincerely and deeply grateful to my supervisors Dr. Richard T. Newman, Prof. Robbie Lindsay and the collaborator, Prof. Dr. de Meijer (Stiching Earth, the Netherlands) for the tireless supervision, guidance and encouragement throughout the entire course of this work. Your motivation and inspiration is highly appreciated.

Special thanks to iThemba LABS and the Department of Physics, University of the Western Cape (UWC) for financial support and other facilitations which made this work possible. Sincere thanks goes to Francois Malan of Simonsig Wine Farm for allowing us to conduct the study on their estate. I further extend my thanks to the collaboration provided by the Agricultural Research Council (ARC Infruitec-Nietvoorbij) particularly Philisiwe Sange for production of wine samples.

I also express my gratitude to the former and current Environmental Radioactivity Laboratory (ERL) staff, collaborators and students particularly Israel Hlatshwayo, Dr. Atulya K. Mohanty, Peane Maleka, Siddig Talha, Tiro Modisane, Ramudzuli Manavhela, Nkanyiso Mbatha and Angelo Joseph.

Many thanks to the Technical Support Service division (iThemba LABS), particularly Mr. Z. Zweni for designing and manufacturing the trolley used for gamma-ray mapping of the vineyard soils.

Sincere thanks to the Tanzania Atomic Energy Commission (TAEC) for granting me study leave.

To my dear family, especially Imakulatha (my wife) and Anton (my son), I thank you all for your understanding, support and prayers throughout the entire period of my academic journey.

Last but not least, I humbly thank God Almighty who has made this possible.

CONTENTS

LIST OF FIGURES

LIST OF TABLES

CHAPTER 1 INTRODUCTION

Terroir is a French term which can be interpreted as "a sense of place" which is embodied in certain qualities and is the sum of the effects that the local environment has had on the manufacture of a wine [Www01]. *Terroir* refers to climatic, physical, chemical, and even human skill factors that combine to impose a unique character and certain quality to wine from a particular wine-producing region. Each of these components can vary significantly over small distances. In addition, the results of the interactions between the *terroir* elements can change dramatically when even just one component varies. According to Bonnardot *et al.*, [Bon02], aspects of the vineyard environment which are of specific importance from a *terroir* viewpoint include soil hydrology, geology or pedology (particle size distribution and mineralogy), morphoclimatology (insolation or solar energy influx) and climatology (rainfall and temperature). Finding the right balance of each one of these important *terroir* components or units is the ultimate achievement in wine making.

In this study, vineyard soil is studied to investigate further whether radiometry based on γ-ray spectrometry can be used to infer soil physical and chemical properties [Mod05, Jos07], thereby partially characterizing the relevant *terroir.*

Before proceeding to present the study motivation and research objectives some relevant background on soil and radiometry is first given.

1.1 Soil – a short review with focus on viticulture

Soil is a naturally occurring, unconsolidated (loose) covering of broken rock particles and decaying organic matter on the surface of the earth, capable of supporting life. It is thus a heterogeneous mixture of different organisms and mineral, organic and organo-mineral substances supplying air, water, nutrients and mechanical support for the roots of the growing plants [Kab04]. Soil formation is the combined effect of physical, chemical and biological processes on soil parent material namely rock. Through the weathering process, the rock is broken down by the combination of water, gases and living matter. Materials formed from the rock weathering process are carried by water, wind and ice and eventually dropped in other places where they settle and mix with

organic materials to form soil. A desirable surface soil in good condition for plant growth contains approximately 50% solid material and 50% pore spaces (porosity). The solid material is composed of mineral material (45-48%) and organic matter (2-5%). Under ideal moisture conditions for growing plants, the soil porosity would contain approximately equal amounts of air (25%) and water (25%) [Dan06]. Soil is made up of distinct horizontal layers known as horizons. These horizons are formed as a result of the combined effects of organic matter additions to the surface soil, oxidation of minerals and long-term leaching [Cou84]. According to a study by Courtney *et al.*, [Cou84], the differences observed between soil horizons are characterized by physico-chemical properties such as colour, texture, organic content, structure and stoniness.

Depending on the soil type, some soils have an O-horizon which is the top organic layer of the soil made up mostly of leaf litter and humus (decomposed organic matter). The A-horizon is found below the O-horizon and above B-horizon. It is characterized by organic accumulation which is mainly composed of decaying leaf litter. This horizon can be identified by its dark colour. The B-horizon is beneath the A-horizon and above the C-horizon. This is generally a mineral-rich horizon since it contains clay and mineral deposits such as iron, aluminium oxides and calcium carbonate. The C-horizon is the layer beneath the B-horizon. This layer consists of slightly broken-up bedrock and unweathered parent material [Www02].

Good vineyard soils amongst others must allow sufficient water and nutrient supply. Moreover, it should have high capacity to retain water.

The fineness or coarseness of the soil particles in the soil determines *soil texture* [Dan06]. It is determined by the relative amounts of *sand*, *silt* and *clay* fractions. According to the normal definition in standard soil analyses [Soi99], sand particles vary in size from very fine (0.063 mm) to very coarse (2 mm) in average diameter. Silt particles range in size from 0.002 mm to 0.063 mm, while clay is the finest soil particle size class (<0.002 mm) [Dan06]. Soil texture is one of the most important agricultural physical properties of the soil resulting from the action of climatic factors such as rainfall and temperature on soil parent materials. The physical structure of the soil influences the eventual wine quality. According to Saayman [Saa92], soil is thought to affect vine growth pattern and wine characteristics mainly through its physical and water regulating

properties. This includes characteristics like depth, rockiness, and degree of structural layering, clay content and its ability to drain well. Clay has higher water and nutrient holding capacity than sandy soils. However, it drains very slowly. A study by Wilson [Wil98] reveals that the ideal soil type for vine is pebbly, sandy-clayey soil with considerable amount of organic matter.

A mineral is a naturally occurring solid with a definite chemical composition and a specific crystalline structure that has been formed through geological processes. The minerals present in the soil are predominantly determined by the mineralogical composition of the parent material (rocks) and the degree of weathering [Wil93]. The most common mineral in soil is quartz (SiO_2), but in soils that have not been strongly weathered *micas* and *feldspars* may also be present. The minerals occurring in rocks such as granite (muscovite, microcline, quartz, biotite etc.), basalt (goethite, chlorite, augite etc.), gneiss and schist are termed *primary minerals* [Bra74, Fit86]. These minerals in the soil are decomposed to form *secondary minerals*, particularly the clay minerals [Fit86]. The processes for the formation of various clay minerals are shown in Figure 1-1. In each case, clay mineral genesis is accompanied by the removal of soluble elements such as K, Na, Ca, and Mg [Bra74]. Generally, minerals can be divided into *silicates* and *non-silicates*. The silicate minerals have very complex structures in which the fundamental unit is the silicon-oxygen tetrahedron, whereas non-silicates have relatively simple structures but vary widely in their solubility and resistance to weathering. The non-silicates include oxides, oxyhydroxides, sulphates, chlorides, carbonates and phosphates [Fit86].

Soil nutrients (chemical elements) are of paramount importance for plant growth. In addition to the nutrients, water is also important aspect to be considered to ensure optimum plant growth. Major categories of plant nutrients are *primary nutrients* (from air such as C, O and H and from soil such as N, P and K) and *secondary nutrients* such as S, Mn and Ca. As far as micronutrients (trace elements) are concerned, Fe, Mn, B, Cl, Zn, Cu, Mo, Na, Co, Ni and Si are considered essential for plant growth. For optimum growth, a grapevine requires a balance between Ca, Mg and K. Various soil nutrients play different roles in plants to ensure balanced plant metabolism. Macronutrients such as N, K, Ca and S are required for building the plant tissue and production of proteins used

to protect plant stem and stalk against diseases [Wil98]. Moreover, Ca is most important in the soil due to its relationship with the soil pH. Mg plays a major role during photosynthesis process whereas P encourages rapid growth in seedling and early root formation [Www03].

In addition to the macronutrients, the plant also requires balanced quantities of micronutrients or trace elements. Trace elements such as Mn, Co, Zn, B and Mo are said to play an important role in grapevine nutrition [Cou84]. Mn plays a major role in plant respiration and protein synthesis while Cu is necessary for chlorophyll synthesis and also may reduce the toxicity of other elements in large concentration in the soil. Zn is involved in fruit production as well as hormone synthesis. B ensures proper sugar movements and general metabolic activities including pollen tube growth, whereas Mo is required for conversion of nitrates and is thus important in nitrogen-fixing in the soil, an important part of the cycle that makes atmospheric N available to the vines [Www03].

Chemical elements (major and trace) are known to be key indicators of wine quality [Lar05]. Thus, qualitative and quantitative determination of these elements in wines is of paramount importance. Several studies have tried to point out possible origins of elements found in wines [Esc88, Gal02, Kme05, Lar05]. Recently, a number of studies by Pohl [Poh07], Ferreira *et al.*, [Fer08], Catarino *et al.*, [Cat06] have shown that the origin of chemical elements in wine can be classified in two categories. The first category involves elements which are absorbed from soils on which vines are grown and reach wines *via* grapes. This group of elements is sometimes referred to as primary metals [Poh07]. The second category of elements found in wine (secondary metals) originate from external sources such as environmental pollution, viticultural and enological practices [Cat06]. The external source can reach grapes at different stages of vine growth or during wine making (from harvesting to cellaring) [Poh07].

From the consumer viewpoint, elemental analysis in wine is essential for assessing its quality. Specifically, the analysis is undertaken to determine the acceptable limits for export purposes, to monitor trace contaminants, to assess certain metal salts such as Ca and K [Coz08]. However, different analytical approaches are used in the preliminary studies to classify wines based on their geographic origin or grape variety from its trace composition [Mar99]. In this regard, the application of Inductively Coupled

Plasma Mass Spectroscopy (ICP-MS) technique to wine elemental analysis is extensive [Cat06]. To date, numerous studies have reported detections and quantifications of major and trace elements in various wine brands by using different analytical techniques. A study by Cozzolino *et al.,* [Coz08] reported significant concentration levels of Ca, K, Mg, P, Na, S, Fe, B and Mn in Australian wines by using ICP-MS. Another study by Kment *et al.,* [Kme05] reported the analysis results of wine from Czech Republic vineyards by using ICP-MS and Atomic Absorption Spectrometry (AAS). The results showed mutual dependence of Mg, Mn, Cs, Ba and Sr. A study by Lara *et al.,* [Lar05] by using Inductively Coupled Plasma Optical Emission Spectroscopy (ICP-OES) technique presented concentration levels of Al, Cd, Ca, Cu, Fe, Pb, Zn and Cr in wine from Argentina.

Soil pH or acidity is the measure of H^+ in the soil, and is given as $pH = -\log [H^+]$. Soil acidity varies widely from region to region and is basically influenced by both climatic and soil factors. The ideal pH for viticultural purposes should range between 5.0 to 7.5 [Saa92]. In vineyard management, soils which are found to be relatively high in acidity, liming has to be applied. Lime refers to all limestone-derived materials used to neutralize acid soil. Adding lime increases soil pH and hence increases the availability of some elements such as N, P, Ca and Mg. The levels of nutrients found in the soil vary depending on the values of soil pH.

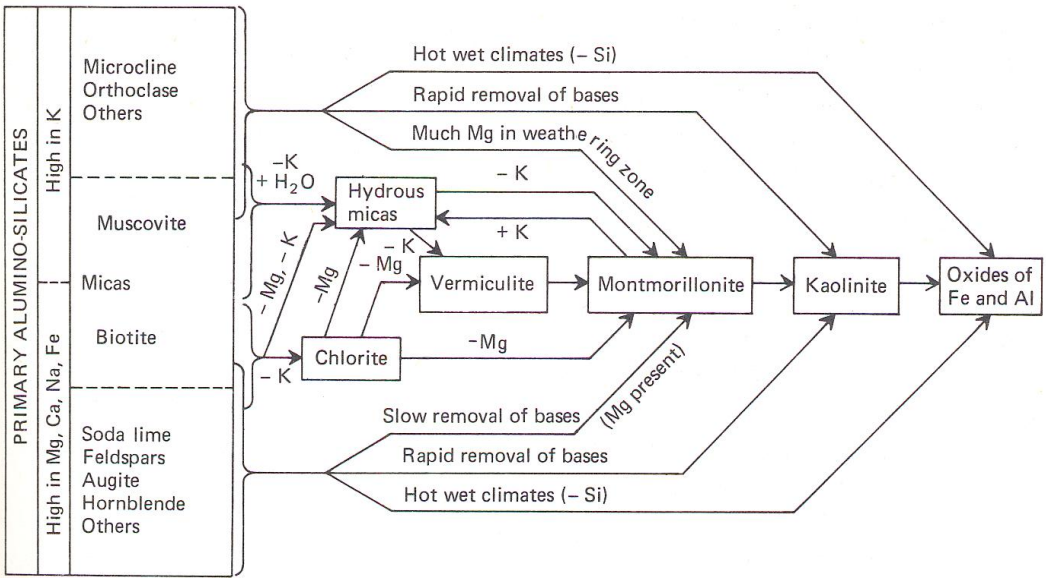

Figure 1-1: *Processes and general conditions for the formation of the various clay minerals and oxides of iron and aluminium [Bra74].*

1.2 Radiometry – some relevant background

In this section radioactivity, radioactive decay, primordial radionuclides, γ-ray interactions with matter, and soil γ-ray measurements are briefly discussed.

1.2.1 Radioactivity

Radioactivity is the spontaneous disintegration of atomic nuclei. The most common decays involve the emission of alpha (α) particles, beta (β) particles and high energy electromagnetic rays (γ-rays and *X*-rays). Many naturally occurring, heavy nuclei, with $82 < Z \leq 92$ decay by α emission, in which case a parent nucleus loses both mass and charge. An alpha particle is basically a He nucleus, thus, when an atom undergoes α decay, its atomic number decreases by 2 and its atomic mass decreases by 4. The daughter may or may not be stable, but it invariably lies closer to the region of stable nuclei which, eventually, is reached [Lil01]. An α decay process can be schematically represented as:

$$ {}^{A}_{Z}X \rightarrow {}^{A-4}_{Z-2}Y + {}^{4}_{2}\alpha + n\gamma \qquad (1.1) $$

where *X* and *Y* represents a parent and its daughter, respectively, and $n \neq 0$ in this case. Not all alpha emissions produce γ-rays.

Beta (β) particle decay takes place due to nuclear transition modes that increase or decrease the atomic number Z of the nucleus by one while the mass number remains unchanged. Unstable nuclei, either proton rich or neutron rich, decay by positive or negative β-particle emission, respectively, or by an electron capture [Lil01]. During the emission process, light particles called leptons are created leading to a more stable final product. The created particles are classified as leptons ($^{0}_{-1}\beta^{-}$, $\bar{\nu}$) and anti-leptons ($^{0}_{1}\beta^{+}$, ν). These particles are created as a result of the weak nuclear force, leading to the β decay process being relatively slow compared to transitions involving the strong force or the electromagnetic interaction [Lil01].

In β^{-} particle emission, a neutron-rich nuclide undergoes a process in which a neutron is converted into a proton and anti-neutrino ($\bar{\nu}$), a particle which interacts extremely weakly with matter. During emission, the charge on the nucleus increases by one unit. Schematically, this can be represented as:

$$^{A}_{Z}X \rightarrow {}^{A}_{Z+1}Y_{N-1} + \beta^{-} + \bar{\nu}. \qquad (1.2)$$

A β^{+} particle is called a *positron* (e^{+}) and its emission occurs in proton-rich nuclides. When a β^{+} particle is emitted, the nuclear charge decreases by one unit. During this transition, a proton is converted into a neutron, positron (β^{+}) and a neutrino (ν), which is a chargeless particle. This transition can be schematically represented as:

$$^{A}_{Z}X \rightarrow {}^{A}_{Z-1}Y_{N+1} + \beta^{+} + \nu \qquad (1.3)$$

An alternative to β^{+} decay, for a proton-rich nucleus, is *electron capture* (EC) in which a proton and an atomic electron are transformed into a neutron and neutrino. The electron is usually captured from the innermost orbit, or K shell, of the atom, a process sometimes referred to as K capture [Lil01]. Schematically, this can be represented as:

$$p + e^{-} \rightarrow n + \nu \qquad (1.4)$$

Alpha (α) and β^{-} particle emissions may be followed by emission of one or more γ-rays, which are photons of electromagnetic radiation. This emission occurs when the nucleus is unstable after the alpha and β^{-} decay. When the daughter nucleus is formed in an

excited state, it can eventually either fall directly to the ground state or descend in steps to lower energy states through emission of energy as gamma radiation (for example, in the β^- decay of $^{60}_{27}Co$ to $^{60}_{28}Ni$, two γ-rays of 1.332 and 1.173 MeV, are emitted). Gamma-rays have energies typically ranging from 0.1 to 10 MeV characteristic of energy difference between nuclear states. They are emitted at energies corresponding to the energy state transitions a nuclide may undergo when in an excited state. The γ-ray energies of interest to this study ranges from about 0.1 MeV to 3 MeV. The energy, E_γ, of a γ-ray is described as the difference in energy of nuclear energy levels:

$$E_\gamma = h\nu = E_1 - E_2 \tag{1.5}$$

where $h\nu$ is the energy of electromagnetic radiation and E_1 and E_2 represents the energy levels.

The main quantity used for quantification of radioactive nuclides is *activity*, which is defined as the rate of nuclide decay as given by the fundamental law of radioactive decay:

$$A = -\frac{dN}{dt} = \lambda N \tag{1.6}$$

where N is the number of radioactive nuclei, t is the time and λ is a decay constant, which is the probability per unit time that a given nucleus will decay. The minus sign indicates that N is decreasing with time.

The unit of activity is the becquerel (Bq), named after Henri Becquerel. The historical unit that was previously used is the curie (Ci) which corresponds to 3.70×10^{10} disintegrations per second (one curie was originally defined to be equal to the activity of 1 g of ^{226}Ra). Since the number of radionuclides in a substance diminishes in time, integrating eq. (1.6) above gives a very useful relation:

$$N(t) = N_0 e^{-\lambda t} \tag{1.7}$$

where, $N(t)$ is the number of nuclides at time t, N_0 is the number of radioactive nuclei present at time t_0. The decay constant (λ) is related to the half-life time ($t_{1/2}$) of the radionuclide by:

$$\lambda = \frac{\ln 2}{t_{1/2}} \tag{1.8}$$

Half-life is the average time, required for a given amount of radioactive nuclide to lose half of its activity. Each radionuclide has its own unique half-life that is independent of its chemical or physical state. Half-lives of radionuclides can be as small as nanoseconds and some can be as long as billions of years (see Figures 1-2 and 1-3).

Radioactive equilibrium in a decay chain occurs when each radionuclide decays at the same rate as that it is produced [Leo87]. However, radioactive equilibrium depends on the half-life of the decay product.

Consider a very often encountered situation in a radioactive decay chain in which a parent nuclide N_1 disintegrates into an unstable daughter nuclide N_2 which itself disintegrates to another unstable nuclide and eventually reaches a stable nuclide. The application of the fundamental law of radioactive decay can describe this scenario as:

$$\frac{dN_1}{dt} = -\lambda_1 N_1 \tag{1.9}$$

$$\frac{dN_2}{dt} = \lambda_1 N_1 - \lambda_2 N_2 \tag{1.10}$$

where λ_1 and λ_2 are the corresponding decay constants of the parent and its daughter nuclide respectively. N_1 and N_2 are their corresponding numbers of radioactive nuclei [Leo87]. The solution of eq. (1.10) gives the ratio of the activity of any daughter to its immediate parent in longer chains:

$$\frac{\lambda_2 N_2}{\lambda_1 N_1} = \frac{\lambda_2}{\lambda_2 - \lambda_1}\left\{1 - \exp\left[-(\lambda_2 - \lambda_1)t\right]\right\} \tag{1.11}$$

From eq. (1.11) above, secular and transient equilibrium can be achieved depending on the half-life of the parent nuclide and the daughter nuclides in the respective decay chain. For the radioactive secular equilibrium to be achieved, two conditions are necessary. First, the parent nuclide must have a half-life much longer than any of the daughter nuclides in the decay series. Secondly, a sufficiently long period of time must have elapsed to allow the in-growth of the decay products [EPA06]. Basically, the criterion for secular equilibrium is $\frac{\lambda_1}{\lambda_2} \leq\sim 10^{-4}$, i.e. when the $\lambda_2 >> \lambda_1$, then the ratio of the activities in eq. (1.11) levels off to approximately one and reaches a state of secular equilibrium. In

that situation, the activity of the daughter nuclide "grows in" to reach the activity of the parent nuclide and both activities will be equal and decrease at the same rate, thus:

$$\lambda_1 N_1 = \lambda_2 N_2 \tag{1.12}$$

Transient equilibrium between the parent and the daughter product is achieved when λ_1 in eq. (1.11) is not zero but less than λ_2 ($\lambda_2 > \lambda_1$) and the half-life of the parent nuclide is only slightly longer or about the same as the half-life of the decay product [EPA06]. This is the equilibrium that varies with time such that the activity of the daughter product peaks slightly before it starts to decay.

1.2.2 Primordial radionuclides

Primordial radionuclides are naturally present in the earth`s crust since its formation several billion years ago. These radionuclides have very long half-lives, sufficiently long that they have survived since their creation and thus, have not decayed substantially. These radionuclides can be found in soil, water and air, even in plants and human bodies. The most abundant and important long-lived primordial radionuclides with their half-lives and isotopic abundances are given in Table 1-1.

Table 1-1: Some long-lived primordial radionuclides with their half-lives and isotopic abundances [Tyk95].

Nuclide	Half-life (yr)	Isotopic abundance (%)
^{235}U	7.04×10^8	0.720
^{238}U	4.47×10^9	99.28
^{232}Th	1.41×10^{10}	100
^{40}K	1.28×10^9	0.0117

Three radioactive series (decay chains) are headed by naturally occurring unstable nuclei ^{238}U, ^{235}U and ^{232}Th [Tyk95]. These three sets are usually called the uranium series, actinium series and thorium series, respectively. The three important primordial

radionuclides considered in this study (^{40}K, ^{232}Th and ^{238}U) are generally found in low concentration levels in the earth`s crust, but the levels may significantly vary from place to place. The decay chains of ^{238}U and ^{232}Th are shown in Figures 1-2 and 1-3, respectively. In the Figures, the half-lives and decay modes of nuclides in the series are shown. The vertical arrow (blue) indicate α-decay while upward, slanted arrows (black) indicate β-decay. Radionuclides that significantly decay *via* γ-ray emission are shown in yellow boxes. ^{40}K decays directly to stable daughters (^{40}Ca and ^{40}Ar). Gamma-ray emissions are of importance in this study since the detection systems used are for γ-rays (see Chapter 2, sections 2.2 and 2.4.1). Since ^{238}U and ^{232}Th are not γ-ray emitters, their activities are deduced from the members of their decay chains ^{234m}Pa, ^{214}Pb and ^{214}Bi for the ^{238}U series and ^{212}Pb, ^{208}Tl and ^{228}Ac for the ^{232}Th series, provided that the system is closed and secular equilibrium is achieved.

All ^{238}U measurements in this thesis with the exception of ^{234}Pa measure nuclei in the decay of ^{226}Ra, since ^{226}Ra with a half-life of 1600 years may behave differently to ^{238}U in nature. Considering a situation where soil erosion occurs in the field, it is possible for ^{226}Ra to separate from the source term (^{238}U). Furthermore, ^{222}Rn, the decay product of ^{226}Ra, can escape the soil since it is a gas. Radon is contained in the laboratory samples due to sealing, but not during the field measurements.

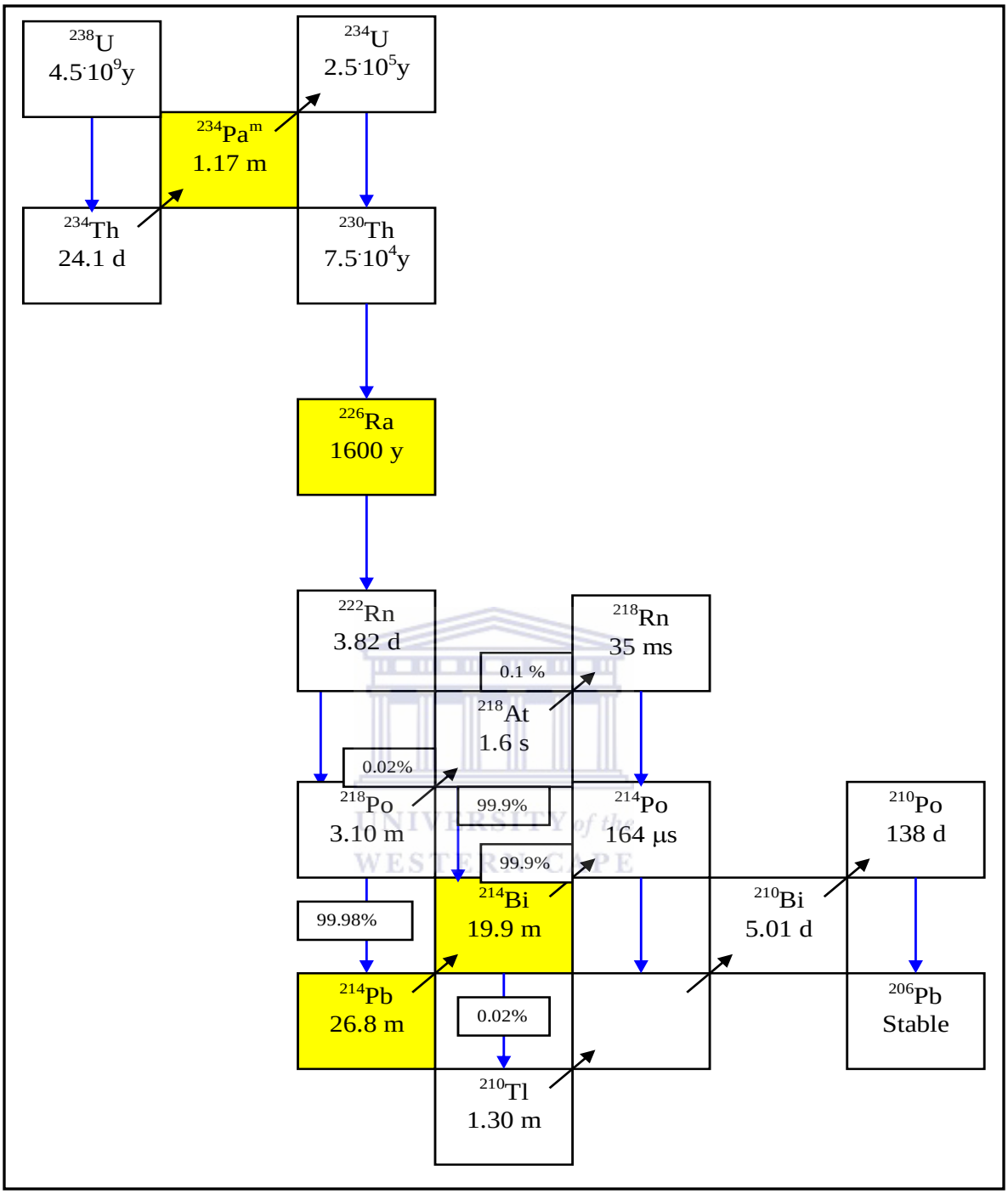

Figure 1-2: *A schematic illustration of the uranium decay series. The half-life of each radionuclide in the series is indicated in years (y), days (d), minutes (m) and seconds (s). The yellow box represents the γ-ray emitters. The vertical arrow (blue) indicate α-decay while upward, slanted arrows (black) indicate β-decay. Adopted from [Tyk95].*

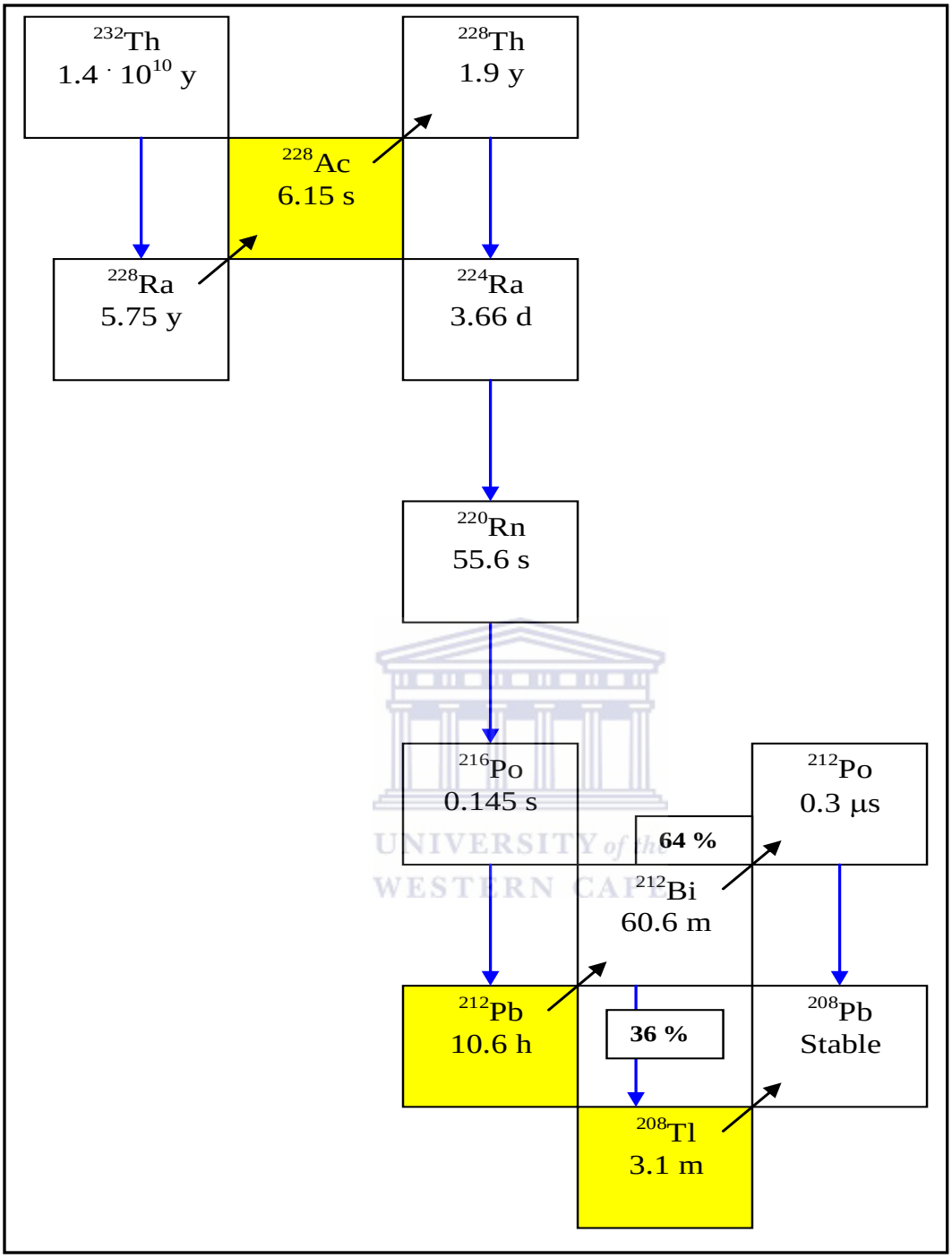

Figure 1-3: *A schematic illustration of the thorium decay series. The half-life of each radionuclide in the series is indicated in years (y), days (d), minutes (m) and seconds (s). The yellow box represents the γ-ray emitters. The vertical arrow (blue) indicate α-decay while upward, slanted arrows (black) indicate β-decay. Adopted from [Tyk95].*

1.2.3 Interaction of γ-rays with matter

When γ-rays pass through matter, various interactions with the atoms in the material can take place. Three types of interactions are important, namely *photoelectric absorption, Compton scattering* and *pair production*. The first two of these processes lead to the partial or complete transfer of the γ-ray photon energy to the electrons of the atoms in the material [Kno99]. Figure 1-4 illustrates the regions of the atomic number *Z* and the γ-ray energy (MeV) where each of the processes predominate [Tyk95].

In the photoelectric process, a photon interacts with an electron in an absorbing atom, while the photon disappears completely. The photoelectric effect is the dominant mode of interaction for low energy γ-rays (<0.5 MeV) and increases with the atomic number *Z* of the absorber material (see Figure 1-4). The probability that a photon will undergo the photoelectric effect can be expressed as a cross section (τ) per unit mass over all ranges (E_γ) and atomic number (*Z*) by:

$$\tau = CZ^{n}E_{\gamma}^{-3} \tag{1.13}$$

where n varies between 3 and 5 depending upon energies of interest and *C* is a constant [Deb01].

Compton scattering occurs between the incident γ-ray photon and an electron in the absorbing material. In this process, the photon transfers only a fraction of its energy to the electron. This mechanism is often the dominant interaction for γ-ray energies between 0.5 and 5 MeV (see Figure 1-4). In this mechanism, the incoming γ-ray is scattered at an angle θ with respect to its original direction. An approximate cross-section for Compton scattering (σ_c) per unit mass can be given by:

$$\sigma_c \propto 1/E_\gamma . \tag{1.14}$$

Since the Compton cross-section is independent of the atomic number *Z* of the absorbing material the Compton scattering is independent of the medium.

When the γ-ray quantum energy exceeds twice the rest-mass energy of an electron (1.02 MeV), pair production can occur. In this interaction mechanism, a γ-ray quantum produces an electron-positron pair. This process is dominant for energies > 4 MeV (see Figure 1-4).

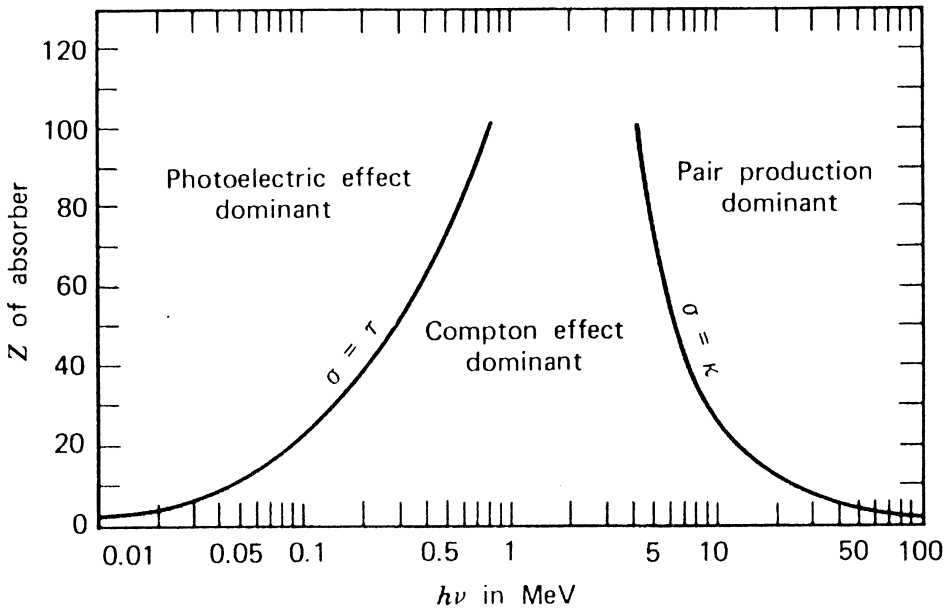

Figure 1-4: *The relative importance of the three major types of γ-ray interaction. The lines show the values of Z and hν for which the two neighboring effects are just equal [Kno99].*

1.2.4 γ-ray spectrometry of soil

There are generally two approaches to soil γ-ray spectrometry, namely laboratory-based measurements using soil samples and *in-situ* measurements. The measurements are made with either high energy resolution (e.g. using a semiconductor-based detector) or with poorer energy resolution but higher γ-ray detection efficiency (e.g. with a scintillator-based detector). In this work both general approaches and energy-resolution modes were used.

The laboratory-based measurements used in this study made use of a conventional high purity germanium (HPGe) detector (high energy resolution) which is encased in a lead shield to reduce the influence of background γ-radiation.

A relatively novel feature of this study is the use of a scintillator-based detector to perform *in-situ* γ-ray mapping of the vineyards soils being investigated (see references [Mod05, Hla07, Jos07, Van08] for recent examples of similar approaches).

In-situ γ-ray spectrometry is a rapid and powerful method for the determination of the concentrations of radioisotopes in the environment [ICRU94]. When applying it to ground-level measurements, the method usually requires a *priori* assumptions to be made about the distribution of the nuclides of interest in the soil to derive their specific activities from the spectra.

In-situ measurements of naturally occurring terrestrial γ-radiation of ^{40}K and the decay series of ^{232}Th and ^{238}U have broadly been used in the earth sciences for mapping and monitoring purposes. Various set-ups have been used to carry out *in-situ* γ-ray measurements. The approaches include motorized vehicles, manually pushed carts, remote controlled trolleys, heavy construction equipment and forklifts [Jos98]. An important aspect of the *in-situ* γ-ray measurement approach is the calibration of the detector response, for a given detector field of view, in order to extract activity concentrations from acquired γ-ray spectra.

The idealized *in-situ* measurement is shown in Figure 1-5 where a detector is situated in air at height, *h*, above an infinite horizontal soil surface. In the soil there is a certain radionuclide emitting a γ-ray with certain energy and relative intensity. Assuming that the activity distribution depends only on the depth (*z*), a photon flux will be independent of horizontal position [Kas05].

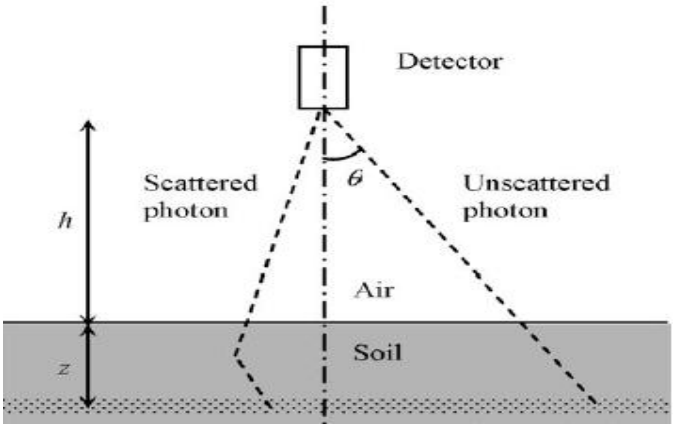

Figure 1-5: *Cross-section view of the in-situ γ-ray measurement [Kas05].*

In this study, a scintillation detector system called MEDUSA that uses a CsI(Na) crystal is used for *in-situ* γ-ray measurements. More technical details on this system are provided in chapter two. For the detection set-up used in this study, *h* is around 60 cm and *z* is up to about 30 cm. The soil activity concentrations are extracted from the *in-situ* γ-ray spectra acquired by the MEDUSA detector by a full-spectrum analysis approach [Hen01] detailed in chapter three.

The MEDUSA system was designed, built and tested by the Nuclear Geophysics Division (NGD) of the accelerator facility, *Kernfysisch Versneller Instituut* (KVI) at the University of Groningen (RUG) in the Netherlands [deM97, deM02]. This development was a result of the collaboration between KVI and British Geological Survey (BGS). The design of the γ-ray detector of this system was strongly influenced by the experiences that BGS obtained with their EEL-system in the early 1970s [Mil77, Jon94]. The MEDUSA system contains a number of modified components of an earlier EEL system to improve its sensitivity [Jon94]. This increase in sensitivity was achieved by a more efficient detector scintillator material, BGO (bismuth germanate, $Bi_4Ge_3O_{12}$) rather than the usual NaI crystal. BGO has a density of 7.13 g/cm^{-3} and high atomic number whereas the density of NaI is much lower than for BGO. Therefore, the combination of the high detection efficiency of a BGO detector, together with the advanced data analysis method makes the MEDUSA detection system one order of magnitude more sensitive than a NaI detection system [Hen01].

The MEDUSA system was initially invented with the purpose of mapping out the distribution of the natural radionuclides ^{40}K, ^{232}Th series and ^{238}U series underwater only [Lim00]. However, it was further modified for terrestrial applications, by replacing the BGO crystal with the CsI(Na) crystal which is less sensitive to temperature changes (see Appendix 1, section A1.8) and hence can be suitably used in both aquatic and terrestrial environments. The MEDUSA system can only detect γ-rays associated with the decay of radionuclides up to a depth of 30 cm below the soil surface because of self-absorption of the γ-rays within the soil.

1.3 Motivation for this study

To date, the viticulturists like other farmers use traditional soil analysis methods to assess the status of their soil for agricultural management purposes. Often the traditional techniques are laborious, time consuming, expensive and in many cases provide unreliable results. Soil plays an important role in the development of the vine and ultimately the grapes harvested from the vine. It is therefore important to characterize vineyard soils (qualitatively and quantitatively) and to study the impact of soil properties on the vines. These properties amongst others, include the soil pH, concentrations of trace and major elements, grain size and clay content. Part of the motivation of this study is to investigate whether radiometry can be used as a predictor of some soil properties.

The Western Cape Province in South Africa, is one of the leading wine-growing areas of the world. The region, known as the Cape Winelands is divided into six main wine producing regions, each offering their own unique wine route. The most popular regions are Constantia, Stellenbosch, Franschhoek, Paarl, Robertson and Wellington. Both red grapes and white grapes are produced. There are many varieties or cultivars. Cultivars are bred to obtain vines with features suitable for use in a particular microclimate and also for making a certain kind of wine [Ken83]. Of the districts mentioned the Stellenbosch district is considered by many to be the best wine-producing region in South Africa. Stellenbosch lies 45 km east of Cape Town (see Figure 1-6). The region has a large number of estates producing about 300 brands of wines in a range of styles. The climate of the Western Cape is that of the Mediterranean with characteristic winters that are wet, mild and frost-free, and summers that are long, dry and warm [Ken83].

Figure 1-6: *Map of the Western Cape showing the location of Stellenbosch [Www04].*

Previous studies by Joseph and Modisane [Mod05, Jos07] made use of *ex-situ* and *in-situ* γ-ray spectrometry to analyse vineyard soils on three vineyard blocks at the Simonsig wine estate in the Stellenbosch district (see Figure 1-6). This *in-situ* γ-ray technique was shown to allow for rapid mapping of a vineyard, with a high effective sampling density and is therefore cost effective when compared to the traditional method based on radiometrically analyzing soil samples in the laboratory. Ofcourse if the radiometry can be used to infer some soil physico-chemical parameters the value of the *in-situ* γ-ray technique can be considerably enhanced.

Joseph studied only Simonsig vineyard Block 2. He acquired only γ-ray data (*in-situ* and *ex-situ*). It should be noted that he acquired no soil physico-chemical data. Modisane studied only vineyard blocks Nuweland and Pomphuis. He acquired γ-ray data and had access to reports containing data on soil physico-chemical data and inferred soil forms for the two blocks.

Both these studies revealed statistically significant differences in the radiometric maps. An obvious question that then arose was whether the differences in radiometry are correlated with the soil physico-chemical properties. The study by Modisane [Mod05] showed significant correlations (at 0-30 cm soil depth) between ^{238}U series radionuclide activity concentrations and C, K and Mg, whereas the ^{40}K activity concentrations were found to correlate with Na, B, Mg and soil resistance*. These findings motivated this follow-up study.

1.4 Aims and objectives of this study

The aim of this study is to investigate whether the activity concentration of primordial radionuclides in vineyard soils can be used to infer some soil physico-chemical properties. If this inference can be established for some key properties there is potential to use radiometry to improve the management of vineyards. In particular, *in-situ* radiometric measurements using a detector system like MEDUSA, will then have the advantage that costs associated with traditional soil characterization can be reduced.

The scope of this study is to characterize the soil of three vineyard blocks of Simonsig wine farm. Simonsig (www.simonsig.co.za) is one of the privately owned wine estates in the Stellenbosch District and provided access to the three vineyard blocks (Block 2, Pomphuis and Nuweland) studied in this work. The estate, owned by the Malan family is situated North West of Stellenbosch (33º 52.236' S and 18º 49.582' E).

The research objectives of this study were the following:

- to determine the optimal selection of γ-ray lines associated with the ^{238}U and ^{232}Th decay series to use for the radiometric analysis of soil samples – the choice of lines should minimize the systematic effect due to coincident summing [Gar01, New08];
- to determine the potential systematic effects on radiometric results due to different soil sample preparation methods;

* Refers to the measure of salts which conduct electricity such as calcium and sodium in soil solution.

- to investigate the feasibility of using radiometry to identify different sediment groups present on the respective vineyard blocks;
- to study the correlation between radiometric results and soil physico-chemical properties;
- to study the temporal variation (over a five year period) in soil primodial activity concentrations (up to a depth of 30 cm), for the three Simonsig blocks;
- and to start investigating whether a differences in soil physico-chemical properties translate into differences in grape and wine chemical content.

The aims and objectives of this study are schematically illustrated in Figure 1.7.

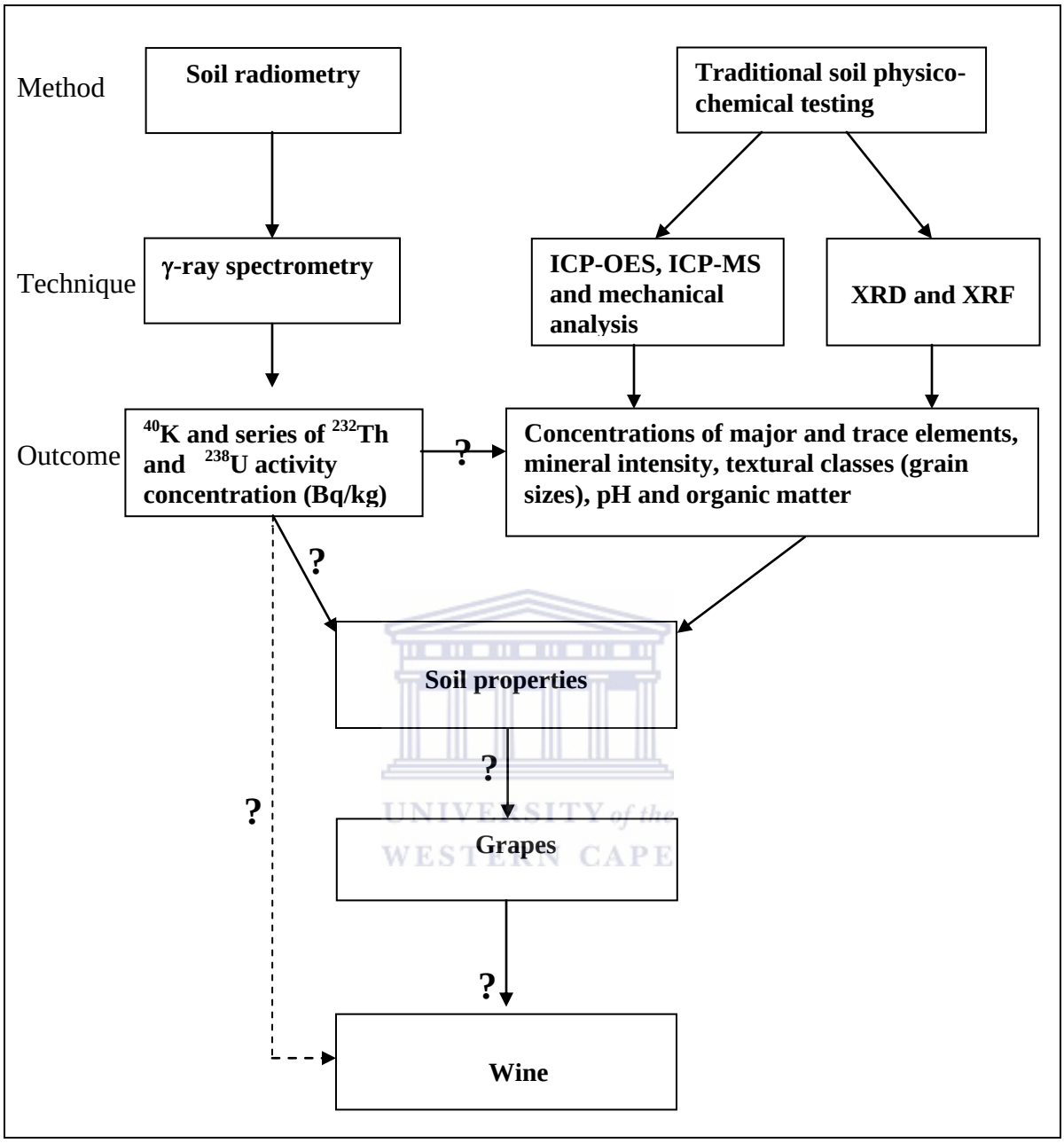

Figure 1-7: *Schematic representation showing the feasibility of how the radiometric technique can be used as an alternative to the determination of soil physico-chemical parameters significant for grape and wine production. XRD, XRF, ICP-OES and ICP-MS refers to X-ray diffraction, X-ray fluorescence, Inductively coupled plasma optical emission spectroscopy and Inductively coupled plasma mass spectroscopy, respectively. (Note: "?" refers to a question that "is there any correlation between the two parameters?").*

1.5 Thesis structure

The remainder of this thesis consists of five chapters. The measurement techniques and procedures used to acquire *in-situ* radiometric and laboratory-sample data are presented in Chapter 2. In this chapter, the set-ups of the MEDUSA and HPGe detector systems together with their associated calibration approaches are described. Furthermore, an overview of the XRD system and measurement procedure used is briefly presented. Other laboratory-measurement techniques (XRF, ICP-MS and ICP-OES) with which samples were analysed are also briefly discussed in this chapter.

In Chapter 3, the analysis procedures used on radiometric data acquired by the MEDUSA system and the HPGe detector are presented.

The results, interpretations and discussions of the laboratory-based radiometric analyses are presented in Chapter 4. In this chapter, an approach to characterize the vineyard soils based on correlation analyses is presented. Furthermore, the link between radiometry and soil physico-chemical parameters is assessed in this chapter.

Chapter 5 presents results and discussions from field-measurement data acquired from the survey of the three vineyard blocks in 2007. Radiometric maps produced from these data are compared to the maps produced from data acquired over a period of about five years before. Investigation of radionuclide AC distributions to characterize the soils is presented in this chapter and compared to results from Chapter 4. Moreover, an approach to correlate in-situ radiometric data with physico-chemical data is proposed in this chapter.

In Chapter 6 a summary of the work done and main findings for this study are presented, followed by suggested further future work.

CHAPTER 2 METHODOLOGY

In this chapter the approach and procedures that are used for the *in-situ* γ-ray mapping and in the laboratory are presented. The *in-situ* measurement is described in the following order: MEDUSA system, MEDUSA system set-up, calibration of the system set-up and data acquisition. The laboratory measurement will mainly focus on the measurement procedures with the HPGe γ-spectrometric system. Furthermore, an overview and brief discussion on X-Ray Diffraction (XRD) measurement procedure will be given.

2.1: Site description

The plots of land (vineyards) studied on the Simonsig wine farm near Stellenbosch, South Africa are located at an average altitude of about 163 m, 139 m and 141 m above sea-level, for Block 2, Pomphuis and Nuweland, respectively. Block 2 (9.2 ha) has latitude values that range between 33°51.699' S and 33°51.972' S, with longitude values ranging between 18°49.144' E and 18°49.401' E. Pomphuis block (6.4 ha) lies between latitude 33°52.113' S and 33°52.266' S, whereas the longitude values range between 18°49.121' E and 18°49.339' E. Nuweland block (5.6 ha) has latitude values that range between 33°51.762' S and 33°52.048' S, with longitude values ranging between 18°48.714' E and 18°48.839' E. Pomphuis block is approximately 0.7 km south east of Block 2, whereas Nuweland block is approximately 0.75 km and 0.8 km south of Block 2 and south west of Pomphuis block, respectively.

The plots can be classified into two physical features depending on their status during the survey period. During the November 2002 and December 2003 surveys [Jos07, Mod 05], Nuweland and Pomphuis blocks were unplanted, while Block 2 was already planted. However, during the December 2007 survey, all plots were planted along constructed ridges (rows) with a spacing of about 2.5 m (see Figure 2-1). The land terrain between ridges is characterized by growing grass, with Nuweland having young vines and tall grasses (see Figure 2-1a).

Simonsig Wine Farm has three main soil horizons, the A (characterized by organic matter), B (rich in minerals) and C (composed mainly of parent material) horizons

[Nuw03, Pom03]. The A horizon stretches from 0 - 10 cm while the B horizon follows from around 10 – 40 cm and C Horizon from 40 - 60+ cm.

(a)

(b)

(c)

(d)

Figure 2-1: *Status of the blocks during the survey (a) Nuweland block during December, 2007 survey (b) Pomphuis block during December 2007 MEDUSA survey (c) Block 2 during December 2007 MEDUSA survey (d) Block 2 during November 2002 MEDUSA survey.*

2.2: *In-situ* measurements

Rapid *in-situ* γ-ray spectrometry measurements were performed in November 2002, December 2003 and December 2007 with a γ-ray detector system called MEDUSA, an acronym for **M**ulti-**E**lement **D**etector for **U**nderwater **S**ediment **A**ctivity (see section 2.2.1). The detector and its electronics were purchased from MEDUSA EXPLORATION B.V., Groningen, the Netherlands [New04b].

A 4×4 vehicle was used for *in-situ* surveys conducted in 2002 and 2003, while a trolley was used for the December 2007 surveys in the planted vineyard blocks which could not be easily accessible by the 4×4 vehicle at the stage of mature vine plants. The trolley was designed and constructed by the iThemba LABS Mechanical Workshop (see Figure 2-4b).

2.2.1: ERL MEDUSA system

The MEDUSA system at the Environmental Radioactivity Laboratory (ERL) at the iThemba LABS is encased in an aluminum tube consisting of γ-ray detector (CsI(Na) crystal of 15 cm length and 7 cm diameter), photomultiplier tube (PMT), a Cockcroft Walton high-voltage generator (HVG), spectroscopic amplifier (Amp), temperature sensor (AD 590), pressure sensor, microphone and a telemetry board. Figures 2-2 and 2-3 shows the pictures of some units encased in the aluminium tube and schematic diagram of components of MEDUSA system, respectively. The output of the amplifier is sent to the telemetry board where the detector signal, along with signals from a pressure sensor, temperature sensor and microphone, are digitized. The microphone data are used to infer the coarseness of the sediment over which the detector moves during underwater work. The detector unit is connected to an ALADIN interface box *via* an armored co-axial cable. The ALADIN interface box that contains a data acquisition system supplied by the German company ANTARES Datensysteme GmbH. ALADIN stands for **A**NTARES **L**og **A**cquisition and **D**ata **In**terpretation system. For further details on ALADIN refer to www.antares-geo.de.

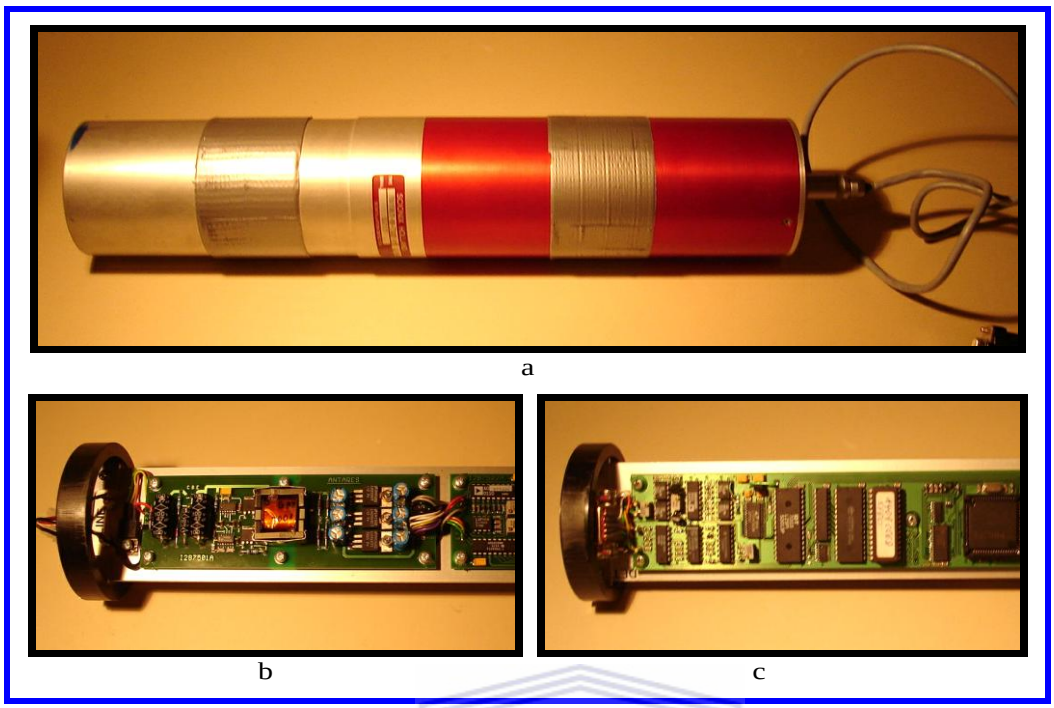

Figure 2-2: *Photographs showing physical features of some of the units encased in aluminium tube, (a) CsI(Na) crystal, PMT and HVG (b) Detector power supply board (c) probe electronics board [Hla07].*

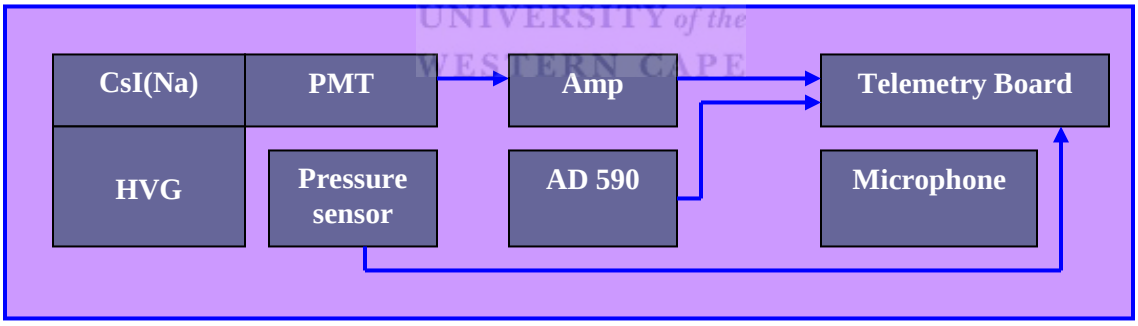

Figure 2-3: *A schematic diagram showing the components of the encased probe part of the MEDUSA system.*

For spatial radioactivity measurements, to precisely locate the measurement and sampling points, Global Positioning System (GPS) technology is incorporated in the MEDUSA system. The location of the detector is given in the form of position (latitude, longitude and altitude). The GPS unit used during this study is a Garmin GPS 76 model.

2.2.2: MEDUSA system set-up

The ERL MEDUSA detector and associated electronics for amplification and digitization of pulses, were mounted in a watertight casing and placed on a rack 60 cm off the ground on the front of a 4 x 4 vehicle during the 2002 and 2003 surveys and on a trolley during the 2007 survey (see Figure 2-4). To determine detector coordinates, the GPS receiver was placed directly above the detector on the rack and connected to the laptop computer placed on the back of the vehicle, where an extraheavy duty 12 V battery (Turbostart) and ALADIN interface box were mounted. The battery was first connected to a DC/AC power inverter (Allways300 model) with 300 W power rating to supply a required amount of power to the ALADIN box and laptop computer. However, while using the trolley, the laptop and all other components were accommodated in specially designed shelves/compartments. Figure 2-5 shows a photo of the basic physical features of the interlinking units in the MEDUSA system.

(a) (b)

Figure 2-4: *Photographs showing the ERL MEDUSA detector mounted on the 4 x 4 vehicle (a) and the portable trolley (b) used for the in-situ gamma-ray mapping.*

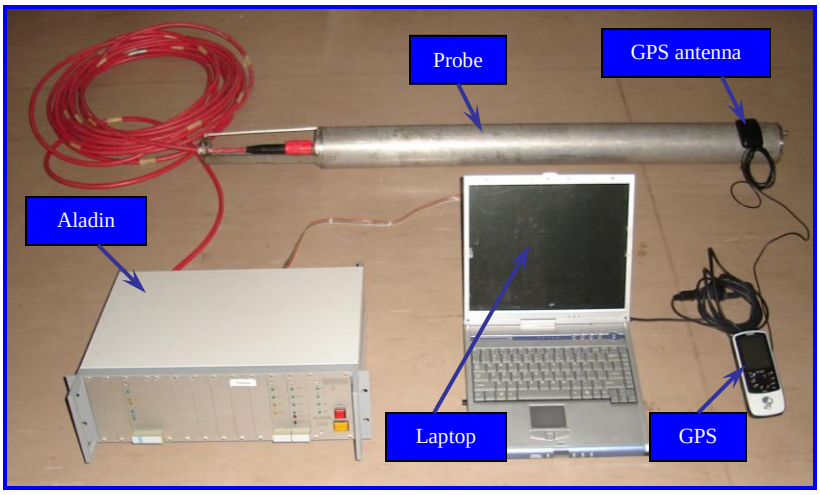

Figure 2-5: *Photograph showing the components linked in the MEDUSA detection system [Hla07].*

2.2.3: Calibration of the ERL MEDUSA system set-up

Calibration measurements were performed using the detector set-up configuration shown in Figure 2-4. To investigate normalization factors* (NF) in the vineyard blocks, the ERL MEDUSA detector was field calibrated by measuring at seven locations of the three vineyard blocks marked B5, B14, B21, P19C, P21, P22C and N9, as shown in the sampling strategy maps in Figures 2-11, 2-12 and 2-13. The selection of the calibration spots was based on the variations (from minimum to maximum count rate) in the MEDUSA count rates maps produced for each block. At each calibration spot, an approximate 30-minute stationary MEDUSA calibration measurement was made and samples were taken at 0-30 cm depth directly beneath the detector for HPGe measurements (see Appendix 1, section A1.1). Figure 2-6 shows photographs of the calibration measurements at B14 and N9. Initially, five soil samples were collected at each calibration spot marked P19 and P22 based on the sampling design presented in Figure 2-7. However, the laboratory analysis results suggested no significant difference when one sample is taken beneath the detector. Hence, one sample was collected at each point for the other calibration measurement spots.

* Refers to ratio of HPGe activity concentration to the MEDUSA activity concentration.

(a) (b)

Figure 2-6: *Photographs showing the MEDUSA calibration measurements at (a) B14 and (b) N9 (see Figure 2-11 and 2-13).*

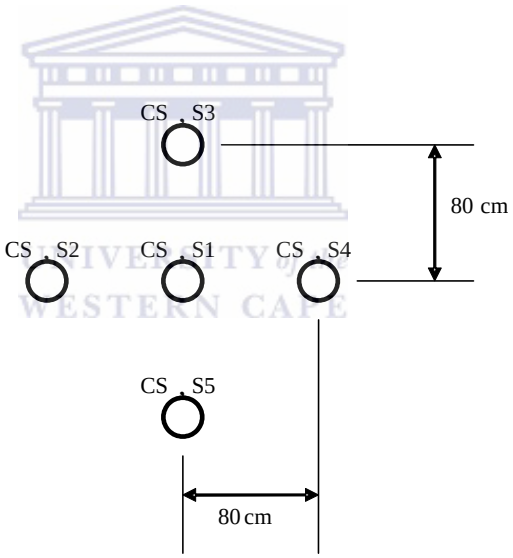

Figure 2-7: *Schematic top-view representation of the initial sampling design used for the calibration spots. The circles indicate the sampling points.*

2.2.4: Data acquisition and recording

Land surfaces of the three blocks were traversed in a grid-like pattern every 3rd row at a speed of ~2 $m.s^{-1}$ (with a spacing of 20 m [Mod05]) and 0.8 $m.s^{-1}$ (with a spacing of 5±1 m) by vehicle and trolley, respectively. The spatial data from a GPS signal receiver, pressure, temperature and count rate were recorded onto a laptop computer every 1 s whereas γ-ray spectra (0–3 MeV) were recorded every 2 s, respectively. These data were automatically written to a file *via* the MEDUSA Data Logger (MDL) software program installed on the laptop computer.

2.3 Sampling

The type of sampling approach used in this study was purposeful [Mar93], based on variations observed in radiometric maps produced from the MEDUSA data acquired in the 2002 and 2003 surveys. Soil sampling was performed after the *in-situ* survey in 2007.

2.3.1 Soil sampling

Soil sampling at 0-30 cm depth (Figure 2-8) took place at locations marked B1-B23, P1-P25 and N1-N24 for Block 2, Pomphuis and Nuweland blocks, respectively (see Figures 2-11 to 2-13). However, additional samples to investigate depth variations to 30-60 cm depth were collected at B18-B23. Figures 2-11, 2-12 and 2-13 indicate the interpolated MEDUSA detector count rate maps showing all sampling points used in this study. Samples were taken by using large and small hand spades while measuring sampling depth with a tape measure. At each sampling point, about 3 kg of sample was collected and packed into polyethylene bags and transported to the Environmental Radioactivity Laboratory (ERL), iThemba LABS.

The conventional geological way of sampling was not used in this study since the top soil (0-30 cm) required for sampling in this work is slightly mixed up due to ploughing.

Figure 2-8: *Soil sampling process at P21 Pomphuis block.*

2.3.2 Grape sampling

The sampling process (Figure 2-9) involved four locations of block 2 (9.2 ha) marked B1, B6, B16 and B17 (see Figure 2-11). At each location, about 1.5 kg of grapes were sampled. The sampling design used in each location is shown in Figure 2-10.

Figure 2-9: *Grape sampling process at B14 Block 2.*

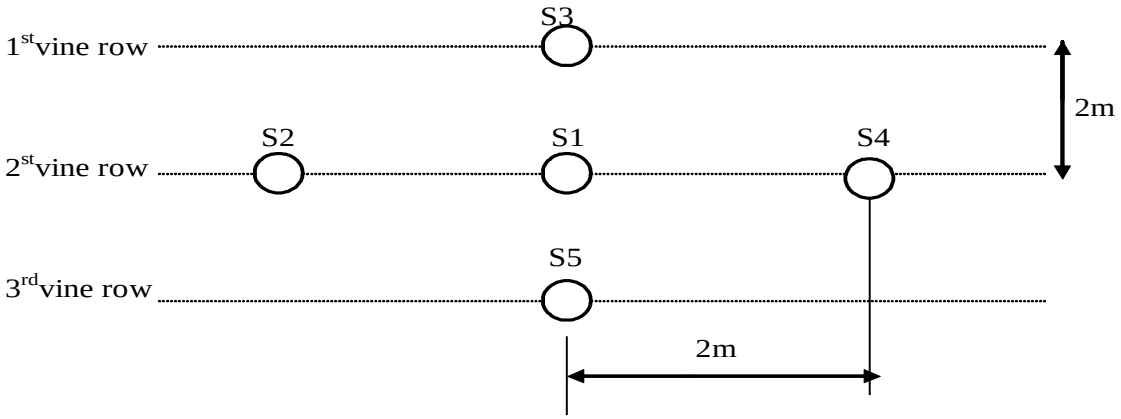

Figure 2-10: *Grape sampling design for each sampling location. The circles marked with S1, S2, S3, S4 and S5 indicate the sample units forming a representative composite sample of each sampling location.*

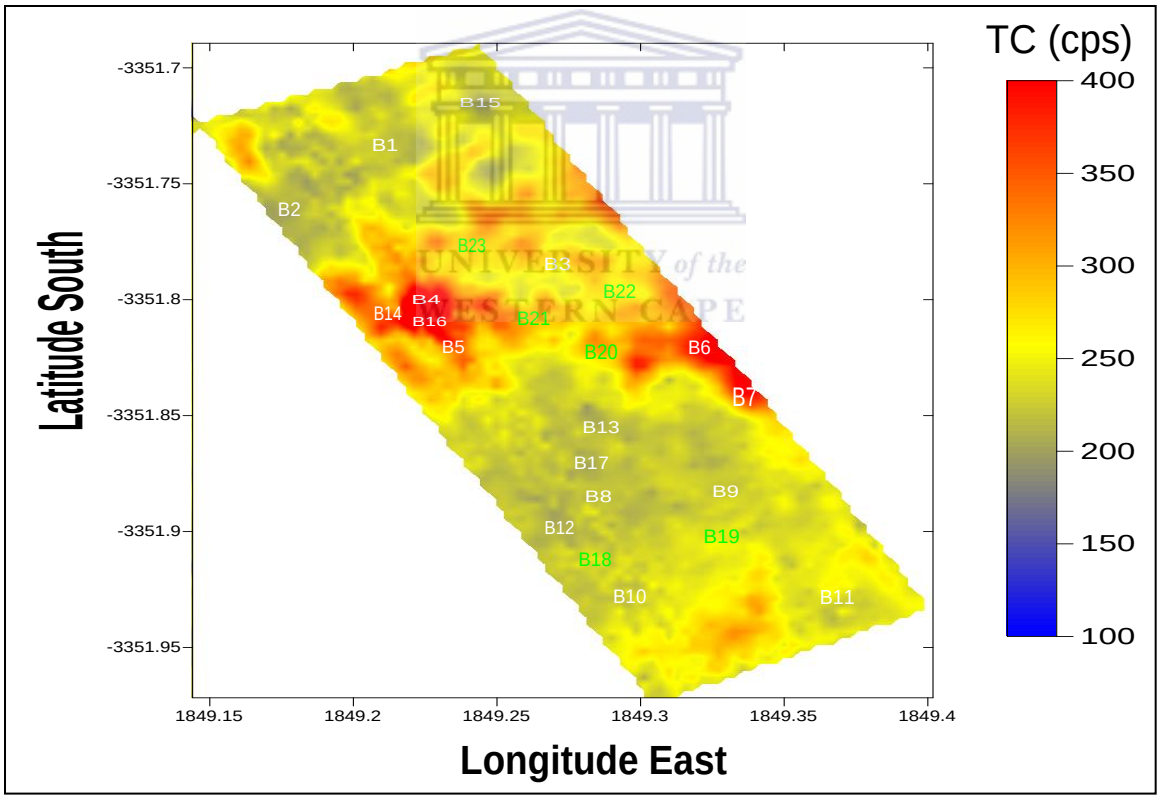

Figure 2-11: *Interpolated ERL MEDUSA detector total count-rate (TC) map for Block 2 showing the soil sampling locations at 0-30 and 30-60 cm depths. Locations marked in white indicate 0-30 cm depth sampling whereas locations in green indicate both sampling depths. This map was made from data acquired in 2002 [Jos07]. (Note: The MEDUSA-software algorithm gives the latitude and longitude in the format xxyy.yy instead of the usual xx˚yy.yy' where xx and yy.yy correspond to degrees and minutes, respectively).*

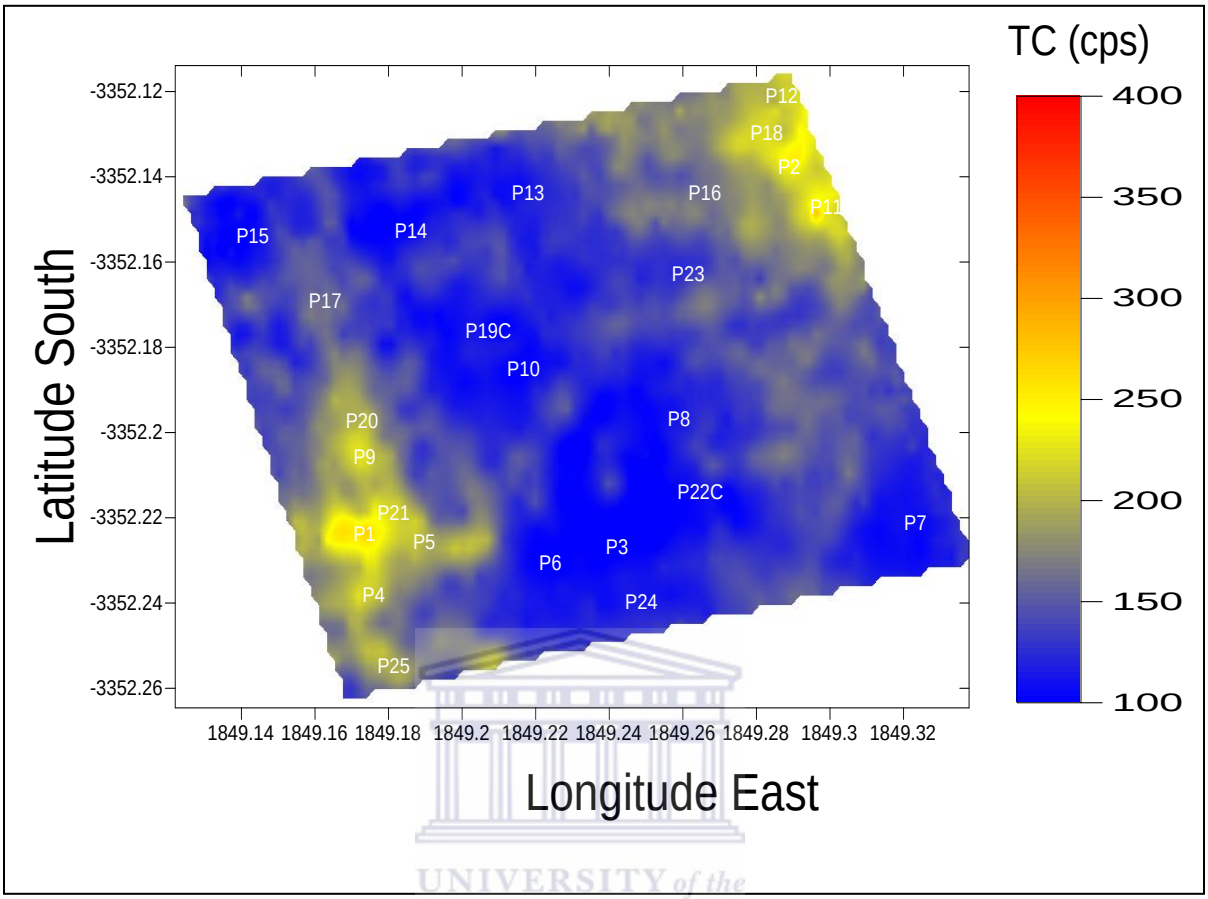

Figure 2-12: *Interpolated ERL MEDUSA detector total count-rate (TC) map for Pomphuis block showing the soil sampling locations at 0-30 cm depth. This map was made from data acquired in 2003 [Mod05]. (Note: The MEDUSA-software algorithm gives the latitude and longitude in the format xxyy.yy instead of the usual xx˚yy.yy' where xx and yy.yy correspond to degrees and minutes, respectively).*

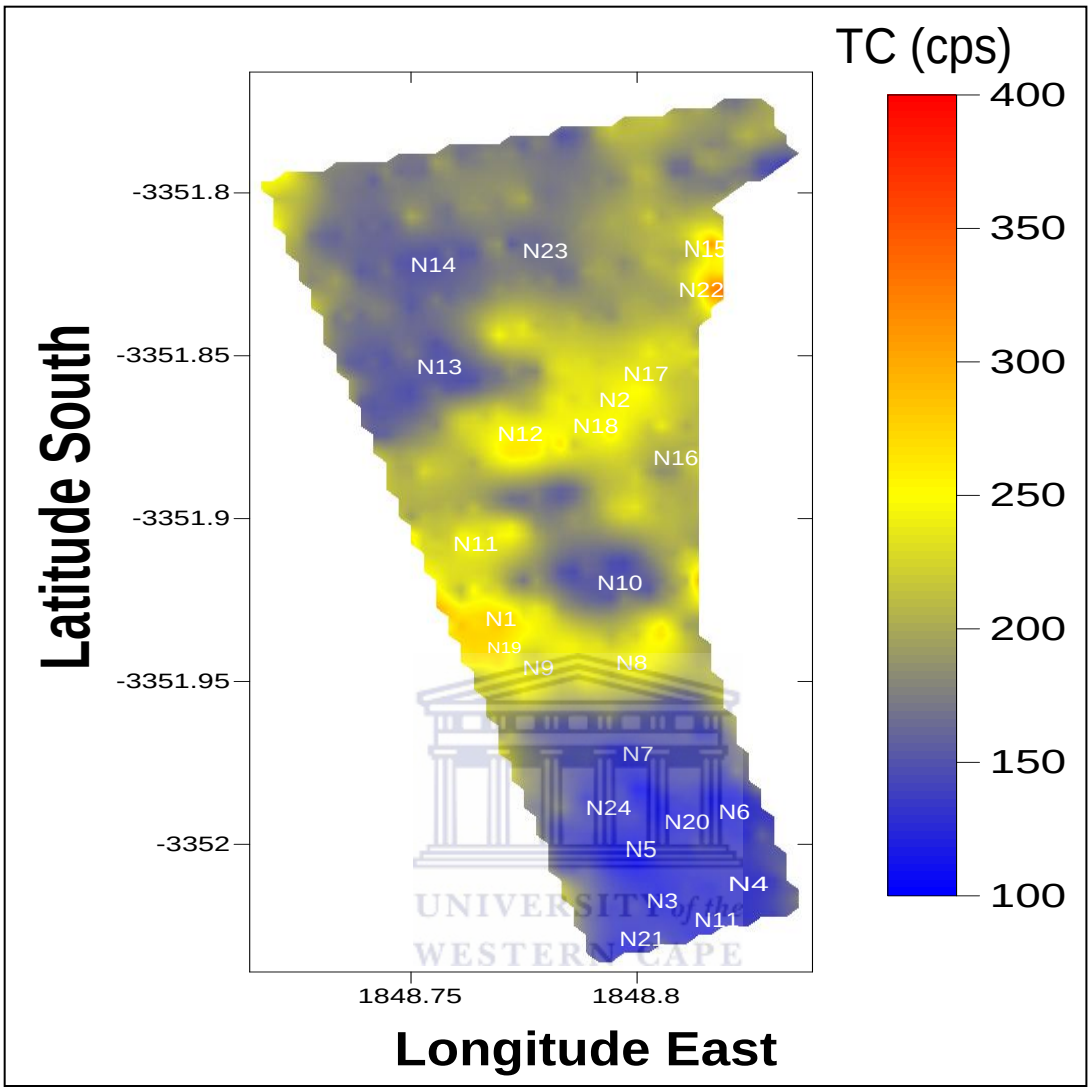

Figure 2-13: *Interpolated ERL MEDUSA detector total count-rate (TC) map for Nuweland block showing the soil sampling locations at 0-30 cm depth. This map was made from data acquired in 2003 [Mod05]. (Note: The MEDUSA-software algorithm gives the latitude and longitude in the format xxyy.yy instead of the usual xx˚yy.yy' where xx and yy.yy correspond to degrees and minutes, respectively).*

2.4 Laboratory-based measurements

Soil and grape samples collected were brought to the ERL at iThemba LABS. Before preparing soil samples for HPGe measurements, each sample was sub-sampled *via* coning and quartering as shown in Figure 2-19 to obtain about 300g for XRF, XRD, ICP-MS, ICP-OES and mechanical analyses as shown on the flow chart in Figure 2-14. The remaining samples were then prepared for radiometric analysis by HPGe detector at the ERL. XRD analysis was carried out at the Material Science Department Laboratory at

iThemba LABS. XRF and ICP-MS analyses took place at the Department of Geology, University of Stellenbosch whereas ICP-OES and mechanical analyses were conducted at BEMLAB, a commercial laboratory in Somerset West (www.bemlab.ac.za).

Grape samples were taken to the Agricultural Research Council (ARC Infruitec-Nietvoorbij) for wine production. The wine samples produced were then taken to BEMLAB for chemical content analysis.

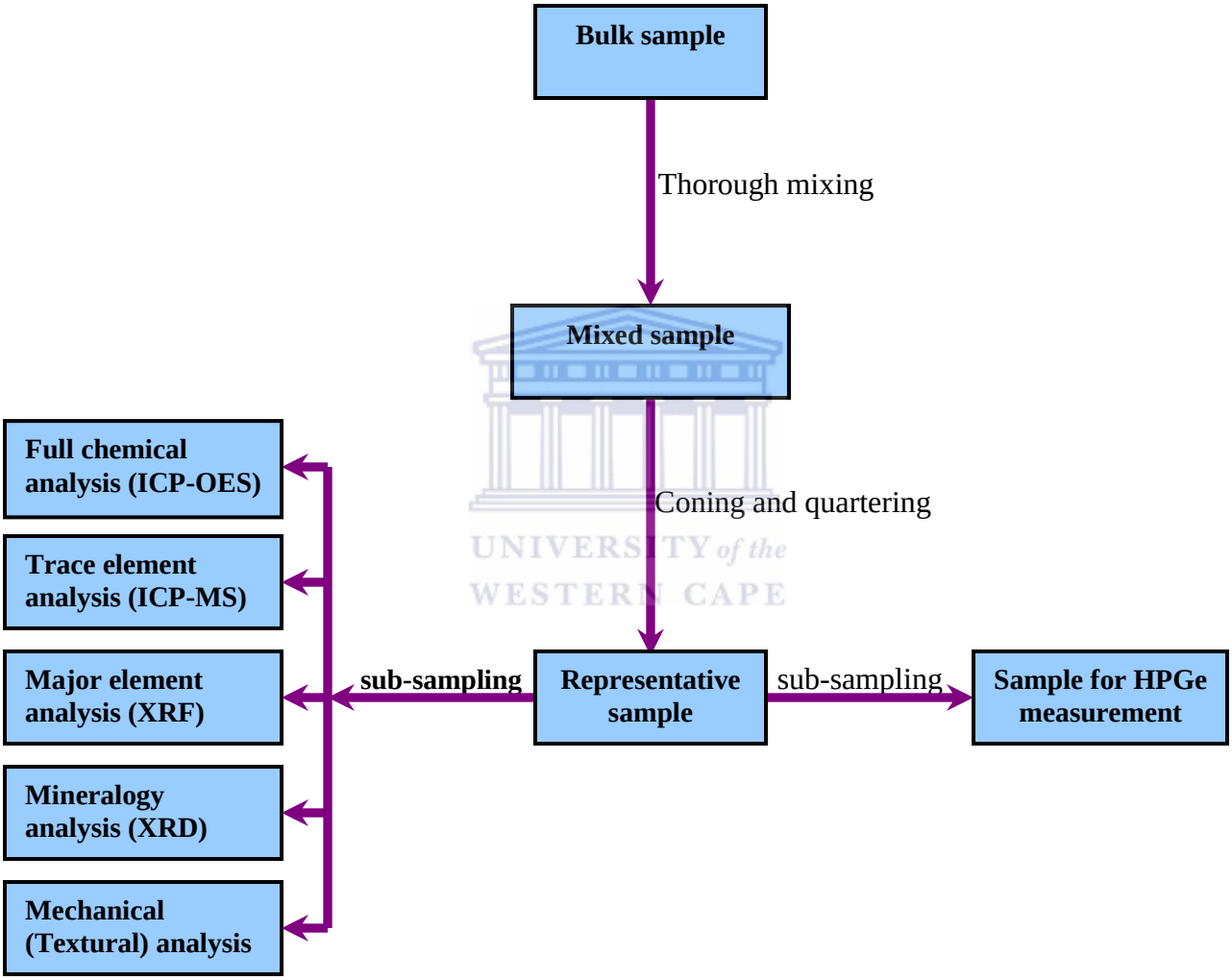

Figure 2-14: *Flow diagram showing soil sub-sampling processes for ex-situ measurements.*

2.4.1 Overview of the ERL HPGe detector system

The hyper-pure germanium (HPGe) detector, used for this study is a lead-shielded Canberra *p*-type model GC4520 with a built-in pre-amplifier. It has a closed-ended coaxial configuration, in which only part of the central core is removed and the outer electrode is extended over one flat end of the cylindrical crystal [Kno99]. It has a crystal diameter of 62.5 mm and a length of 59.0 mm. The detector has a 45% relative efficiency at 1332 keV with a 2.2 keV FWHM energy resolution at the 1332 keV γ-line of ^{60}Co. The HPGe crystal is housed in a rigid cryostat with a LN_2 dewar to inhibit thermal conductivity between the crystal and the surrounding air. The detector is operated at liquid nitrogen (LN_2) temperatures (77 K) to prevent thermally-induced leakage currents which would result from its small band gap (0.7 eV) [Leo87, Kno99]. A capacity of about 20 litres of LN_2 in the detector dewar is sufficient to allow for weekly filling. The detector crystal is enclosed in a Pb castle, approximately 10 cm thick, for shielding against background radiation. Figure 2-15 illustrates the HPGe detector system set-up. The main components of the system are detector castle, detector bias supply (SILENA model 7716), preamplifier (model 2002CSL), amplifier (model ORTEC 572) and multi-channel analyzer (MCA) and desktop computer (intel celeron™, processor 1.70 GHz). In the interior of the Pb castle, there is a Cu lining of about 2mm thick to absorb X-rays emanating from the Pb [Deb01, Mal01]. The ERL HPGe detector operates at a bias voltage of +3500 volts. Figure 2-16 is a photograph showing the ERL HPGe detector inside the Pb castle lined with Cu. Pb is the most widely used material in shielding detectors because of its high density (atomic number, *Z* is 82).

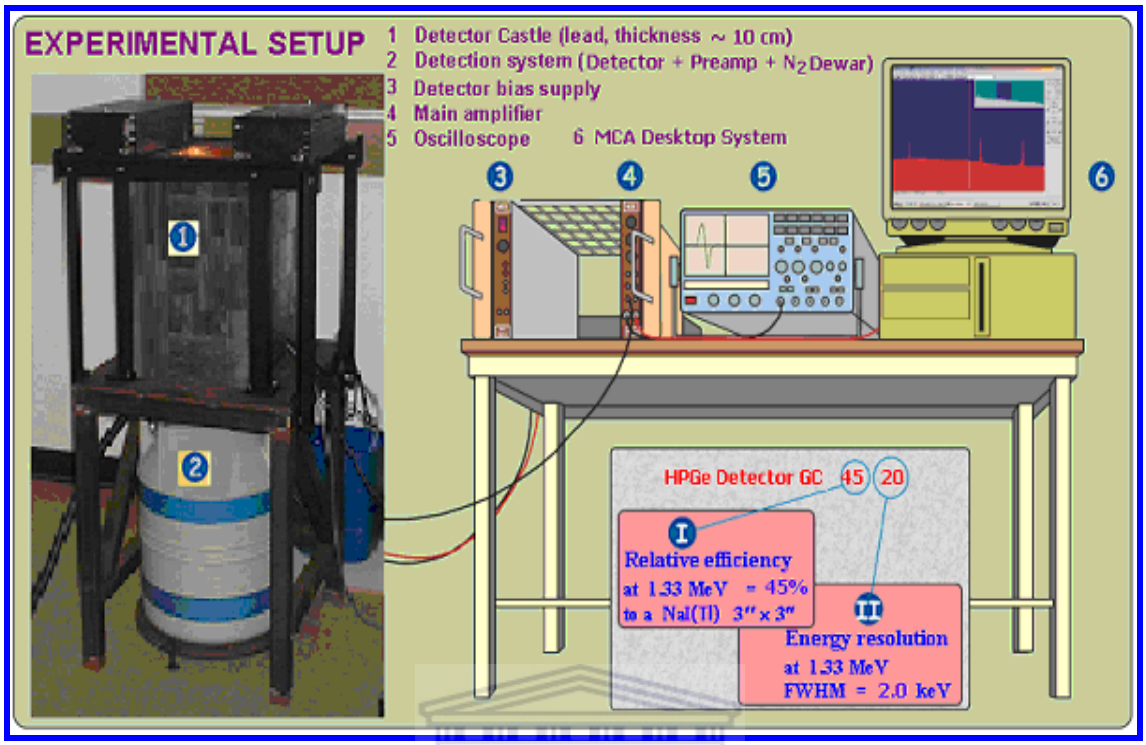

Figure 2-15: *Schematic illustration of the experimental setup for the ERL HPGe detector system. Photograph adopted from reference [Dam05].*

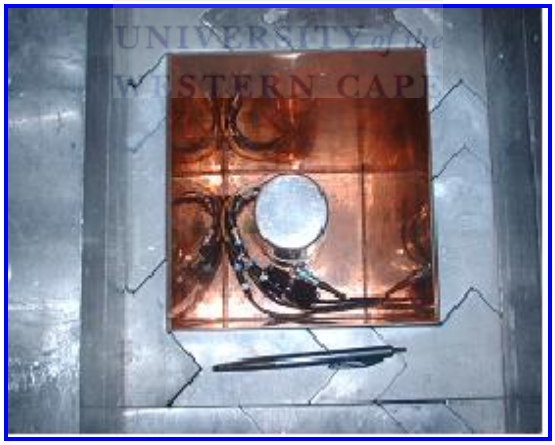

Figure 2-16: *Picture showing a top view of the ERL HPGe detector set-up.*

To collect the charges formed in the detector, a bias-voltage must be supplied over the detector [Deb01]. Weak signals from the detector crystal are amplified by the pre-amplifier before they are sent to the main amplifier. The pre-amplifier is located close to the detector so as to minimize capacitance which reduces signal-to-noise ratio [Leo87].

To further reduce the electronic noise, the input stages of the preamplifier are cooled along with the detector [Kno99]. At the main amplifier (gain drift $\leq \pm 0.0075\%/^{o}C$ for 0 to $50^{0}C$; DC level $\leq \pm$ 50 $\mu V/^{0}C$ for 0 to $50^{0}C$), the pulses are shaped and increased in size. Pulses from the amplifier are supplied to the Multi-channel analyzer (MCA), which comprises an analog-to-digital converter (ADC), digital spectrum stabilizer (DSS), single channel analyzer (SCA) and multi-channel scalar (MCS) [Oxf97]. The basic function of an ADC is to produce a digital code (or number) at its output that is proportional to an analog voltage supplied to its input [Kno99]. All the digitized pulse heights are finally stored as a spectrum file containing counts and channels. For this study, two types of MCA system, with their software packages were used. The first was an OxfordWin (Oxford Instruments Inc.) MCA and software (version 3.80). The second was a Palmtop MCA (MCA 8k-01) from the Institute of Nuclear Research of the Hungarian Academy of Sciences (ATOMKI), 2005. The two softwares packages were used for data acquisition and γ-spectral analysis.

2.4.1.1 Energy calibration

In γ-ray spectroscopy, the pulse height scale must be calibrated in terms of absolute γ-ray energy if the energy of peaks in the spectrum is to be accurately identified. Basically, the energy calibration constitutes the relationship between the peak position in the MCA spectrum and its corresponding γ-ray energy. At the ERL, the detector is energy calibrated weekly. This is achieved by measuring a standard γ-ray reference source with precisely known energies and comparing it to the measured peak position. A standard IAEA reference material, Thorium Ore (RGTh-1) sealed in Marinelli beaker is used for energy calibration, with a preset spectrum acquisition time of 1800 seconds. Accurate energy calibration involves a standard source with γ-ray energies that are not widely different from those to be measured in the unknown spectrum [Kno99]. Once energy calibration points are established over the entire energy range of interest, the full-energy peak (FEP) is represented by a linear function of channel number by using the least-square fitting of the form;

$$E_i = B*C_i + E_0 \qquad (2.1)$$

where E_i is the energy corresponding to the channel number C_i. The parameters B and E_0 are gradient and intercept of the calibration line, respectively. In the MCA system, one is able to specify the energy associated with each relevant centroid channel corresponding to a particular region of interest. Figure 2-17 shows the energy calibration plot (energy versus channel). The γ-ray energies used for the calibration are 0.129 MeV, 0.209 MeV, 0.338 MeV, 0.583 MeV, 0.911 MeV and 2.614 MeV

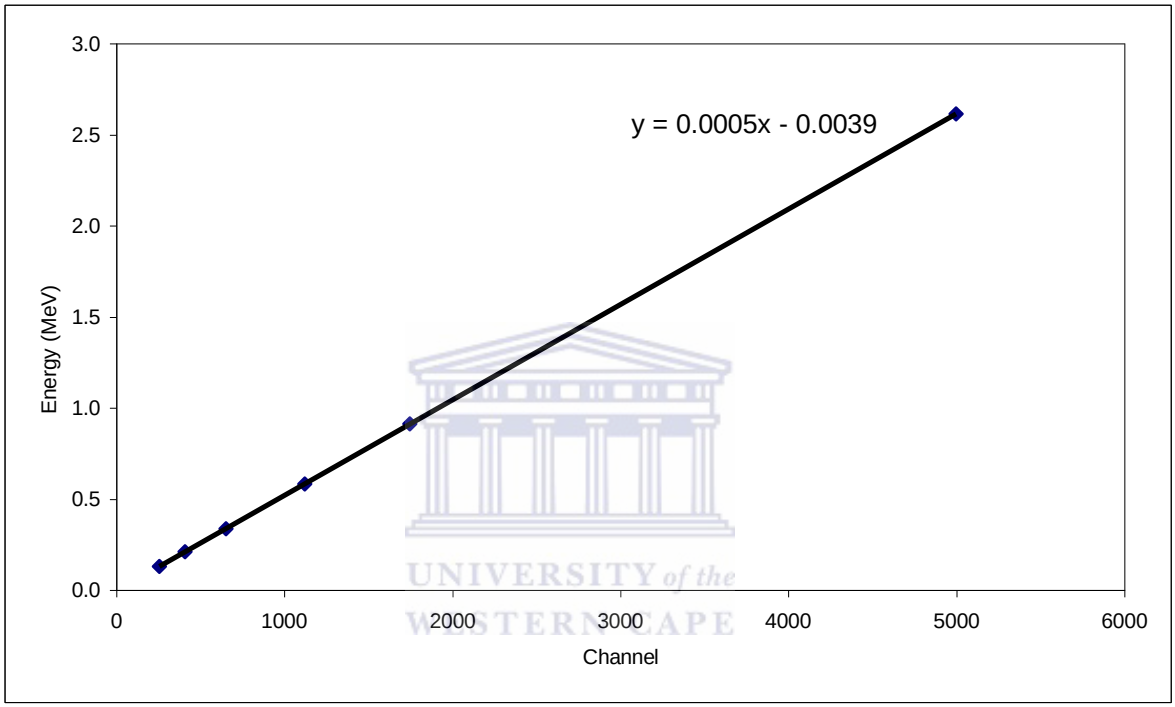

Figure 2-17: *An example of a plot of γ-ray energy versus spectrum channels used for the energy calibration of the HPGe system.*

2.4.1.2 Efficiency calibration

To quantitatively determine the concentrations in a sample measured with the HPGe detector with a windows analysis (WA) method, the associated absolute full-energy peak (FEP) detection efficiency response is required. This is the number of FEP counts detected by the HPGe detector relative to that emitted by the source [Kno99]. In the case of low-level environmental measurements with a volume geometry, much care has to be dedicated to the efficiency calibration of the spectrometer used because the absolute FEP efficiency is a complicated function of many parameters, such as the energy of γ-ray, the dimension of the detector, the dimensions of the source, the geometrical

arrangement of detector and source, the density of the sample and its chemical composition [Sha97]. In this study, this response was measured for each sample using γ-ray lines associated with the decay of ^{232}Th series and ^{238}U series radionuclides present in the sample, and the 1460.8 keV ^{40}K line as measured with a KCl source (16259 Bq.kg^{-1} ^{40}K). This is similar to the approach described in reference [Cro99] and [New08]. The method involves first generating a relative photopeak efficiency curve for each sample, then the absolute photopeak efficiency response can finally be determined by scaling the relative curve to match the measured absolute photopeak efficiency at 1460.8 keV obtained using the KCl source which has a volume matching that of the sample. More details on the efficiency calibration are presented in the sample analysis, Chapter 3 (section 3.2.1).

2.4.1.3 Sample preparation and measurements

Samples were contained in pre-weighed trays and weighed on a scale Sartorius AG model EA6DCE-1, then oven dried in the (Eco Therm^{s} LABOTEC) oven overnight at 105°C to remove moisture. Samples were again weighed after drying and their weights recorded in the sample preparation book. All samples were ground by using a pestle and mortar to ensure the homogeneity of the sample. Moreover, rocks and stones contained in each soil sample were crushed to achieve true representative samples (see Figure 2-18a). All samples were sieved through a mesh (2-mm diameter holes) to remove uncrushed organic materials, stones and lumps (see Figure 2-18b).

(a) (b)

Figure 2-18: *(a) crushing and grinding soil samples by using pestle and mortar (b) sample sieving through 2mm mesh size.*

After sieving, the samples were split by coning and quartering. This process is aimed at ensuring that there is true representation of all sample grain sizes when transferring samples into the Marinelli beakers (see Figure 2-20a). Opposite quarters of samples in Figure 2-19(b) were to be transferred into the Marinelli beaker for analysis.

(a) (b)

Figure 2-19: *(a) Coning process (b) a quartered sample.*

After coning and quartering processes, the samples were transferred into a pre-weighed Marinelli beaker (1-litre polyethylene from AEC-Amersham, type 1W) (see Figure 2-20a) and then weighed to obtain sample mass by subtracting the mass of the empty beaker from that of the filled one. A copper lid (~2 mm thick) was used as an extra lid (for radon sealing) to cover the sample by placing on top of soil sample inside of the Marinelli beaker before sealing. Samples were then sealed with silicone (Bostik Bath type) to keep radon in the Marrinelli beaker (see Figure 2-20b) and eventually achieving secular equilibrium between the γ-emitters in the uranium (mainly ^{226}Ra, ^{214}Bi and ^{214}Pb) and thorium (^{228}Ac, ^{208}Tl and ^{212}Pb) decay series (see Appendix 1, section A1.4). After being sealed for at least 21 days to achieve the secular equilibrium, the samples were each counted by placing the Marinelli beaker directly over the upward facing HPGe detector to allow the largest quantity of sample to be closely presented to the active volume of the detector. A Marinelli beaker filled with tap water was used to measure the background spectrum for about 67 hours to be used in the data analyses. Soil samples were each measured for a minimum of 10 hours under the same measuring parameters as

for the efficiency measurements. Investigations of systematic effects associated with sample preparations are presented in Appendix 1, section A1.3.

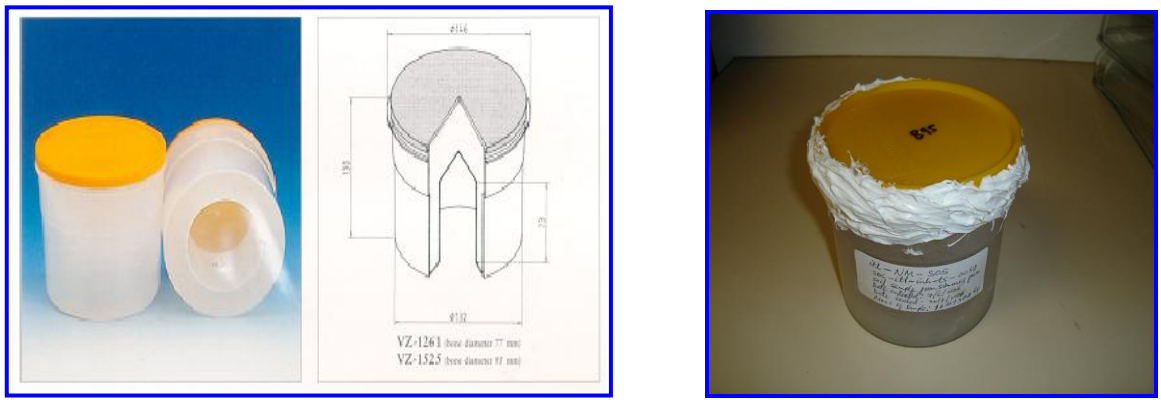

(a) (b)

Figure 2-20: *(a) The Marinelli beaker geometry used for measuring soil samples (b) Picture showing a sealed and labeled soil sample.*

2.4.3 X-Ray Diffraction (XRD)

As previously stated, XRD soil mineral characterization (mineralogy) of samples collected from the three blocks was performed at the Materials Research Department (MRD), iThemba LABS.

2.4.3.1 An overview of the MRG diffractometer system

The instrument used for the XRD measurements is a D8 Advance diffractometer from BRUKER AXS. The measurements take place in a locked coupled mode by making a θ-θ scan. The tube used provides Cu-K_α radiation (λ $K_{\alpha 1}$ = 0.15406 nm) which is detected with the Lynx-Eye detector, a Si-strip detector with 196 channels. The BRUKER unit consists of the X-ray generator, collimators, sample holder, detector and desktop computer (see Figure 2-21).

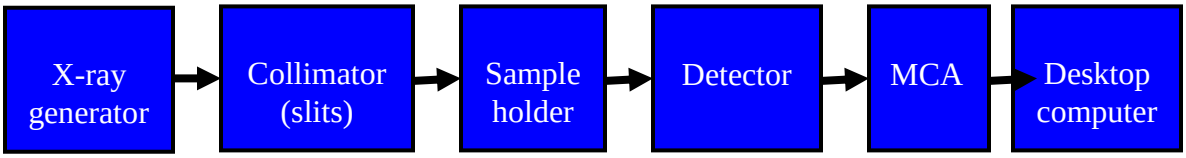

Figure 2-21: *Schematic diagram showing the linkage between the MRD diffractometer components.*

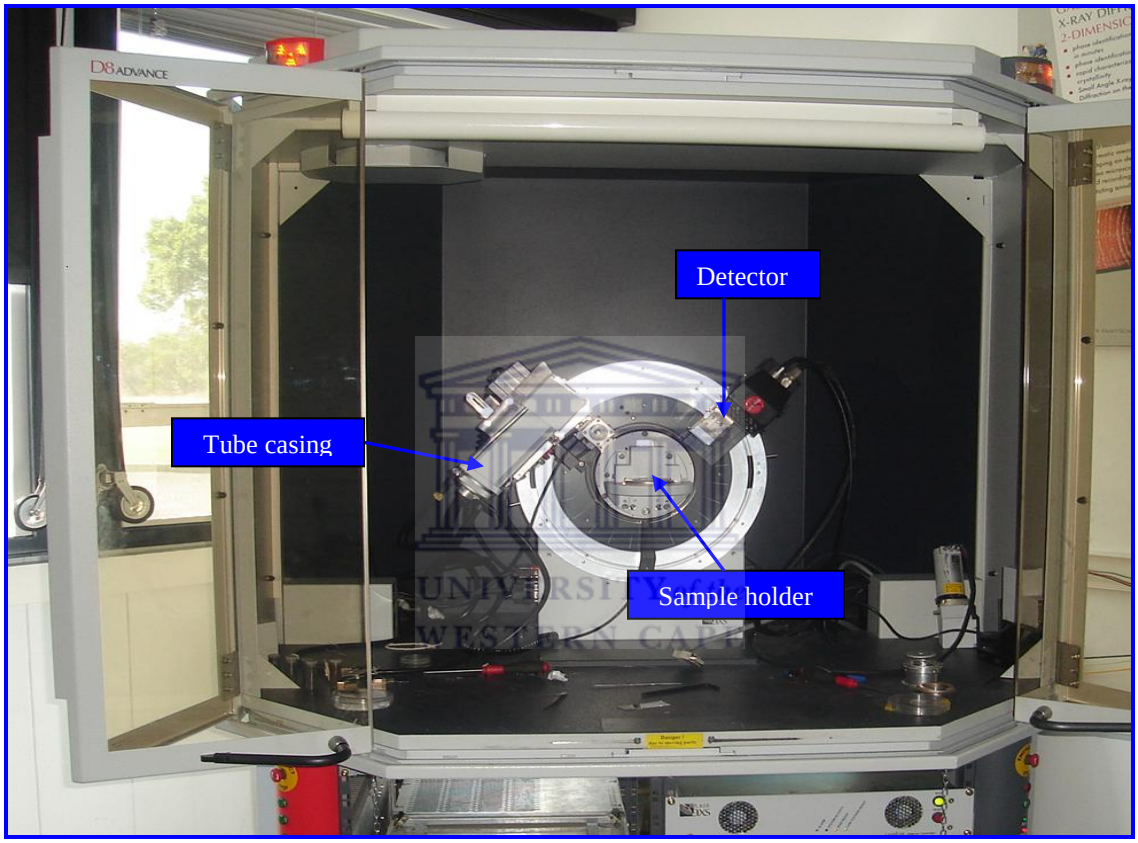

Figure 2-22: *Photograph showing the main components of the MRG diffractometer system.*

2.4.3.2 Sample preparation and measurements

Approximately 200 g of each sample was sub-sampled from bulk samples *via* coning and quartering. The samples were air-dried and then ground to obtain very fine powder by using pestle and mortar. Distilled water was used to clean the pestle and mortar to avoid cross-contamination between samples during grinding.

To ensure true representativeness of the samples to be analyzed, coning and quartering of each sample was repeated to obtain about 2 g required for analysis. During the measurements, the samples were placed on the sample holder (Corning glass) positioned between the X-ray tube and the detector. Figure 2-22 shows the photograph of the main components of the MRG diffractometer system.

The X-ray tube was operated at a voltage of 40 kV and a current of 40 mA. The measurement range (2θ) used was 15-80° with an increment (Δ2θ) of 0.03 degree/step and measurement times of 10 sec/point for each sample.

The EVA software package from BRUKER was used to analyse the diffraction patterns. This includes a Powder Diffraction File (PDF) database 1998 from the International Centre for Diffraction Data (ICDD). Moreover, the software has an option of eliminating duplicates, thus, the list of results will contain additional phases, which are important in the identification process [Bru03]. The phase content of each sample was obtained from searching the software database for all possible phases leading to the identification of all peaks present in the diffraction pattern. Search results were displayed in various colour codes showing phases of minerals identified in each sample, hence achieving qualitative analysis of soil minerals. The selection criteria of soil minerals searched for were based on data of common soil minerals previously published [Bol79, Spa95, Tan98, Kab01].

2.4.4 Other laboratory-based measurements

The procedures used for preparations, measurements and analyses of physico-chemical soil parameters with XRF, ICP-OES, ICP-MS and mechanical (textural) analysis are based on standard methods described elsewhere [Van66, Dym95, Roh86, Edg88, Jar92, New96, Soi99].

As discussed in section 2.4, soil samples for XRF, ICP-OES and ICP-MS analyses obtained *via* coning and quartering were first sun-dried and then sub-sampled to obtain sample duplicates for statistical checks. The representative samples were then sent to the respective laboratories for analyses (see section 2.4).

CHAPTER 3 DATA ANALYSIS

This chapter discusses the details on how data acquired were analysed. It covers the analysis and interpretation of *in-situ* and laboratory-radiometric measurement data.

3.1 In-situ data analysis

The MEDUSA data are stored directly in an MDL file during acquisition. MDL stands for **M**EDUSA **D**ata **L**ogger. The MDL program stores the acquired data with an extension of the form .mxx files, where the xx refers to the number of MDL file acquired counting as 01, for the first MDL file, 02 for the second MDL file and so on. Two other MEDUSA software programs are used to complete the analysis process. The programs are MEDUSA Data Synchronizer (MDS) and MEDUSA Post Analysis (MPA). Figure 3-1 shows a flow diagram of the analysis procedure from one software program to another.

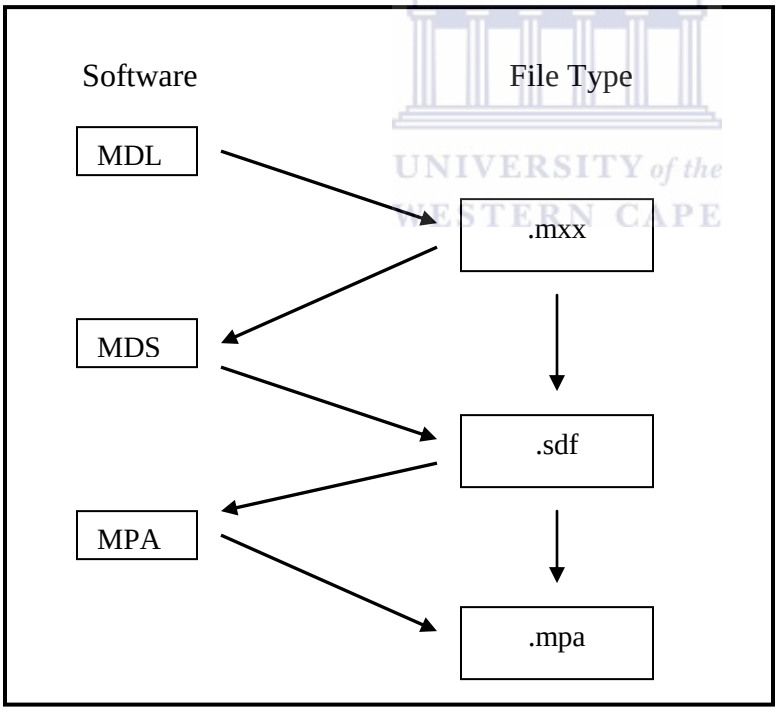

Figure 3-1: *Flow diagram showing the procedure for analysing MEDUSA-acquired data.*

3.1.1 Data synchronization

The MDL acquired data are in an unsynchronized format due to the difference in acquisition rate between γ-ray spectra data (acquired every 2 seconds) and auxiliary data acquired every second (see Table 3-1). The MDS computer program is used to synchronize the acquired data such that a one-to-one correspondence is created between each γ-ray spectrum and the associated auxiliary data set acquired. During the synchronization process, every file of the form .mxx was loaded onto MDS and its contents displayed. Before running the synchronization, action settings were first specified in which the spectrum data field was first marked with the *synchronizer* action status, and other data field settings used in this study are shown in Table 3-1. The synchronization was then run and results were saved as a MDS file (.sdf format) compatible with the MPA software program. Figure 3-2 shows a flow diagram demonstrating the steps followed during the synchronization process.

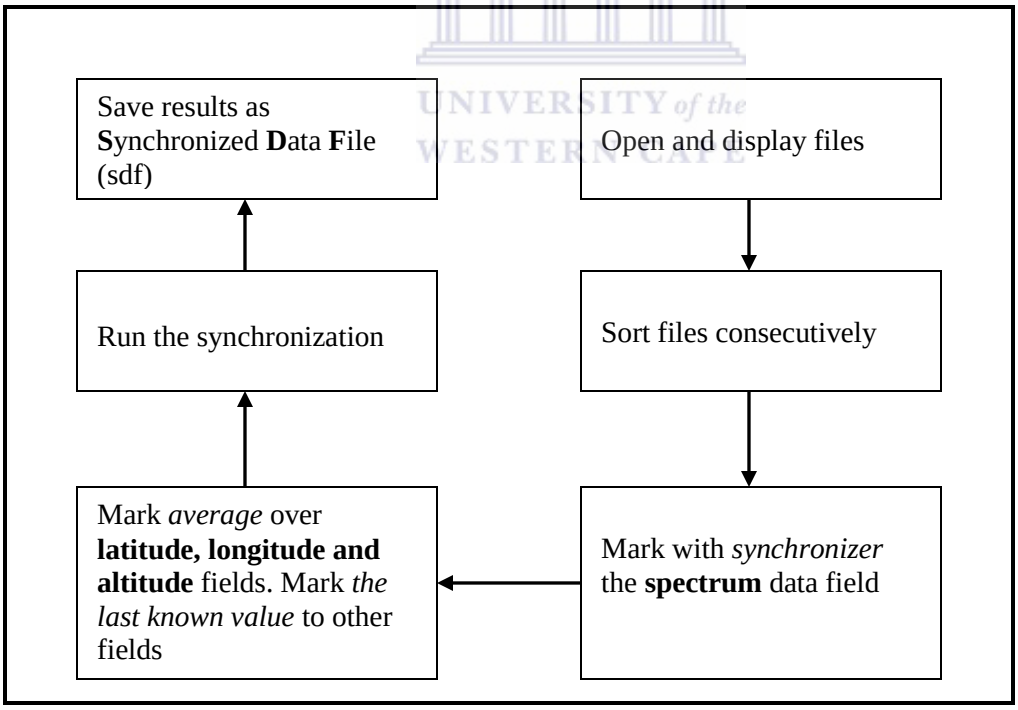

Figure 3-2: *Flow diagram showing the steps followed during the synchronization process of the MEDUSA-acquired data.*

Table 3-1: MEDUSA data synchronisation settings used in this study.

Data field	Action	Digits	Acquisition rate
Spectrum	Synchronizer	-	Every 2s
Altitude	Average values	2	Every 2s
Latitude and Longitude	Average values	4	Every 2s
Time	The last known value	-	Every 2s
Pressure, Sound, Temperature, Cable volts, Total counts	The last known value	-	Every 1s

3.1.2 Full Spectrum Analysis (FSA)

With the MPA software acquired spectra are analyzed using the Full Spectrum Analysis (FSA) method, which uses a large part of the entire spectrum (see Appendix 1, Figure A1-2). In this technique the full energy-spectrum is considered and the measured spectrum Y is described as the sum of *standard spectra* X_j multiplied by the unknown activity concentrations C_j for the individual radionuclides, plus a background spectrum (BG) [Hen01] (see eq. 3.1). By definition, a standard spectrum for radionuclide X is the expected response of the detector per second when exposed, in a particular geometry, in this case soil, containing an activity concentration of 1 $Bq.kg^{-1}$ of nuclide X [deM97]. The FSA method involves fitting the standard spectra and a background spectrum to the measured spectrum by means of a least-squares minimization procedure, in which certain parameters are manually modified by a software tool called Manual Stabilization. For more details on FSA procedure, see intermezzo 3.1 below.

Intermezzo 3.1: FSA procedure

In this study, each measured spectrum "S" and three standard spectra of ^{40}K (S_K), γ-ray emitters in the ^{232}Th (S_{Th}) and ^{238}U (S_U) decay series shown in Figure 3-3 were used in the FSA procedure [New08]. As explained above, the measured spectrum represents the sum of the standard spectra each multiplied by the concentration of its respective nuclide plus the measured background spectrum, thus, for each spectrum channel *i*:

$$S(i) = C_K S_K(i) + C_{Th} S_{Th}(i) + C_U S_U(i) + S_{bg}(i) \tag{3.1}$$

C_K, C_{Th} and C_U represent the activity concentration of ^{40}K, ^{232}Th series and ^{238}U series, respectively [deM97]. With the MPA, the least squares procedure is used to deduce the optimum values of C_K, C_{Th} and C_U by means of the reduced chi-square approach, which is given by [deM97, Hen01]:

$$\chi_R^2 = \frac{1}{N_{\max} - N_{\min} - M} \sum_{i=N_{\min}}^{N_{\max}} \frac{[S(i) - C_K S_K(i) - C_{Th} S_{Th}(i) - C_U S_U(i) - S_{bg}(i)]^2}{\sigma^2[S(i) - S_{bg}(i)]} \tag{3.2}$$

N_{min} to N_{max} represents minimum and maximum channel number representing the reliable part of the spectrum where good fitting is obtainable and *M* is the number of standard spectra used, in this study, *M* = 3.

The standard spectra (^{40}K, ^{232}Th series and ^{238}U series) used in this work were obtained from Monte Carlo simulations with the MCNPX code [Hen02, Mal07]. MCNPX version 2.6 b running on a PC with an AMD Athlon™ 64 processor (1.81 GHz) was used to simulate a flat-bed geometry with 30% soil porosity (50% filled with water and other 50% with air). The soil was assumed to consist of only SiO_2 since the most common mineral in soil is quartz (SiO_2). Source definitions used for the simulations considered ^{238}U and ^{232}Th series radionuclides in equilibrium in a semi-infinite soil medium. The radionuclides were considered to be uniformly distributed in a semi-infinite medium. The background spectrum used for the analysis was measured by immersing the MEDUSA detector in water at Theewaterskloof Dam near Grabouw, about 60 km from Cape Town. The dam which is about 15 m deep ensures effective shielding of γ-rays from the soil.

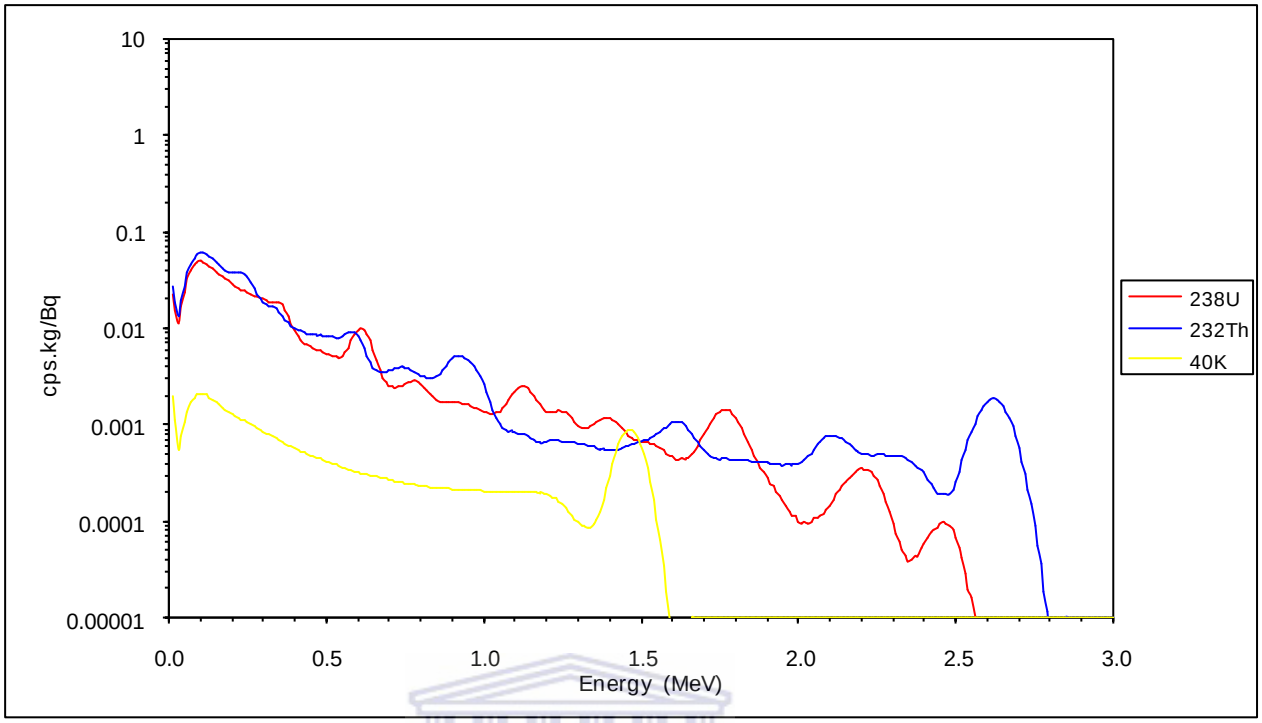

Figure 3-3: *Simulated standard spectra of ^{232}Th-series (blue), ^{238}U-series (red) and ^{40}K (yellow). The ordinate represents the MEDUSA detector response to one Bq/kg per second of each radionuclide [Mal07].*

The parameters which were obtained during FSA (least-squares minimization)[‡] were saved for the next steps of analyses, namely "Sum & Analyse" and "Analyse all records" operations of all acquired spectra to extract relative activity concentrations of ^{40}K, ^{232}Th and ^{238}U with their associated uncertainties. According to the patent of the MEDUSA system [Eur98], if S_i represents the number of γ-ray spectra detected per second carrying energy E_i, then $\Delta S_i = \sqrt{S_i}\,/\,T$ gives the uncertainty during time interval T. In this case, i refers to 1, 2,...n, where n is a positive integer [Eur98]. Figure 3-4 shows a flow diagram of the entire procedure followed during the extraction of the radionuclide relative activity concentrations.

[‡] An approach to obtain optimum values of C_K, C_{Th} and C_U by fitting the standard spectra and a background spectrum to the measured spectrum *via* reduced chi-squares fitting.

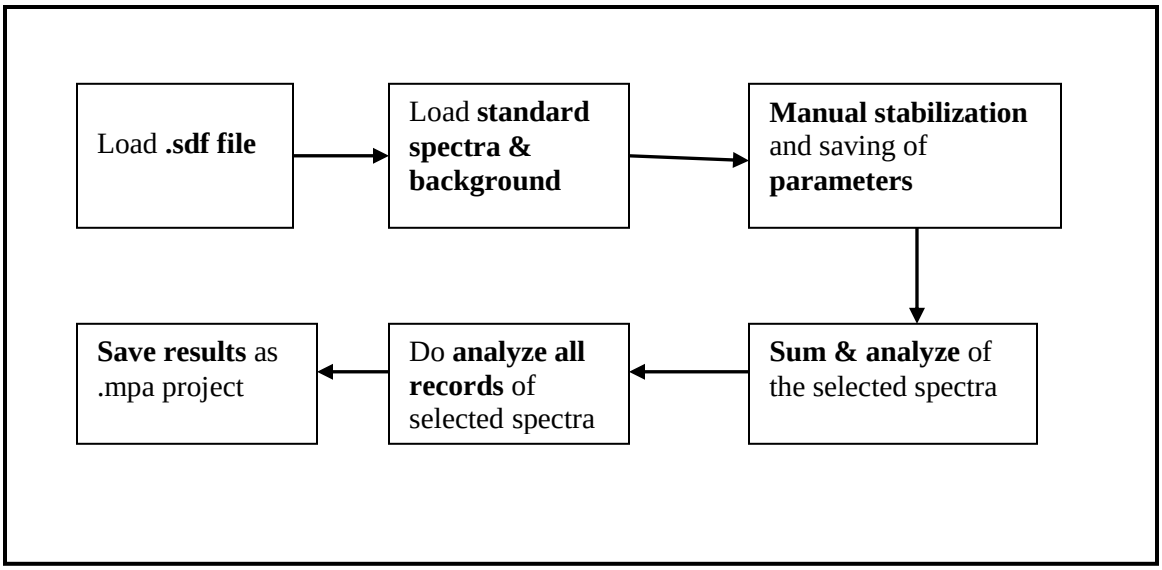

Figure 3-4*: Flow diagram showing the summarized steps followed to extract the ^{40}K, ^{232}Th series and ^{238}U series relative activity concentrations.*

3.1.3 Spectral analysis using the hybrid approach

A new approach for spectral analysis, was recently proposed [deM09, Tal09]. This hybrid approach was used to analyze MEDUSA acquired γ-ray spectra of the calibration measurements as explained in section 3.1.4. The method is based on setting several energy gates (intervals) in the range of 1.3 to 3.0 MeV. This range covers the γ-rays emitted by the natural radionuclides of ^{40}K and the decay series of ^{232}Th and ^{238}U. Details of each energy interval and the basis of gating are described by [Tal09]. The four energy intervals used in this study are: *I* (2.85-3.0 MeV) the flat part of the cosmic background spectrum; *II* (2.41-2.85 MeV) called Th and contains mainly the ^{208}Tl peak plus background; *III* (1.62-2.41 MeV) called U and contains mainly three ^{214}Bi peaks, some Th plus background; *IV* (1.3-1.62 MeV) called K and contains mainly ^{40}K, some ^{232}Th and ^{238}U peaks plus background. In this work, the four energy intervals of the hybrid analysis were reset considering the observed peak tailing contribution especially of the energy interval *II* (Th) into interval *I* (cosmic background) mostly for the spectra acquired from the block hot spots. For further details of the hybrid approach, see intermezzo 3.2 below.

Intermezzo 3.2: Hybrid analysis model

The analysis starts from the high energy side [Tal09]. The cosmic ray spectrum assumed to have the shape of the background spectrum, in this case from the Theewaterskloof measurement, but it may differ in magnitude by a factor f_c, as compared with the count rate (CR) of interval *I* in the actual spectrum, n_I, and that of the Theewaterskloof (Twk) spectrum, n_I^{Twk}:

$$f_c = \frac{n_I}{n_I^{Twk}} \tag{3.3}$$

The CR of interval *II*, referred as n_{II}, consists of two components. The first one is the contribution of the cosmics and the other is the decay of Th. Subtracting cosmics in this interval, and then normalizing by f_c determines the Th contribution:

$$n_{II}^{net}(Th) = n_{II} - f_c n_{II}^{twk} - (\text{small U contribution}). \tag{3.4}$$

The effective Th concentration, C_{Th}, is then determined by dividing the net CR in interval *II*, by the CR per Bq/kg from the simulated standard spectrum of Th (Th_SS) in interval *II* then multiplying by the detector calibration factor, *f*, which accounts for some of the detector properties (light-collection properties of the detector and the efficiency of the PMT) which are not taken into account in the standard spectra simulated by MCNPX (see section 3.1.2 above), hence:

$$C_{Th} f = \frac{n_{II}^{net}}{n_{II}^{Th\_SS}} \tag{3.5}$$

The net CR in U region, in interval *III* is determined by subtracting the cosmics and Th contributions:

$$n_{III}^{net}(U) = n_{III} - f_c n_{III}^{twk} - C_{Th} f n_{III}^{Th\_SS} \tag{3.6}$$

Hence, the effective U concentration, C_U, is calculated in a similar way to C_{Th} using the net CR in interval *III* and the CR per Bq/kg in interval *III* of a simulated standard spectrum of U (U_SS).

$$C_U f = \frac{n_{III}^{net}}{n_{III}^{U\_SS}} \tag{3.7}$$

The net CR in K in the interval *IV* is given by:

$$n_{IV}^{net} = n_{IV} - f_C n_{IV}^{twk} - f C_{Th} n_{IV}^{Th\_SS} - C_U f n_{IV}^{U\_SS} \quad (3.8)$$

The effective K concentration, C_K, is determined by using the net CR in interval *IV* and the CR per Bq/kg of the standard spectrum of K (K_SS) in interval *IV*:

$$C_K f = \frac{n_{IV}^{net}}{n_{IV}^{K\_SS}} \quad (3.9)$$

3.1.4 Normalization of the MEDUSA relative activity values

To obtain absolute activity concentrations of ^{40}K, ^{232}Th series and ^{238}U series radionuclides, their extracted relative values have to be normalized. The normalization (calibration) factors for each radionuclide as described in Chapter 2, section 2.2.3 are determined from the ratio of weighted average activity concentrations (Bq/kg) of samples determined from the HPGe measurements (window analysis) to that determined from the MEDUSA data acquired at each calibration spot, using the specified set of standard spectra. The formula to determine the weighted average is given in (see Appendix 1, section A1.7). In this study, both FSA and hybrid approaches were used to extract MEDUSA relative activity concentrations of the calibration measurements. The hybrid approach is a recently proposed γ-ray analysis technique that combines the advantage of FSA and "windows" methods [Tal09]. The HPGe data analysis approach used in this study is detailed in section 3.2 below. The normalization factors for each radionuclide were inserted in the MPA software as new conversion factors to determine the absolute activity values of all MEDUSA data acquired in the three blocks. The two calibration spots (P19C and P22C) together with the other spots described in Chapter 2, section 2.2.3 were used to further investigate the normalization factors in the range of radionuclide activity concentrations observed in the three blocks (see Chapter 5, section 5.1).

3.1.5 Radiometric mapping

Since each spectrum analysed is associated with a unique set of coordinates and other auxiliary data, it is possible to generate radiometric maps (total detector count rate and activity concentration maps). With MPA, the synchronized data were used to plot grid-like pattern maps of total detector count-rates of the three blocks. Figure 3-5 shows un-interpolated total detector count-rate maps obtained during the process of analyzing the MEDUSA data of the three blocks. The red colour in the maps represents higher count-rates while the blue colour indicates lower countrates. The uninterpolated maps gave an idea of the radioactivity level distribution in the vineyard block surfaces. The total detector count-rates for the blocks ranged from 140-500 cps, 150-340 cps and 170-400 cps for Block 2, Pomphuis and Nuweland, respectively. The normalized MPA data of ^{40}K, ^{232}Th series and ^{238}U series activity concentrations (ACs) were plotted using relevant software functions. The AC values found to be less than zero (negative values) were tagged and deleted to filter unphysical data in the entire row data set. Furthermore, the data in which the co-ordinates were found to be zero were automatically tagged by the software. The filtered data were then exported from MPA to an Excel spreadsheet for editing of the co-ordinate formats to the one compatible with Surfer8 package [Gol02]. The MPA radiometric maps were finally interpolated (smoothed) by means of the Surfer8 software package *via* a Kriging gridding technique [Gol02] as shown in Figure 3-5.

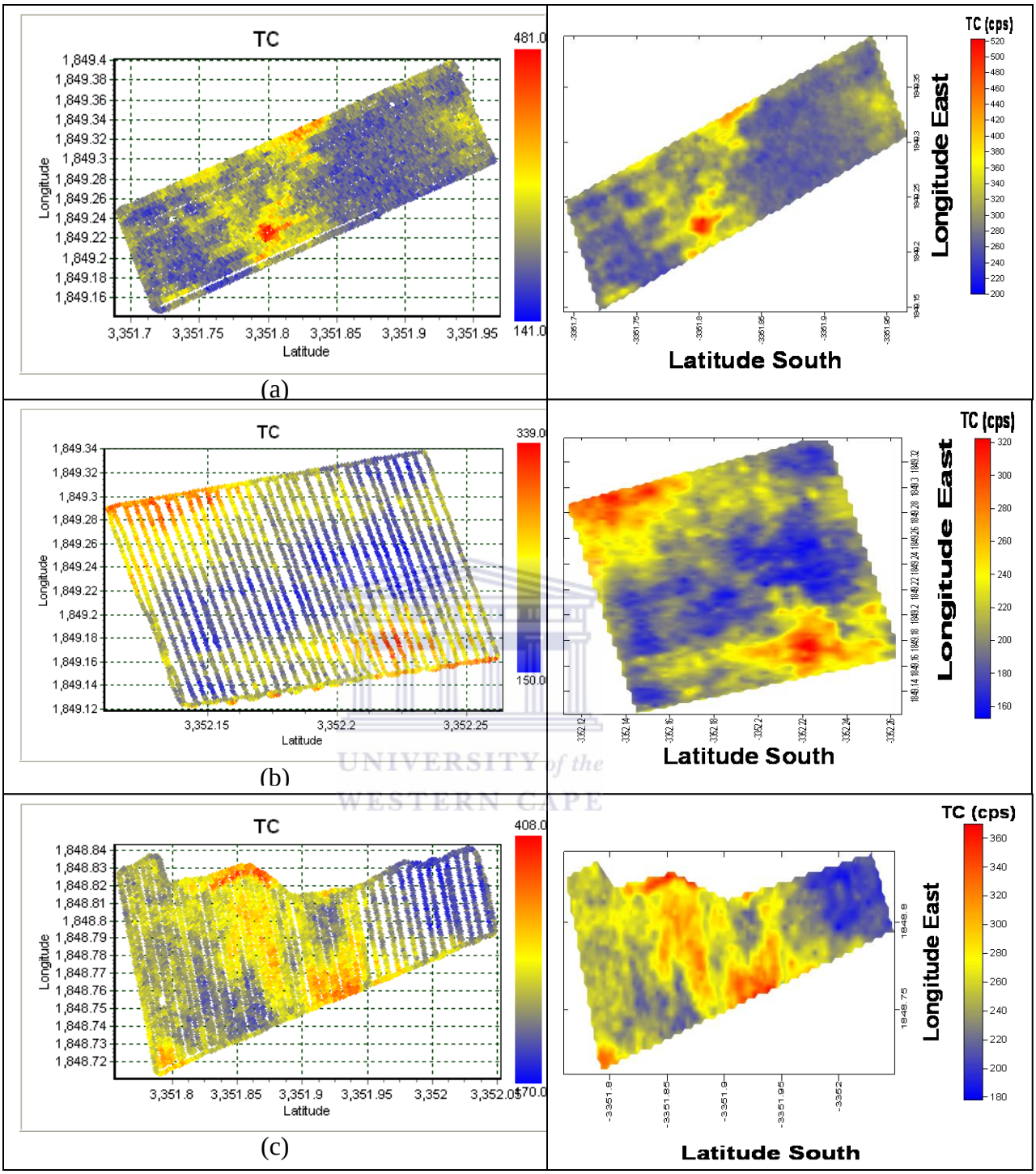

Figure 3-5: *Uninterpolated (left-hand side) and interpolated (right-hand side) MEDUSA detector count-rate (counts per second) maps for (a) Block 2 (b) Pomphuis block (c) Nuweland block. The uninterpolated maps were extracted using MPA software whereas the Surfer8 software package was used to produce interpolated maps from data acquired in 2007. (Note: The MEDUSA-software algorithm gives the latitude and longitude in the format xxyy.yy instead of the usual xx˚yy.yy' where xx and yy.yy correspond to degrees and minutes, respectively).*

3.2 HPGe data analysis

Spectra were analysed using the usual technique known as a "peak" or window" analysis method. The spectra were viewed and analysed using the OxfordWin and Palmtop softwares (see Chapter 2 section 2.4.1). With the OxfordWin, the regions of interest (ROIs) for both photopeak and continuum were set manually. This software uses its built-in algorithm to deduce the net counts in the photopeak area and its uncertainty. For the Palmtop software, the photopeak ROIs were also set manually to calculate the photopeak area and its percentage uncertainty. The photopeak area net counts and their uncertainties were then used to determine the activity concentrations of ^{40}K, ^{232}Th series and ^{238}U series in vineyard soil samples by using the following eqs:

$$A = \frac{C_n}{mTI_\gamma \varepsilon_{\text{det}}} \tag{3.10}$$

where A is the activity concentration in Bq per kilogram (kg), m is the mass of sample measured in kg, T is the live time of the measurement in seconds (s) and ε_{det} is the absolute detection efficiency at the γ-ray energy line (E_γ). Details of the procedures to determine ε_{det} are presented in section 3.2.1 below. I_γ is the branching ratio associated with a particular γ-ray energy line and gives a statistical probability that a particular γ-ray is emitted per decaying nucleus. C_n stands for net full-energy peak counts obtained by subtracting the background net counts from a measured tap water sample as follows:

$$C_n = (C_g - C_c) - (\frac{L_c}{L_b})C_b \tag{3.11}$$

where C_g is the gross counts, C_c is the continuum counts under the peak and C_b is the background counts. L_c and L_b are sample live time and background live time measurements, respectively.

The window method defines the area under the energy peak as:

$$Area = \sum_{left}^{right} Y_i - B_i \tag{3.12}$$

where i is the channel number, *left* is the leftmost channel of the peak region, *right* is the rightmost channel of the peak region, Y_i is the number of gross counts in channel i, and B_i

is the continuum contribution to channel *i*. All the uncertainties associated with each parameter in eqs. 3.10-3.12 above were propagated in accordance with uncertainty propagation rules presented in Intermezzo 3.3:
Before the analysis process, the energy calibration of each spectrum was checked.

Intermezzo 3.3:

Generally, uncertainty propagations associated with a quantity z = z(x; y…) are given by:

$$\sigma_z^2 = \left(\frac{\partial z}{\partial x}\right)^2 \sigma_x^2 + \left(\frac{\partial z}{\partial y}\right)^2 \sigma_y^2 + ... + 2\left(\frac{\partial z}{\partial x}\right)\left(\frac{\partial z}{\partial y}\right)\sigma_x \sigma_y + ... \quad (3.13)$$

The symbols σ_x, σ_y and σ_z are uncertainties associated with variables x, y and function z, respectively. The last term in eq. (3.13) is called the covariance term, and accounts for possible linear correlation between each pair of variables. The term is equal to zero when the variables are independent [Ame93].

3.2.1 Gamma-ray detection efficiency

To determine the AC in a particular sample measured with the HPGe detector, the associated absolute FEP detection efficiency response is required. In this work, this response was measured by using γ-ray lines associated with the decay of ^{232}Th series and ^{238}U series present in the sample, and the 1461 keV ^{40}K line as measured with the KCl source. The absolute FEP efficiency as a function of energy, in the geometry of the 1 litre Marinelli beaker was determined by means of a three-step procedure, an approach similar to that described by [Cro99] and used by [New08].

The first step was to generate the relative FEP efficiency curve for each sample based on the γ-ray lines in the ^{238}U and ^{232}Th series (^{238}U + ^{232}Th). A least-squares minimization approach [Chum94] was used to fit the relative efficiency using the model:

$$\varepsilon(E) = a\left(\frac{E}{E_0}\right)^{-b} \quad (3.14)$$

where E_0 = 1 MeV and E ranges from 0.186 to 2.204 MeV, a and b are fit parameters,

$a > 0$ and $1.0 > b > 0$ [Cro99]. Details of the γ-ray lines used for this purpose are given in Table 3-2. The uncertainties associated with the interpolated efficiencies are estimated using eq. 3.13, and the linear correlation between the variables was calculated by using a correlation coefficient $\rho(x, y)$, which is related to the covariance by:

$$\rho(x, y) = \frac{\mathrm{cov}(x, y)}{\sigma_x \sigma_y} = 2\left(\frac{\partial z}{\partial x}\right)\left(\frac{\partial z}{\partial y}\right) \tag{3.15}$$

Table 3-2: Gamma-ray lines and associated branching ratios [Fir96] used for FEP efficiency and activity concentration determination.

Series/radionuclide	Nuclide	Energy (MeV)	Branching ratio, I_γ (%)
^{238}U			
	^{226}Ra^{+}	0.186	6.2(2)
	^{214}Pb*	0.295	18.5(3)
	^{214}Pb*	0.352	35.8(5)
	^{234}Pa*	1.001	0.84(1)
	^{214}Bi*	1.238	5.86(8)
	^{214}Bi	1.378	3.92(8)
	^{214}Bi	2.204	4.86(9)
^{232}Th			
	^{228}Ac*	0.338	11.3(3)
	^{208}Tl*	0.860	4.5(1)
	^{228}Ac*	0.911	26.6(7)
	^{228}Ac	0.969	21.3(3)
^{40}K	^{40}K*	1.461	10.7(2)

The second step involves scaling the relative efficiency curve to match the measured absolute FEP at 1461 keV obtained using the KCl source which has a volume matching that of the sample. The activity concentration of the KCl powder from the company Merck (99.5% purity) was found to be 16259 Bq/kg. More details on the KCl activity calculation are presented in intermezzo 3.4 below.

The scaling factor (K_f), used to convert relative efficiency to absolute efficiency is then determined by the relation:

* Denotes γ-ray lines which are used for activity concentration calculations.

+ The186 keV branching ratio adjusted to correct for the contribution from ^{235}U.

$$K_f = \frac{\varepsilon_{abs}(^{40}K)}{\varepsilon_{rel}(^{40}K)} \tag{3.16}$$

Intermezzo 3.4:

The activity (A) of ^{40}K in KCl was obtained by utilizing its decay constant λ, and the number of ^{40}K (N) nuclei in KCl using the relation:

$$A = \lambda N \tag{3.17}$$

To obtain N, one needs to find the number of moles (n) in the KCl, and then use Avogadro`s number N_A (6.02×10^{23} atoms/mol) and abundance (a) of ^{40}K in natural KCl (1.17×10^{-4} ±0.85%) by using the relation:

$$N = n \times N_A \times a \tag{3.18}$$

The number of moles n, is given by the relation:

$$n = \frac{m}{M} \tag{3.19}$$

where m is the mass of the KCl (995 g) and M is the molar mass (74.551 g/mol).

The decay constant (λ) is given by the relation:

$$\lambda = \frac{\ln 2}{t_{1/2}} \tag{3.20}$$

where $t_{1/2}$, is the half-life of ^{40}K (4.027×10^{16} ± 0.63%) seconds [Fir98].

The third step involves a density correction to account for the dependence of absolute efficiency at 1461 keV with sample bulk density. A power law relationship was empirically established, namely:

$$\varepsilon_k = a\left(\frac{\rho}{\rho_0}\right)^b \tag{3.21}$$

where ε_k is the absolute photopeak detection efficiency (%) at 1461 keV, ρ is the sample density ($g.cm^{-3}$), ρ_0 is a density of 1 $g.cm^{-3}$ and a and b are fit parameters. The values of a and b were found to be 0.8954 and -0.04788, respectively [Jos07].

The parameters a and b and their associated uncertainties used to generate absolute photopeak efficiency were determined using the statistical package Physica [Chu94], and are given in Table 3-3 below. The co-variances determined by eqs. 3.15 are used to estimate the uncertainties of the interpolated efficiencies given by eq. 3.13. A weighted average (A_w) efficiency of each γ-ray line used for activity concentration determination was calculated from ten measured sample efficiencies as presented in Table 3-4. From the table, it is noted that the sample efficiencies for a particular γ-ray energy are consistent. The absolute efficiency (KCl) method used in this study has been validated using an IAEA standard reference soil sample (IAEA-375). Table 3-5 represents the validation results showing good agreement (within 95% confidence interval) between the analysed reference soil sample (using KCl approach) and the IAEA-certified activity concentrations.

Table 3-3: Parameters a and b with their associated uncertainties used to determine the A_w absolute photopeak efficiencies of ten samples. Details of the samples are presented in Chapter 2 section 2.3.1.

Sample	Parameter a	Parameter b
B5	1.82 ± 0.20	-0.731 ± 0.019
B6	2.3 ± 0.3	-0.763 ± 0.018
B16	1.81 ± 0.20	-0.731 ± 0.018
B21	1.94 ± 0.19	-0.740 ± 0.014
P2	2.2 ± 0.3	-0.758 ± 0.020
P11	2.0 ± 0.3	-0.743 ± 0.020
P19	1.26 ± 0.14	-0.681 ± 0.018
N5	2.4 ± 0.3	-0.768 ± 0.017
N9	1.75 ± 0.19	-0.726 ± 0.017
N10	2.6 ± 0.3	-0.782 ± 0.018

Table 3-4: Absolute Photopeak efficiencies for the γ-ray lines used for the activity concentration determination. The efficiencies were obtained by measuring ten samples and KCl powder (1.274 kg) which was used to scale relative efficiencies. The last two columns present their A_w with associated internal uncertainties and reduced chi-squares (χ_ν^2).

Nuclide	Eγ (MeV)	Absolute photopeak efficiencies (%)											
		B5	B6	B16	B21	P2	P11	P19	N5	N9	N10	A_w	χ_ν^2
^{214}Pb	0.295	2.85(6)	2.99(5)	2.85(6)	2.89(6)	2.97(6)	2.90(6)	2.63(5)	3.02(6)	2.82(6)	3.09(6)	2.89(2)	5
^{228}Ac	0.338	2.58(5)	2.70(5)	2.58(5)	2.61(5)	2.68(5)	2.62(5)	2.59(4)	2.72(5)	2.56(5)	2.78(5)	2.63(2)	3.3
^{214}Pb	0.352	2.50(5)	2.62(4)	2.50(4)	2.53(5)	2.60(5)	2.55(5)	2.43(4)	2.64(5)	2.49(4)	2.69(5)	2.54(2)	2.8
^{208}Tl	0.860	1.30(2)	1.32(2)	1.30(2)	1.31(2)	1.32((2)	1.31(2)	1.27(2)	1.33(2)	1.30(2)	1.34(2)	1.310(6)	0.9
^{228}Ac	0.911	1.25(2)	1.27(2)	1.25(2)	1.26(2)	1.26(2)	1.26(2)	1.24(2)	1.27(2)	1.25(2)	1.28(2)	1.256(6)	0.7
^{234}Pa	0.1001	1.17(2)	1.18(2)	1.17(2)	1.17(1)	1.18(2)	1.17(2)	1.14(2)	1.18(2)	1.16(2)	1.19(2)	1.171(6)	0.4
^{214}Bi	1.238	0.99(2)	1.00(2)	0.99(2)	0.99(1)	1.00(2)	1.00(2)	0.99(2)	1.00(2)	1.00(2)	1.01(2)	1.000(6)	0.06
^{40}K	1.460	0.88(2)	0.88(2)	0.88(2)	0.88(1)	0.88(2)	0.88(2)	0.88(2)	0.88(2)	0.88(2)	0.88(2)	0.88(1)	0.0003

Table 3-5: Comparison of the activity concentrations (Bq.kg^{-1}) in the measured standard reference soil sample (IAEA-375) and the certified values for the validation of the method used in this study.

Nuclide	Measured activity concentration (Bq.kg^{-1})	IAEA certified reference values in Bq/kg (95% confidence interval)
^{238}U	17.5 ± 0.8	18 – 22 (^{226}Ra)
^{232}Th	20.0 ± 0.4	19.2 - 21.9
^{40}K	412 ± 6	417 - 432

3.2.2 Energy line selection for activity determination

Natural radionuclides of relevance to this study are mainly γ-ray emitting nuclei of ^{40}K and the decay series of ^{232}Th and ^{238}U nuclides. ^{232}Th and ^{238}U are not directly γ-ray emitters, but it is possible to quantify their concentrations by measuring γ-rays of their decay products when secular equilibrium is achieved between the parent nuclide and its daughter products in the decay series (see Chapter 1, section 1.2.2). Gamma-ray lines and associated branching ratios used for activity concentration determination are shown in Table 3-2. The prominent lines such as 609.3, 1120 keV (^{238}U series) and 583.2, 727.3, 795 keV (^{232}Th series), γ-ray lines were omitted from the analyses since a sensitivity analysis showed that they yield activity concentrations that deviate significantly from the

mean activity concentration by maximally, -14%, -6%, -11%, +15% and -10%, respectively (where ‘‘+’’ and ‘‘-’’ denotes activity concentrations which are, larger and smaller, respectively, than the mean), due to coincident summing [New08] (see Appendix 1, section A1.5). Weighted averages of the selected lines in Table 3-2 were used to estimate the activity concentrations of ^{232}Th series and ^{238}U series radionuclides in each sample analysed.

To determine the AC (^{40}K), the content of the 1.46 MeV peak, containing both the contents of the 1459 keV line of ^{228}Ac (^{232}Th series) and the 1460 of ^{40}K, was corrected for the ^{228}Ac contribution since the energy difference between peaks is less than the energy resolution of the detector spectrum (see Chapter 2, section 2.4.1). This was achieved by first calculating the sample ^{232}Th weighted activity concentration using other lines associated with the thorium series, after which the counts to ^{40}K and ^{228}Ac decay were ascribed.

CHAPTER 4 RESULTS FROM SAMPLE ANALYSES

This chapter presents the results of laboratory-based radiometric analyses on samples of the three vineyard blocks. Based on these results, a method of identifying sediment* groups using the γ-ray spectrometry technique is proposed. The method may become an alternative to traditional-soil form classification. In this chapter, correlation analysis of the radionuclide activity concentrations (AC) suggested reducing the three radionuclides to new eigenvector, *W*.

The samples were also analyzed to determine the exchangeable cations, minerals, major and trace elements. As was stated in Chapter 2, section 2.4, the analyses for exchangeable cations, major and trace elements were carried out by external research and commercial laboratories, whereas mineralogy measurements and analyses were performed at the Material Science Department laboratories, iThemba LABS. For these analysis techniques, the reproducibility of results is discussed as well as the correlation with radiometric data.

4.1 Sample activity concentrations (ACs)

Samples were collected at locations described in Chapter 2. Activity concentrations (ACs) of ^{40}K, ^{232}Th series and ^{238}U series and their ratios for the three blocks measured using the HPGe at iThemba LABS as described in Chapter 2, are listed in Tables 4-1, 4-2 and 4-3. From the tables one notices a constant Th/U** ratio in the samples of the blocks Pomphuis and Nuweland. For the samples of block 2 the ratio ranges between 1.0 and 1.9. This indicates that for all three blocks there is a significant correlation between the two radionuclides, and hence that the two ACs are dependent variables.

Figure 4-1 shows 2D correlation plots (^{38}U series AC versus ^{232}Th series AC) for the three blocks, confirming that for all three blocks Th and U should be treated as dependent variables $(U = aTh + b)$, suggesting a new variable *V* with:

* Refers to solid fragmented material, such as silt, sand and gravel that come from the weathering of rock and are carried and deposited by wind, water or ice.
** Th and U refer to the AC of ^{232}Th and ^{238}U series, respectively.

$$V = Th + \frac{1}{a}(U - b) \tag{4.1}$$

where *a* is the weighted average of the (U-b)/Th ratio and *b* is the value of the intercept. The values of *a* and *b* with their external uncertainties are a=0.43±0.04 and b=15.7±1.8 (χ_ν^2=25), a=0.91±0.04 and b=1.3±0.7 (χ_ν^2=30), and a=0.76±0.06 and b=4.3±1.7 (χ_ν^2=44), for the Block 2, Pomphuis and Nuweland blocks, respectively. The reduced chi-squares (χ_ν^2) presented were obtained from the weighted uncertainties of both coordinates, using an approach proposed by [Pre92, Ree92]:

For a straight-line fit model with uncertainties in both x and y direction given by;

$$y(x) = a + bx \tag{4.2}$$

The χ^2 function for *N* data points is given by:

$$\chi^2(a,b) = \sum_{i=1}^{N} \frac{(y_i - a - bx_i)}{\sigma_{y_i}^2 + b^2\sigma_{x_i}^2} \tag{4.3}$$

where σ_{xi} and σ_{yi} are the *x* and *y* standard deviations for the *i*th point, respectively[Pre92].

Table 4-1: Activity concentrations of ^{40}K, ^{232}Th series and ^{238}U series and their ratios for samples from Block 2.

Sampling points	Activity concentrations (Bq/kg)					
	^{40}K	^{232}Th	^{238}U	Th/U	K/Th	K/U
B1	168±3	32.6±0.5	33.0±1.1	0.99±0.04	5.15±0.12	5.09±0.19
B2	208±3	38.2±0.5	33.0±1.4	1.16±0.05	5.45±0.11	6.3±0.3
B3	146±2	47.5±0.6	39±2	1.22±0.06	3.07±0.06	3.74±0.20
B4	221±3	110.0±1.2	62±2	1.77±0.06	2.01±0.03	3.56±0.12
B5	227±3	111.0±1.2	68±2	1.63±0.05	2.05±0.03	3.34±0.11
B6	139±2	44.6±0.5	35.2±0.9	1.27±0.04	3.12±0.06	3.95±0.12
B7	171±3	51.9±0.6	36.0±1.2	1.44±0.05	3.29±0.07	4.75±0.18
B8	161±2	37.5±0.5	35.0±1.3	1.07±0.04	4.29±0.08	4.60±0.18
B9	180±3	40.2±0.5	33.0±1.5	1.22±0.06	4.48±0.09	5.4±0.3
B10	168±3	45.4±0.6	40.0±1.4	1.13±0.04	3.70±0.08	4.20±0.17
B11	140±2	37.1±0.7	30.1±0.4	1.23±0.03	3.77±0.09	4.65±0.09
B12	157±2	36.0±0.6	30.0±0.3	1.20±0.03	4.36±0.09	5.23±0.08
B13	175±3	36.0±0.6	30.0±0.3	1.20±0.02	4.86±0.12	5.83±0.12
B14	200±3	87.0±1.4	46.0±0.6	1.89±0.04	2.30±0.05	4.35±0.09
B15	150±2	28.0±0.6	28.0±0.3	1.00±0.02	5.36±0.14	5.36±0.09
B16	193±3	73.6±1.0	49.2±0.4	1.50±0.02	2.62±0.05	3.92±0.07
B17	144±2	36.1±0.5	33.0±0.3	1.09±0.02	3.99±0.08	4.36±0.07
B18	208±3	47.7±0.7	37.2±0.4	1.28±0.02	4.36±0.09	5.59±0.10
B18*	223±3	58.0±0.8	41.1±0.4	1.41±0.02	3.84±0.07	5.43±0.09
B19	172±3	36.0±0.5	32.0±0.3	1.13±0.02	4.78±0.11	5.38±0.11
B19*	184±3	36.1±0.5	32.5±0.3	1.11±0.02	5.10±0.11	5.66±0.11
B20	154±2	44.1±0.6	36.3±0.3	1.21±0.02	3.49±0.07	4.24±0.07
B20*	176±3	66.5±1.0	40.4±0.4	1.65±0.03	2.65±0.06	4.36±0.09
B21	127±2	32.0±0.5	30.5±0.3	1.05±0.02	3.97±0.09	4.16±0.08
B21*	140±2	41.2±0.6	32.4±0.3	1.27±0.02	3.40±0.07	4.32±0.07
B22	132±2	48.5±0.7	32.0±0.3	1.52±0.03	2.72±0.06	4.13±0.07
B22*	146±2	56.7±0.8	35.2±0.3	1.61±0.03	2.57±0.05	4.15±0.07
B23	213±3	49.6±0.7	41.6±0.4	1.19±0.02	4.29±0.09	5.12±0.09
B23*	219±3	59.1±0.9	47.7±0.5	1.24±0.02	3.71±0.08	4.59±0.08
Mean±SD				1.30±0.20	3.75±1.00	4.68±0.70

* Refers to results of 30-60 cm soil sampling depths. Results of other points are based on 0-30 cm soil depths.

Table 4-2: Activity concentrations of ^{40}K, ^{232}Th series and ^{238}U series for the measured samples and their ratios for samples from Pomphuis block.

Sampling points	Activity concentrations (Bq/kg)					
	^{40}K	^{232}Th	^{238}U	Th/U	K/Th	K/U
P1	304±4	46.7±0.7	44.2±0.4	1.06±0.02	6.51±0.13	6.88±0.11
P2	60.0±1.2	24.3±0.2	23.1±0.3	1.05±0.02	2.47±0.05	2.60±0.05
P3	32.9±0.8	14.2±0.14	13.70±0.18	1.02±0.02	2.36±0.07	2.41±0.08
P4	73.2±1.2	32.0±0.3	28.4±0.3	1.12±0.02	2.30±0.04	2.57±0.04
P5	160±2	33.3±0.5	37.3±0.4	0.89±0.02	4.80±0.09	4.29±0.07
P6	29.5±0.7	11.8±0.2	11.39±0.13	1.04±0.02	2.44±0.09	2.54±0.09
P7	57.4±0.9	14.0±0.2	14.09±0.14	0.99±0.02	4.10±0.09	4.04±0.08
P8	42.9±0.8	13.7±0.2	12.14±0.13	1.13±0.06	3.07±0.09	3.47±0.09
P9	185±3	36.5±0.6	35.5±0.4	1.03±0.02	5.07±0.10	5.21±0.08
P10	38.3±0.7	11.8±0.2	12.38±0.13	0.95±0.02	3.22±0.10	3.06±0.08
P11	104±2	35.6±0.4	27.4±0.4	1.30±0.02	2.92±0.07	3.80±0.09
P12	71.7±1.3	27.6±0.3	23.2±0.3	1.19±0.04	2.57±0.05	3.06±0.06
P13	48.0±0.8	14.3±0.2	14.70±0.15	0.97±0.02	3.36±0.08	3.27±0.07
P14	55.3±0.9	15.1±0.3	14.38±0.15	1.05±0.02	3.64±0.10	3.82±0.09
P15	51.0±0.9	13.3±0.2	13.26±0.14	1.00±0.03	3.83±0.09	3.83±0.08
P16	84.6±1.3	24.5±0.4	20.5±0.2	1.19±0.02	3.47±0.07	4.15±0.06
P17	87.2±1.3	19.5±0.3	20.0±0.2	0.98±0.02	4.46±0.09	4.35±0.07
P18	73.8±1.4	22.2±0.4	22.6±0.3	0.98±0.02	3.33±0.08	3.27±0.05
P19C	45.7±0.9	12.27±0.12	13.01±0.15	0.940±0.011	3.74±0.09	3.51±0.08
P20	287±5	53.0±0.8	50.0±0.5	1.06±0.02	5.42±0.14	5.74±0.12
P21	288±4	55.6±0.8	67.8±0.6	0.82±0.02	5.14±0.12	4.24±0.09
P22C	38.0±0.7	11.29±0.13	12.01±0.13	0.920±0.011	3.45±0.07	3.17±0.06
P23	58.8±1.0	17.1±0.3	15.18±0.16	1.13±0.02	3.45±0.08	3.88±0.08
P24	35.0±0.7	11.20±0.19	11.67±0.13	0.96±0.02	3.13±0.11	2.99±0.09
P25	62.4±1.0	22.1±0.4	23.0±0.2	0.96±0.02	2.82±0.07	2.71±0.05
Mean±SD				1.03±0.11	3.64±1.10	3.72±1.00

Table 4-3: Activity concentrations of ^{40}K, ^{232}Th series and ^{238}U series for the measured samples and their ratios for samples from Nuweland block.

Sampling points	Activity concentrations (Bq/kg)					
	^{40}K	^{232}Th	^{238}U	Th/U	K/Th	K/U
N1	234±3	54.2±0.8	46.8±0.4	1.16±0.02	4.31±0.09	5.00±0.08
N2	187±3	48.7±0.7	33.7±0.3	1.45±0.03	3.84±0.08	2.56±0.09
N3	80.2±1.4	21.9±0.4	20.5±0.3	1.07±0.03	3.67±0.10	3.91±0.09
N4	84.3±1.2	22.6±0.3	19.46±0.18	1.16±0.02	3.73±0.08	4.33±0.07
N5	70.3±0.9	18.6±0.3	17.77±0.15	1.048±0.017	3.77±0.07	3.95±0.06
N6	62.6±1.1	18.4±0.3	17.83±0.19	1.03±0.02	3.41±0.08	3.51±0.07
N7	71.1±1.0	14.0±0.3	19.46±0.19	1.060±0.019	3.45±0.07	3.65±0.06
N8	129.0±1.9	29.1±0.5	26.3±0.3	1.11±0.02	4.43±0.09	4.91±0.09
N9	200±3	44.2±0.6	43.6±0.4	1.014±0.017	4.52±0.09	4.58±0.07
N10	110.4±1.5	25.5±0.4	23.6±0.2	1.079±0.019	4.34±0.09	4.68±0.08
N11	220±3	47.3±0.7	35.0±0.3	1.36±0.02	4.65±0.09	6.30±0.10
N12	315±4	56.6±0.9	44.1±0.4	1.28±0.02	5.57±0.11	7.14±0.12
N13	138.7±2.0	32.9±0.5	30.8±0.3	1.07±0.02	4.21±0.09	4.50±0.08
N14	98.6±1.6	25.2±0.4	24.5±0.3	1.030±0.019	3.91±0.09	4.03±0.08
N15	88.0±1.4	27.7±0.4	32.1±0.3	0.86±0.02	3.18±0.07	2.74±0.05
N16	104.5±1.5	27.3±0.4	22.81±0.2	1.197±0.016	3.83±0.08	4.58±0.08
N17	166±4	51.3±0.8	36.6±0.4	1.40±0.02	3.24±0.10	4.54±0.13
N18	219±3	52.4±0.7	41.2±0.4	1.27±0.03	4.18±0.08	5.32±0.08
N19	151.2±2.0	35.6±0.5	35.4±0.3	1.007±0.018	4.25±0.09	4.28±0.07
N20	74.9±1.3	18.7±0.3	19.50±0.2	0.961±0.019	4.00±0.10	3.84±0.08
N21	106.2±1.4	24.0±0.4	22.89±0.2	1.050±0.018	4.42±0.09	4.64±0.08
N22	78.2±1.3	27.4±0.4	30.2±0.3	0.906±0.017	2.86±0.06	2.59±0.05
N23	98.2±1.6	26.7±0.4	26.5±0.3	1.008±0.019	3.68±0.09	3.71±0.07
N24	63.0±1.2	18.8±0.3	19.4±0.2	0.967±0.019	3.36±0.08	3.25±0.07
Mean±SD				1.106±0.150	3.95±0.60	4.40±1.03

Figure 4-2 shows 2D correlation plots and a best fit (^{238}U versus ^{232}Th series ACs) for the Pomphuis and Nuweland blocks. The values of *a* and *b* are a=0.85±0.03 and b=2.1±0.6 (χ_ν^2=38); The quoted uncertainties represent the external uncertainties (see Appendix 1, A1.7). From the figure it is clear that one cannot reject the hypothesis that the blocks Pomphuis and Nuweland have the same U/Th ratio. For all three blocks we conclude that the larger values of χ_ν^2 combined with a visually good fit indicate that the statistical uncertainties in the analysis results is much smaller than the natural spread in the values. Hence the large χ_ν^2 values indicate an inherent systematic uncertainty. From the data we will treat the ^{238}U and ^{232}Th series ACs as an expression of the variables V_1, for the blocks Pomphuis and Nuweland and V_2 for the Block 2, respectively.

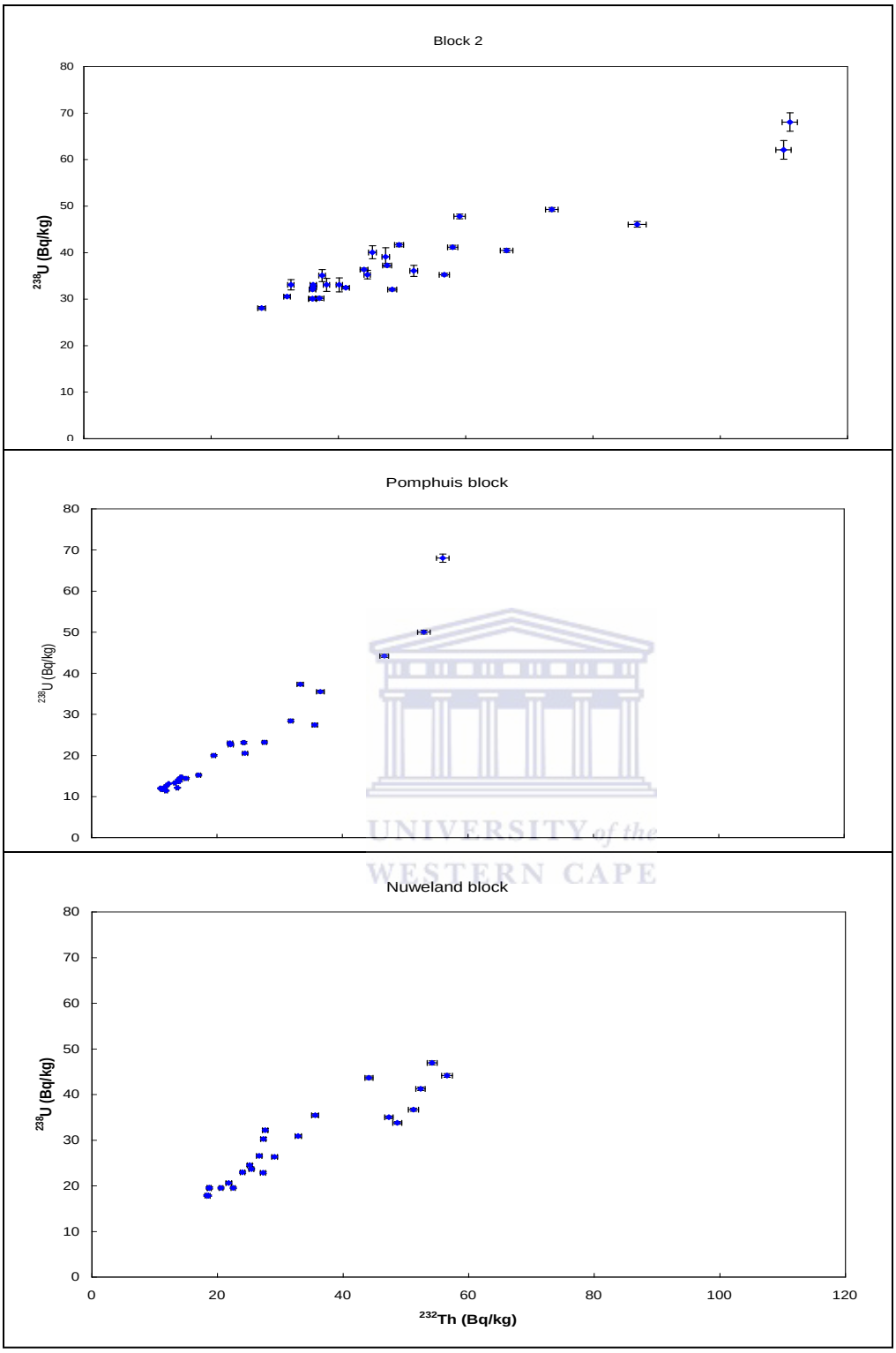

Figure 4-1: *Correlation plots of the ^{238}U series and ^{232}Th series ACs for the samples in the three blocks.*

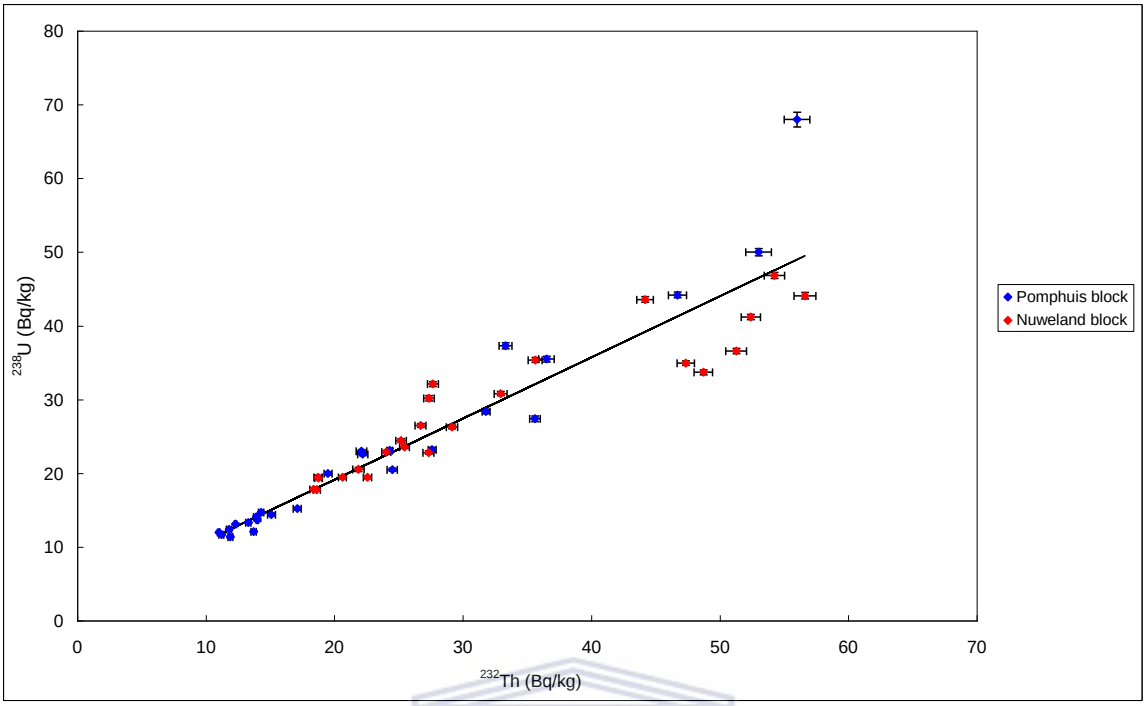

Figure 4-2: *Weighted fit showing the correlation between ^{238}U series and ^{232}Th series ACs from Pomphuis and Nuweland block data.*

Table 4-4 presents the values of the new variables *V* with their ratio to the ^{40}K AC for samples in the three blocks. $^{40}K/V$ ratios ranges from 1.7 to 2.7, 1.2 to 3.2 and 1.3 to 2.9 for Block 2, Pomphuis and Nuweland blocks, respectively. From the table, it is noted that the blocks Pomphuis and Nuweland have almost the same $^{40}K/V$ ratios. Again, this shows significant correlation between the two variables in the two blocks similar to the correlation between ^{238}U series and ^{232}Th series. Figure 4-3 shows 2D correlation plots (^{40}K versus *V* ACs) for the three blocks, revealing that ^{40}K and *V* can also be treated as dependent variables. Thus, this implies that all the three radionuclides can be reduced to one eigenvector, *W* given by:

$$W = K + \frac{1}{c}(V - d) \tag{4.4}$$

where *c* is the weighted average of the (V-d)/K ratio and *d* is the value of the intercept. The values of *c* and *d* with their external uncertainties are c=0.66±0.05 and d=-20±18 (χ_ν^2=13), c=0.35±0.03 and d=13±3 (χ_ν^2=29), c=0.36±0.03 and d=15±3 (χ_ν^2=5), for the Block 2, Pomphuis and Nuweland blocks, respectively. One notices again high χ_ν^2 values, indicating that the precision in the AC determination is smaller than the natural

spread in the AC values in the block. From these values it is also clear that the new variable, *W*, has similar behaviour for the blocks Pomphuis and Nuweland.

Table 4-4: Variable *V* (as defined in eq. 4.1) and its ratios with ^{40}K ACs for samples in the three blocks.

Block 2			Pomphuis block			Nuweland block		
Sampling points	V_2	$^{40}K/V_2$	Sampling points	V_1	$^{40}K/V_1$	Sampling points	V_1	$^{40}K/V_1$
B1	73±6	2.3±0.2	P1	94±2	3.24±0.10	N1	110±5	2.13±0.11
B2	78±7	2.7±0.2	P2	48.3±1.5	1.24±0.04	N2	87±4	2.15±0.10
B3	101±8	1.44±0.12	P3	27.7±1.1	1.19±0.06	N3	43±3	1.86±0.13
B4	217±12	1.02±0.06	P4	61.6±1.7	1.19±0.04	N4	42±3	1.99±0.13
B5	232±14	0.98±0.06	P5	73±2	2.20±0.07	N5	36±3	1.94±0.15
B6	90±7	1.55±0.12	P6	23.0±1.0	1.26±0.07	N6	36±3	1.73±0.13
B7	99±7	1.73±0.13	P7	28.0±1.1	2.04±0.09	N7	40±3	1.76±0.12
B8	82±7	1.96±0.17	P8	25.6±1.0	1.64±0.08	N8	58±3	2.23±0.13
B9	80±7	2.24±0.19	P9	74±2	2.50±0.08	N9	96±5	2.09±0.11
B10	102±8	1.65±0.13	P10	24.0±1.1	1.58±0.08	N10	51±3	2.18±0.14
B11	70±5	1.99±0.16	P11	64.3±1.7	1.62±0.05	N11	87±4	2.52±0.12
B12	69±5	2.27±0.18	P12	51.7±1.5	1.37±0.04	N12	109±5	2.90±0.14
B13	69±5	2.5±0.2	P13	29.1±1.1	1.65±0.07	N13	68±4	2.05±0.12
B14	157±8	1.27±0.07	P14	29.5±1.2	1.86±0.08	N14	52±3	1.91±0.12
B15	56±5	2.7±0.3	P15	26.5±1.1	1.92±0.09	N15	64±4	1.37±0.08
B16	151±9	1.27±0.08	P16	45.6±1.4	1.86±0.06	N16	52±3	2.03±0.12
B17	76±6	1.89±0.15	P17	40.1±1.4	2.17±0.08	N17	93±4	1.77±0.09
B18	98±7	2.13±0.15	P18	45.6±1.5	1.62±0.06	N18	101±5	2.18±0.11
B18*	117±7	1.91±0.12	P19C	25.3±1.1	1.82±0.09	N19	76±4	1.98±0.11
B19	74±6	2.33±0.19	P20	106±3	2.69±0.09	N20	39±3	1.94±0.14
B19*	75±6	2.5±0.2	P21	129±4	2.23±0.07	N21	48±3	2.19±0.14
B20	92±6	1.68±0.12	P22C	22.8±1.0	1.67±0.08	N22	61±4	1.28±0.08
B20*	124±7	1.42±0.09	P23	32.4±1.2	1.82±0.07	N23	56±3	1.76±0.11
B21	66±5	1.91±0.16	P24	22.7±1.0	1.54±0.08	N24	38±3	1.63±0.12
B21*	80±6	1.75±0.13	P25	46.0±1.5	1.36±0.05			
B22	86±6	1.53±0.11						
B22*	102±6	1.43±0.09						
B23	110±7	1.94±0.13						
B23*	133±9	1.64±0.11						

* Refers to results of 30-60 cm soil sampling depths. Results of other points are based on 0-30 cm soil depths.

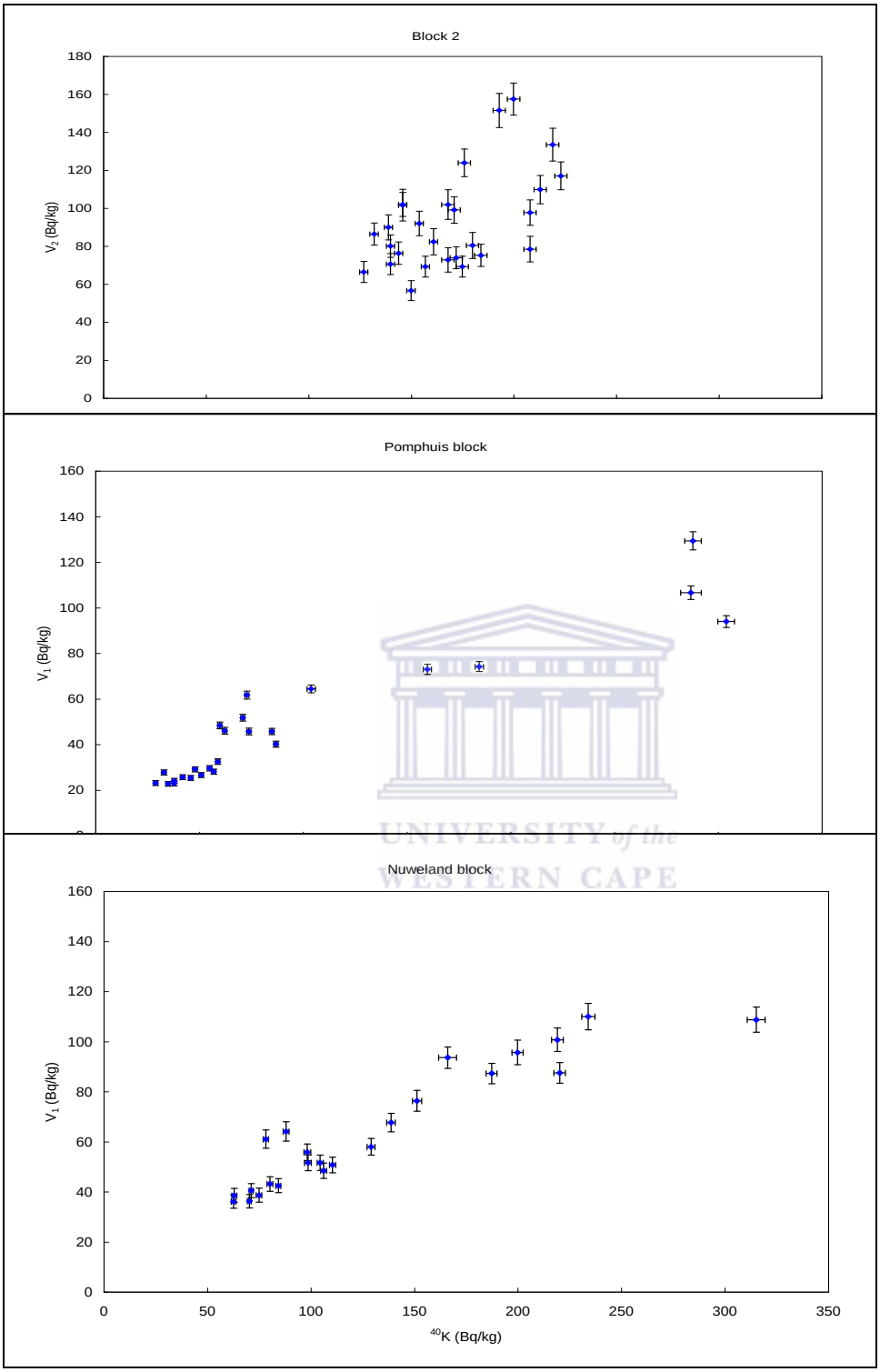

Figure 4-3: *Correlation plots between V and ^{40}K ACs for samples from the three blocks. V is the linear combination of the U and Th ACs as defined in eq. 4.1.*

Figure 4-4 shows the combined correlation plots and best fit (V versus ^{40}K AC) for the blocks Pomphuis and Nuweland. The values of c and d are c=0.36±0.02 and d=13±2 (χ_ν^2=16). The figure and χ_ν^2 value which is better than for the individual Pomphuis block value, confirms that the new variable determined by eq.4.4 is the same for the two blocks. We will therefore use W_1, for the blocks Pomphuis and Nuweland and W_2 for Block 2, respectively.

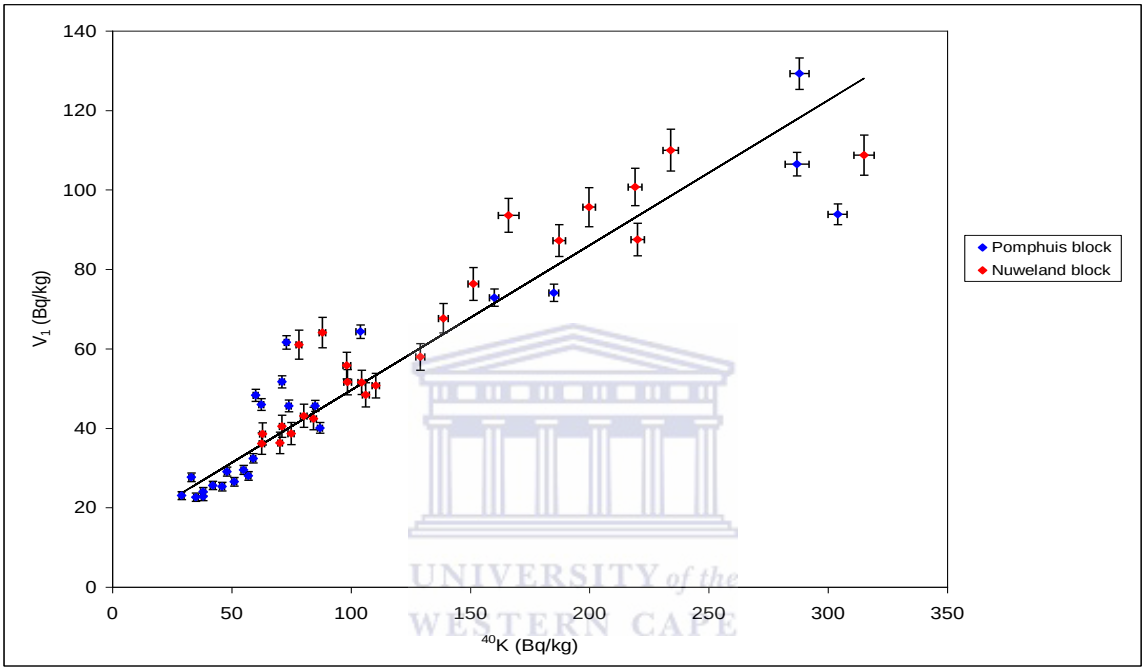

Figure 4-4: *Weighted fits showing the correlation between V_1 and ^{40}K ACs from Pomphuis and Nuweland block data. V_1 is the linear combination of the U and Th ACs for Pomphuis and Nuweland blocks.*

Table 4-5 presents the values of the new variables *W* for samples in the three blocks. The values range from 258 to 610 Bq/kg, 56 to 615 Bq/kg and 68 to 341 Bq/kg for Block 2, Pomphuis and Nuweland blocks, respectively.

The fact that all three radionuclides in a block are correlated and can be replaced by a single variable (*W*), raises the question whether the total count rate (TC) is a valuable measure for the variables *W*. One advantage is that TC is directly measured, whereas the ACs depend on the analysis of the γ-ray spectra. Figure 4-5 shows correlation plots of TC versus *W* for the three blocks. As expected, the correlation for Block 2 differs significantly from the two other blocks. However, certainly for Block 2 the correlation is not as good as the correlations shown in Figures 4.1and 4.3, especially the high TC values are clearly not well represented. A similar observation is made for the high W_1 values in the block Pomphuis. Although initially not expected, in retrospect this effect may not be a surprise since in the total count rate of the detector, the contributions of each radionuclide to the γ-ray spectrum comes in with a weighting factor, reflecting the spectrum averaged efficiency. These values are not the same for the three radionuclides and hence the TC need not be a perfect representation of the variables *W*.

Table 4-5: Activity concentrations (Bq/kg) of variable *W* for the measured samples in the three blocks.

Block 2		Pomphuis block		Nuweland block	
Sampling points	W_2	Sampling points	W_1	Sampling points	W_1
B1	309±31	P1	531±25	N1	261±4
B2	357±31	P2	158±13	N2	208±3
B3	331±33	P3	73±9	N3	88.0±1.9
B4	581±43	P4	209±16	N4	91.9±1.7
B5	610±45	P5	328±20	N5	76.1±1.6
B6	306±32	P6	56±8	N6	68.4±1.7
B7	352±32	P7	98±9	N7	78.1±1.6
B8	316±31	P8	77±9	N8	141±2
B9	332±32	P9	356±20	N9	222±3
B10	353±33	P10	68±9	N10	120±2
B11	277±30	P11	248±17	N11	241±3
B12	292±30	P12	179±14	N12	341±5
B13	310±30	P13	92±9	N13	153±3
B14	469±36	P14	101±9	N14	109±2
B15	266±30	P15	88±9	N15	102±2
B16	453±36	P16	176±12	N16	115±2
B17	290±31	P17	162±11	N17	188±5
B18	386±32	P18	165±12	N18	243±3
B18*	431±33	P19C	80±9	N19	168±3
B19	314±31	P20	549±29	N20	81.4±1.8
B19*	328±31	P21	615±36	N21	115±2
B20	324±32	P22C	65±8	N22	91.1±1.9
B20*	394±34	P23	113±10	N23	110±2
B21	258±30	P24	61±8	N24	69.4±1.8
B21*	292±31	P25	154±13		
B22	293±31				
B22*	331±32				
B23	410±33				
B23*	452±35				

* Refers to results of 30-60 cm soil sampling depths. Results of other points are based on 0-30 cm soil depths.

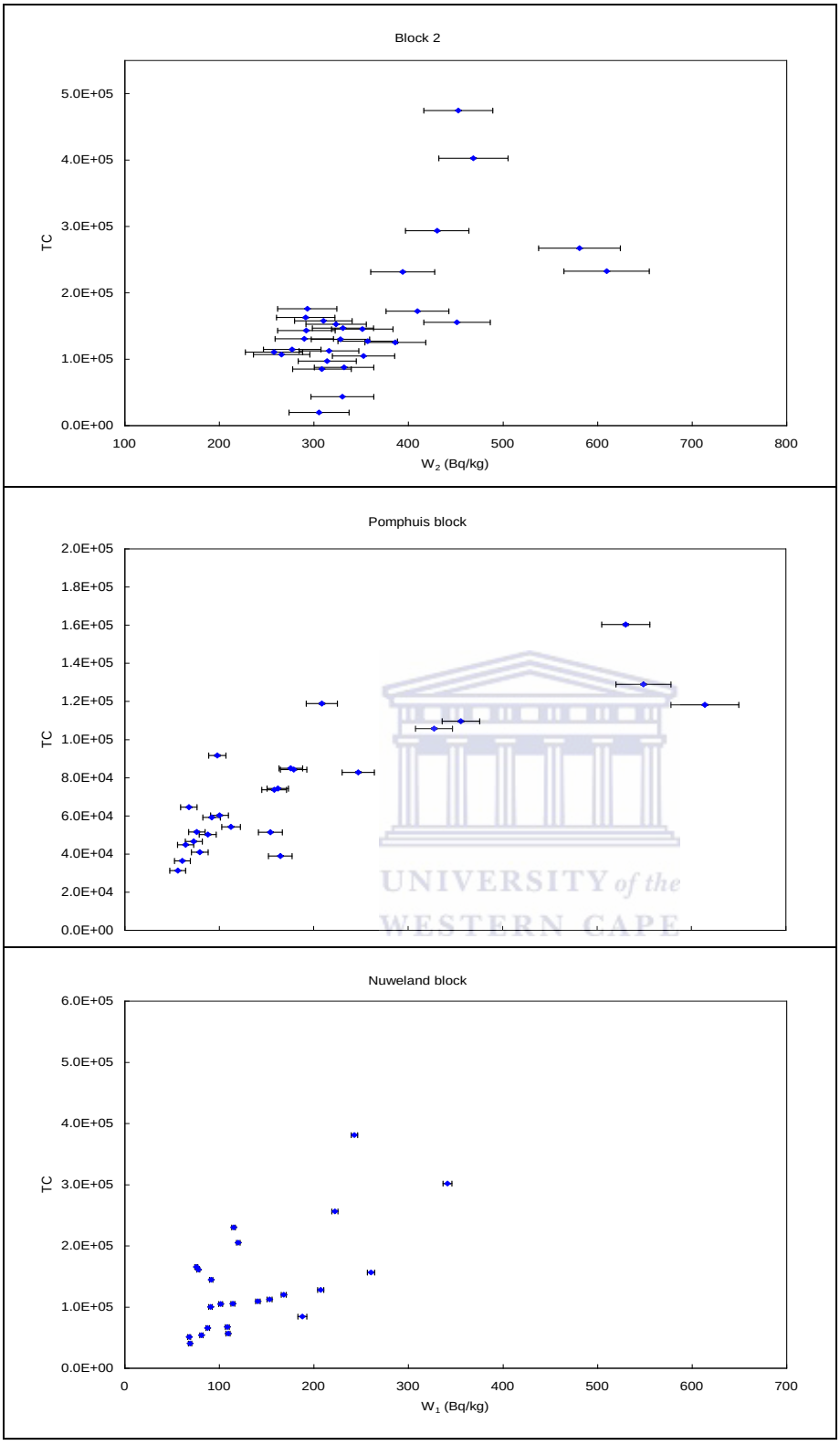

Figure 4-5: *Two dimensional plots showing the correlations between total counts (TC) and variable W for the samples from the three blocks. W is a value that contains the information on the radionuclides as defined in eq. 4.4.*

4.2 Characterisation of sediment groups

In this section we investigate the possibility that the two sediment groups may consist of a base sediment group, W_o (for each group), with a varying other sediment type *w* with variable intensity *P* with $0 \le P \le 1$. To determine the variable *P* for each group, the following interrelationship is used:

$$W = W_o + Pw \tag{4.5}$$

From the above relation (4.3), *P* can be determined by:

$$P = (W - W_o)/w \tag{4.6}$$

where W_o is determined by eq. (4.4) and *w* is obtained from *P* = 1 and maximum *W* using eq. (4.4). The *W* values for the samples are tabulated in Table 4-5 (see section 4.1).

Table 4-6 lists the parameters/variables within and between the two sediment groups. For the group W_1 (Pomphuis and Nuweland blocks), there is quite a significant difference between the radionuclide ACs in the base sediment (minimum *P*) and sediment group (maximum *P*) by a factor of 11, 5 and 6 for ^{40}K, ^{232}Th series and ^{238}U series, respectively. This indicates that ^{40}K differs most clearly between the base sediment and the sediment group, hence implying that ^{40}K is the dominant radionuclide characterising P_1. A similar comparison for variables *V* and *w* shows that they differ by a factor of 6 and 10, respectively.

A similar comparison for the other group W_2 (Block 2) shows that the radionuclide ACs in the base sediment and the sediment group differs by a factor of 2, 4 and 2 for ^{40}K, ^{232}Th series and ^{238}U series, respectively. This indicates that in this group, ^{232}Th is an indicator characterising P_2 contrary to group W_1. On the other hand, the variables *V* and *w* differ by a factor of 4 and 1.5, respectively. The factors for ^{232}Th and *V* are consistent as expected due to the ^{232}Th being the main indicator.

As far as the comparison between the two groups is concerned, a significant difference in radionuclide ACs is observed between the base sediments of Pomphuis/Nuweland and Block 2, by a factor of 4.3, 2.5 and 2.4 for ^{40}K, ^{232}Th series and ^{238}U series, respectively. This also implies that, ^{40}K is the most clear difference between the two base-sediment groups. For variables V_o and W_o, the groups differ by a factor of 2.5 and 4.3, respectively. This factor in W_o is expected from the observed ^{40}K difference.

A similar comparison in the sediment group does not show any difference for ^{238}U, contrary to the base sediment. However, a significant difference by a factor of 0.7 and 2 is observed for ^{40}K and ^{232}Th, respectively. Furthermore, in the comparison between the values for Pomphuis/Nuweland and Block 2, the variable V differs by a factor of 1.8 whereas w (sediment) differs by a factor of 2. By using eq. (4.6) and the data in Table 4-6, the minimum P value for Block 2 occurs at P_1 value of about 0.97.

From the differences observed (W_o and w) between the groups, it is clear that the minimum P value is expected for the Pomphuis/Nuweland block.

Table 4-6: Comparison of the variables/parameters between the group components (W_o and w). The uncertainties are in 1σ.

Group component	Parameter/variable	Pomphuis/Nuweland block (W_1)	Block 2 (W_2)
Minimum (base sediment)	^{238}U	11.8±0.2	28.0±0.3
	^{232}Th	11.39±0.13	28.0±0.6
	^{40}K	29.5±0.7	127±2
	V_o	22.7±1.0	56±5
	W_o	56±6	242±30
Maximum (sediment group)	^{238}U	67.8±0.6	68±2
	^{232}Th	55.6±0.8	111.0±1.2
	^{40}K	315±4	227±2
	V	129±4	232±14
	w	559±36	368±50

Table 4-7 presents the contents of the variable amplitudes (P_1 and P_2) for the samples in the two sediment groups. For the present data, the values range from 0.001 to 1.00 and 0.04 to 1.00 for groups W_1 and W_2, respectively. This implies that the other variable (1-P) characterising the base sediment also ranges from 1 to 0 and 0.96 to 0 for groups W_1 and W_2, respectively.

Table 4-7: Contents of the variable amplitude *P* for samples in the two groups.

Pomphuis and Nuweland blocks				Block 2	
Sampling point	P_1	Sampling point	P_1	Sampling point	P_2
P1	0.85±0.07	N5	0.036±0.011	B1	0.18±0.11
P2	0.18±0.03	N6	0.022±0.011	B2	0.31±0.13
P3	0.031±0.019	N7	0.040±0.011	B3	0.24±0.13
P4	0.27±0.03	N8	0.152±0.015	B4	0.92±0.20
P5	0.49±0.05	N9	0.30±0.02	B5	1.00±0.21
P6	0.001±0.019	N10	0.115±0.013	B6	0.17±0.12
P7	0.08±0.02	N11	0.33±0.02	B7	0.30±0.13
P8	0.037±0.019	N12	0.51±0.04	B8	0.20±0.12
P9	0.54±0.05	N13	0.175±0.016	B9	0.24±0.12
P10	0.022±0.019	N14	0.095±0.013	B10	0.30±0.13
P11	0.34±0.04	N15	0.082±0.012	B11	0.10±0.11
P12	0.22±0.03	N16	0.105±0.013	B12	0.14±0.11
P13	0.06±0.02	N17	0.24±0.02	B13	0.19±0.12
P14	0.08±0.02	N18	0.34±0.03	B14	0.62±0.16
P15	0.058±0.019	N19	0.202±0.017	B15	0.06±0.11
P16	0.22±0.03	N20	0.046±0.011	B16	0.57±0.15
P17	0.19±0.03	N21	0.107±0.013	B17	0.13±0.12
P18	0.20±0.03	N22	0.063±0.012	B18	0.39±0.13
P19C	0.043±0.019	N23	0.096±0.013	B18*	0.51±0.14
P20	0.88±0.08	N24	0.024±0.011	B19	0.20±0.12
P21	1.00±0.09			B19*	0.23±0.12
P22C	0.016±0.018			B20	0.22±0.12
P23	0.10±0.02			B20*	0.41±0.14
P24	0.010±0.018			B21	0.04±0.11
P25	0.18±0.03			B21*	0.13±0.12
N1	0.37±0.03			B22	0.24±0.12
N2	0.27±0.02			B22*	0.46±0.14
N3	0.057±0.012			B23	0.57±0.15
N4	0.064±0.012			B23*	0.64±0.08

* Refers to results of 30-60 cm soil sampling depths. Results of other points are based on 0-30 cm soil depths.

4.3 Radiometric characterisation of group physico-chemical properties

In this section an approach to radiometrically characterize physico-chemical parameters in the two sediment groups is described. Furthermore, the link between radiometry and soil physico-chemical properties is investigated. The approach may become an alternative to the traditional determination techniques of soil physico-chemical parameters.

4.3.1 Data-quality assurance and control

In this sub-section the quality of soil physico-chemical data determined by the XRF, ICP-MS and ICP-OES techniques is investigated. To determine the reproducibility and precision in each technique used, ten sub-samples from one sample (B13) randomly chosen, were analysed and are presented in this section. All other results from the physico-chemical analyses are listed in Appendix 2, Tables A2-1 to A2-6.

(a) XRF
Reproducibility

To ensure accurate results for major elements analysed, standard certified reference materials were used for quality control [Fra08]. The standards used were BHVO (Basalt from USGS), NIM-G (Granite from MINTEK) and AGV (Andesite from USGS) [Fra08]. Table 4-8 gives the measured and certified values of the three standard reference materials. From the table, the measured and certified values of all elements with the exception of Cr_2O_3 agree to within 6%, 30% and 18%, for BHVO, NIM-G and AGV standards, respectively. However, results for Cr_2O_3 show significant deviation by 70%, 100% and 100%, for the BHVO, NIM-G and AGV standards, respectively. A likely important reason for the discrepancy in the XRF results arises from the statistical fluctuation (counts) during XRF spectral measurement. The poor agreement observed in Cr_2O_3 results might be attributed to background interference in the XRF spectrum due to the very low Cr_2O_3 concentrations [Fra08].

Table 4-9 presents the XRF results and standard deviation for ten sub-samples of one sample. As expected, results of all elements with exception of Cr_2O_3 show good reproducibility within relative standard deviation of 14%. In these samples the

concentration of Cr_2O_3 is higher than in the standard samples and the relative standard deviation of Cr_2O_3 is 18%. The quoted uncertainties of all major elements presented in this study are at the 1 σ level from the standard deviations presented in Table 4-9. Furthermore, the absolute uncertainties are used in this work rather than relative uncertainties since for the concentrations lower than in the sub-samples the relative uncertainties will likely increase.

Table 4-8: Comparison of measured and certified values of standard reference materials used as quality control standards for major element analyses by XRF [Fra08] (refer Chapter 2, section 2.4).

Standard	Value (%)	SiO_2	Al_2O_3	Fe_2O_3	MnO	MgO	CaO	Na_2O	K_2O	TiO_2	P_2O_5	Cr_2O_3
BHVO	measured	49.35	13.30	12.50	0.16	7.06	11.73	2.14	0.52	2.76	0.28	0.051
	certified	49.94	13.80	12.23	0.17	7.23	11.40	2.26	0.52	2.71	0.27	0.030
NIM-G	measured	75.63	12.54	2.03	0.02	0.06	0.76	3.47	5.00	0.10	0.007	0.000
	certified	75.70	12.08	2.02	0.02	0.06	0.78	3.36	4.99	0.09	0.010	0.001
AGV	measured	58.03	17.00	6.79	0.10	1.26	4.89	4.27	2.94	1.10	0.50	0.0000
	certified	58.79	17.14	6.76	0.09	1.53	4.94	4.26	2.91	1.05	0.49	0.0001

Table 4-9: Concentrations by mass (%) of soil major elements in ten sub-samples of one sample.

Sub-samples	SiO2	Al_2O_3	MgO	CaO	Fe_2O_3	MnO	TiO_2	Cr_2O_3	Na_2O	K_2O	P_2O_5
SS-01	84.6	6.01	0.15	0.105	4.1	0.029	0.573	0.041	0.08	0.612	0.052
SS-02	83.6	6.10	0.19	0.128	4.7	0.026	0.555	0.054	0.22	0.620	0.066
SS-03	83.9	6.04	0.18	0.121	4.8	0.029	0.559	0.041	0.18	0.610	0.064
SS-04	84.0	6.17	0.19	0.124	4.4	0.029	0.574	0.034	0.22	0.622	0.063
SS-05	84.9	5.96	0.20	0.117	4.0	0.027	0.565	0.045	0.31	0.633	0.058
SS-06	84.9	6.01	0.14	0.121	4.4	0.029	0.576	0.059	0.09	0.617	0.055
SS-07	84.4	6.02	0.14	0.105	4.7	0.029	0.564	0.055	0.30	0.607	0.055
SS-08	83.8	6.17	0.13	0.108	4.8	0.029	0.570	0.060	0.13	0.620	0.062
SS-09	84.9	6.02	0.18	0.116	4.0	0.029	0.570	0.042	0.12	0.613	0.056
SS-10	83.9	6.29	0.16	0.130	4.9	0.029	0.566	0.050	0.11	0.631	0.069
Mean	**84.3**	**6.08**	**0.17**	**0.118**	**4.5**	**0.0285**	**0.567**	**0.048**	**0.18**	**0.619**	**0.060**
Standard dev.	**0.5**	**0.10**	**0.02**	**0.009**	**0.4**	**0.001**	**0.007**	**0.009**	**0.08**	**0.009**	**0.006**

Radiometry versus chemistry for XRF measurements

To investigate the agreement between radiometry and major elements, K_2O concentrations were compared to ^{40}K (Bq/kg) by using an approach similar to that used for obtaining the activity concentration of ^{40}K in KCl (16.3 kBq/kg), presented in Chapter 3 (intermezzo 3.4). It is found that 1% of K_2O by mass corresponds to 257 Bq/kg of ^{40}K. Figure 4-6 shows a 2D correlation plot and best fit (K_2O% versus ^{40}K) for the blocks

Pomphuis/Nuweland and Block 2, with the χ_v^2 of 14. The combination of large χ_v^2 value and a good fit obtained indicates that the statistical uncertainties in the analysis results are much smaller than the natural spread in the values. Hence, uncertainty estimates from sub-samples is not a reliable approach in this case. However, from the plot one notices that there is a good qualitative correlation between K_2O% and ^{40}K AC. From the plot a relation is found of 1% K_2O corresponding to 306 Bq/kg. This corresponds to an absolute deviation of 19%. The likely reason for the deviation may be the fact that the major-element concentrations are normalized to unity and are not taking into account trace elements and carbon lost in heating. Deviations due to trace elements and loss of mass [Fra08] accounts for approximately on average 8% and 4%, respectively. However, this is not a full explanation for the deviation observed especially at ^{40}K ACs above 250 Bq/kg (see Figure 4-6), hence suggesting a possible systematic effect associated with XRF measurements. For radiometry, ^{40}K analysis was validated using the IAEA standard reference soil and was found to agree within 95% confidence interval (see Chapter 3, section 3.2.1).

Figure 4-7 shows a 2D correlation plot and best fit (K_2O% versus ^{40}K AC) after correcting for the mass loss during XRF analysis. The χ_v^2 value for the best fit is 12, almost consistent with Figure 4-6. From the plot the qualitative correlation between K_2O% and ^{40}K AC is also similar as in Figure 4-6. It is found from the plot that 1% K_2O corresponds to 301 Bq/kg, leading to an absolute deviation of 17%. This confirms that mass loss in heating does not significantly contribute to the deviations observed. On the other hand, the amount of trace elements could not be corrected for due to the fact that not all the same samples analysed for major elements were also run for trace-element analyses.

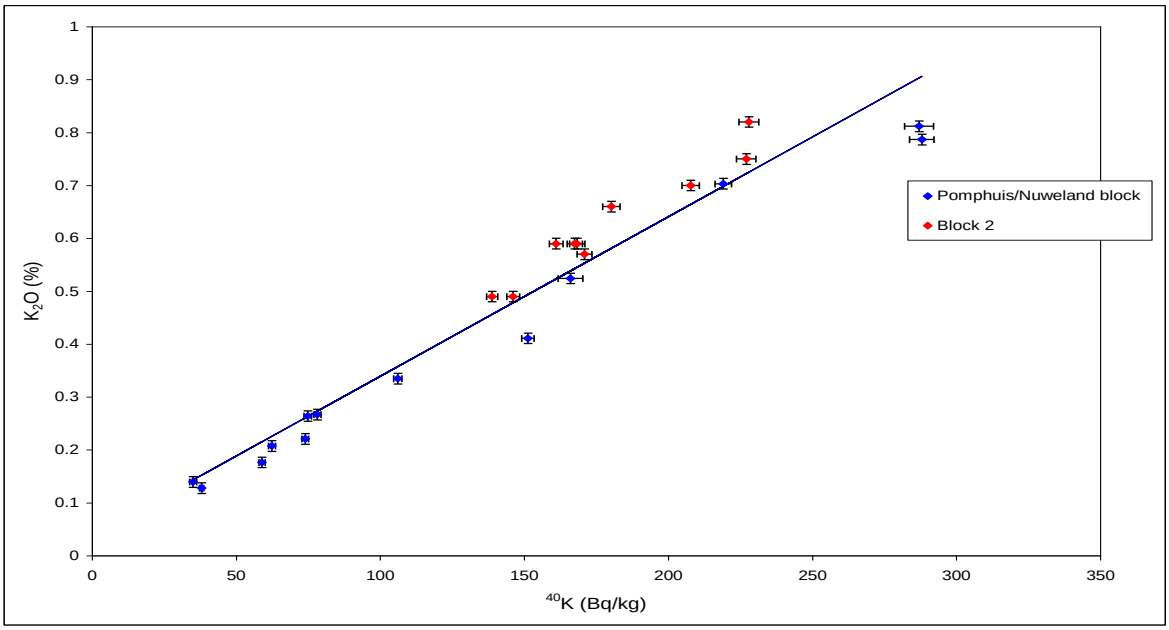

Figure 4-6: *Weighted fit showing correlation between ^{40}K ACs (HPGe) and K concentrations (XRF) for groups W_1 and W_2. The XRF data are given in Appendix 2, Tables A2-1 and A2-2.*

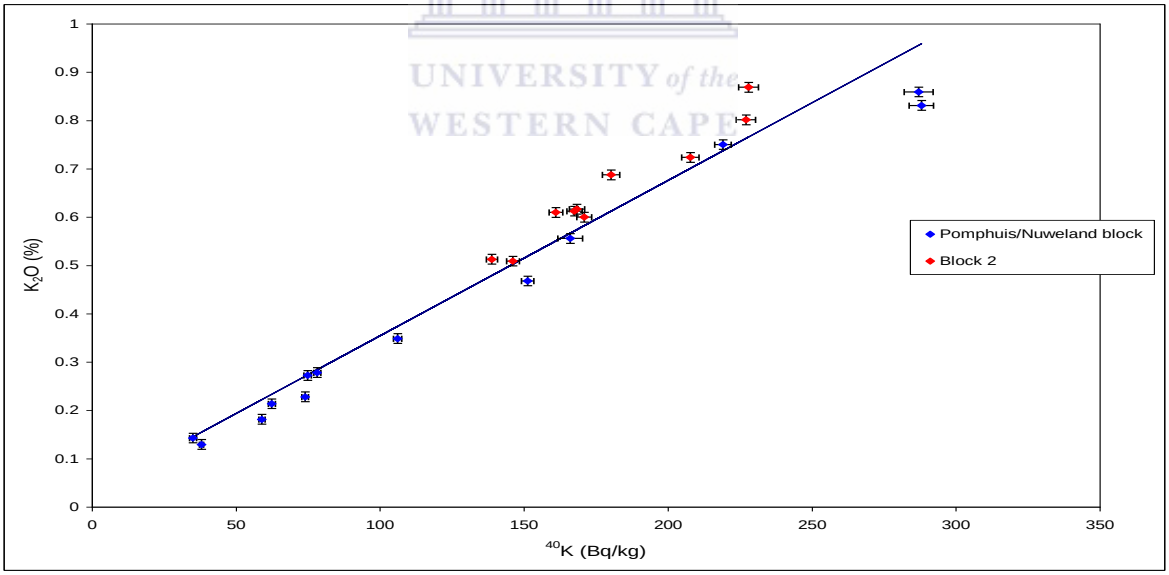

Figure 4-7: *Weighted fit showing correlation between ^{40}K ACs (HPGe) and K concentrations (XRF) after correcting for the loss on ignition (LOI) for groups W_1 and W_2. LOI refers to the mass of carbon lost during sample heating.*

(b) ICP-MS
Reproducibility

As in the case of the XRF data quality control, BHVO-2G standard certified reference material was used to investigate the quality of trace-element data obtained *via* leaching[††]. Table 4-10 compares the measured and certified values with their relative standard deviation (% RSD). From the table it is clear that there is good agreement for most elements to within about 5%.

Table 4-11 shows the trace-element results and standard deviations of ten sub-samples. With the exception of Zn and Cd, all elements show good reproducibility within the relative standard deviation of 10%. Zn and Cd yields the relative standard deviations of 40% and 20%, respectively. It is unclear whether these large uncertainties are due to interference or that they are weak lines. As in the case of major elements, the quoted uncertainties of all trace elements in this study are the standard deviations of ten-sub samples.

Table 4-10: Measured and certified values of standard reference material used as quality control standard for trace element analyses by ICP-MS (refer Chapter 2, section 2.4).

Trace elements	Certified value (ppm)	Measured value (ppm)	% RSD
Li	17	17.9	5
Be	13.6	13.3	2
B	154	170.7	11
K	1984	1836	7
V	36.9	36.2	1.9
Cr	19.9	20.9	5
Co	26.4	26.3	0.3
Ni	60.9	59.3	3
Cu	22.2	22.1	0.5
Zn	76.5	74.3	3
As	59	60.2	2
Se	11.7	12	3
Sr	315.2	332.1	5
Mo	118.5	106.5	10
Cd	6.408	6.405	0.05
Ba	531	510.1	4
Pb	19.2	18.7	2

[††] The analysis procedure first involves digesting a sample in HNO_3 and H_2O_2 to obtain leachable trace elements. The approach avoids the effects of silicates to accurately determine the concentration of trace elements.

Table 4-11: Concentrations (mg/kg) of soil leachable trace elements as determined by ICP-MS in ten sub-samples of one sample.

Sub-samples	Li	Be	B	K	V	Cr	Mn	Co	Ni	Cu	Zn	As	Se	Sr	Mo	Cd	Ba	Pb
SS-01	2.70	0.631	1.09	535	37	27	23.3	0.79	2.73	10.5	2.0	31.2	1.118	5.0	0.221	0.032	26.9	9.93
SS-02	2.65	0.639	1.07	569	35	26	23.9	0.87	3.01	11.4	6.5	29.5	1.151	5.5	0.211	0.033	27.5	9.92
SS-03	2.66	0.642	1.14	543	36	26	24.1	0.79	2.94	9.8	3.7	31.2	1.142	5.2	0.219	0.030	26.8	9.93
SS-04	2.71	0.638	1.23	512	40	30	23.4	0.77	2.77	11.3	2.4	30.3	1.163	4.8	0.233	0.032	26.6	9.96
SS-05	2.74	0.629	1.05	506	36	28	22.7	0.75	2.61	10.8	5.3	28.5	1.145	4.9	0.220	0.030	24.5	9.90
SS-06	2.57	0.644	1.08	529	36	26	24.0	0.87	3.05	11.2	7.7	28.9	1.141	5.8	0.212	0.034	28.5	9.94
SS-07	2.61	0.629	1.06	542	36	26	22.7	0.82	2.96	11.3	2.9	28.4	1.161	4.8	0.221	0.046	26.7	9.90
SS-08	2.61	0.630	1.04	541	42	33	24.3	0.80	2.95	12.1	5.1	31.1	1.147	4.6	0.224	0.029	28.6	9.91
SS-09	2.67	0.640	1.07	564	35	26	24.6	0.83	3.04	10.5	6.3	28.6	1.140	5.1	0.210	0.034	27.6	9.94
SS-10	2.70	0.631	1.05	520	34	26	24.3	0.81	2.72	9.9	4.8	26.8	1.143	5.2	0.220	0.053	25.8	9.91
Mean	**2.66**	**0.635**	**1.09**	**536**	**37**	**27**	**23.7**	**0.81**	**2.88**	**10.9**	**4.6**	**29.5**	**1.145**	**5.1**	**0.219**	**0.035**	**26.9**	**9.92**
Standard dev.	**0.05**	**0.006**	**0.06**	**20**	**3**	**3**	**0.7**	**0.04**	**0.16**	**0.7**	**1.9**	**1.5**	**0.012**	**0.3**	**0.007**	**0.008**	**1.2**	**0.02**

Radiometry versus trace element K for ICP-MS measurements

To investigate the relationship between radiometry and soil leachable trace elements, soil activity concentrations ^{40}K (Bq/kg) and trace element K (mg/kg) were compared. Figure 4-8 shows a 2D correlation plot and best fit (K conc. versus ^{40}K AC) for the blocks Pomphuis/Nuweland and Block 2, with the χ_ν^2 of 17. This χ_ν^2 value indicates that the uncertainties estimated from sub-samples are reliable. Hence, from the plot a relation is found of 1 Bq/kg of ^{40}K corresponds to 2.30±0.11 mg/kg. For situations where all K is leached, 1 Bq/kg of ^{40}K is expected to correspond to 32.3 mg/kg (from the relation of 1% K corresponding to 310 Bq/kg of ^{40}K). From these results only about 7% of K is soil-leachable.

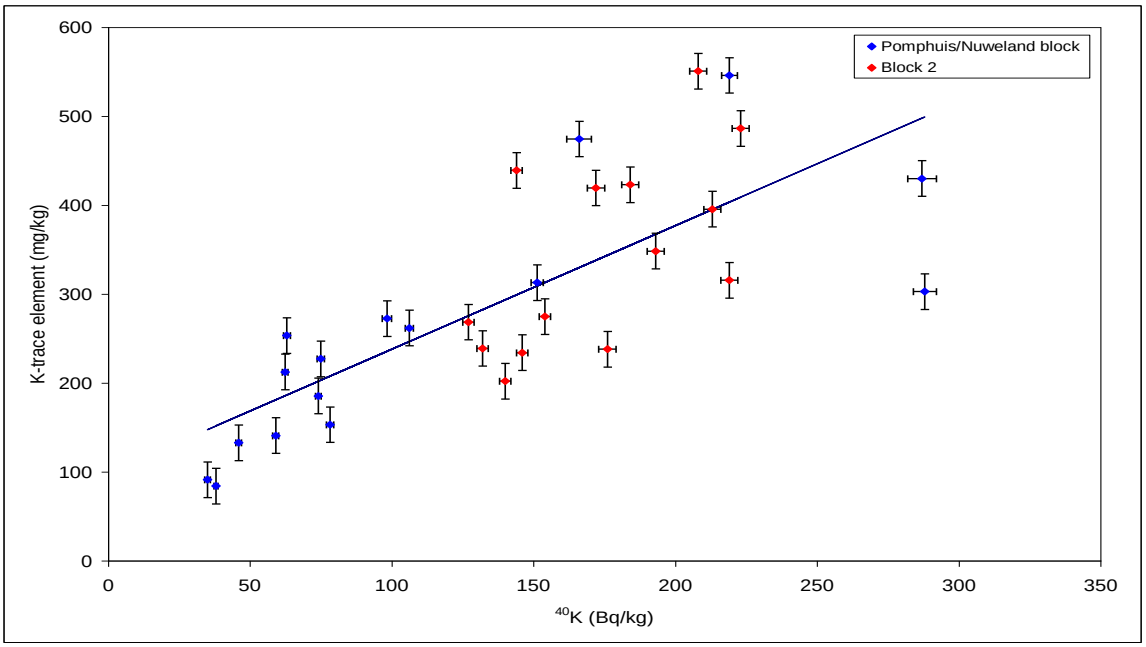

Figure 4-8: *Weighted fit showing correlation between ^{40}K activity concentrations (HPGe) and trace element K concentrations (ICP-MS) for groups W_1 and W_2. The ICP-MS data are in Appendix 2, Tables A2-3 and A2-4.*

(c) ICP-OES
Reproducibility

As for the XRF and ICP-MS techniques, the reproducibility of physico-chemical parameters extracted by ICP-OES was checked. Table 4-12 presents the results of physico-chemical parameters and standard deviations of ten sub-samples analysed. All parameters with the exception of B show good reproducibility to within 18%. However, the relative standard deviation of B is 45%. Again, similar to the case of Cr_2O_3, this higher uncertainty might be attributed to background interference due to its very low concentration (average of 0.2 mg/kg).

Table 4-12: Soil physico-chemical parameters in ten sub-samples from one sample.

sub-samples	pH	Resist.	H^+	Exchangeable cations (cmol(+)/kg)*				Extractable elements (mg/kg)					C	Clay	Silt	Sand
	(KCl)	(Ohm)	(cmol/kg)	Na	K	Ca	Mg	P	Cu	Zn	Mn	B	%	%	%	%
SS-01	5.80	2190	0.15	0.070	0.31	3.04	0.46	19	2.48	1.6	4.8	0.17	0.37	12.6	9.8	78.6
SS-02	5.80	1420	0.20	0.080	0.37	3.38	0.52	17	2.28	1.6	4.5	0.19	0.38	12.9	9.0	79.8
SS-03	5.80	1540	0.15	0.060	0.29	2.81	0.39	18	2.11	1.5	4.2	0.19	0.38	12.2	9.4	78.4
SS-04	5.80	1470	0.20	0.060	0.30	2.84	0.40	21	2.07	1.5	4.2	0.19	0.38	11.9	10.0	78.8
SS-05	5.80	1480	0.25	0.060	0.29	2.78	0.39	20	2.07	1.5	4.4	0.13	0.37	12.6	10.0	77.8
SS-06	5.80	1750	0.25	0.060	0.28	2.79	0.39	19	2.10	1.6	5.2	0.19	0.43	12.0	9.0	77.8
SS-07	5.80	1510	0.25	0.060	0.29	2.8	0.39	18	1.92	1.5	4.3	0.23	0.37	11.9	9.0	77.8
SS-08	5.80	1610	0.20	0.060	0.29	2.79	0.39	22	1.94	1.5	4.4	0.52	0.35	12.0	9.0	77.8
SS-09	5.80	1590	0.20	0.060	0.30	2.82	0.40	20	1.86	1.4	4.3	0.30	0.33	12.4	9.0	76.8
SS-10	5.80	1670	0.25	0.060	0.28	2.74	0.38	24	2.00	1.5	4.6	0.31	0.33	12.2	8.0	77.8
Mean	**5.80**	**1623**	**0.21**	**0.063**	**0.30**	**2.88**	**0.41**	**20**	**2.08**	**1.52**	**4.5**	**0.24**	**0.37**	**12.3**	**9.2**	**78.1**
Standard dev.	**0.00**	**200**	**0.04**	**0.007**	**0.03**	**0.19**	**0.04**	**2**	**0.18**	**0.06**	**0.3**	**0.11**	**0.03**	**0.3**	**0.6**	**0.8**

* cmol(+)/kg refers to centimoles of positive charge per kilogram.

Radiometry versus exchangeable cation K for ICP-OES measurements

Similar to the ICP-MS, the relationship between radiometry and exchangeable cations was investigated. Figure 4-9 shows a 2D plot (Exchangeable K versus ^{40}K AC) for the blocks Pomphuis/Nuweland and Block 2. From the plot there is no correlation found as expected from the literature that exchangeable cations in soils are influenced by clay minerals and amounts of organic matter present [Kab04, Dan06].

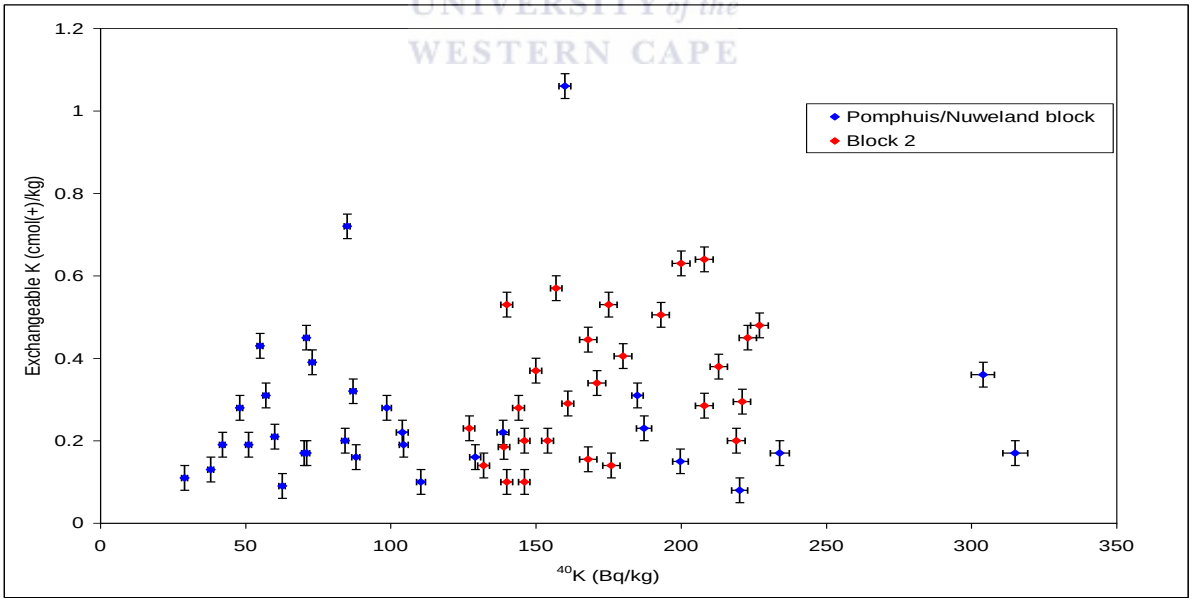

Figure 4-9: *Plot showing the relationship between ^{40}K activity concentrations (HPGe) and exchangeable K concentrations (ICP-OES) for groups W_1 (Pomphuis and Nuweland) and W_2 (Block 2). The ICP-OES data are in Appendix 2, Tables A2-5 and A2-6.*

Summary

There is reasonably good agreement between certified and measured values for all elements except Cr_2O_3 which seems to significantly deviate. As far as reproducibility is concerned, all elements yield good precision with the exception of Zn (trace element) and B (extractable element), hence these are expected to show significant deviations in the analysed samples. A good qualitative correlation between K_2O% and ^{40}K AC is found although the relationship shows an absolute deviation of 17%. The correction for mass loss due to heating does not explain the significant deviation observed. There is a correlation between ^{40}K and leachable K and it is found that the amount that is leached is about 7%.

4.3.2 Comparison of physico-chemical parameters for the sediment groups

In this section the differences in physico-chemical parameters between sediment groups (w) and base sediments (W_o) of each group are investigated. Figure 4-10 shows 2D correlation plots (V versus ^{40}K) for the two groups indicating the classification of the groups and the sampling points of w and W_o used for the comparison.

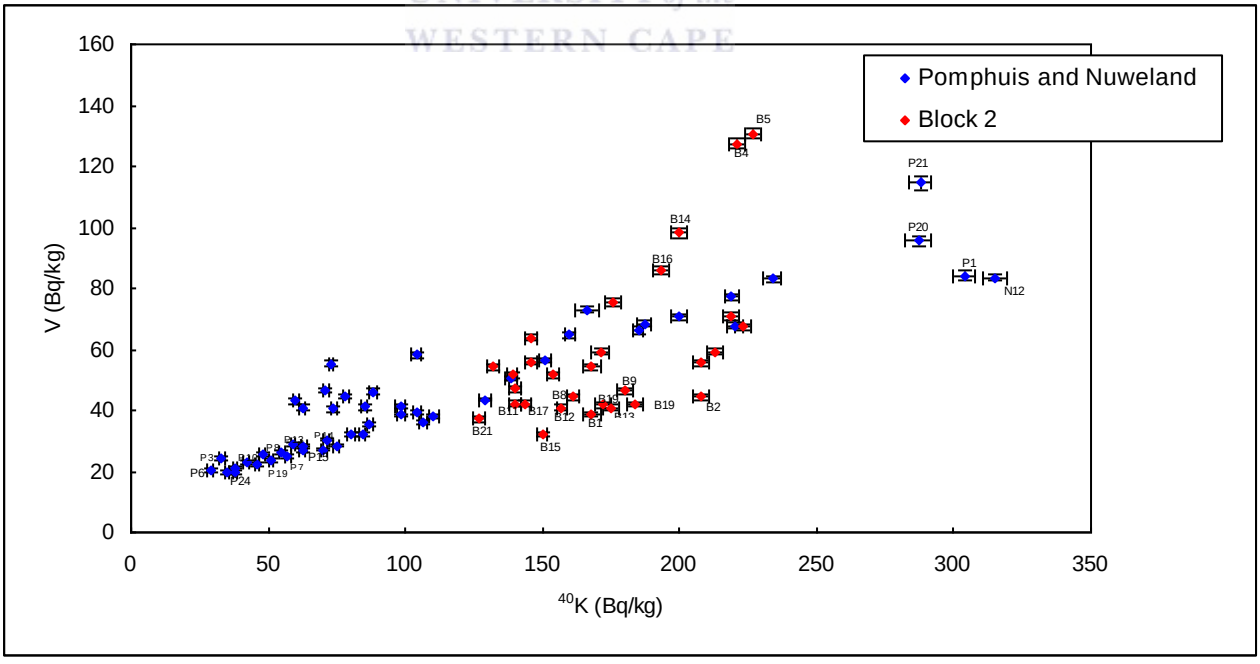

Figure 4-10: *Two dimensional plot showing the correlations between V versus ^{40}K ACs from W_1 (Pomphuis and Nuweland) and W_2 (Block 2) group data.*

Table 4-13 presents the ratios of soil major elements between *w* and W_o for group Pomphuis/Nuweland (W_1) from results listed in Appendix 2 (Table A2-1). From the table one notices quite a significant difference in major element concentrations between *w* and W_o in Al_2O_3, MgO, CaO, Fe_2O_3, TiO_2 and K_2O by approximately average factors of 5, 4, 2, 2, 2 and 6, respectively. On the other hand, SiO, Cr_2O_3 and P_2O_5 differ by average factors of 0.8, 0.7 and 1.3, respectively. However, there is no significant difference observed in MnO. The clear difference observed in Al_2O_3, MgO and K_2O implies that they are dominant major elements characterising *w*. Similar comparison for the group W_2 (Block 2) is presented in Table 4-14 and the data are listed in Appendix 2 (Table A2-2). In this group significant difference is observed in Al_2O_3 and MgO by approximately an average factor of 1.5 and 1.7, respectively. This implies that only two major elements characterise *w* in this group contrary to the case for W_1. The difference observed in other elements suggests that there is no clear distinction in the elements between *w* and W_o. Table 4-15 presents the comparison of the sediment-group values (major elements) between blocks Pomphuis/Nuweland and Block 2. From the table it is noted that there is no significant difference in all major elements with the exception of MnO and TiO_2 which differ by an average factor of 1.6 and 1.5, respectively.

Table 4-13: Ratios of soil major elements between sediment group (*w*) and base sediment W_o for group W_1 (Pomphuis and Nuweland). The quoted uncertainties are at the 1 σ level.

Ratio	SiO_2	Al_2O_3	MgO	CaO	Fe_2O_3	MnO	TiO_2	Cr_2O_3	Na_2O	K_2O	P_2O_5
P20/P19	0.868±0.007	5.0±0.3	6±2	2.5±0.3	0.75±0.14	1.13±0.14	1.83±0.07	0.6±0.2	BDL*	7.0±0.6	1.18±0.16
P20/P22	0.852±0.007	5.2±0.3	3.3±0.8	2.8±0.4	1.3±0.3	0.94±0.10	2.32±0.10	1.1±0.5	0.4±0.3	6.4±0.5	1.7±0.3
P20/P24	0.873±0.007	5.0±0.3	2.7±0.5	1.57±0.15	0.81±0.15	1.03±0.12	2.24±0.09	0.8±0.3	0.4±0.3	5.8±0.4	0.91±0.11
P21/P19	0.833±0.007	5.0±0.3	5.2±0.3	1.9±0.3	1.8±0.2	1.19±0.17	1.96±0.08	0.5±0.2	BDL*	6.8±0.5	1.16±0.19
P21/P22	0.818±0.007	5.2±0.3	3.0±0.8	2.1±0.3	3.1±0.6	1.00±0.13	2.48±0.12	0.8±0.5	0.5±0.4	6.2±0.4	0.7±0.3
P21/P24	0.837±0.007	5.1±0.3	2.4±0.5	1.20±0.12	1.9±0.3	1.09±0.15	2.39±0.11	0.6±0.3	0.6±0.3	5.6±0.4	0.90±0.14
Mean±SD	0.85±0.02	5.09±0.10	3.7±1.4	2.0±0.6	1.6±0.9	1.06±0.09	2.2±0.3	0.7±0.2	0.44±0.04	6.3±0.5	1.3±0.4

Notes:

*: Below detection limit

Table 4-14: Ratios of soil major elements between sediment group (w) and base sediment W_o for group W_2. The quoted uncertainties are at the 1 σ level.

Ratio	SiO_2	Al_2O_3	MgO	CaO	Fe_2O_3	MnO	TiO_2	K_2O	P_2O_5
B4/B1	0.974±0.009	1.54±0.003	2.0±0.3	1.35±0.13	0.47±0.06	0.91±0.06	1.09±0.02	1.11±0.02	1.23±0.14
B4/B2	0.945±0.008	1.28±0.003	1.6±0.2	1.37±0.14	1.4±0.3	0.81±0.05	1.03±0.02	0.94±0.02	2.1±0.3
B4/B8	0.956±0.008	1.46±0.03	1.7±0.3	1.13±0.10	0.75±0.11	0.78±0.05	1.01±0.02	1.12±0.02	1.15±0.12
B4/B9	0.982±0.009	1.18±0.02	1.7±0.3	1.77±0.21	0.68±0.10	0.88±0.06	0.95±0.02	1.00±0.02	1.21±0.13
B5/B1	0.933±0.008	1.91±0.04	1.8±0.3	0.87±0.11	0.56±0.06	0.87±0.05	1.23±0.02	1.27±0.02	1.10±0.13
B5/B2	0.905±0.008	1.59±0.03	1.5±0.2	0.88±0.11	1.6±0.3	0.77±0.05	1.16±0.02	1.08±0.02	1.9±0.3
B5/B8	0.916±0.008	1.81±0.04	1.6±0.2	0.73±0.08	0.89±0.12	0.74±0.05	1.23±0.02	1.28±0.02	1.03±0.11
B5/B9	0.940±0.009	1.46±0.03	1.6±0.2	1.14±0.16	0.80±0.10	0.83±0.05	1.16±0.02	1.14±0.02	1.08±0.12
Mean±SD	0.94±0.03	1.53±0.20	1.68±0.15	1.2±0.3	0.9±0.4	0.82±0.06	1.08±0.09	1.12±0.12	1.3±0.4

Table 4-15: Comparison of the ratios of the soil major elements between the two sediment groups.

Ratio	SiO_2	Al_2O_3	MgO	CaO	Fe_2O_3	MnO	TiO_2	K_2O	P_2O_5
B4/P20	1.010±0.009	0.872±0.014	1.00±0.10	0.85±0.07	1.23±0.20	1.68±0.18	1.49±0.03	0.809±0.014	1.29±0.14
B4/P21	1.053±0.010	0.859±0.014	1.11±0.12	1.11±0.10	0.51±0.07	1.58±0.16	1.39±0.03	0.835±0.014	1.32±0.14
B5/P20	0.967±0.009	1.077±0.016	0.91±0.09	0.55±0.06	1.5±0.3	1.60±0.17	1.68±0.03	0.925±0.015	1.16±0.13
B5/P21	1.008±0.010	1.061±0.015	1.01±0.11	0.72±0.08	0.61±0.07	1.51±0.16	1.57±0.03	0.955±0.015	1.18±0.13
Mean±SD	1.01±0.04	0.97±0.12	1.01±0.08	0.81±0.20	1.0±0.5	1.59±0.07	1.53±0.12	0.88±0.07	1.24±0.07

Comparison of soil trace elements between w and W_o for group W_1 data listed in Appendix 2 (Table A2-3), is presented in Table 4-16. As noted, all trace elements with the exception of Cr indicate significant variation ranging from an average ratio of 0.7 (Mo) to 11 (Ba). Furthermore, one notices that elements Li, Be, K, Co, Se, Sr and Ba show quite clear distinction implying that they are indicators characterising w, with Ba being a strong indicator. Table 4-17 presents similar comparison for group W_2 from data listed in Appendix 2 (Table A2-4). From the table, it is observed that, with the exception of Ti, Mn and Cr, all elements show significant variation ranging from an average ratio of 0.6 (Si) to 3.5 (Be), contrary to group W_1. Compared to group W_1, there is unclear difference in trace elements between w and W_o in this group, although Be, As, Ni and V seem to characterize w. Table 4-18 presents the comparison of the sediment-group values (trace elements) between Pomphuis/Nuweland (w_1) and Block 2 (w_2). From the table it is noted that the values show significant difference ranging from an average ratio of 0.2 (Ba) to 3.2 (Be). Furthermore, it is noted that while Be, V, Cr, Ni, As and Mo are indicators characterising sediment group w_2, Sr and Ba are indicators for sediment group w_1.

Table 4-16: Ratios of soil trace elements between sediment group (w) and base sediment W_o for group W_1. The quoted uncertainties are at the 1 σ level.

Ratio	Li	Be	B	K	V	Cr	Co	Ni	Cu	Zn	As	Se	Sr	Mo	Cd	Ba
P20/P19	4.5±0.4	4.1±0.4	2.4±0.4	3.2±0.5	1.4±0.4	2.2±1.5	2.6±0.5	2.0±0.7	1.22±0.09	1.8±0.3	0.9±0.2	5.5±0.5	2.9±0.3	0.90±0.09	2.05±0.85	3.28±0.16
P20/P22	5.3±0.6	2.53±0.15	2.2±0.3	5.1±1.3	0.60±0.13	1.4±0.7	1.8±0.3	2.2±0.8	1.9±0.2	3.4±1.1	0.65±0.13	5.9±0.5	5.3±0.8	0.48±0.04	2.8±1.5	10.3±1.5
P20/P24	6.9±1.0	4.3±0.4	1.6±0.2	4.7±1.1	1.4±0.5	1.7±0.9	2.6±0.5	1.6±0.4	1.10±0.08	0.93±0.11	1.3±0.4	7.7±0.9	3.2±0.3	0.75±0.07	2.3±1.1	13±3
P21/P19	3.1±0.3	3.9±0.4	1.6±0.3	2.3±0.4	1.6±0.5	3.1±1.9	4.6±0.9	2.5±0.8	0.84±0.08	0.8±0.2	1.3±0.3	3.6±0.3	2.7±0.2	0.80±0.09	1.6±0.7	4.8±0.2
P21/P22	3.6±0.4	2.38±0.15	1.5±0.2	3.6±0.9	0.69±0.14	2.0±0.9	3.2±0.4	2.8±0.9	1.34±0.16	1.5±0.5	0.98±0.15	3.9±0.4	4.9±0.8	0.42±0.04	2.2±1.2	15±2
P21/P24	4.7±0.7	4.0±0.4	1.06±0.14	3.3±0.8	1.7±0.5	2.3±1.1	4.6±0.9	2.0±0.5	0.76±0.07	0.40±0.09	2.0±0.5	5.1±0.6	3.0±0.3	0.66±0.07	1.8±0.9	20±4
Mean±SD	4.7±1.2	3.5±0.9	1.7±0.5	3.7±1.0	1.2±0.5	2.1±0.6	3.2±1.1	2.2±0.4	1.2±0.4	1.5±1.1	1.2±0.5	5.3±1.5	3.7±1.1	0.7±0.2	2.1±0.4	11±6

Table 4-17: Ratios of soil trace elements between sediment group (w) and base sediment W_o for group W_2. The quoted uncertainties are at the 1 σ level.

Ratio	Li	Be	Si	K	Ti	V	Cr	Mn	Co	Ni	Cu	Zn	As	Se	Sr	Mo	Cd	Ba	Pb
B16/B17	1.25±0.03	2.45±0.05	0.58±0.04	0.79±0.06	0.94±0.05	2.4±0.5	3.4±1.3	0.336±0.014	0.73±0.06	1.46±0.13	1.34±0.15	1.2±0.5	2.0±0.3	0.98±0.03	1.19±0.16	2.13±0.16	1.2±0.4	1.10±0.09	1.357±0.005
B16/B19	1.29±0.03	2.22±0.04	0.70±0.05	0.83±0.06	0.99±0.06	2.4±0.5	3.1±1.1	0.179±0.007	0.50±0.04	1.38±0.12	0.73±0.06	0.8±0.3	1.6±0.2	0.82±0.03	1.13±0.15	0.75±0.03	1.5±0.5	0.94±0.07	1.319±0.005
B16/B21	2.04±0.08	3.17±0.08	0.65±0.05	1.72±0.20	1.07±0.06	2.3±0.5	1.7±0.4	2.5±0.3	2.9±0.6	2.8±0.4	2.6±0.5	2.6±1.7	1.4±0.2	1.78±0.09	1.32±0.19	0.66±0.02	2.2±1.0	1.9±0.2	1.359±0.005
Mean±SD	1.5±0.4	2.6±0.5	0.65±0.06	1.1±0.5	1.00±0.07	2.34±0.08	2.8±0.9	1.0±1.3	1.4±1.3	1.9±0.8	1.6±0.9	1.5±0.9	1.6±0.3	1.2±0.5	1.22±0.09	1.2±0.8	1.7±0.5	1.3±0.5	1.34±0.02

Table 4-18: Comparison of the ratios of the soil trace elements between the two sediment groups.

Ratio	Li	Be	V	Cr	Co	Ni	Cu	Zn	As	Se	Sr	Mo	Cd	Ba
B16/P20	1.30±0.04	3.11±0.07	2.2±0.5	2.6±0.7	1.14±0.11	2.9±0.5	0.73±0.06	0.35±0.09	2.6±0.5	0.589±0.017	0.33±0.03	2.4±0.2	1.0±0.3	0.271±0.015
B16/P21	1.93±0.07	3.31±0.08	1.9±0.4	1.9±0.4	0.64±0.05	2.3±0.3	1.05±0.10	0.8±0.3	1.7±0.2	0.89±0.03	0.35±0.03	2.8±0.3	1.2±0.4	0.184±0.010

Table 4-19 compares the physico-chemical parameters between w and W_o for group W_1 from results listed in Appendix 2 (Table A2-5). From the table, all parameters except pH show significant differences with average ratio ranging from 0.4 (resistance) to 11 (Na). Moreover one notices that parameters such as Na, Mg, Ca, clay and silt show clear distinction by average factors of 11, 5, 4, 11, and 5, respectively. Again this implies that they are strong indicators characterising w.

Table 4-20 presents similar comparison for group W_2 from the data in Appendix 2 (Table A2-6). From the table one notices a similar trend of variation as in W_1, but in this group the separation is not as clear as in group W_1 such that the difference ranges from an average factor of 0.6 (Mn) to 2.3 (Na). Similar to group W_1, parameters Na, Mg and clay show clear differences by average factors of 2.3, 1.8 and 2.3, respectively.

Table 4-19: Ratios of soil physico-chemical data between sediment group (*w*) and base sediment W_o for group W_1. The quoted uncertainties are at the 1 σ level.

Ratio	pH	Resistance	Exchangeable cations				Extractable elements					C	Clay	Silt	Sand
	(KCl)		Na	K	Ca	Mg	P	Cu	Zn	Mn	B				
P1/P6	1.13	0.12±0.09	31±7	3.3±0.8	6.9±1.3	9.4±0.5	1.95±0.11	0.78±0.06	1.69±0.03	2.43±0.14	3.2±2.1	1.84±0.14	5.2±0.5	15±5	0.576±0.010
P1/P7	1.05	0.20±0.15	15.3±1.7	1.2±0.13	3.0±0.3	4.7±0.3	0.80±0.03	0.84±0.07	1.23±0.02	1.08±0.03	1.6±0.6	1.25±0.07	18±6	4.9±0.5	0.589±0.010
P1/P8	1.17	0.21±0.16	23±4	1.9±0.3	4.3±0.5	7.5±0.5	2.22±0.14	0.82±0.07	1.65±0.02	1.55±0.06	2.1±0.9	3.0±0.4	9.1±1.4	6.7±0.9	0.584±0.010
P1/P10	1.10	0.21±0.16	23±4	2.8±0.6	3.9±0.4	8.0±0.9	1.37±0.06	0.94±0.08	1.59±0.02	1.54±0.06	1.9±0.8	4.4±0.7	7.3±0.9	5.3±0.6	0.594±0.010
P1/P13	1.17	0.24±0.19	13.1±1.3	1.27±0.15	4.3±0.5	5.3±0.4	0.91±0.03	0.97±0.08	1.23±0.02	1.92±0.09	2.9±1.7	1.52±0.10	6.6±0.8	4.4±0.4	0.604±0.010
P1/P14	1.05	0.5±0.4	5.1±0.2	0.84±0.08	4.0±0.5	5.6±0.9	0.84±0.03	1.33±0.14	1.53±0.02	1.90±0.09	2.1±0.9	2.26±0.20	4.9±0.4	3.7±0.3	0.619±0.011
P1/P15	1.05	0.3±0.2	5.4±0.2	1.9±0.3	3.2±0.3	4.6±0.5	1.22±0.05	1.32±0.14	2.25±0.04	1.57±0.06	2.2±0.9	1.65±0.12	8.11±1.14	4.9±0.5	0.596±0.010
P1/P6	1.20	0.23±0.09	11±3	1.6±0.4	5.2±1.0	6.2±0.3	0.19±0.05	0.31±0.05	0.479±0.015	2.55±0.14	3.4±2.0	0.28±0.07	8.2±0.7	10±3	0.601±0.010
N12/P7	1.11	0.39±0.16	5.7±0.7	0.55±0.10	2.3±0.2	3.1±0.5	0.08±0.02	0.33±0.06	0.348±0.010	1.33±0.03	1.7±0.6	0.19±0.05	29±8	3.2±0.3	0.615±0.010
N12/P8	1.24	0.41±0.17	8.5±1.4	0.89±0.19	2.3±0.4	5.0±0.9	0.22±0.06	0.32±0.05	0.469±0.014	1.63±0.06	2.2±0.9	0.46±0.12	14±2	4.3±0.6	0.610±0.010
N12/P10	1.16	0.42±0.17	8.5±1.4	1.3±0.3	2.3±0.3	5.3±0.4	0.13±0.04	0.37±0.06	0.451±0.014	1.61±0.06	2.0±0.8	0.67±0.19	11.5±1.4	3.4±0.4	0.620±0.010
N12/P13	1.24	0.5±0.2	4.9±0.5	0.61±0.11	2.3±0.4	3.6±0.9	0.09±0.02	0.38±0.07	0.348±0.010	2.01±0.09	3.1±1.8	0.23±0.06	10.5±1.2	2.8±0.3	0.630±0.010
N12/P14	1.11	1.0±0.5	1.89±0.08	0.40±0.07	2.3±0.4	3.7±0.4	0.08±0.02	0.53±0.09	0.434±0.013	1.99±0.09	2.2±0.9	0.34±0.09	7.7±0.6	2.4±0.2	0.646±0.011
N12/P15	1.11	0.6±0.3	2.00±0.09	0.89±0.19	2.3±0.2	3.1±0.9	0.12±0.03	0.52±0.09	0.639±0.020	1.65±0.06	2.3±1.0	0.25±0.06	13±2	3.2±0.3	0.622±0.010
Mean±SD	1.13±0.07	0.4±0.2	11±8	1.4±0.8	3.7±1.2	5.4±1.9	0.7±0.6	0.7±0.4	1.0±0.6	1.8±0.4	2.4±0.6	1.3±1.2	11±6	5±3	0.61±0.02

Table 4-20: Ratios of soil physico-chemical data between sediment group (*w*) and base sediment W_o for group W_2. The quoted uncertainties are at the 1 σ level.

Ratio	pH	H^+	Exchangeable cations				Extractable elements					C	Clay	Silt	Sand
	(KCl)		Na	K	Ca	Mg	P	Cu	Zn	Mn	B				
B4/B1	0.83	2.5±0.4	2.5±0.4	1.9±0.4	1.53±0.14	2.8±0.3	0.71±0.14	1.86±0.14	1.24±0.06	1.22±0.08	1.9±1.8	1.77±0.07	1.24±0.07	0.95±0.05	0.874±0.014
B4/B2	0.92	1.67±0.18	2.5±0.4	1.04±0.13	1.30±0.11	1.72±0.13	1.4±0.4	1.72±0.12	1.17±0.05	1.03±0.06	1.42±1.01	1.40±0.02	1.19±0.02	0.85±0.05	0.994±0.017
B4/B8	0.92	1.50±0.15	2.8±0.4	1.02±0.13	1.16±0.09	2.48±0.20	1.50±0.09	1.18±0.06	0.491±0.016	0.68±0.03	1.2±0.7	1.39±0.07	2.19±0.07	1.07±0.06	0.856±0.014
B4/B9	1.01	1.20±0.10	2.5±0.4	0.73±0.08	0.79±0.18	1.74±0.13	1.2±0.3	1.91±0.14	1.40±0.07	1.45±0.10	1.1±0.7	1.46±0.03	1.22±0.03	1.09±0.07	0.935±0.016
B4/B11	0.81	BDL	1.56±0.16	0.56±0.06	0.88±0.06	0.97±0.05	0.47±0.08	1.00±0.05	0.420±0.014	0.53±0.02	0.44±0.20	0.82±0.13	3.03±0.13	1.01±0.06	0.838±0.013
B4/B12	0.89	1.20±0.10	1.79±0.20	0.52±0.05	0.85±0.06	1.31±0.08	0.50±0.09	1.68±0.12	0.318±0.010	0.46±0.02	0.33±0.14	0.8±0.3	5.0±0.3	1.03±0.06	0.812±0.013
B4/B13	1.05	0.71±0.05	2.1±0.3	0.56±0.06	1.36±0.12	2.25±0.20	0.64±0.12	1.40±0.08	0.429±0.014	0.88±0.05	0.96±0.05	0.8±0.3	5.0±0.3	0.95±0.05	0.824±0.013
B4/B15	0.77	BDL	1.79±0.20	0.80±0.09	1.22±0.10	1.40±0.09	0.90±0.19	1.33±0.08	0.583±0.020	0.55±0.02	0.7±0.4	1.56±0.06	2.00±0.06	1.01±0.06	0.874±0.014
B4/B17	0.89	2.1±0.3	2.1±0.3	1.05±0.14	1.35±0.11	2.3±0.2	0.68±0.13	2.9±0.3	1.24±0.06	1.58±0.12	1.2±0.7	1.75±0.04	1.57±0.04	1.64±0.13	0.841±0.013
B4/B19	0.87	2.9±0.5	0.66±0.04	1.13±0.15	1.52±0.14	1.43±0.09	2.3±0.9	1.23±0.07	1.05±0.06	1.11±0.07	0.8±0.4	2.21±0.04	1.52±0.04	1.64±0.13	0.845±0.013
B5/B1	1.65	2.6±0.4	3.2±0.4	3.1±0.5	1.48±0.14	2.8±0.3	0.63±0.13	0.89±0.09	0.77±0.05	0.29±0.05	4±3	1.75±0.06	1.90±0.06	0.49±0.04	1.005±0.015
B5/B2	1.82	1.72±0.19	3.2±0.4	1.68±0.18	1.25±0.10	1.72±0.12	1.3±0.4	0.82±0.08	0.72±0.04	0.25±0.04	3±2	1.38±0.02	1.01±0.02	0.44±0.04	1.144±0.018
B5/B8	1.82	1.54±0.15	3.6±0.5	1.66±0.18	1.12±0.09	2.47±0.20	0.47±0.09	0.56±0.05	0.304±0.015	0.16±0.03	2.4±1.2	1.37±0.06	1.86±0.06	0.55±0.05	0.985±0.015
B5/B9	2.00	1.23±0.11	3.2±0.4	1.19±0.10	1.72±0.18	1.73±0.13	1.0±0.3	0.91±0.09	0.87±0.06	0.35±0.06	2.3±1.1	1.44±0.02	1.04±0.02	0.56±0.05	1.076±0.017
B5/B11	1.61	BDL	2.00±0.19	0.91±0.07	0.85±0.06	0.97±0.05	0.41±0.08	0.48±0.04	0.260±0.013	0.13±0.02	0.9±0.3	0.81±0.11	2.58±0.11	0.52±0.05	0.965±0.014
B5/B12	1.75	1.23±0.11	2.3±0.2	0.84±0.06	0.81±0.05	1.30±0.08	0.44±0.09	0.80±0.08	0.197±0.010	0.11±0.02	0.65±0.16	0.8±0.3	4.2±0.3	0.53±0.05	0.934±0.013
B5/B13	2.08	0.73±0.05	2.7±0.3	0.91±0.07	1.31±0.11	2.24±0.20	0.57±0.12	0.67±0.06	0.265±0.013	0.21±0.04	1.9±0.8	0.8±0.3	4.2±0.3	0.49±0.04	0.948±0.014
B5/B15	1.52	BDL	2.3±0.2	0.30±0.12	1.17±0.09	1.39±0.09	0.80±0.18	0.64±0.06	0.361±0.019	0.13±0.02	1.4±0.5	0.54±0.05	1.70±0.05	0.52±0.05	1.005±0.015
B5/B17	1.75	2.1±0.3	2.7±0.3	1.71±0.19	1.30±0.11	2.24±0.20	0.60±0.12	1.40±0.18	0.77±0.05	0.38±0.07	2.4±1.2	0.73±0.03	1.33±0.03	0.84±0.09	0.967±0.014
B5/B19	1.72	3.0±0.5	0.84±0.05	1.9±0.2	1.46±0.13	1.42±0.09	2.0±0.8	0.59±0.05	0.65±0.04	0.27±0.05	1.6±0.6	2.18±0.03	1.29±0.03	0.84±0.09	0.972±0.014
Mean±SD	1.3±0.5	1.7±0.7	2.30±0.70	1.2±0.6	1.3±0.3	1.8±0.6	0.9±0.5	1.2±0.6	0.7±0.4	0.6±0.5	1.5±0.9	1.4±0.4	2.3±1.3	0.9±0.4	0.93±0.09

Comparison of grape and wine physico-chemical parameters (for Block 2) from the sediment group and base-sediment samples (*cabernet Sauvignon* cultivar) are presented in Tables 4-21 and 4-22, respectively. From the tables, it can be noted that there are no clear differences contrary to the soil results. This suggests further investigation is needed on the link between soil chemical properties and grape quality of various cultivars since there is an indication of slight difference in B. Comparing with the previous studies, the elemental composition of wine presented in Table 4-22 is found to be consistent with the Australian wine discussed in Chapter 1, section 1.1.

There are clear differences in the major elements, trace elements and other physico-chemical parameters between w and W_o of each sediment group. While few major elements (MnO and TiO_2) show difference between the sediment groups, a number of trace elements are found to show differences between the groups as discussed above.

Table 4-21: Ratios of grape physico-chemical data between sediment group samples (B4, B14) and base sediment samples (B17, B1) of Block 2 (W_2).

Ratios	N	P	K	Ca	Mg	Na	Mn	Fe	Cu	Zn	B	Water	Fruit mass
	mg/100g fresh mass							mg/kg fresh mass				%	g/fruit
B4/B17	0.97	1.04	0.98	1.11	0.95	1.11	1.48	0.93	1.13	1.11	0.81	0.99	1.04
B4/B1	0.83	0.84	1.02	0.92	0.89	0.84	1.31	0.91	0.87	0.95	0.79	0.99	1.00
B14/B17	1.00	1.12	0.86	1.23	0.96	1.22	0.83	0.92	1.30	1.16	0.87	1.00	1.00
B14/B1	0.86	0.91	0.90	1.01	0.90	0.93	0.73	0.90	1.00	1.00	0.85	1.01	0.96
Mean±SD	0.91±0.08	0.98±0.13	0.94±0.07	1.07±0.13	0.92±0.03	1.02±0.17	1.1±0.4	0.915±0.014	1.08±0.19	1.08±0.19	0.83±0.04	0.996±0.009	1.00±0.03

Table 4-22: Ratios of physico-chemical data of wines produced from grapes sampled at two sediment-group (hotspot) locations (B4, B14) and base-sediment (coldspot) locations (B1, B17) of Block 2 (W_2).

Sampling points	P (mg/l)	K (mg/l)	Ca (mg/l)	Mg (mg/l)	Na (mg/l)	Mn (mg/l)	Fe (mg/l)	Cu (mg/l)	Zn (mg/l)	B (mg/l)	Cl (mg/l)	pH	Ash (%)	SO4 (mg/l)
B4 and B14	399	1698	58	100	19.55	1.28	1.11	0.065	1.09	5.69	24.86	3.75	0.745	352.5
B1 and B17	399	1748	56	97	17.84	1.32	1.37	0.05	1.27	6.39	24.28	3.8	0.67	353
Ratio	1.00	0.97	1.04	1.03	1.10	0.97	0.81	1.30	0.86	0.89	1.02	0.99	1.11	1.00

4.3.3 XRD study

XRD data were collected for some samples using the method described in Chapter 2, section 2.4.3. XRD results for one sample collected at *w* (P21) and two samples (P19 and P24) from W_o locations (see Figure 4-10) of group W_1 are shown in Figure 4-11. From the figure it is clearly noted that the sediment group soil is enhanced in the mineral muscovite. Since muscovite ($KAl_2(AlSi_3O_{10})(OH)_{2,}$) is a potassium-aluminium bearing mineral, its enhancement in this sediment group is in agreement with the elevated major elements Al_2O_3 and K_2O as expected (see Table 4-13). Similar investigation for group W_2 is presented in Figure 4-12. Again, as expected similar patterns as in group W_1 are observed but with relatively small difference in muscovite intensity, consistent with the associated major-element results (see Table 4-14).

There are clear differences in muscovite intensity between *w* and W_o of each sediment group. As expected, the difference observed in the intensity of the mineral-muscovite is consistent with the elements bearing it.

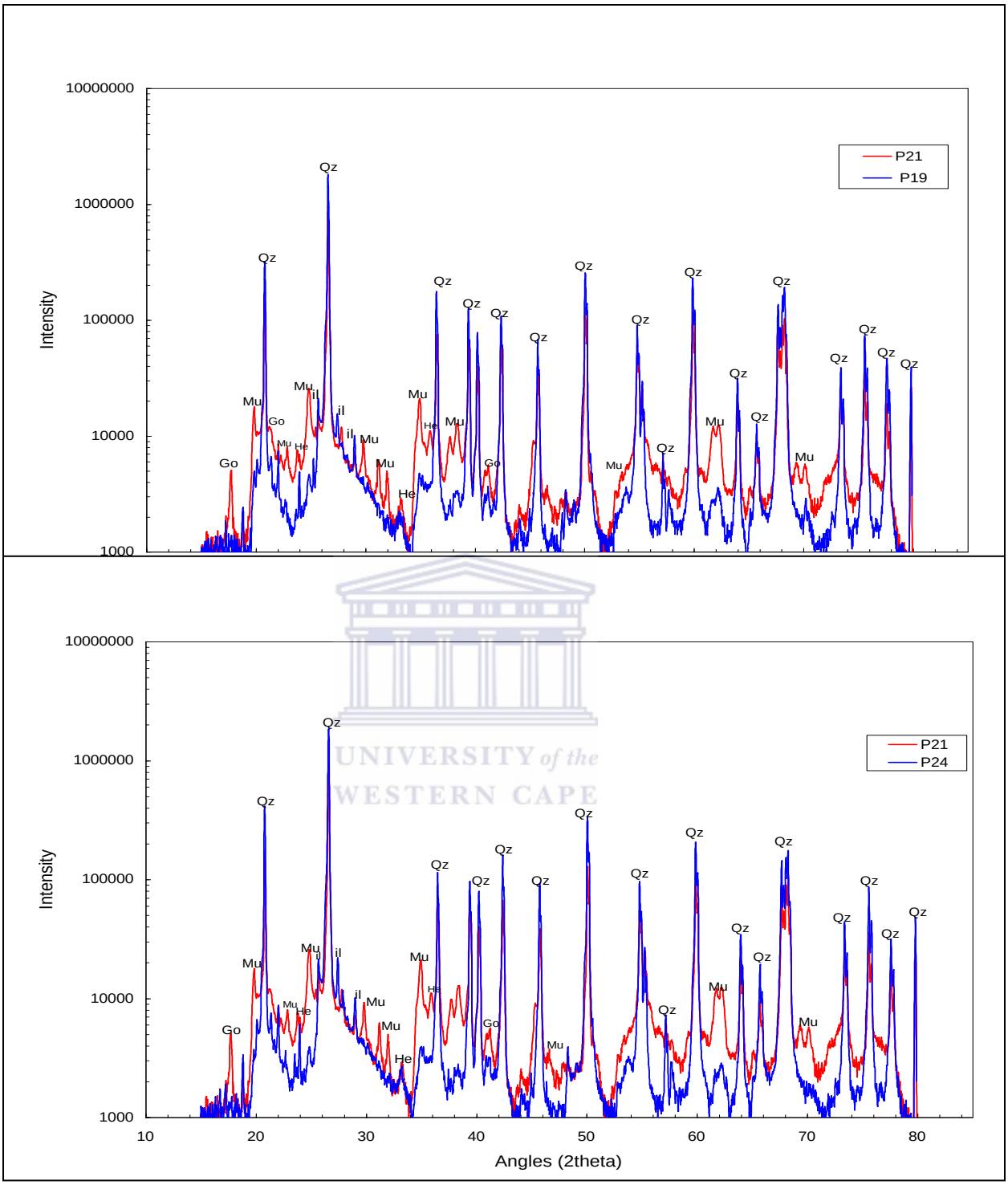

Figure 4-11: *XRD spectra showing minerals detected in sediment group location P21 and base sediment locations P19 and P24 for group W_1. (Qz: Quartz (SiO_2), Go: Goethite ($FeO(OH)$), Mu: Muscovite ($KAl_2(AlSi_3O_{10})(OH)_2$) He: Hematite ($Fe_2O_3$), Il: Illite ($KAl_2Si_3AlO_{10}$), Ka: Kaolinite ($Al_2Si_2O_5$)).*

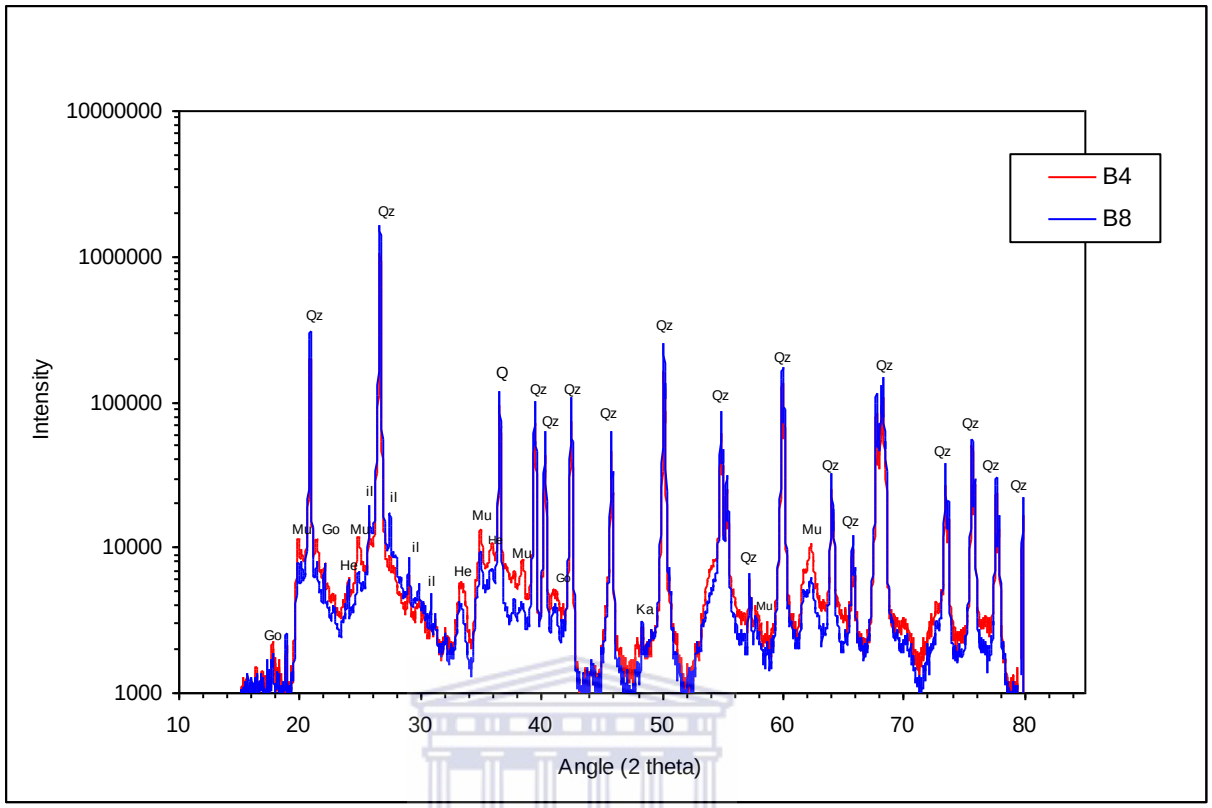

Figure 4-12: *XRD spectra showing minerals detected in sediment group location B4 and base sediment locations B8 for group W_2. (Qz: Quartz (SiO_2), Go: Goethite ($FeO(OH)$), Mu: Muscovite ($KAl_2(AlSi_3O_{10})(OH)_2$) He: Hematite ($Fe_2O_3$), Il: Illite ($KAl_2Si_3AlO_{10}$), Ka: Kaolinite ($Al_2Si_2O_5$)).*

4.3.4 Correlation study

Correlations between radiometry and soil physico-chemical parameters which are found to significantly vary between *w* and W_o of each group as presented in section 4.3.2, are investigated further in this section. In this study, the Pearson Correlation Coefficient (r)* was used for the search of statistically significant correlations at significance levels of 0.05 (95%) and 0.01 (99%) using r critical values [Fis74] presented in Appendix 2, Table A2-7. Results of statistically significant correlations found (highlighted in bold) are presented in Appendix 2, Tables A2-8 to A2-10 and compared to the previous study [Mod05] in Appendix 3. From the results, the physico-chemical parameters which are

* Refers to the measure which indicates the strength and direction of linear relationship between two random variables.

found to significantly correlate with radiometry (W Bq/kg) can be treated as dependent variables and thus, are reduced to new eigenvectors of major elements (W^m), trace elements (W^t) and extractable elements (W^e). To determine the new eigenvectors of chemistry, a similar approach as used in determining the radiometric eigenvector by eqs. (4.1) and (4.4) was used. For example in the case of W^m (% by mass) for Block 2, MgO, TiO and K_2O were included (see Appendix 2, A2-8). Moreover, the standard deviations from the ten sub-samples (see section 4.3.1) were treated as absolute uncertainties in determining the new chemistry eigenvectors.

Tables 4-23, 4-24 and 4-25 present the values of the new variables W for major elements, trace elements and extractable elements in the two groups, respectively. For the Pomphuis/Nuweland block, the values range from 3 to 23, 157 to 940 and 3 to 15 for major elements, trace elements and extractable elements, respectively. In Block 2, the values range from 0.9 to 1.5, 444 to 1015 and 0.7 to 3.2 for major elements, trace elements and extractable elements, respectively.

Table 4-23: Concentrations of variable W^m (major elements) % by mass for the measured samples in the two groups.

Pomphuis/Nuweland block		Block 2	
Sampling points	W_1^m	Sampling points	W_2^m
P18	8.5±1.9	B1	1.13±0.17
P19C	3.3±1.6	B2	1.29±0.17
P20	20±3	B3	0.95±0.16
P21	20±3	B4	1.28±0.18
P22C	3.2±1.7	B5	1.50±0.20
P23	5.8±1.8	B6	1.00±0.16
P24	3.7±1.7	B7	1.13±0.17
P25	5.9±1.8	B8	1.20±0.18
N17	18±3	B9	1.33±0.19
N18	23±3	B10	1.24±0.18
N19	14±2		
N20	9.7±1.9		
N21	12±2		
N22	10.1±1.9		
N23	11±2		
N24	9.6±1.9		

Table 4-24: Concentrations of variable W^t (trace elements) for the measured samples in the two groups.

Pomphuis/Nuweland block		Block 2	
Sampling points	W_1^t (mg/kg)	Sampling points	W_2^t (mg/kg)
P18	290±54	B16	852±140
P19C	243±53	B17	659±125
P20	867±80	B18	900±135
P21	643±67	B18*	1015±150
P22C	157±52	B19	665±127
P23	323±58	B19∗	692±129
P24	220±55	B20	519±123
P25	368±57	B20∗	551±126
N17	937±94	B21	444±120
N18	940±96	B21∗	450±126
N19	613±72	B22	508±124
N20	435±61	B22∗	459±122
N21	544±66	B23	724±130
N22	390±64	B23∗	694±133
N23	515±64		
N24	568±69		

* Refers to results of 30-60 cm soil sampling depths. Results of other points are based on 0-30 cm soil depths.

Table 4-25: Concentrations of variable W^e (extractable elements) for the measured samples in the two groups.

Pomphuis/Nuweland block		Block 2	
Sampling points	W_1^e (cmol(+)/kg)	Sampling points	W_2^e (cmol(+)/kg)
P1	15.0±1.1	B1	1.04±0.20
P2	3.7±0.5	B2	1.31±0.20
P4	6.4±0.6	B3	1.01±0.20
P5	14.2±1.1	B4	2.7±0.3
P6	3.1±0.5	B5	3.2±0.4
P7	4.9±0.6	B6	1.06±0.20
P8	3.8±0.6	B7	1.47±0.20
P9	12.3±1.0	B8	1.03±0.20
P10	3.9±0.5	B9	1.30±0.20
P11	6.1±0.6	B10	1.27±0.20
P12	6.1±0.6	B11	2.2±0.3
P13	4.1±0.6	B12	1.77±0.20
P14	4.6±0.6	B13	1.26±0.20
P15	5.1±0.6	B14	2.5±0.3
P16	4.3±0.6	B15	1.71±0.20
P17	8.2±0.7	B16	1.64±0.20
N1	11.7±0.8	B17	1.26±0.20
N2	9.9±0.8	B18	1.32±0.20
N4	6.5±0.6	B18*	1.30±0.20
N5	5.6±0.6	B20	0.89±0.20
N6	5.2±0.6	B20*	1.31±0.20
N7	5.1±0.6	B21	1.10±0.20
N8	9.1±0.7	B21*	1.04±0.20
N9	10.9±0.8	B22	0.67±0.19
N10	5.9±0.6	B22*	1.00±0.20
N11	6.9±0.6	B23	1.23±0.20
N12	10.2±0.8	B23*	1.27±0.20
N13	6.5±0.6		
N14	5.8±0.6		
N15	5.3±0.6		
N16	6.3±0.6		

* Refers to results of 30-60 cm soil sampling depths. Results of other points are based on 0-30 cm soil depths.

Figures 4-13 shows a 2D correlation plot and the best fit (W^m versus W) for the blocks Pomphuis/Nuweland and Block 2, with r values of 0.725 and 0.666, respectively. Furthermore, the values of *a* and *b* with their external uncertainties for the two blocks are a=0.033±0.010 and b=4.6±1.6 (χ_v^2=4), a=0.0011±0.0005 and b=0.79±0.17 (χ_v^2=0.6), respectively.

Figures 4-14 shows 2D correlation plot and best fit (W^t versus W) for the blocks Pomphuis/Nuweland and Block 2. The r values for the correlation plots are 0.565 and 0.710 for Pomphuis/Nuweland and Block 2, respectively. The values of *a* and *b* for the two blocks are found to be a=0.9±0.4 and b=287±70 (χ_v^2=8), a=2.3±0.6 and b=-156±227 (χ_v^2=0.8), respectively.

Figures 4-15 shows 2D correlation plot and best fit (W^e versus W) for the Pomphuis/Nuweland and Block 2 data. The r value for Pomphuis/Nuweland block is 0.856 whereas for Block 2 is 0.690. From the figure, the values of *a* and *b* for the blocks Pomphuis/Nuweland and Block 2 are a=0.025±0.004 and b=2.6±0.4 (χ_v^2=5), a=0.0058±0.0014 and b=-0.7±0.5 (χ_v^2=2.2), respectively. A correlation plot and best fit (clay versus W) for the blocks Pomphuis/Nuweland (r= 0.460) and Block 2 (r= 0.554) is shown in Figure 4-16. The values of *a* and *b* for the two blocks are a=18.9±5.5 and b=12±37 (χ_v^2=219), a=7.9±2.3 and b=262±28 (χ_v^2=4), respectively.

The correlation analysis shows the link of some physico-chemical parameters with radiometric signals. Hence, the correlation data together with the fit parameters obtained from the derivation of the new radiometric eigenvector (W) in Chapter 4 (section 4.1) are used in projecting *in-situ* radiometric MEDUSA data onto physico-chemical data, an investigation that is presented in Chapter 5, section 5.5.

4.4 Summary

In this chapter, the method to identify sediment groups using radiometric data has been described. By using the method two sediment groups have been identified and characterized. Based on the identified groups, the correlation between radiometric and soil physico-chemical data has been described and discussed. This approach has shown to be useful in characterizing the soils leading to proper soil classification.

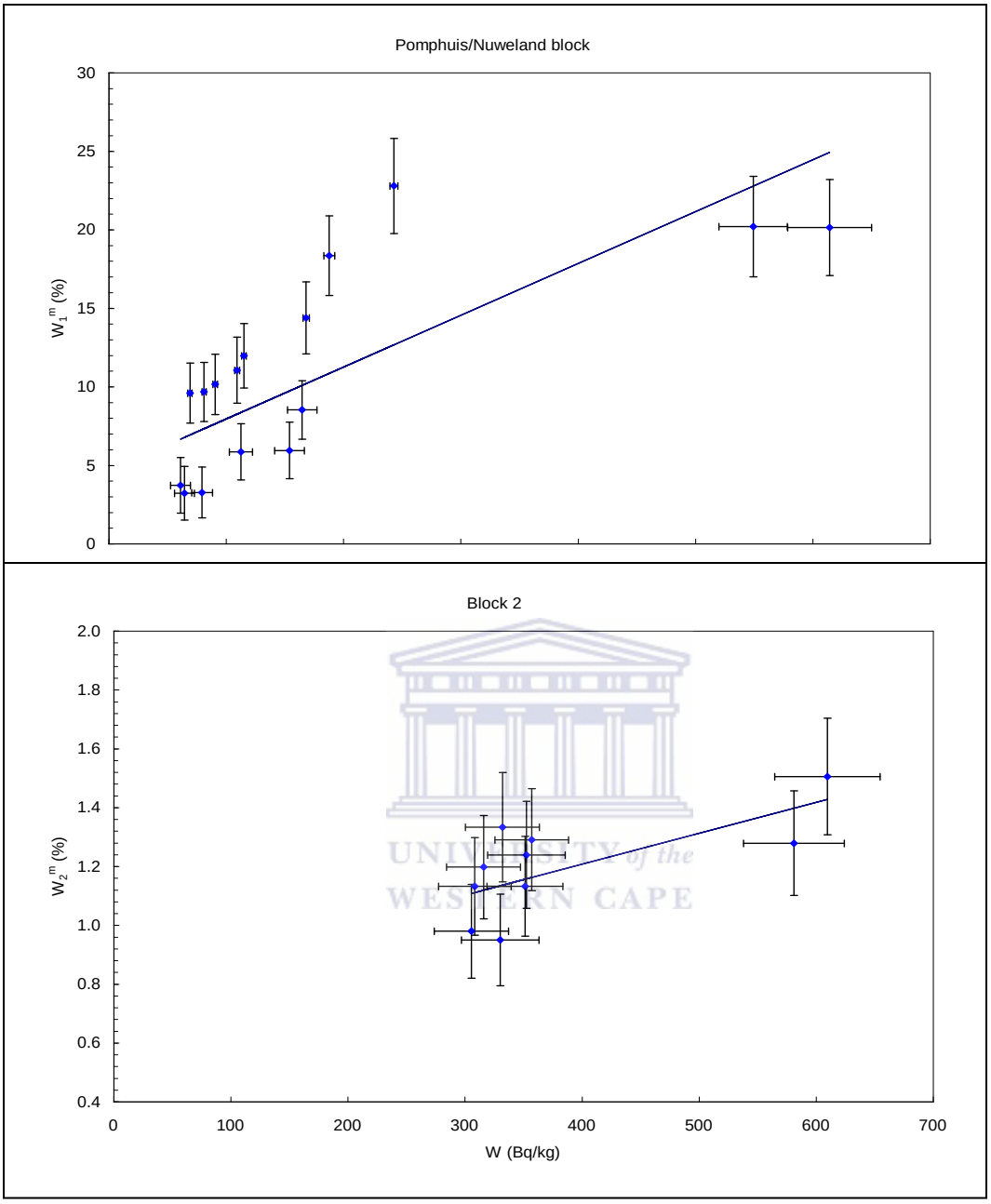

Figure 4-13: *Weighted fits showing the correlation between variable W^m (major elements) versus W (radiometry) from Pomphuis/Nuweland and Block 2 data.*

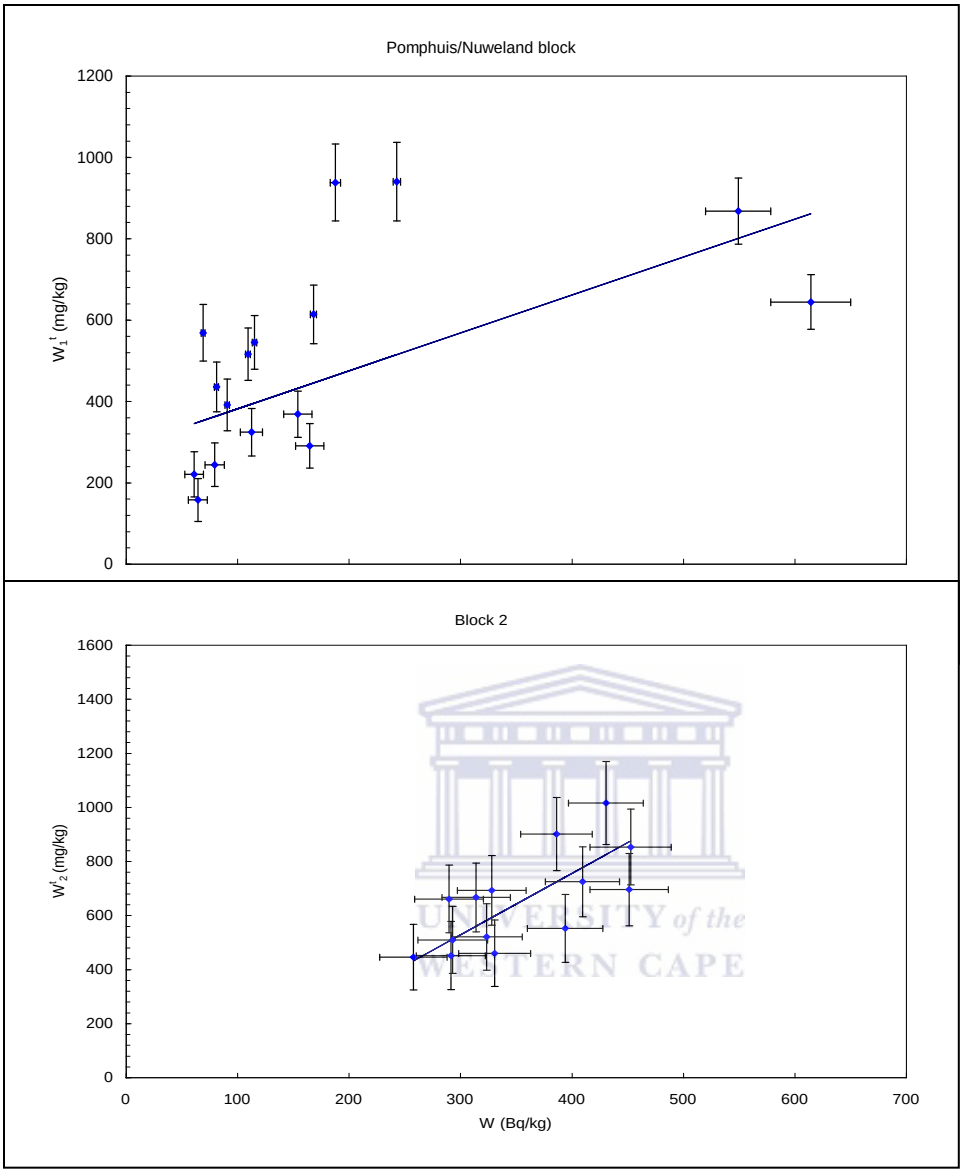

Figure 4-14: *Weighted fits showing the correlation between variable W^t (trace elements) versus W (radiometry) from Pomphuis/Nuweland and Block 2 data.*

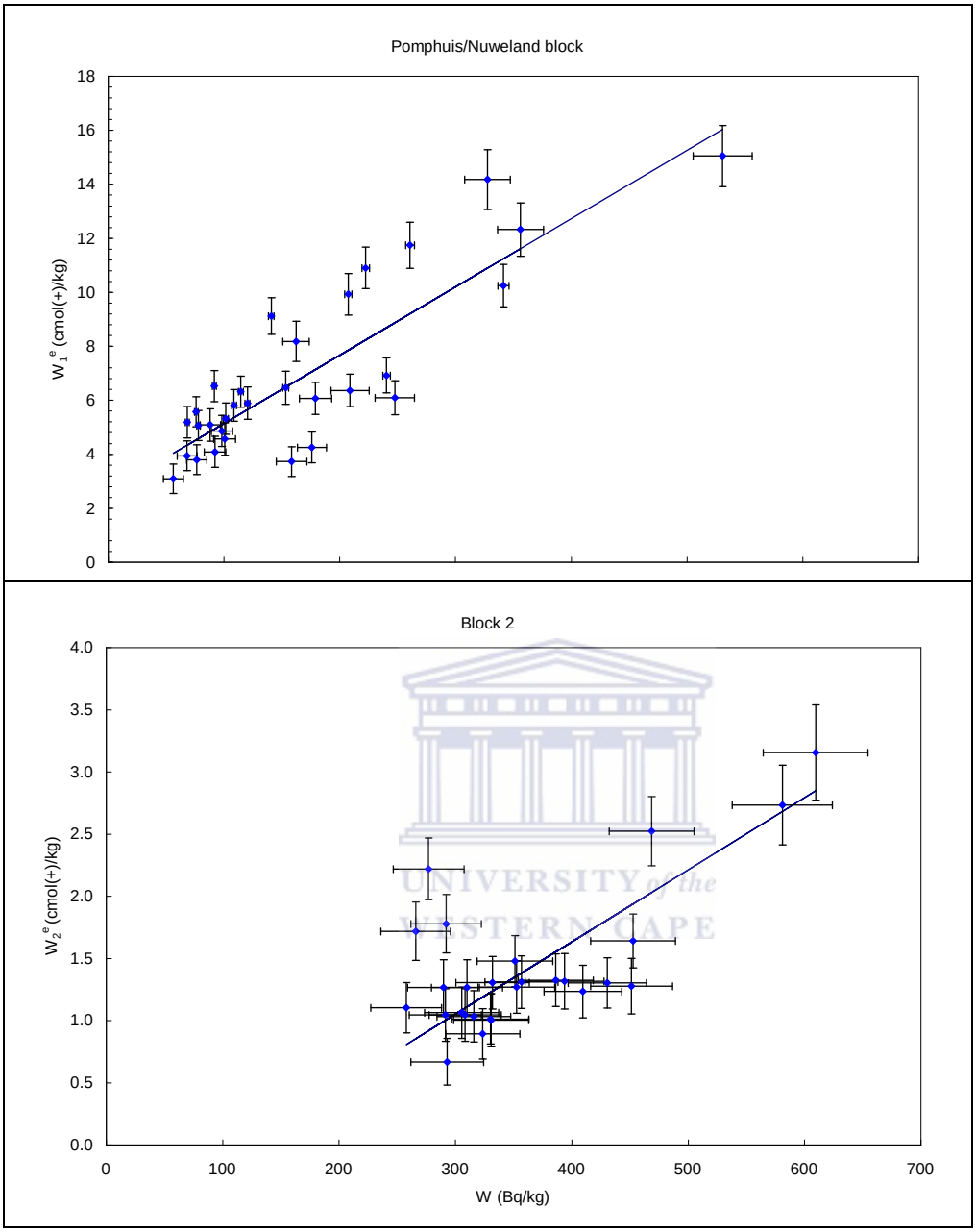

Figure 4-15: *Weighted fits showing the correlation between variable W^e (extractable elements) versus W (radiometry) from Pomphuis/Nuweland and Block 2 data.*

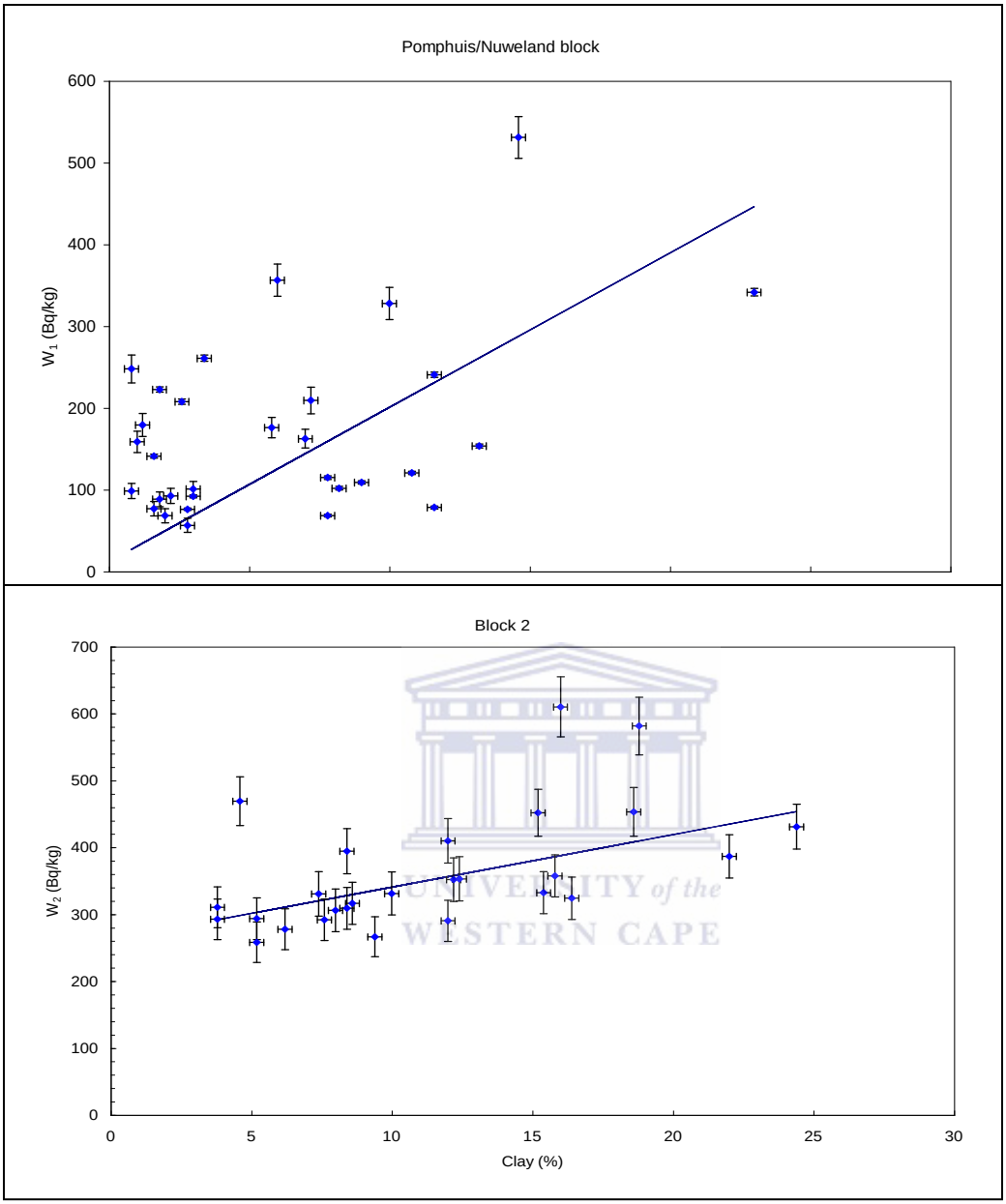

Figure 4-16: *Weighted fits showing the correlation between variable radiometry (W) versus clay from Pomphuis/Nuweland and Block 2 data.*

CHAPTER 5 RESULTS FROM FIELD MEASUREMENT ANALYSES

This chapter presents an overview of the *in-situ* radiometric results obtained from the survey of the three blocks (Block 2, Pomphuis and Nuweland blocks) in 2007. Results on radiometric maps are compared to data acquired earlier in 2002/2003 after re-analyzing with the same set of the standard spectra used for data acquired in 2007. Detailed investigation on the radionuclide distributions (^{40}K, ^{232}Th series and ^{238}U series), correlations and block sections is restricted to the data acquired in 2007 as part of this study. The ACs obtained from the laboratory analyses are critically compared to ACs derived from *in-situ* γ-ray measurements. Furthermore, an assessment to verify the number of sediment groups as was found in chapter 4, but in this Chapter using larger data sets extracted from block sections, is presented. In this chapter, a proposed approach to project *in-situ* radiometric data onto soil physico-chemical data by using radiometric-laboratory results presented in chapter 4 is also discussed.

The data set discussed in this chapter form a much larger set (~6000 data points per block) compared to the ± 25 points per block in Chapter 4. The MEDUSA data presented here has much larger uncertainties than the data points of Chapter 4, but this is compensated for by the large number of points.

5.1 Normalization of the MEDUSA-activity concentration data

As it was discussed in Chapter 2 (section 2.2.3) and Chapter 3 (section 3.1.4) that the NFs were used to extract the absolute activity values of all the MEDUSA data acquired. Table 5-1 presents the normalization factors, weighted averages and chi-squares of ^{40}K, ^{232}Th series and ^{238}U series obtained from the seven calibration measurements as determined by a hybrid and FSA methods as described in Chapter 3, section 3.1.2 and 3.1.3. In this study, weighted mean normalization factors from calibration spots P19 and P22 determined by FSA method were used to extract absolute activity concentrations of the MEDUSA data acquired in 2007 using the trolley set-up. To produce radiometric maps from radiometric data acquired in 2002/2003 using 4×4 set-up, the NFs presented in Appendix 1, Table 1A-2 were used. The statistical spread of NF

values and hence high reduced χ^2 values observed are associated with hotspot[++] points (see Chapter 2, Figures 2-11 to 2-13). The hot spots (with relatively higher clay content) show more absorption of γ-rays in the field measurements (leading to mostly higher NFs) which could be partly contributed by clay soils which have relatively high water holding capacity as compared to sandy soils as discussed in Chapter 1, section 1.1. Moreover, this observation can also be related to differing soil horizons associated with varying underlaying geology (see Chapter 1, section 1.1). More details on factors affecting NFs are presented in Appendix 1, section A1.2. Figure 5-1 compares the normalization factors determined by the hybrid method at a range of nuclide activity concentrations.

Table 5-1: Normalization factors (NF) of ^{40}K, ^{232}Th series and ^{238}U series from the hybrid and FSA methods. Data were acquired using the trolley set-up (see Figure 2-4b).

Calibration spots	Hybrid method			FSA		
	^{40}K	^{232}Th series	^{238}U series	^{40}K	^{232}Th series	^{238}U series
B5	0.47±0.02	0.359±0.005	0.47±0.02	0.498±0.007	0.385±0.004	0.436±0.013
B14	0.47±0.03	0.236±0.004	0.292±0.013	0.470±0.007	0.248±0.004	0.269±0.004
B21	0.44±0.03	0.200±0.004	0.32±0.02	0.452±0.007	0.227±0.003	0.287±0.003
P19C	0.41±0.07	0.202±0.008	0.31±0.03	0.418±0.018	0.217±0.004	0.281±0.007
P21	0.41±0.02	0.427±0.011	0.415±0.014	0.403±0.009	0.445±0.008	0.436±0.006
P22C	0.37±0.06	0.178±0.006	0.28±0.03	0.387±0.016	0.195±0.004	0.245±0.006
N9	0.42±0.02	0.252±0.005	0.39±0.02	0.444±0.006	0.275±0.004	0.356±0.004
Weighted Av. (A_w)	**0.437±0.012**	**0.25±0.03**	**0.35±0.03**	**0.454±0.013**	**0.26±0.03**	**0.31±0.02**
χ_v^2	1.5	180	15	18	314	170

[++] Refers to areas with high count rates

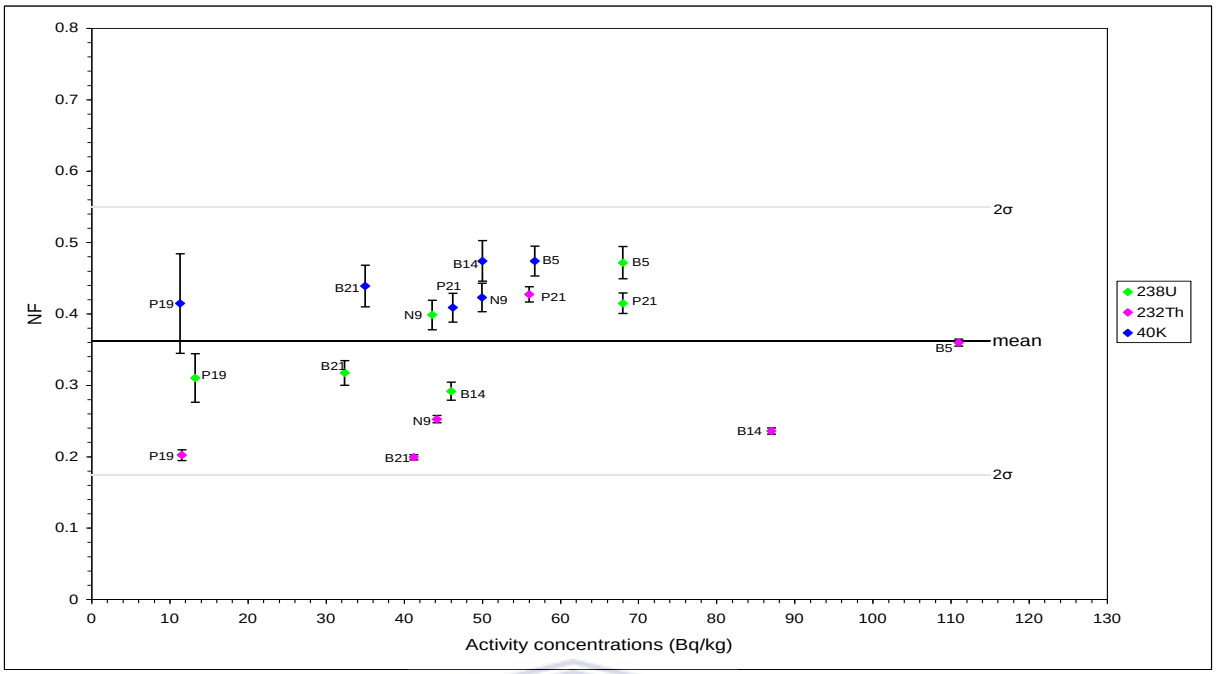

Figure 5-1: *Two dimensional plot showing the normalization factors at a range of nuclide activity concentrations (ACs). The ACs of ^{40}K have been divided by a factor of 4.*

5.2 Reproducibility

Radiometric maps produced from data acquired between 2002 and 2007 and normalized as explained in section 5.1 for Block 2, Pomphuis and Nuweland blocks are presented in Figures 5-2, and 5-3 and 5-4, respectively. For the two sets of measurement, the four radiometric maps for each entire block indicate significant variations mainly in the distribution of the Total Count rate (TC) and activity concentration (AC) of ^{232}Th series and to a lesser extent for AC of ^{238}U series and ^{40}K. Comparatively, the two sets of radiometric maps produced (from data acquired in 2002/2003 and 2007) show similar patterns over a period of four to five years indicating the robustness of the MEDUSA measurement technology. The variations observed in the interpolated maps are likely to be contributed by the different approaches used in collecting data (spacing and speed) as explained in Chapter 2, section 2.2.4. However, some significant differences are noticed in the TC maps of the Nuweland block. The most likely reason for the differences in this particular block is the changes made in the land terrain (including constructing relatively large ridges as shown in Figure 2a (Chapter 2, section 2.1) as compared to the situation when the block was unplanted. In the following the investigation is restricted to the data acquired in 2007.

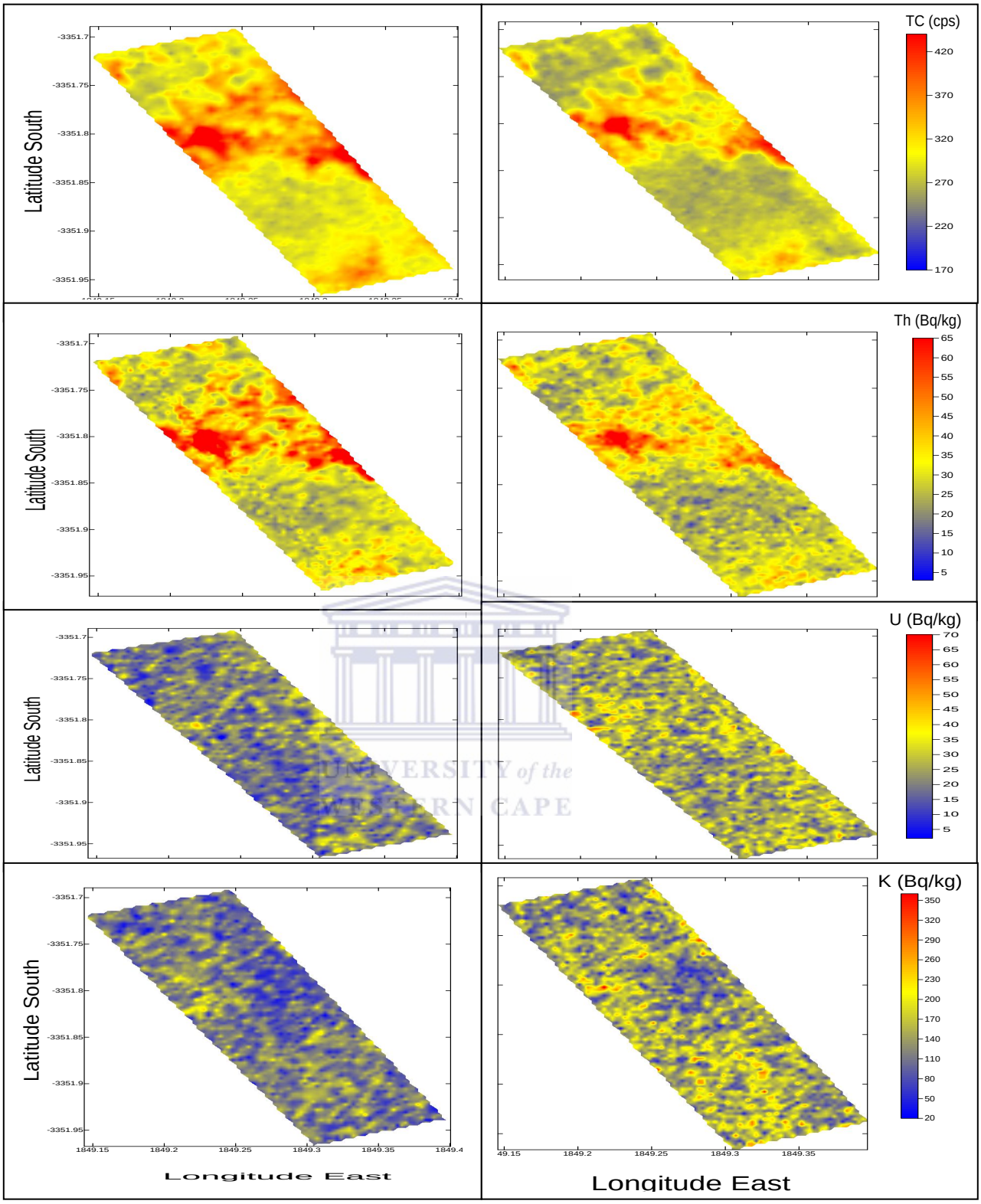

Figure 5-2: *Maps of MEDUSA detector total count rate (counts per second), ^{232}Th and ^{238}U series and ^{40}K activity concentrations for the 9 ha Block 2 plot surveyed in November 2002 (left-hand side) and December 2007 (right-hand side). (Note: The MEDUSA-software algorithm gives the latitude and longitude in the format xxyy.yy instead of the usual xx˚yy.yy' where xx and yy.yy correspond to degrees and minutes, respectively).*

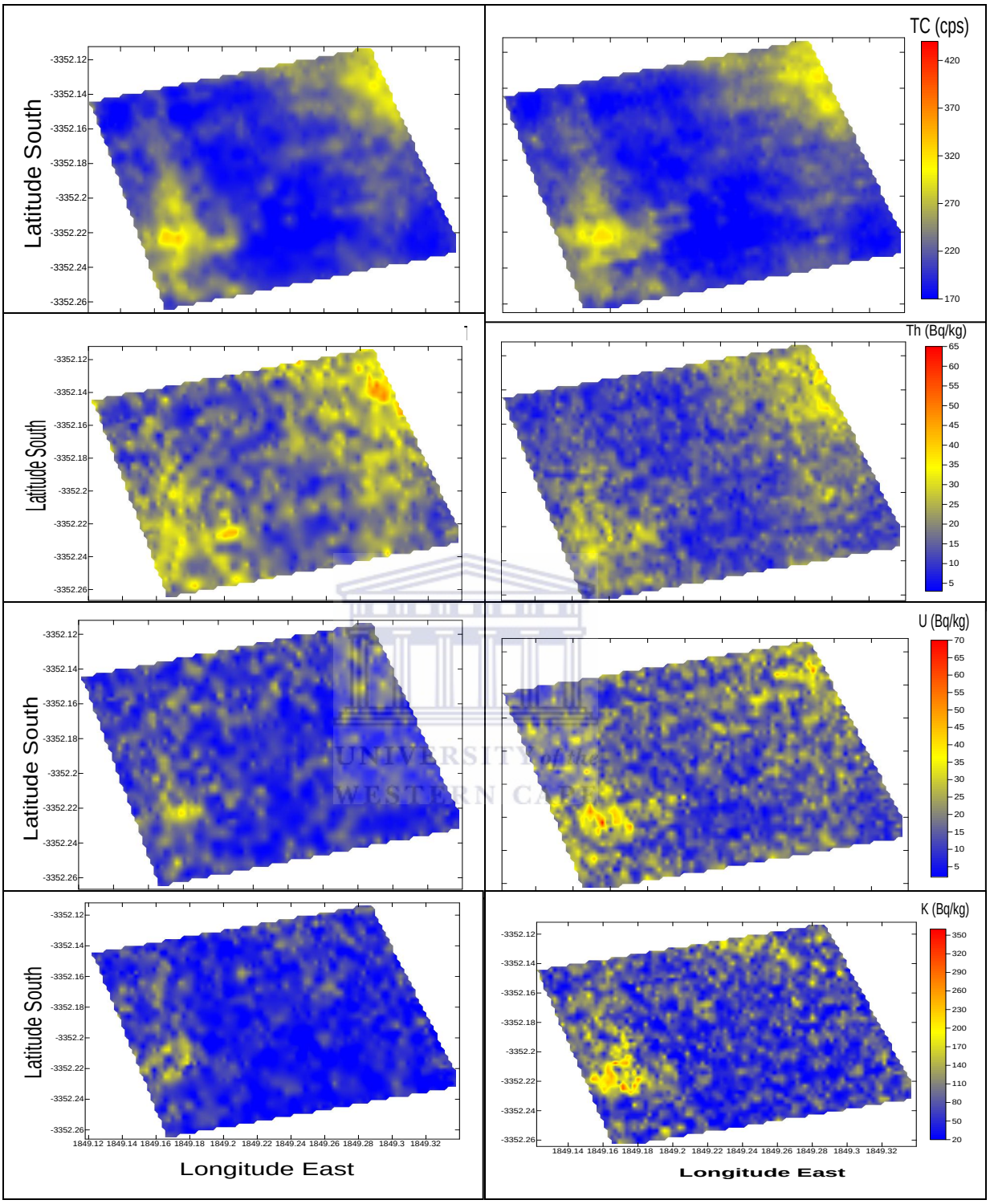

Figure 5-3: *Maps of MEDUSA detector total count rate (counts per second), ^{232}Th and ^{238}U series and ^{40}K activity concentrations for the 6.4 ha Pomphuis plot surveyed in December 2003 (left-hand side) and December 2007 (right-hand side).. (Note: The MEDUSA-software algorithm gives the latitude and longitude in the format xxyy.yy instead of the usual xx˚yy.yy' where xx and yy.yy correspond to degrees and minutes, respectively).*

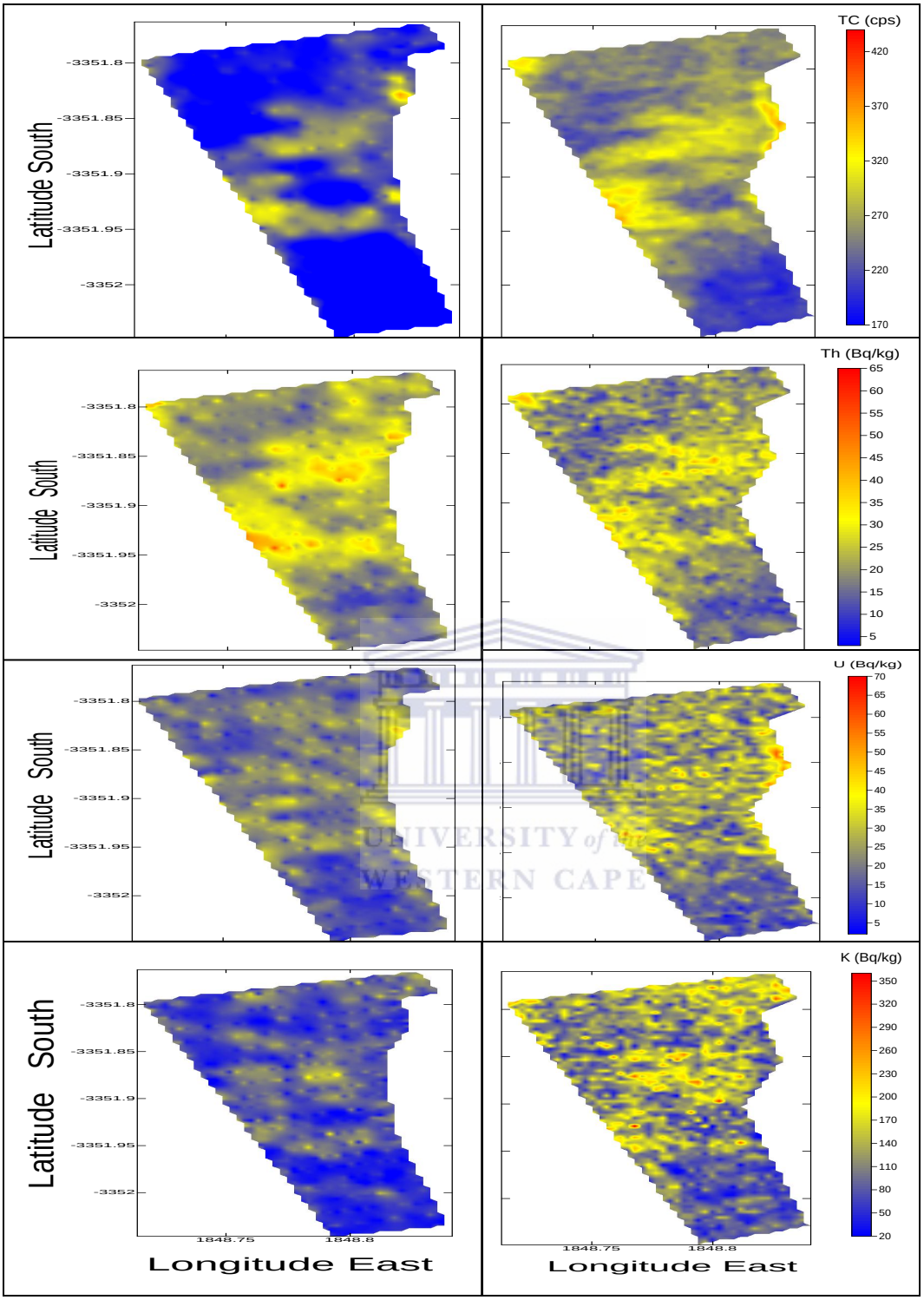

Figure 5-4: *Maps of MEDUSA detector total count rate (counts per second), ^{232}Th and ^{238}U series and ^{40}K activity concentrations for the 5.6 ha Nuweland plot surveyed in December 2003 (left-hand side) and December 2007 (right-hand side).. (Note: The MEDUSA-software algorithm gives the latitude and longitude in the format xxyy.yy instead of the usual xx˚yy.yy' where xx and yy.yy correspond to degrees and minutes, respectively).*

5.3 Activity concentration distributions

Figure 5-5 shows on the left-hand side the distributions of ^{40}K, ^{232}Th series and ^{238}U series ACs in the block 2 as histograms for the data acquired in 2007. The ACs for ^{232}Th series and ^{238}U series have approximately the same mean value (~ 30 Bq/kg) whereas ^{40}K has a mean value of ~ 150 Bq/kg. However, the distribution of ^{232}Th series is somewhat narrower (smaller standard deviation) than ^{40}K and ^{238}U series, implying that ^{232}Th series is a more outspoken indicator for radiometric variations, consistent with the radiometric maps in Figure 5-2. The right-hand side of the figure shows 2D correlation plots of the radionuclide ACs for the entire block data. The data show hardly any correlation between ^{40}K AC with ^{232}Th series and ^{238}U series ACs and some correlation between ^{232}Th series and ^{238}U series ACs, contrary to sample data presented in Chapter 4, Figure 4.1. This is probably due to the fact that in the field measurements, radon escape may affect the data distribution patterns. Moreover, the statistical spread of the normalization factors as presented in section 5.1 also affect the quality of data acquired. When smaller data sets are used, there is an indication of a relation between U and Th as will be discussed in section 5.4.4.

Figure 5-6 (left-hand side) shows the distributions of ^{232}Th series, ^{238}U series and ^{40}K ACs for the Pomphuis block. In this block, the ACs for ^{232}Th series and ^{238}U series have approximately the same mean value (~ 20 Bq/kg) whereas ^{40}K has a mean value of ~ 75 Bq/kg. However, the distribution of ^{232}Th is symmetric and narrower than ^{238}U and ^{40}K as observed in Block 2, hence also consistent with the radiometric maps in Figure 5-3. Compared to Block 2, the difference in mean ACs between the distributions is a factor of 1.5, 1.5 and 2 for ^{232}Th, ^{238}U and ^{40}K, respectively. Figure 5-6 (right-hand side) shows 2D correlation plots of the radionuclide ACs for the block. The data suggest similar consideration of correlations as observed in Block 2 data.

Figure 5-7 (on the left-hand side) shows the distributions of ^{232}Th series, ^{238}U series and ^{40}K ACs for the Nuweland block as a histogram, with the ACs for ^{232}Th series and ^{238}U series having approximately the same mean value (~ 25 Bq/kg) whereas ^{40}K has a mean value of ~ 125 Bq/kg. Again, the distribution of ^{232}Th series is symmetric and narrower than ^{238}U series and ^{40}K, hence also being an indicator for radiometric variation, as shown by the radiometric map in Figure 5-4. The difference in mean ACs between the

distributions with Pomphuis block is a factor of 1.2, 1.2 and 1.7 for ^{232}Th, ^{238}U and ^{40}K, respectively. Figure 5-7 (right-hand side) shows 2D correlation plots of the radionuclide ACs. From the plots, the data distribution pattern is similar as for the Block 2 and Pomphuis block data, and hence leading to the same considerations as for the two blocks.

The similar distribution of the radionuclides (broadness) and relatively small difference in mean ACs between the distributions observed in the Pomphuis and Nuweland blocks (Figures 5-6 and 5-7) contrary to Block 2, confirms that the two blocks are mainly composed of one sediment group, consistent with sample data discussed in Chapter 4, section 4.1.

To compare the distribution of radiometric-data sets measured in the field and laboratory samples, the field data were re-analysed *via* averaging over 20 point intervals to improve the data statistics since the field data are associated with larger uncertainties which cause significant data fluctuations and outliers. This approach was aimed at ensuring the extraction of more accurate radiometric data. Figure 5-8 shows 2D correlation plots (^{238}U versus ^{232}Th ACs) for the three blocks, revealing that despite of the data fluctuation and outliers, the trend and direction of correlations in field data is similar to the laboratory-measured samples presented in Figure 4-1, Chapter 4. Figure 5-9 shows the combined 2D correlation plot (^{238}U versus ^{232}Th ACs) for the three blocks. From the plot, it is shown that the distribution of data in the blocks Pomphuis and Nuweland is similar as opposed to Block 2 data, again suggesting that the blocks are mainly composed of two sediment groups as was found in the sample data in Chapter 4, section 4.1. Figure 5-10 shows preliminary assessment of the averaged block data using ternary plots. From the figure, it is found that when the data points are averaged, the trend of data distribution is such that the data scatter is reduced but data overlapping becomes significant. As far as the concentration fraction is concerned, the data show higher fraction of ^{40}K than ^{232}Th and ^{238}U series as expected.

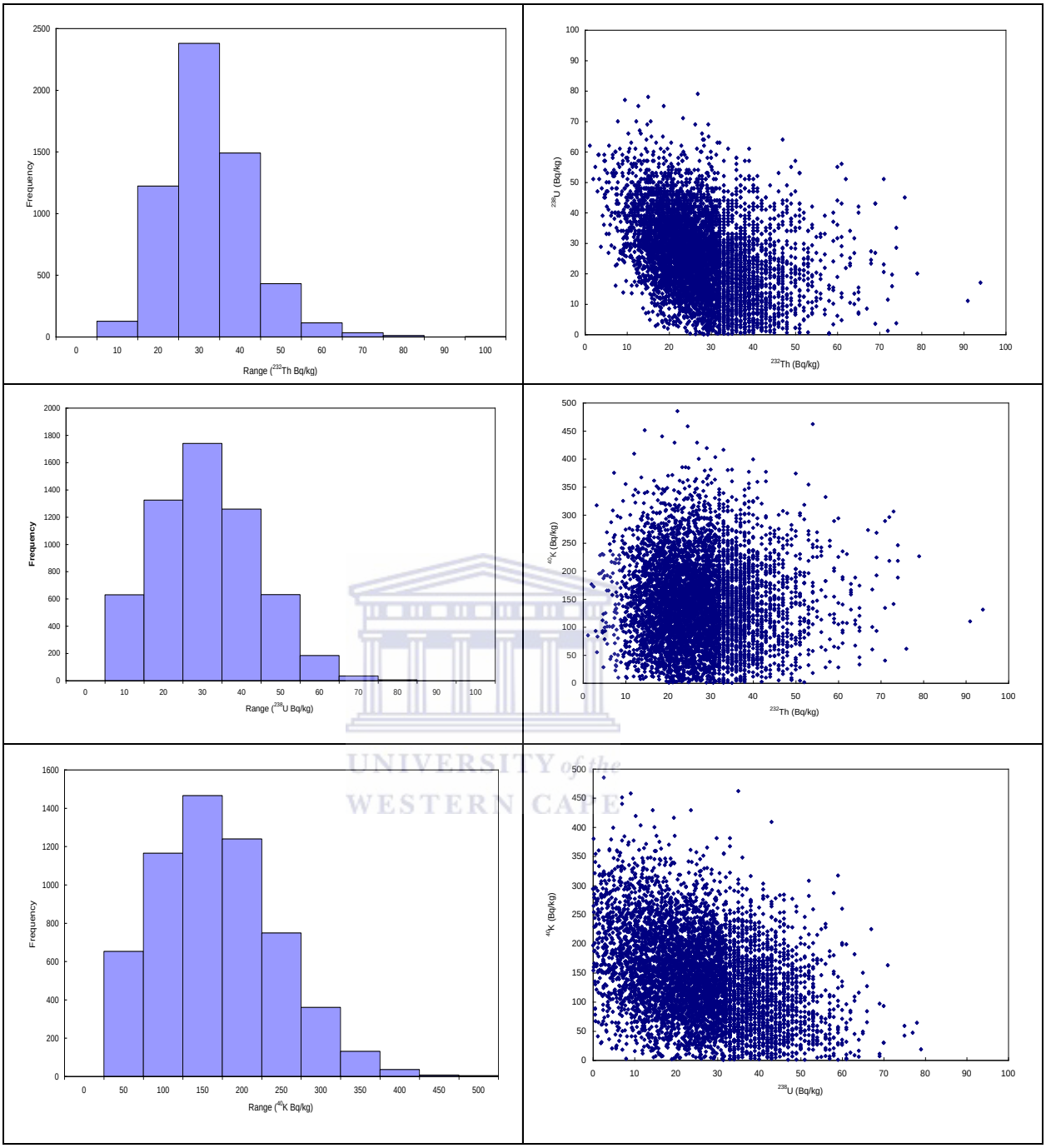

Figure 5-5: *Histograms and two dimensional plots showing the distributions and correlations of the ^{232}Th series, ^{238}U series and ^{40}K ACs in Block 2. Each data point was obtained by analyzing a MEDUSA spectrum acquired over a 2 s period.*

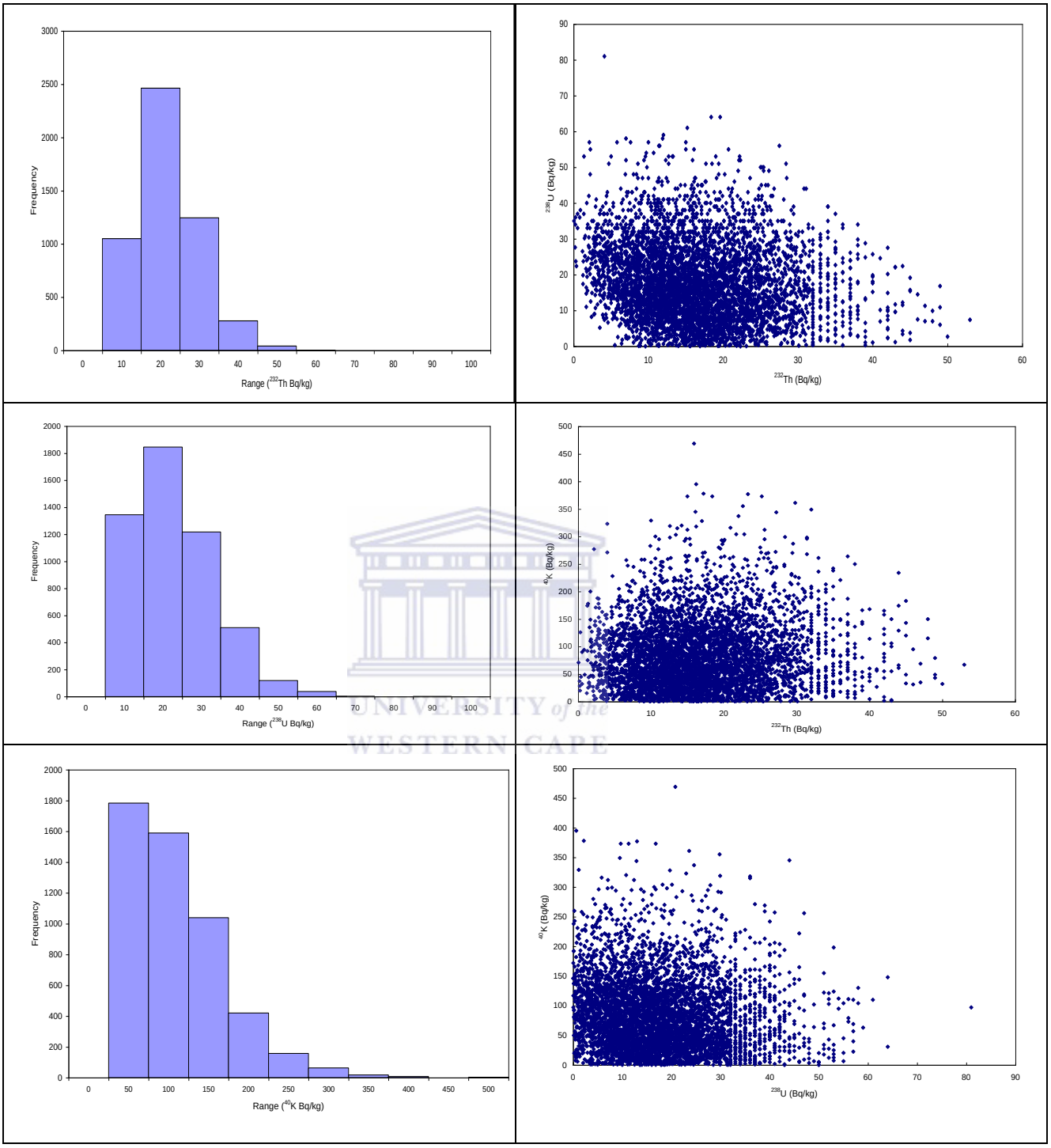

Figure 5-6: *Histograms and two dimensional plots showing the distributions and correlations of the ^{232}Th series, ^{238}U series and ^{40}K ACs in Pomphuis block.*

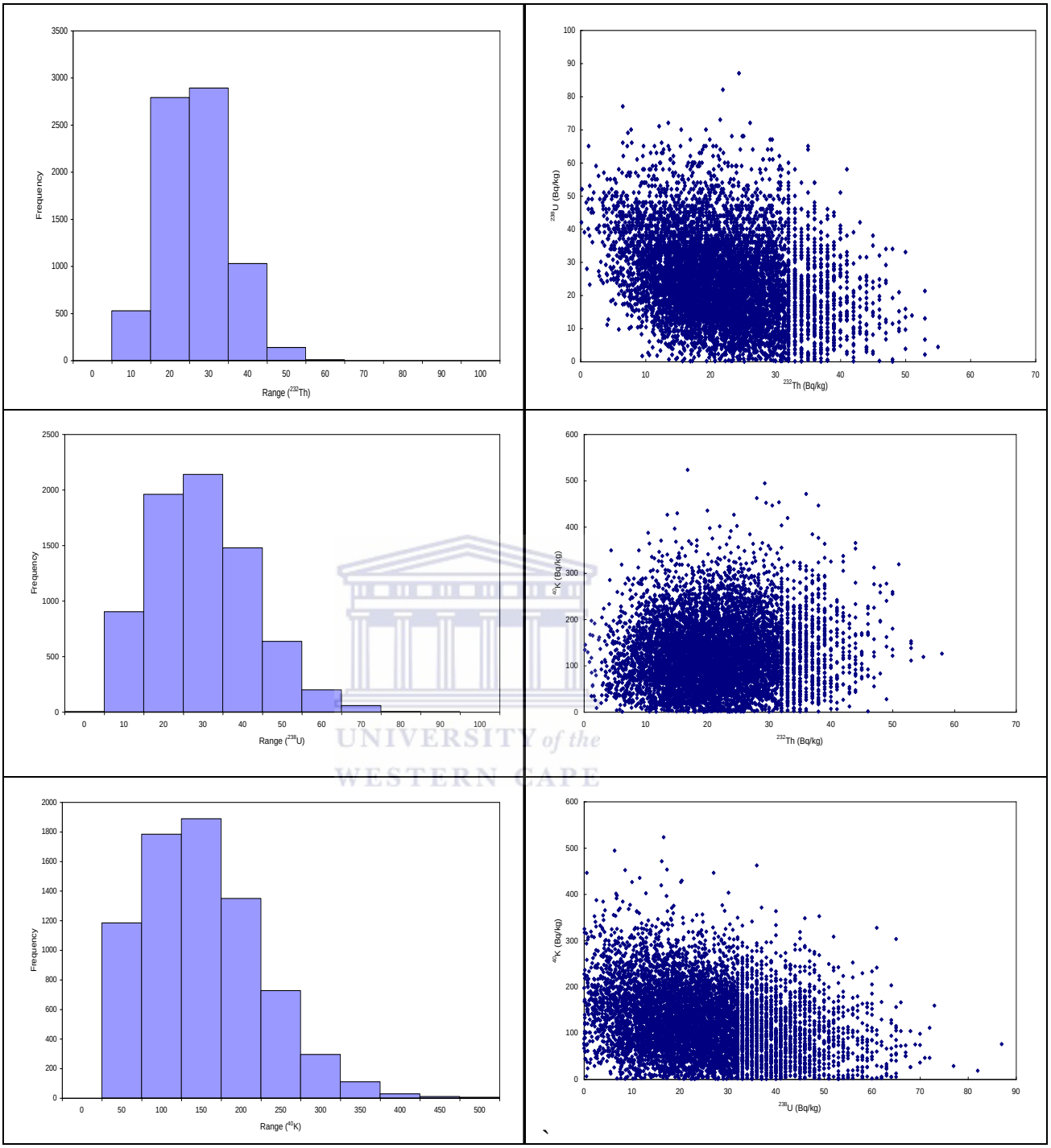

Figure 5-7: *Histograms and two dimensional plots showing the distributions and correlations of the ^{232}Th series, ^{238}U series and ^{40}K ACs in Nuweland block.*

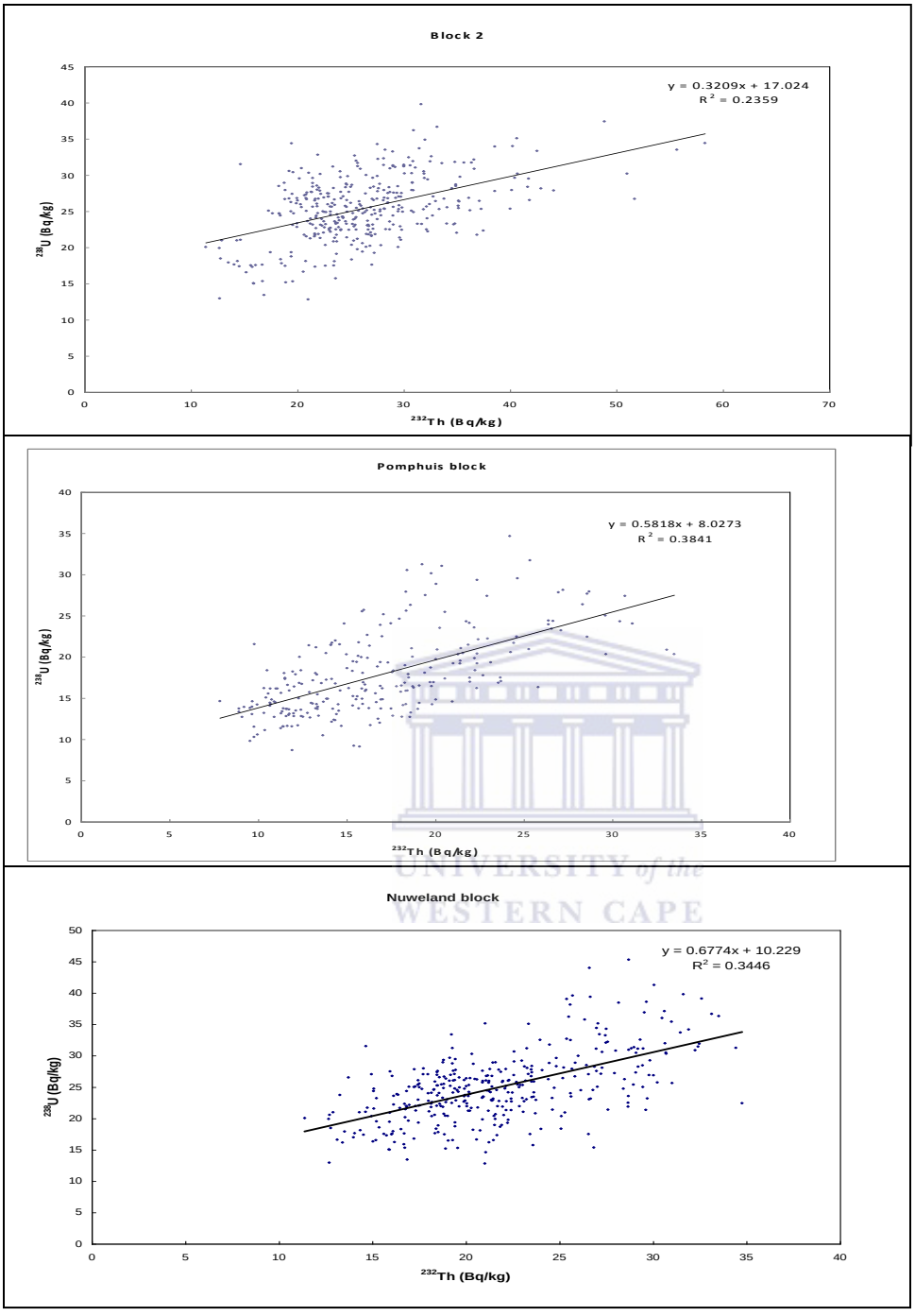

Figure 5-8: *Correlation plots of the averaged ACs (over every 20 data points) of ^{238}U series and ^{232}Th series for the three blocks.*

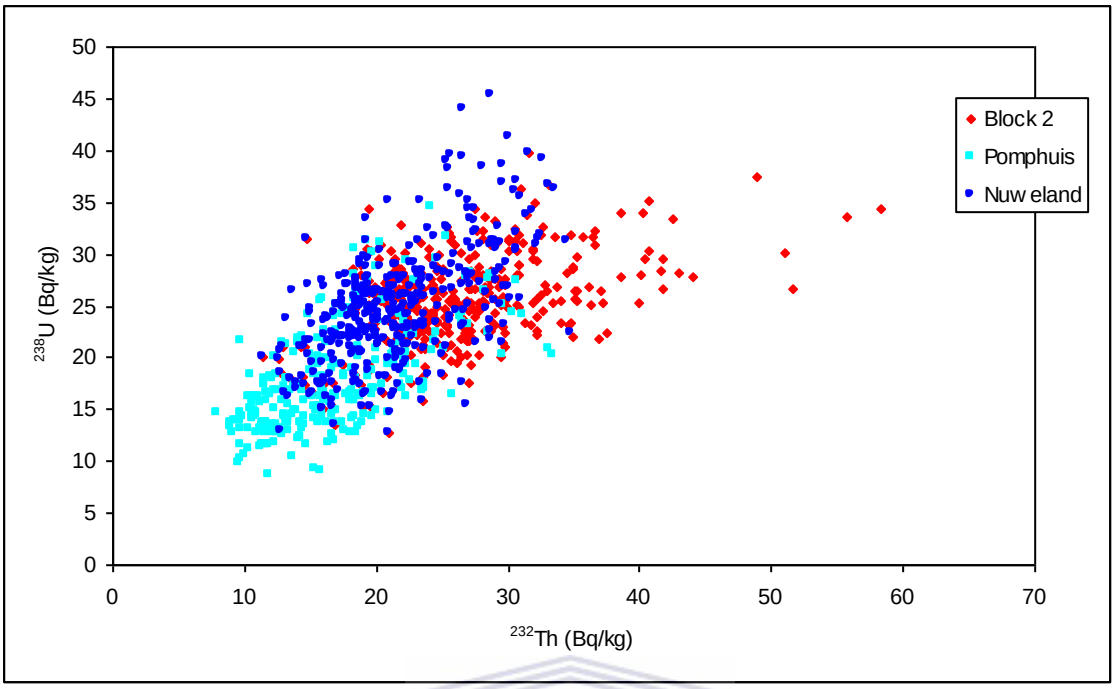

Figure 5-9: *Two dimensional plot showing the correlation plot of the averaged ACs of ^{238}U series and ^{232}Th series in the three blocks.*

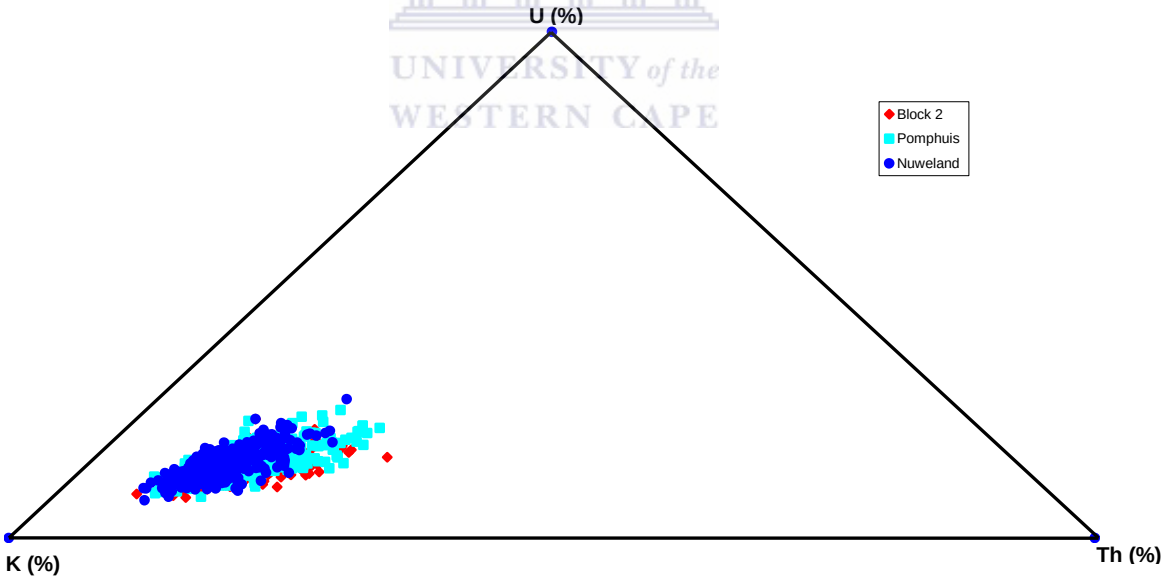

Figure 5-10: *Ternary plot showing the relative distribution of the averaged ACs of the radionuclides in the three blocks.*

5.4 Indication of sediment groups

Since the radiometric maps produced (Figures 5-2 to 5-4) for all three blocks indicate significant variations mainly in the distribution of the Total Count rate (TC) and AC of ^{232}Th series, a categorization of the blocks into sections for detailed investigation characterized by high and low ACs for ^{232}Th series and ^{40}K was made (see Figure 5-11). The coordinates of the sections are given in Table 5-2. It is noted that, section 2 and 4 in Block 2 overlap to some extent. No separate sections for ^{238}U were selected in view of the strong correlation in AC of ^{238}U series with ^{232}Th series as shown in Chapter 4. The AC maps of the ^{40}K, ^{232}Th series and ^{238}U series in each section were extracted to further investigate the correlations. To preliminary assess the distribution pattern of the radionuclide data, ternary plots were used. Figure 5-12 compares the ternary plots for cold spot (low count rate) and hot spot (high count rate) sections of the three blocks. For cold spots, sections 2, 2 and 3 from Block 2, Pomphuis and Nuweland blocks, respectively, were used whereas for hot spots, the sections 1, 1 and 1 for Block 2, Pomphuis and Nuweland, respectively, were used (see Figure 5-11). From the ternary plot, it is noted that for Block 2, the concentration fraction of ^{40}K is less in hot spot than cold-spot sections, implying that there is noticeable contribution of ^{232}Th and ^{238}U in that particular block. Furthermore, data distribution patterns were assessed in each section to accurately identify the sediment groups. The data will be discussed blockwise below.

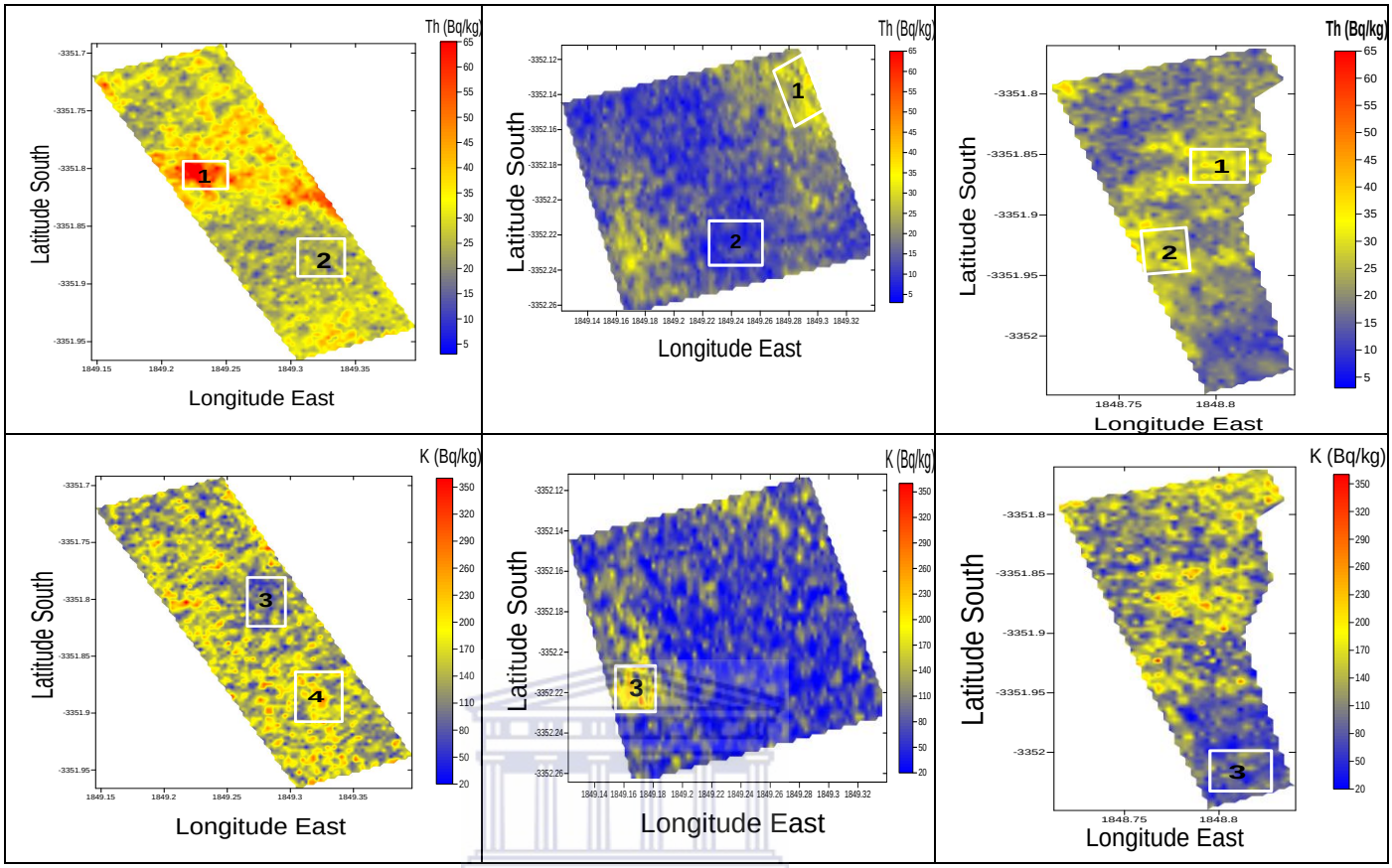

Figure 5-11: *Maps of the ^{232}Th and ^{40}K ACs showing the sections made in Block 2 (left-hand side), Pomphuis block (middle) and Nuweland block (right-hand side).*

Table 5-2: Coordinate ranges (Latitude and Longitude) of the sections made in the blocks.

Blocks	Sections	Coordinate ranges	
		Latitude (south)	Longitude (east)
Block 2	Section 1	33°51.795' - 33°51.817'	18°49.216' - 18°49.250'
	Section 2	33°51.861' - 33°51.893'	18°49.305' - 18°49.336'
	Section 3	33°51.780' - 33°51.826'	18°49.266' - 18°49.294'
	Section 4	33°51.861' - 33°51.913'	18°49.305' - 18°49.336'
Pomphuis	Section 1	33°52.127' - 33°52.157'	18°49.277' - 18°49.302'
	Section 2	33°52.212' - 33°52.237'	18°49.223' - 18°49.259'
	Section 3	33°52.207' - 33°52.229'	18°49.154' - 18°49.182'
Nuweland	Section 1	33°51.846' - 33°51.873'	18°48.787' - 18°48.816'
	Section 2	33°51.913' - 33°51.949'	18°48.762' - 18°48.787'
	Section 3	33°51.999' - 33°52.033'	18°48.795' - 18°48.828'

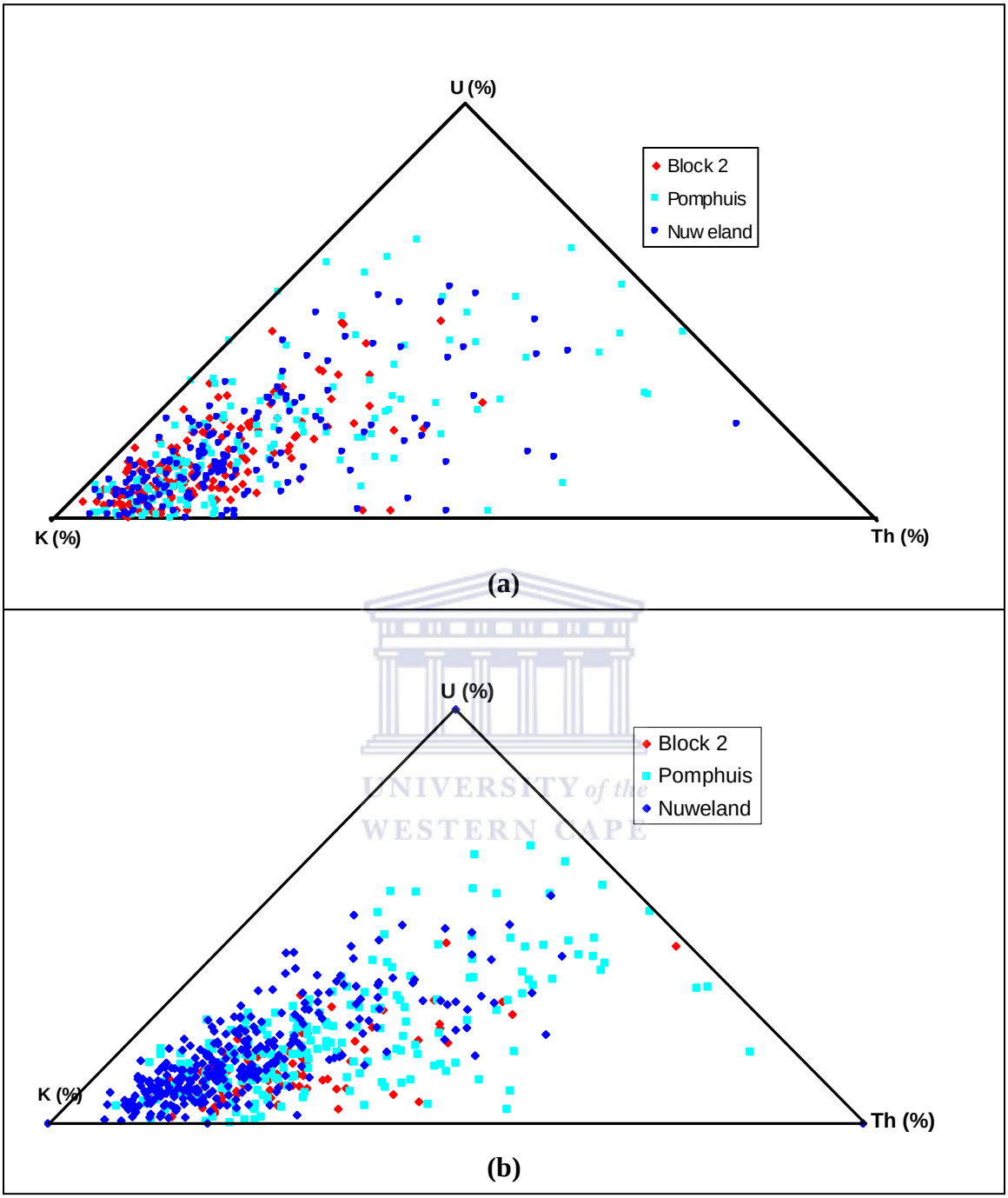

Figure 5-12: *Ternary plot showing the relative distribution of block-section data for (a) cold-spot sections (b) hot-spot sections.*

5.4.1 Block 2

Section 1

The maps, distributions (histograms) and 2D correlation plots of the ^{232}Th series, ^{238}U series and ^{40}K ACs for section 1 are shown in Figure 5-13. The ^{232}Th and ^{238}U AC maps for section 1, indicate that, according to the selection criteria, the ACs of ^{232}Th and ^{238}U are high and that of ^{40}K medium-high to high. The distributions of the radionuclides indicate that the mean ACs for ^{232}Th, ^{238}U and ^{40}K are approximately 55, 32 and 167 Bq/kg, respectively. However, the distribution of ^{232}Th has a similar width as the distributions of ^{238}U and ^{40}K, contrary to the observation for the entire block data. The correlation plot between ^{238}U and ^{232}Th shows an interesting pattern, which will be further investigated in section 5.4.4.

Section 2

The maps, distributions (histograms) and 2D correlation plots of the ^{232}Th series, ^{238}U series and ^{40}K ACs for section 2 are shown in Figure 5-14. The maps show low ACs for Th and medium high ACs for U and K, in agreement with the selection criteria. From the histograms, the mean ACs for ^{232}Th, ^{238}U and ^{40}K are approximately 22, 25 and 164 Bq/kg, respectively. However, one notes that the distribution of ^{232}Th is symmetric and twice as narrow compared to the distributions of ^{238}U and ^{40}K. The correlation plot between ^{238}U and ^{232}Th shows the data distribution pattern similar to, but more confined than the correlation in section 1 (compare to Figure 5-13).

Section 3

The maps, distributions (histograms) and 2D correlation plots of the ^{232}Th series, ^{238}U series and ^{40}K ACs for section 3 are shown in Figure 5-15. The maps show a medium high concentration for Th and U and low values for K, in agreement with the selection criteria. From the histograms, the mean ACs for ^{232}Th, ^{238}U and ^{40}K are approximately 40, 35 and 150 Bq/kg, respectively. Again, the distribution of ^{232}Th is twice as narrow as for ^{238}U and ^{40}K and is symmetric, leading to the same considerations as in section 2. In this section, the correlation plot between ^{238}U and ^{232}Th shows a data distribution pattern as for sections 1 and 2.

Section 4

The maps, distributions (histograms) and 2D correlation plots of the ^{232}Th series, ^{238}U series and ^{40}K ACs for section 4 are shown in Figure 5-16. From the maps one notices that the AC of Th is low and the ACs of U and K are medium high, in agreement with the selection criteria. As to be expected, the maps show quite large resemblance with the maps of section 2, shown in Figure 5-14. The mean ACs from the distributions of ^{232}Th, ^{238}U and ^{40}K are approximately 22, 25 and 164 Bq/kg, respectively. The distribution is similar to those in section 2. From the correlation plots, it is noted that the correlation between ^{238}U and ^{232}Th shows a data distribution pattern similar to section 2.

To assess the data distribution patterns in the sections and eventually the entire block, various correlations were investigated, leading to the ratio K/Th versus Th as a potentially interesting correlation. Figure 5-17 shows a 2D plot of K/Th and Th for the four sections. The plot for section 1 indicates that for AC_{Th} > 30 Bq/kg, the ratio K/Th is constant. For section 2, the plot indicates that contrary to section 1, the K/Th ratio is not constant for AC_{Th} < 30 Bq/kg). The plot for section 3 indicates that K/Th is constant for AC_{Th} > 30 Bq/kg as in section 1, and a correlation between K/Th and Th for AC_{Th} < 30 Bq/kg as in section 2. For the plot of K/Th and Th for section 4, the data show more data points for low Th ACs and based on these results section 4 seems to be more suitable for further analysis than section 2.

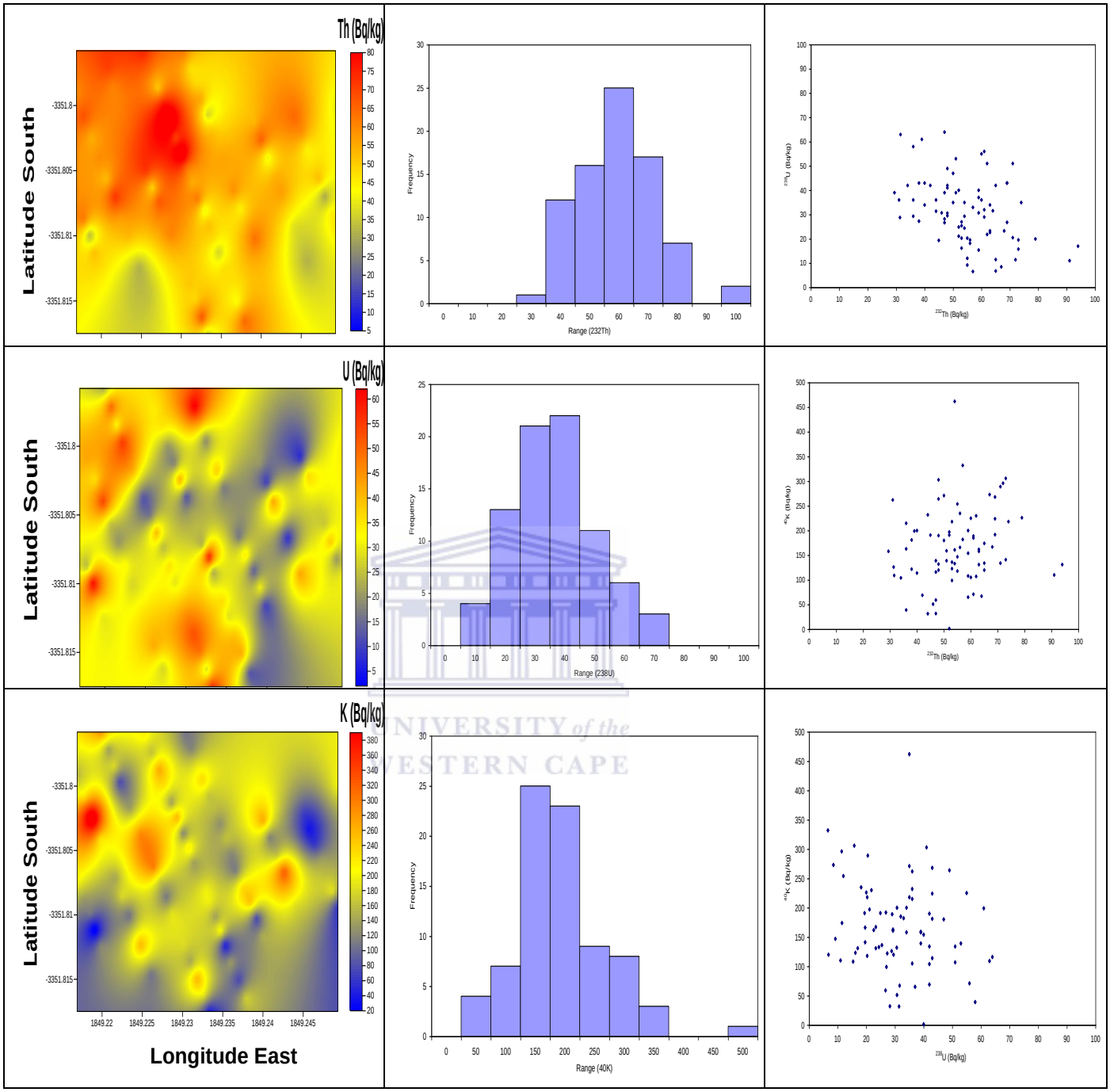

Figure 5-13: *Maps of the ^{232}Th, ^{238}U and ^{40}K ACs (left-hand side), Histograms showing the distributions of the ^{232}Th, ^{238}U and ^{40}K (middle) and two dimensional plots showing the correlations of the radionuclide ACs (right-hand side) for section 1 in Block 2.. (Note: The MEDUSA-software algorithm gives the latitude and longitude in the format xxyy.yy instead of the usual xx˚yy.yy' where xx and yy.yy correspond to degrees and minutes, respectively).*

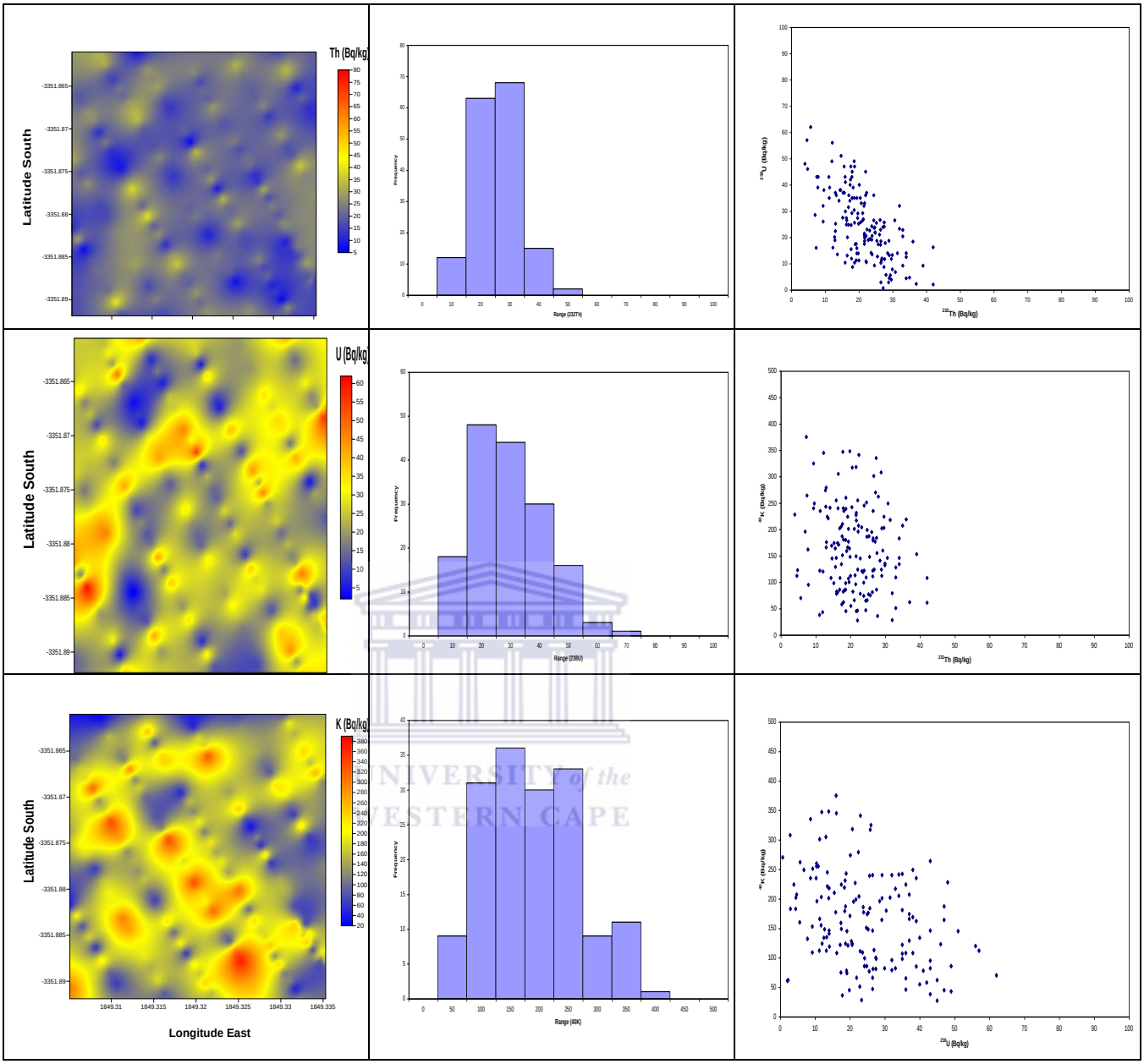

Figure 5-14: *Maps of the ^{232}Th, ^{238}U and ^{40}K ACs (left-hand side), Histograms showing the distributions of the ^{232}Th, ^{238}U and ^{40}K (middle) and two dimensional plots showing the correlations of the radionuclide ACs (right-hand side) for section 2 in Block 2. (Note: The MEDUSA-software algorithm gives the latitude and longitude in the format xxyy.yy instead of the usual xx˚yy.yy' where xx and yy.yy correspond to degrees and minutes, respectively).*

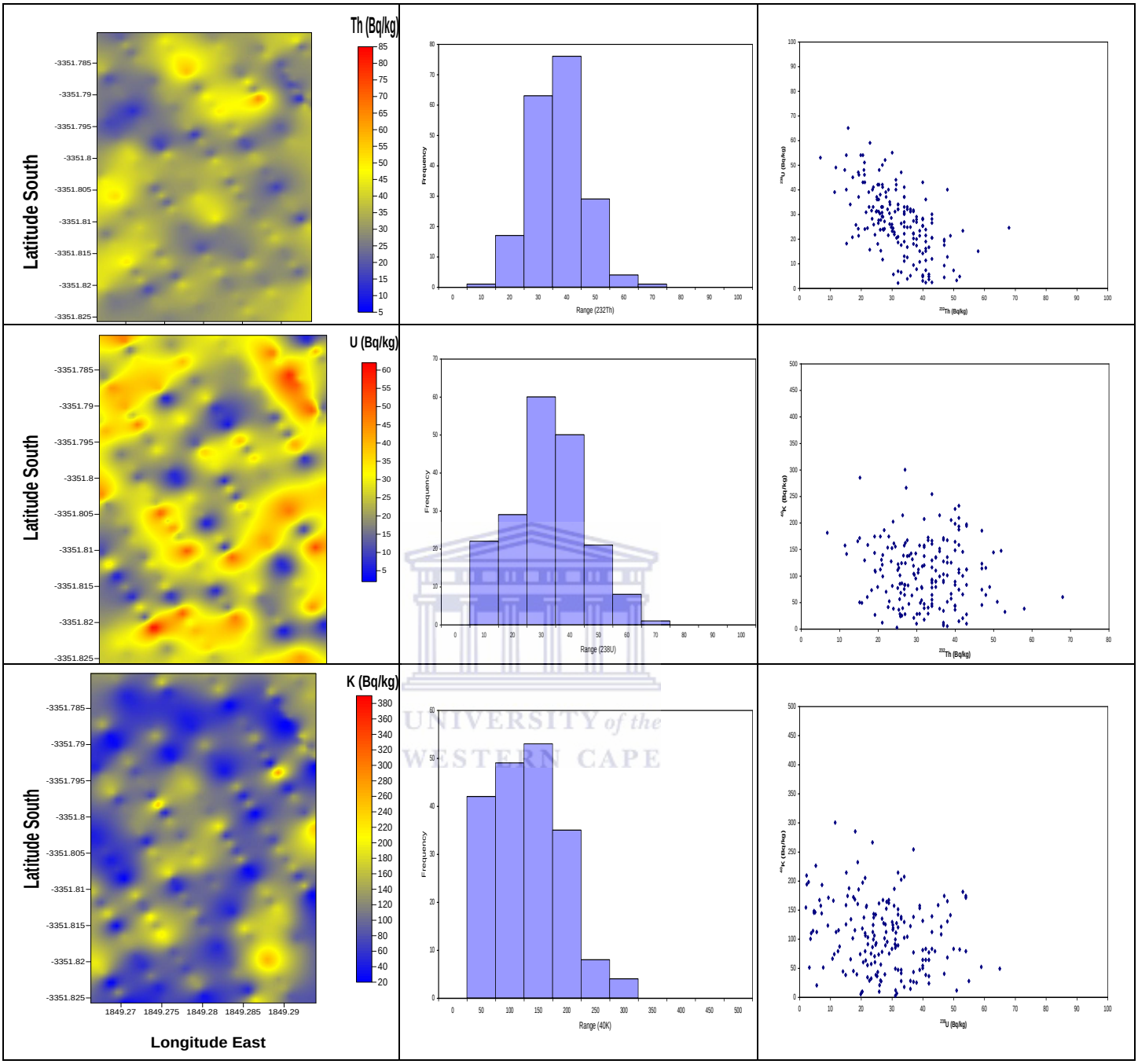

Figure 5-15: *Maps of the ^{232}Th, ^{238}U and ^{40}K ACs (left-hand side), Histograms showing the distributions of the ^{232}Th, ^{238}U and ^{40}K (middle) and two dimensional plots showing the correlations of the radionuclide ACs (right-hand side) for section 3 in Block 2. (Note: The MEDUSA-software algorithm gives the latitude and longitude in the format xxyy.yy instead of the usual xx˚yy.yy' where xx and yy.yy correspond to degrees and minutes, respectively).*

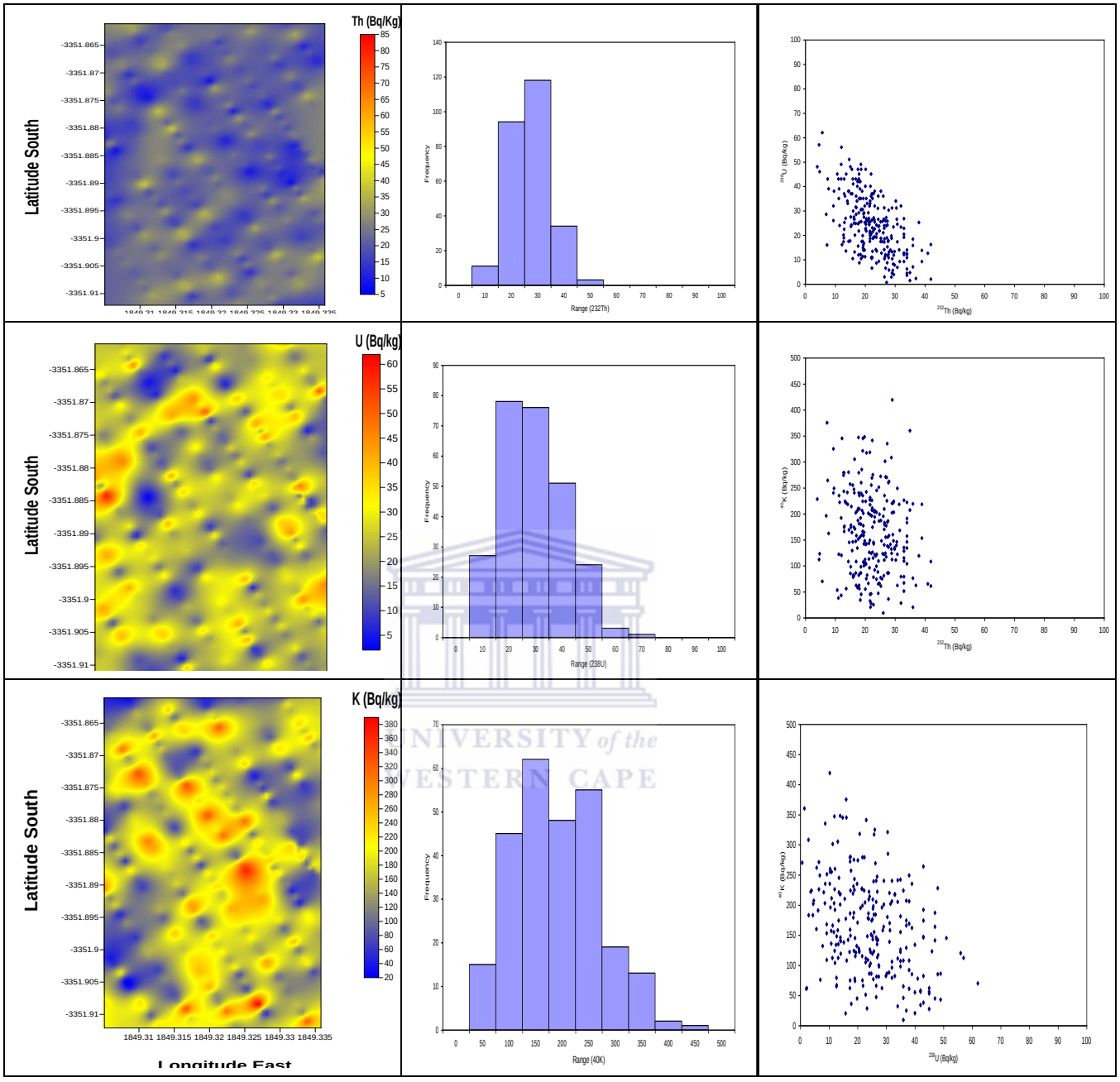

Figure 5-16: *Maps of the ^{232}Th, ^{238}U and ^{40}K ACs (left-hand side), Histograms showing the distributions of the ^{232}Th, ^{238}U and ^{40}K (middle) and two dimensional plots showing the correlations of the radionuclide ACs (right-hand side) for section 4 in Block 2. (Note: The MEDUSA-software algorithm gives the latitude and longitude in the format xxyy.yy instead of the usual xx°yy.yy' where xx and yy.yy correspond to degrees and minutes, respectively).*

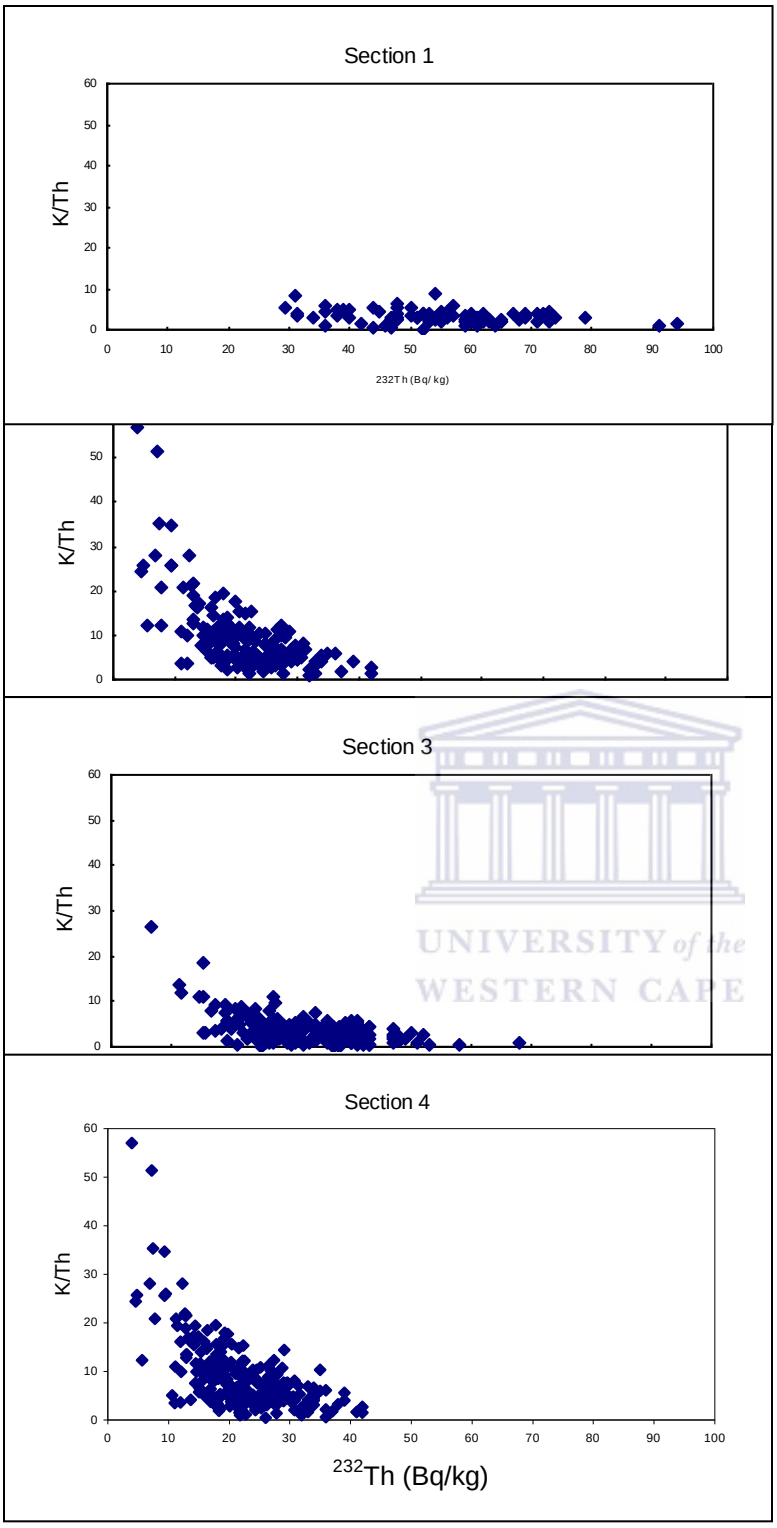

Figure 5-17: *Two dimensional plots of K/Th versus Th showing the trend and classification of the section 1, 2, 3 and 4 data in Block 2.*

5.4.2 Pomphuis block

Section 1

The maps, distributions (histograms) and 2D correlation plots of the ^{232}Th series, ^{238}U series and ^{40}K ACs for Pomphuis section 1 are shown in Figure 5-18. The maps show a high concentration for Th, medium high ACs for U and low values for K, in agreement with the selection criteria. The histogram mean ACs for ^{232}Th, ^{238}U and ^{40}K are approximately 35, 30 and 100 Bq/kg, respectively. The distribution of ^{232}Th is symmetric and narrow compared to the distributions of ^{238}U and ^{40}K, similar as for the entire block data. The correlation plot between ^{238}U and ^{232}Th shows a data distribution pattern similar as in the sections of Block 2. The distribution pattern will be further investigated in section 5.4.4.

Section 2

The maps, distributions (histograms) and 2D correlation plots of the ^{232}Th series, ^{238}U series and ^{40}K ACs for section 2 are shown in Figure 5-19. From the figure, the maps show low ACs for Th, U and K, in agreement with the selection criteria. For the distributions of ^{232}Th, ^{238}U and ^{40}K ACs as histograms, the mean ACs for ^{232}Th, ^{238}U and ^{40}K are approximately 10, 12 and 55 Bq/kg, respectively. However, one notes that the distribution of ^{232}Th has a similar width as the distributions of ^{238}U and ^{40}K, contrary to the observation for the entire block data (compare to Figure 5-6). From the correlation plots, the plot between ^{238}U and ^{232}Th shows the data distribution pattern similar to, but less confined than the correlation in section 1.

Section 3

The maps, distributions (histograms) and 2D correlation plots of the ^{232}Th series, ^{238}Useries and ^{40}K ACs for section 3 are shown in Figure 5-20. From the figure, the maps show a medium high concentration for Th, medium high to high for U and high values for K, in agreement with the selection criteria. From the distribution plots, the mean ACs for ^{232}Th, ^{238}U and ^{40}K are approximately 30, 30 and 160 Bq/kg, respectively. However, the distribution of ^{232}Th is twice as narrow than for ^{238}U and ^{40}K and is symmetric, similar as in section 2 and 3 in Block 2. The correlation plot between ^{238}U and ^{232}Th shows the data distribution pattern similar to, but more confined than the correlations in section 1 and 2 (compare to Figures 5-18 and 5-19).

As for Block 2, various correlations were investigated to assess data distribution pattern in the Pomphuis-block sections. Again, the ratio K/Th versus Th shows a potentially interesting correlation. Figure 5-21 shows 2D plot of K/Th and Th for the three sections. The plots indicate that for section 1 with AC_{Th} > 20 Bq/kg, the ratio K/Th is constant while for section 2, the K/Th ratio is constant for AC_{Th} > 6 Bq/kg. Furthermore, the plot for section 3 indicates that the K/Th ratio is constant for AC_{Th} > 20 Bq/kg as in section 1, and a correlation between K/Th and Th for AC_{Th} < 15 Bq/kg.

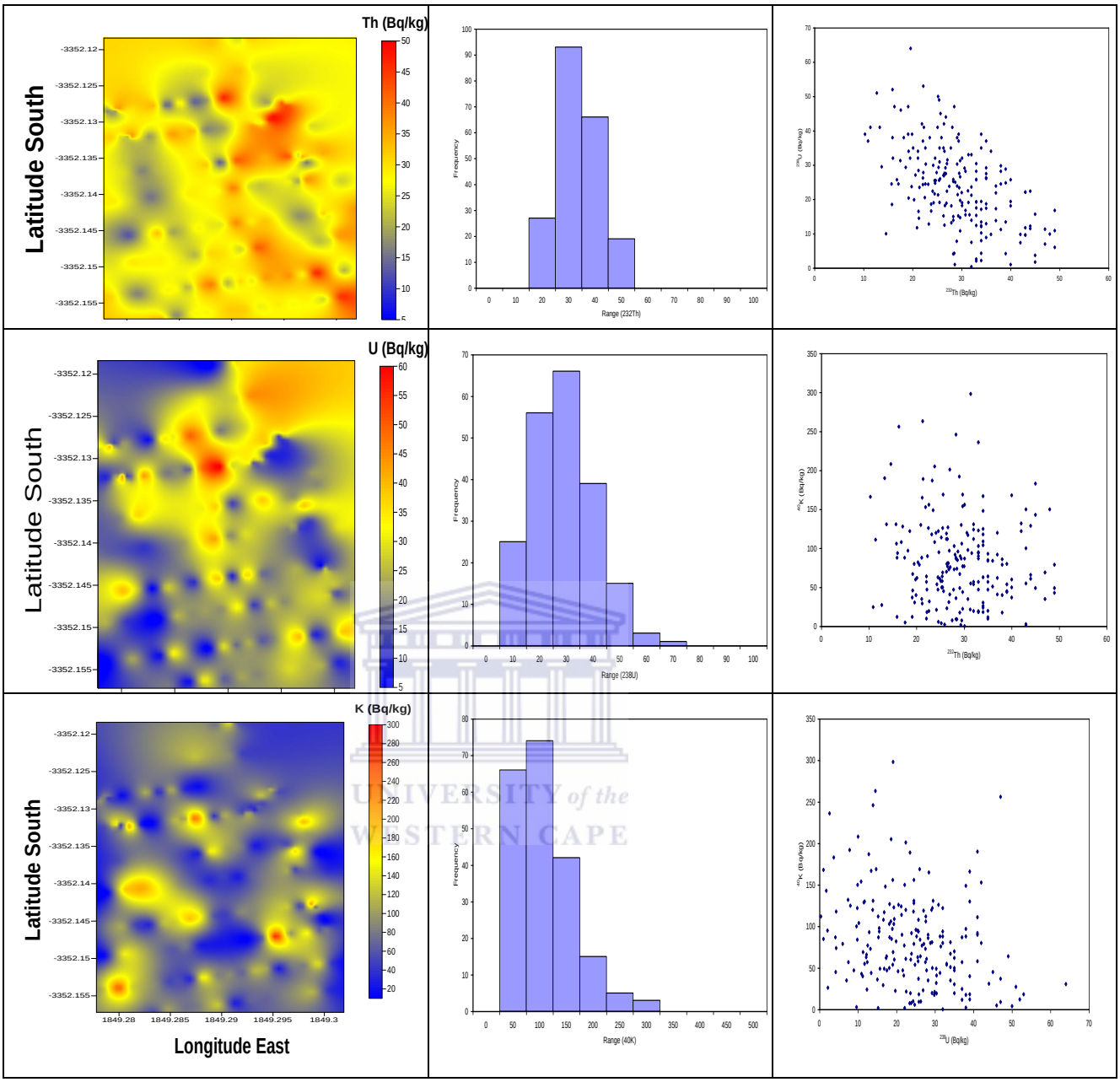

Figure 5-18: *Maps of the ^{232}Th, ^{238}U and ^{40}K ACs (left-hand side), Histograms showing the distributions of the ^{232}Th, ^{238}U and ^{40}K (middle) and two dimensional plots showing the correlations of the radionuclide ACs (right-hand side) for section 1 in the Pomphuis block. (Note: The MEDUSA-software algorithm gives the latitude and longitude in the format xxyy.yy instead of the usual xx°yy.yy' where xx and yy.yy correspond to degrees and minutes, respectively).*

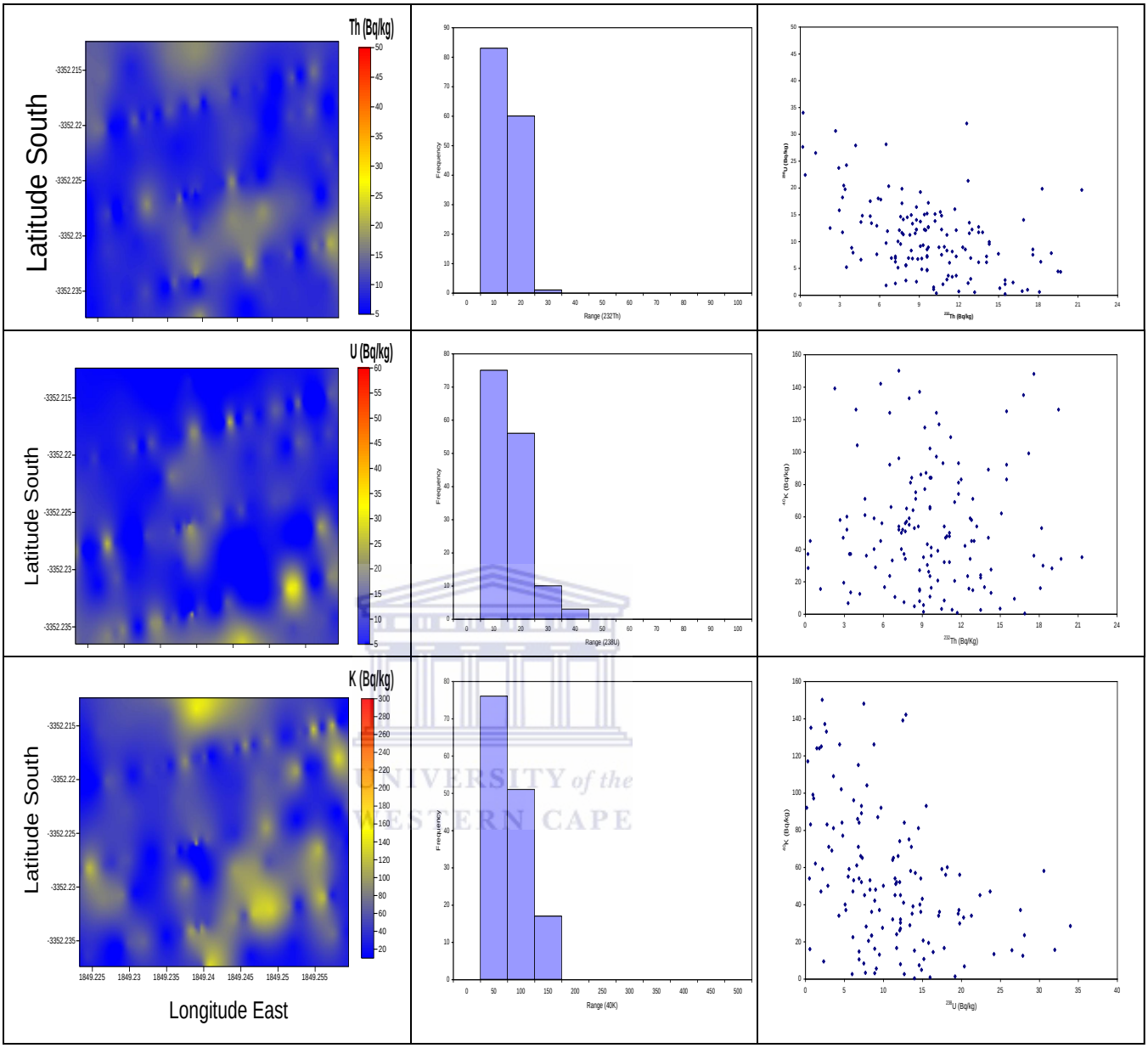

Figure 5-19: *Maps of the ^{232}Th, ^{238}U and ^{40}K ACs (left-hand side), Histograms showing the distributions of the ^{232}Th, ^{238}U and ^{40}K (middle) and two dimensional plots showing the correlations of the radionuclide ACs (right-hand side) for section 2 in the Pomphuis block. (Note: The MEDUSA-software algorithm gives the latitude and longitude in the format xxyy.yy instead of the usual xx˚yy.yy' where xx and yy.yy correspond to degrees and minutes, respectively).*

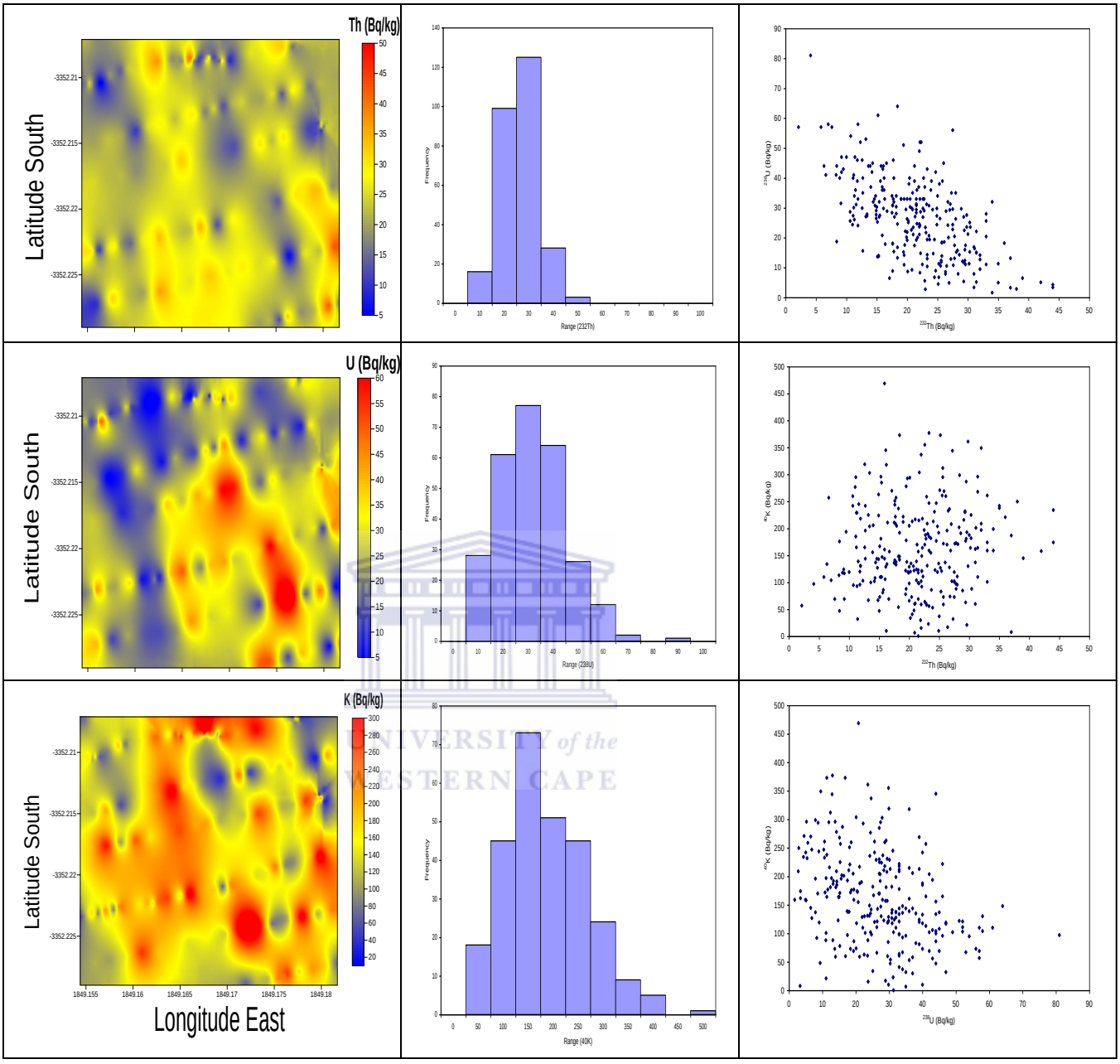

Figure 5-20: *Maps of the ^{232}Th, ^{238}U and ^{40}K ACs (left-hand side), Histograms showing the distributions of the ^{232}Th, ^{238}U and ^{40}K (middle) and two dimensional plots showing the correlations of the radionuclide ACs (right-hand side) for section 3 in the Pomphuis block. (Note: The MEDUSA-software algorithm gives the latitude and longitude in the format xxyy.yy instead of the usual xx˚yy.yy' where xx and yy.yy correspond to degrees and minutes, respectively).*

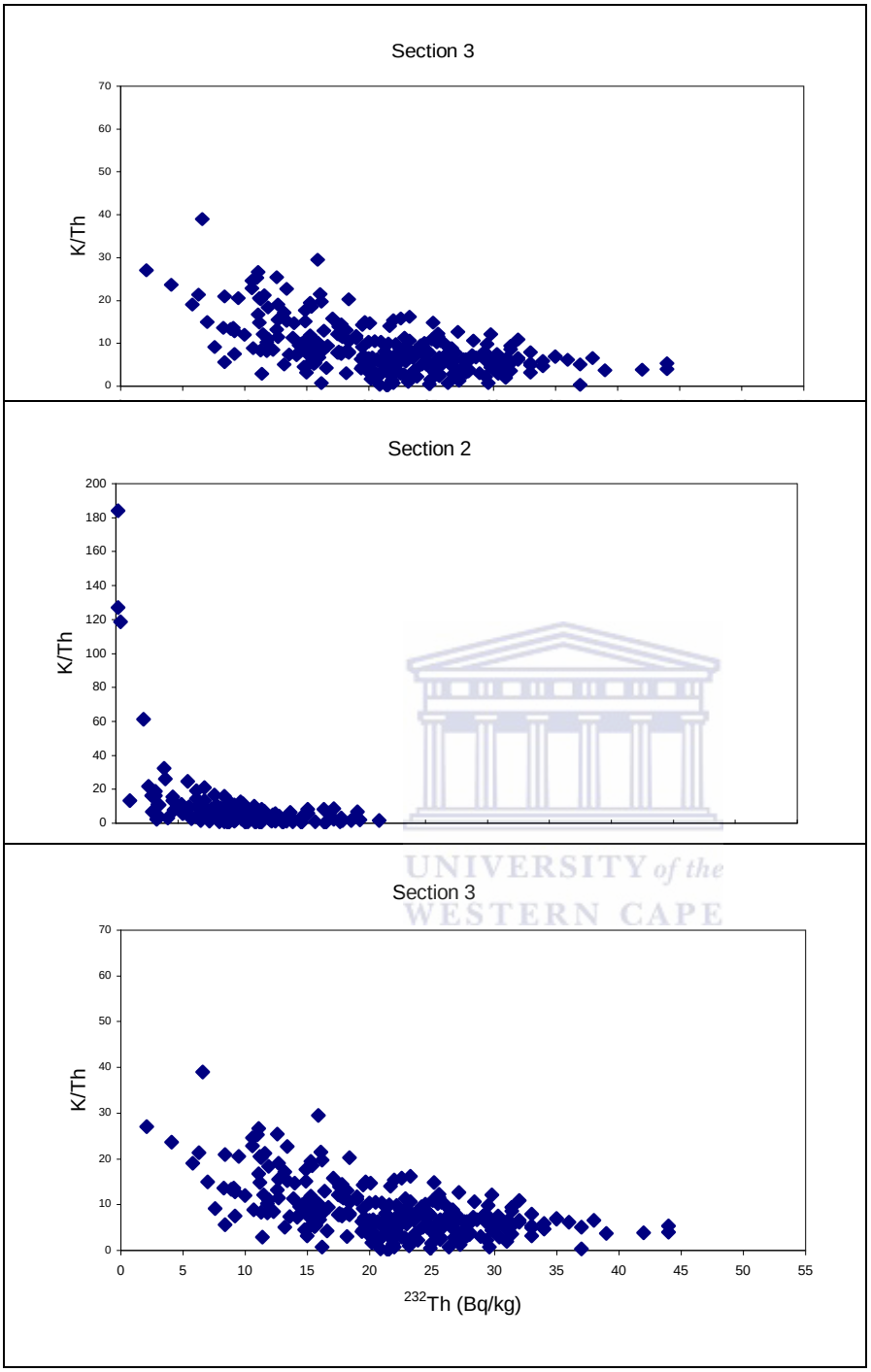

Figure 5-21: *Two dimensional plots of K/Th and Th showing the trend and classification of the section 1, 2 and 3 data in the Pomphuis block.*

5.4.3 Nuweland block

Section 1

The maps, distributions (histograms) and 2D correlation plots of the ^{232}Th series, ^{238}U series and ^{40}K ACs for section 1 are shown in Figure 5-22. The ^{232}Th AC map for section 1, indicates that the AC of ^{232}Th is high, and medium high ACs for ^{238}U and ^{40}K, according to the selection criteria. From the histogram plots, the mean ACs for ^{232}Th, ^{238}U and ^{40}K are approximately 35, 30 and 150 Bq/kg, respectively. It is also noted that the distribution of ^{232}Th is symmetric and twice as narrow compared to the distributions of ^{238}U and ^{40}K, similar as for the entire block. The correlation plot between ^{238}U and ^{232}Th shows data distribution pattern similar to the sections of blocks Pomphuis and Block 2.

Section 2

The maps, distributions and 2D correlation plots of the ^{232}Th, ^{238}U and ^{40}K ACs for section 2 are shown in Figure 5-23. From the figure, the maps show the ACs of ^{232}Th and ^{238}U are high and of ^{40}K medium high, in agreement with the selection criteria. Mean ACs from the distribution of ^{232}Th, ^{238}U and ^{40}K are approximately 30, 32 and 150 Bq/kg, respectively. However, one notes that the distribution of ^{232}Th is twice as narrow as for ^{238}U and ^{40}K and is symmetric, similar to section 1 and hence leading to the same considerations as in section 1. The correlation plot between ^{238}U and ^{232}Th shows the data distribution pattern similar to, but less confined than the correlation in section 1 (compare to Figure 5-22).

Section 3

The maps, distributions (histograms) and 2D correlation plots of the ^{232}Th, ^{238}U and ^{40}K ACs for section 3 are shown in Figure 5-24. The maps show low ACs for Th, U and K, in agreement with the selection criteria. From the histograms, the mean ACs for ^{232}Th, ^{238}U and ^{40}K are approximately 20, 20 and 100 Bq/kg, respectively. However, the distribution of ^{232}Th is symmetric and narrow compared to the distributions of ^{238}U and ^{40}K. The correlation plot between ^{238}U and ^{232}Th shows the data distribution pattern similar as in section 2.

The correlation between K/Th and Th was investigated in Nuweland block for the same consideration as in the blocks Pomphuis and Block 2. Figure 5-25 shows 2D

plots of K/Th and Th for the three sections. For section 1, the plot shows correlation between K/Th and Th for AC_{Th} < 50 Bq/kg. The plot for section 2 indicates that the K/Th ratio is constant for AC_{Th} > 10 Bq/kg, whereas the ratio K/Th is constant for AC_{Th} > 10 Bq/kg in section 3.

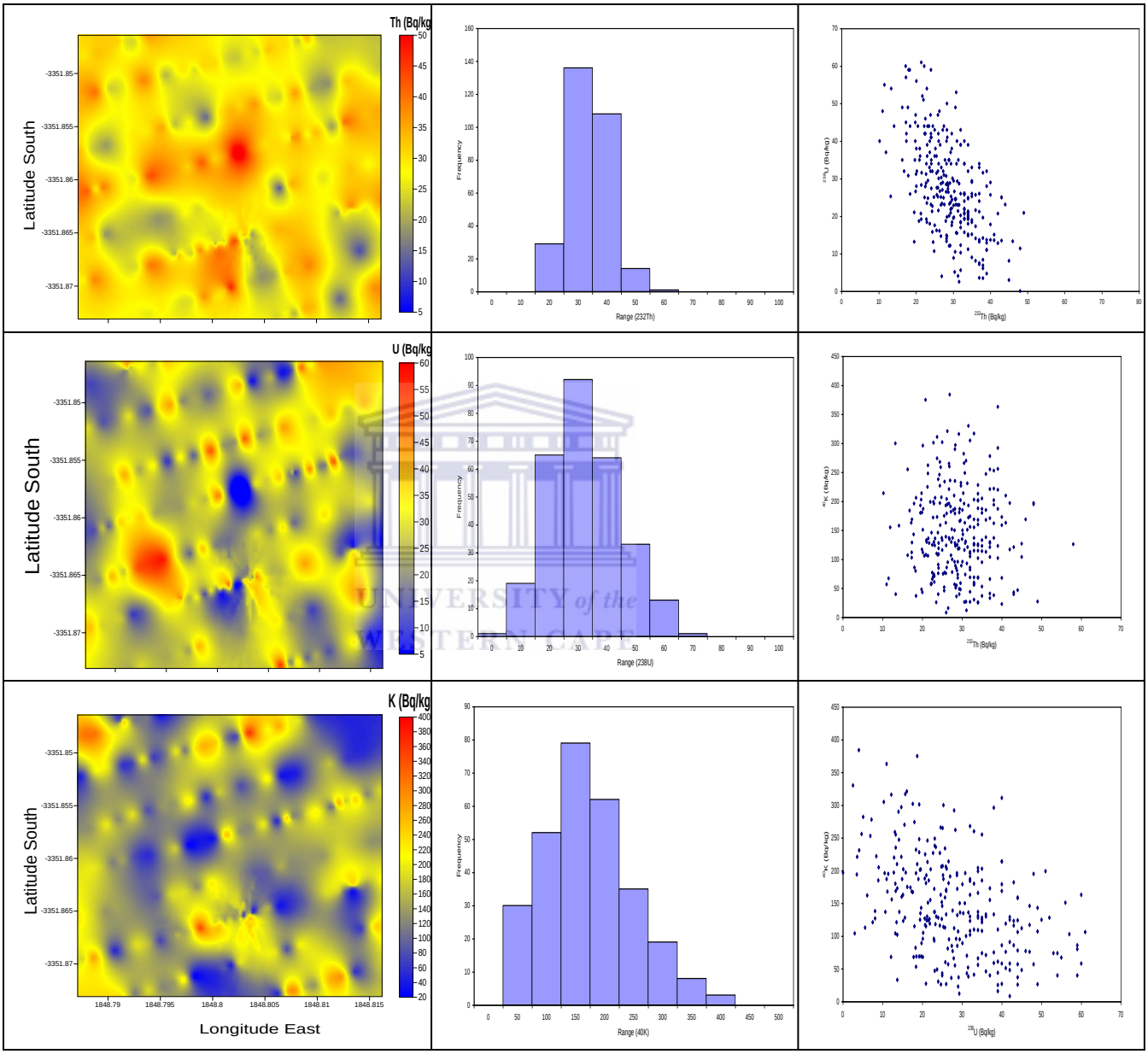

Figure 5-22: *Maps of the ^{232}Th, ^{238}U and ^{40}K ACs (left-hand side), Histograms showing the distributions of the ^{232}Th, ^{238}U and ^{40}K (middle) and two dimensional plots showing the correlations of the radionuclide ACs (right-hand side) for section 1 in the Nuweland block. (Note: The MEDUSA-software algorithm gives the latitude and longitude in the format xxyy.yy instead of the usual xx˚yy.yy' where xx and yy.yy correspond to degrees and minutes, respectively).*

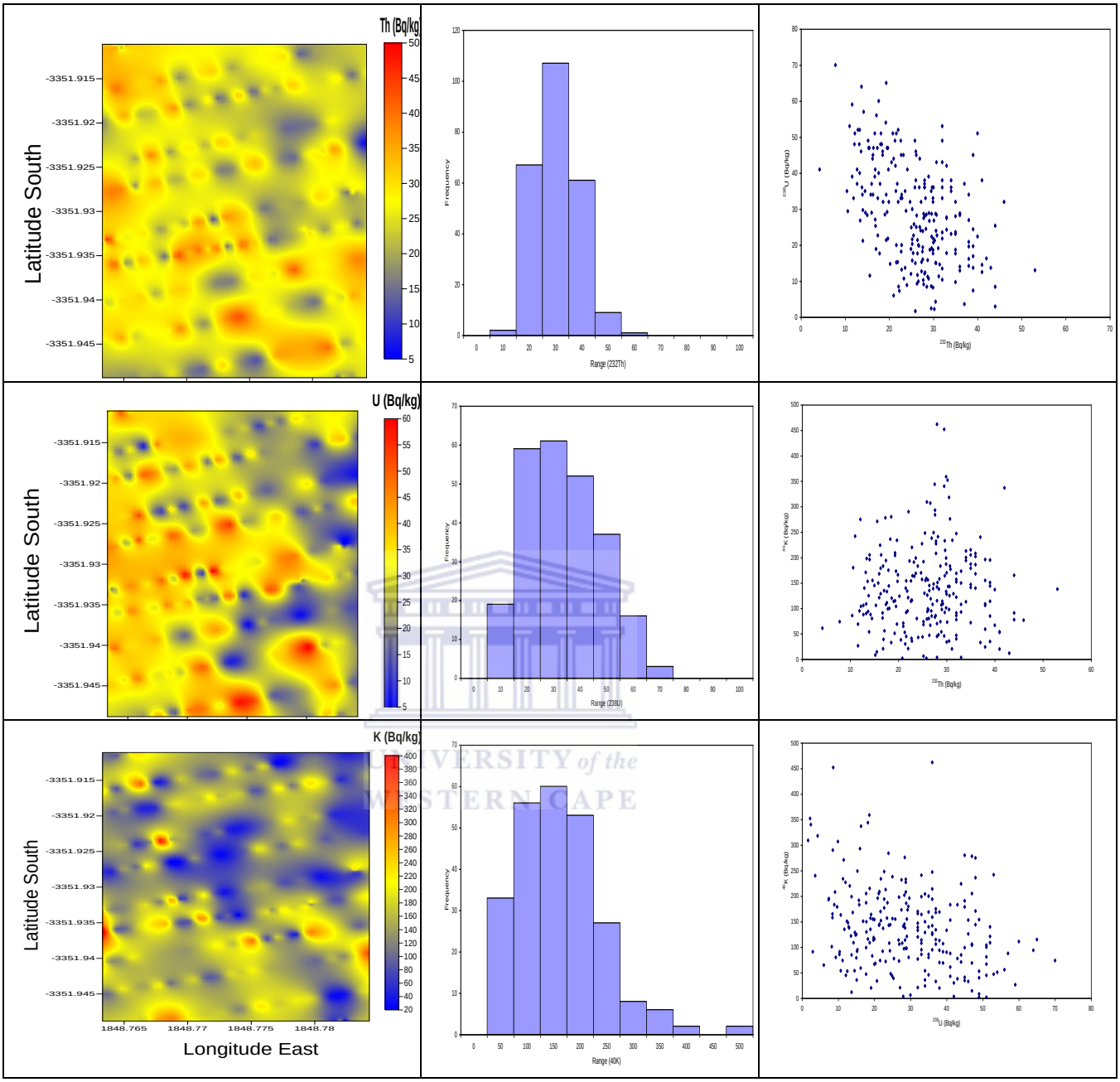

Figure 5-23: *Maps of the ^{232}Th, ^{238}U and ^{40}K ACs (left-hand side), Histograms showing the distributions of the ^{232}Th, ^{238}U and ^{40}K (middle) and two dimensional plots showing the correlations of the radionuclide ACs (right-hand side) for section 2 in the Nuweland block. (Note: The MEDUSA-software algorithm gives the latitude and longitude in the format xxyy.yy instead of the usual xx˚yy.yy' where xx and yy.yy correspond to degrees and minutes, respectively).*

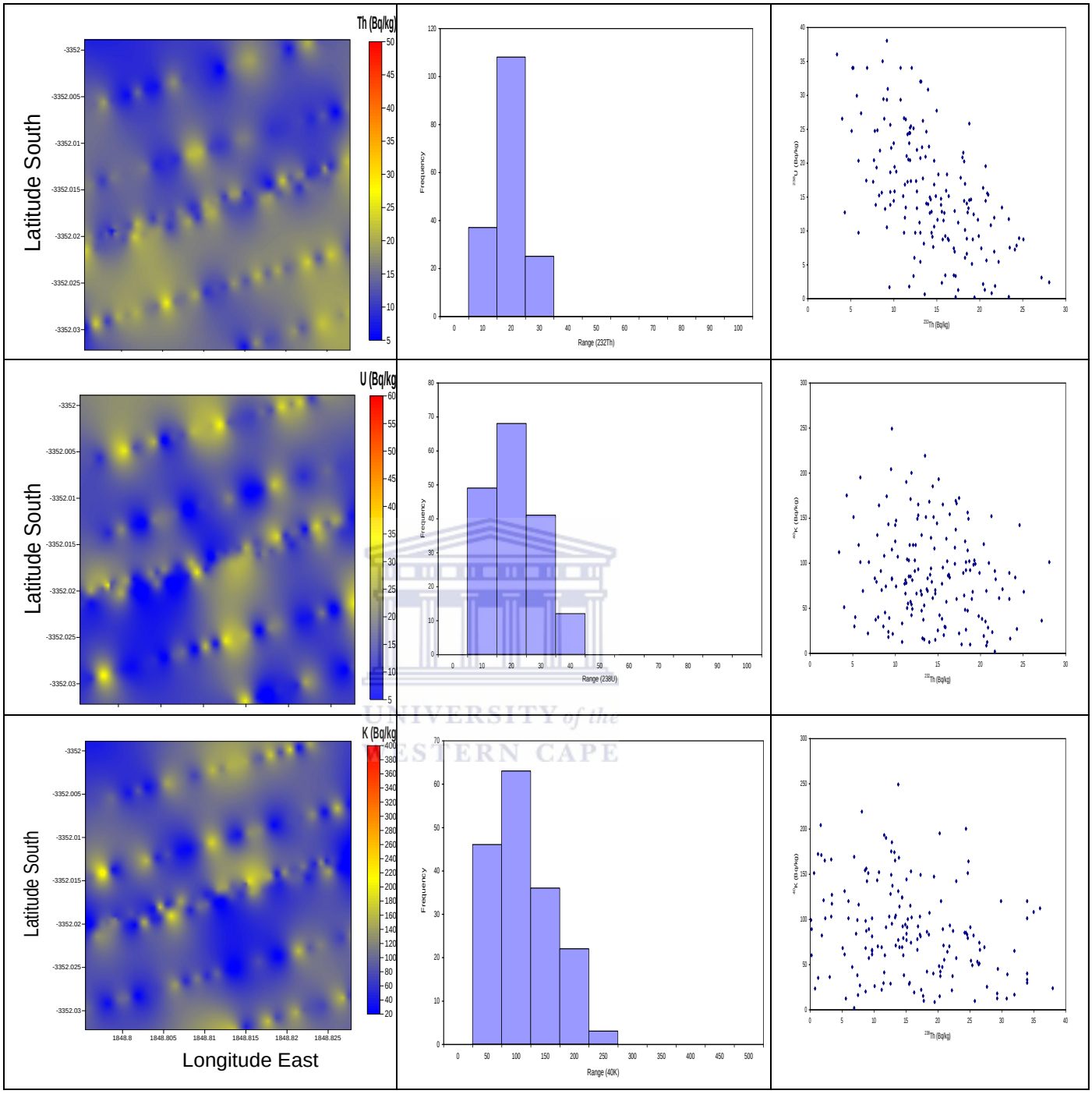

Figure 5-24: *Maps of the ^{232}Th, ^{238}U and ^{40}K ACs (left-hand side), Histograms showing the distributions of the ^{232}Th, ^{238}U and ^{40}K (middle) and two dimensional plots showing the correlations of the radionuclide ACs (right-hand side) for section 3 in the Nuweland block. (Note: The MEDUSA-software algorithm gives the latitude and longitude in the format xxyy.yy instead of the usual xx˚yy.yy' where xx and yy.yy correspond to degrees and minutes, respectively).*

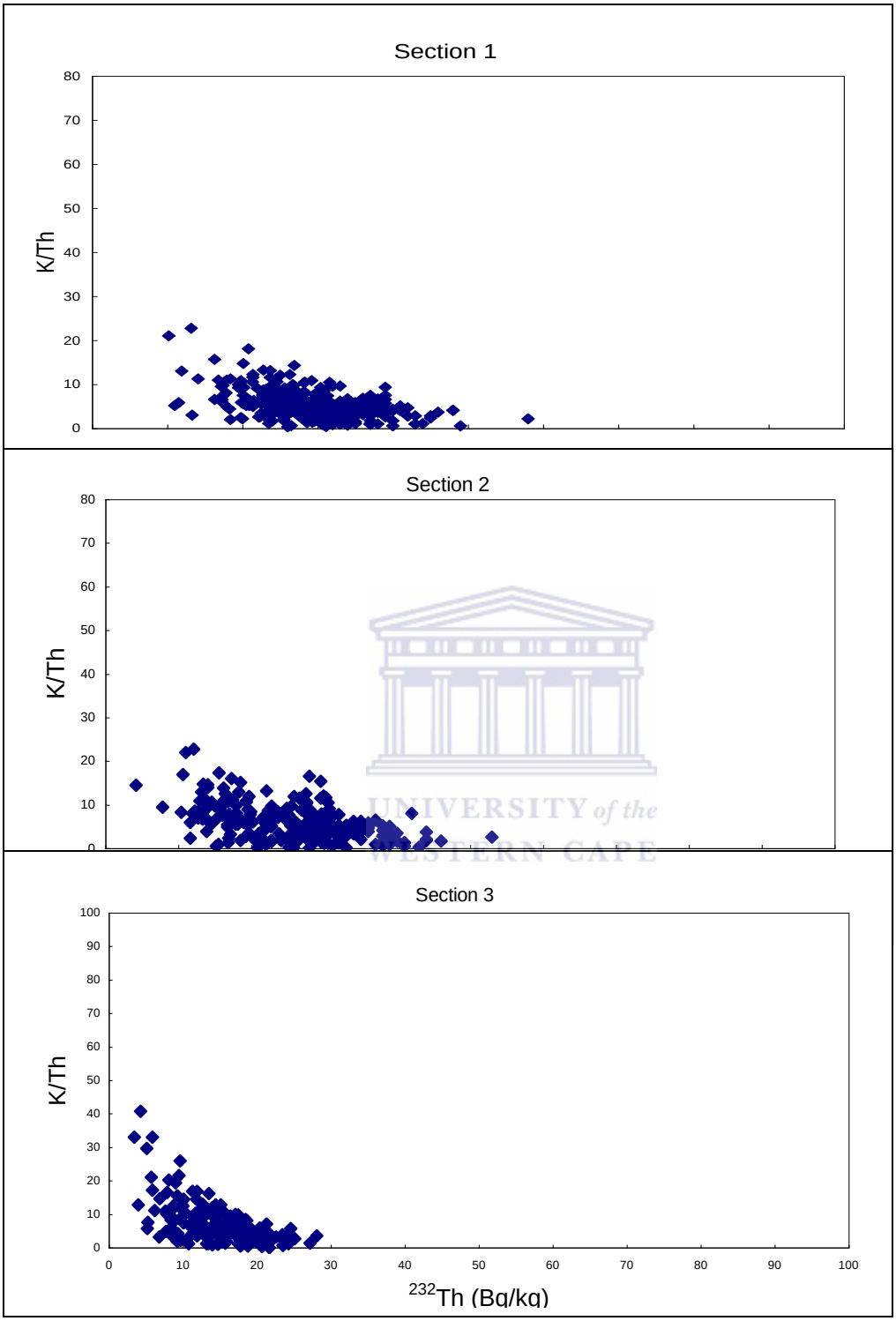

Figure 5-25: *Two dimensional plots of K/Th and Th showing the trend and classification of the section 1, 2 and 3 data in the Nuweland block. K and Th are the ACs of ^{40}K and ^{232}Th, respectively.*

5.4.4 Combined sections

To further investigate the sediment groups in the three blocks, section results were combined and assessed. For Block 2, we have left out section 2 in the further analysis of the combined sections based on the last remark on section 4. Figure 5-26 shows how the correlation between ^{232}Th and ^{238}U for block sections are related. The plots in the sections of the blocks are distributed in a similar pattern suggesting a relation given by;

$$U + aTh = C \tag{5.1}$$

where a is a dimensionless coefficient and C is a value in Bq/kg for the combined ACs distributed along the OY´ line (see Figure 5-26). The value of a was chosen by using the U/Th ratio as a guide and then choosing a so as to minimize the standard deviation of the C values.

From the plot (Figure 5-26), it is also noted that the blocks Pomphuis and Nuweland show similar data distributions that are more confined when compared to Block 2, suggesting that the two blocks are composed of one sediment group, in agreement with sample data presented in Chapter 4 section 4.1. Moreover, the distribution of C in all the block sections and the entire blocks was investigated.

Figure 5-27 shows the distributions of C in the block sections as histograms. For Block 2, the mean values of C for optimum value of a (1.9) in sections 1, 3 and 4 are ~ 130, 95, and 70 Bq/kg, respectively. However, the distribution of C in section 4 is two to three times narrower (smaller standard deviation) than the distributions for sections 1 and 3. This could be partly due to the fact that sections 1 and 3 have a slightly different optimal value for a, but the data in Figure 5-27 show that this is not the full explanation. For the Pomphuis block, the mean values of C for optimum value of a (1.8) in sections 1, 2 and 3 are ~ 75, 35 and 75 Bq/kg, respectively. However, section 1 has a similar distribution and width as the distribution of C in section 3. This shows that from the present data, section 1 and 3 represents the same sediment group. Similar investigation for Nuweland block, shows the mean values of C for optimum value of a (2) in sections 1, 2 and 3 are ~ 88, 85 and 55 Bq/kg, respectively. However, section 1 has a similar distribution and width as the distribution of C in section 2. This also shows that from the

present data, section 1 and 2 represents the same group similar to the one in the Pomphuis block. From the plot, it appears that the blocks Pomphuis and Nuweland are composed of mainly one sediment group with approximately mean *C* value of 80 Bq/kg, whereas Block 2 is composed of another sediment group with *C* value of ~130 Bq/kg and a component of the Pomphuis/Nuweland soil group (*C* value of ~80 Bq/kg). This group classification is in agreement with sample data shown in Figure 4-10 (Chapter 4, section 4.3.2).

The maps showing the distribution of *C* in the entire three blocks are shown in Figure 5-28. The maps show a large resemblance with ^{232}Th AC and the TC maps (Figures 5-2 to 5-4) revealing that ^{232}Th AC is the main indicator for the distribution of *C* in the blocks. Classifying Block 2 sections 1, 3 and 4 in the *C* distribution map using the histograms in Figure 5-27 shows that, the distribution of *C* in section 1 ranges from ~100 to 200 Bq/kg, in section 4 from ~ 30 to 100 Bq/kg, and in section 3 from ~50 to 140 Bq/kg. Similar classification for the Pomphuis block shows the distribution of *C* in section 1 ranges from ~35 to 105 Bq/kg, in section 2 from ~ 10 to 80 Bq/kg, and in section 3 from ~40 to 115 Bq/kg. For the Nuweland block, the distribution of *C* in section 1 ranges from ~55 to 120 Bq/kg, in section 2 from ~ 50 to 120 Bq/kg, and in section 3 from ~35 to 75 Bq/kg.

Figure 5-29 shows a 2D plot of K/Th and Th indicating the distribution of the three block-section data. The distribution shows a clear pattern, suggesting a relation given by;

$$(K/Th)^{b}(Th) = k \tag{5.2}$$

where *b* is a dimensionless coefficient and *k* is a constant for the combined distributions in each block, *K* and *Th* are the ACs of ^{40}K and ^{232}Th, respectively. From the above relation (5.2), *k* can be determined by the following relation in which the ACs are expressed in Bq/kg;

$$b\ln(\frac{K}{Th}) + \ln(Th) = \ln(k) \tag{5.3}$$

From the plot, one notices again similar data distribution patterns for blocks Pomphuis and Nuweland as was observed in Figure 5-26, in agreement with the hypothesis

presented in Chapter 4 (section 4.1) that the two blocks are composed of one sediment group. To further test the hypothesis, the distribution of *k* in the block sections as well as in the entire blocks was investigated. Figure 5-30 shows the distributions of *k* in the block sections as histograms. The mean values of *k* for optimum value of *b* (0.3) in Block 2 sections 1, 3 and 4 are approximately 4.4, 3.8 and 3.7, respectively. As was found in the distribution of *C*, the distribution of *k* indicates the presence of mainly one sediment group (section 1) with a mixing component of the other group characterizing blocks Pomphuis and Nuweland. For the Pomphuis block, the mean values of *k* for optimum value of *b* (0.3) in sections 1, 2 and 3 are approximately 3.8, 2.8 and 3.9, respectively. As was found in the distribution of *C*, the distribution of *k* indicates the presence of only one sediment group (section 1 or 3) with the mixing component (section 2), whereas for the Nuweland block, the mean values of *k* for optimum value of *b* (0.2) in sections 1, 2 and 3 are approximately 3.8, 3.8 and 3.2, respectively. Comparison of the mean *k* values in the blocks Pomphuis and Nuweland, confirms our hypothesis. In conclusion, the analysis shows the Pomphuis and Nuweland blocks are basically composed of one sediment group, while Block 2 seems to be mainly characterized by another group.

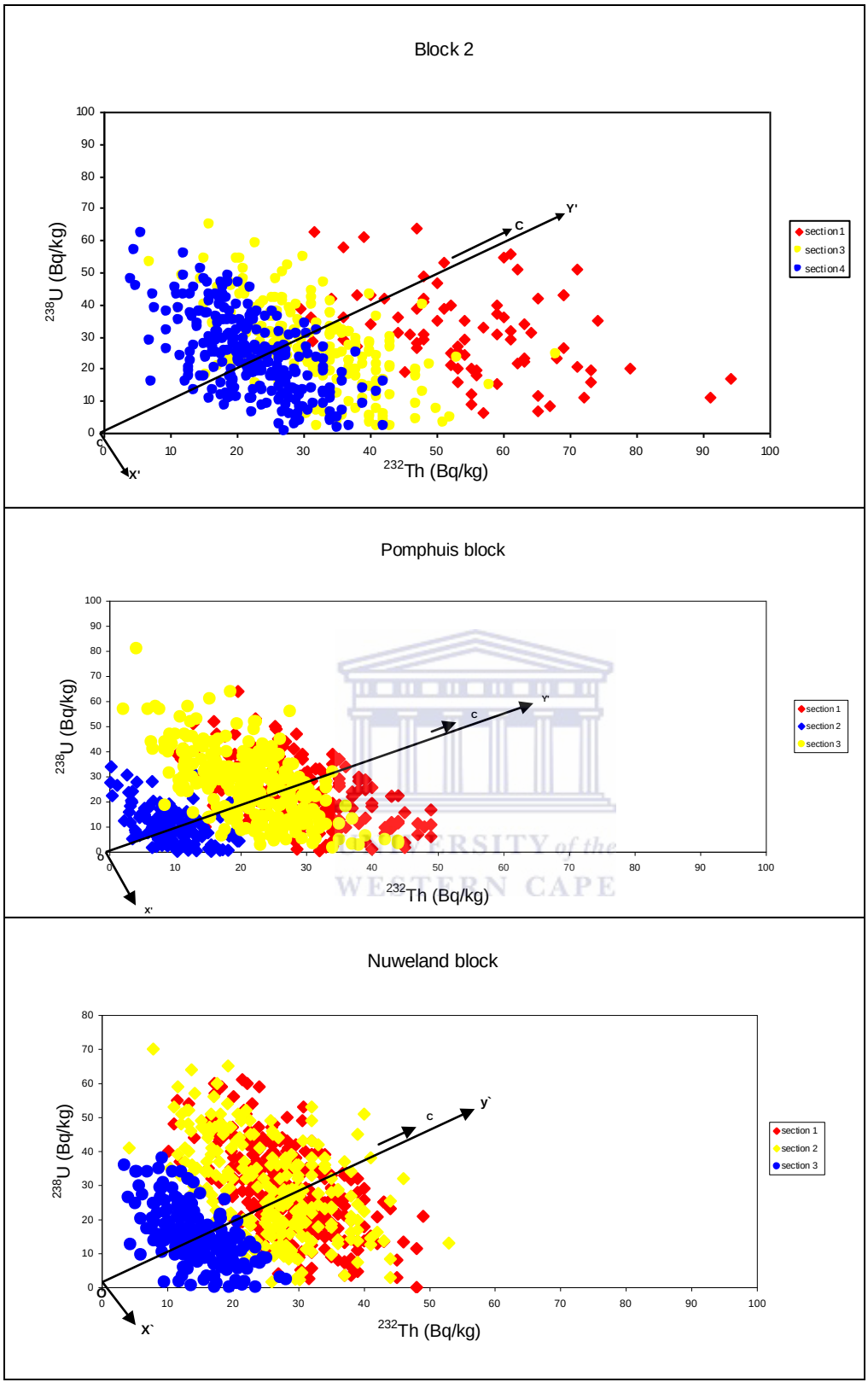

Figure 5-26: *Two dimensional plot showing the correlation between AC of ^{238}U and ^{232}Th series for the sections in the three blocks.*

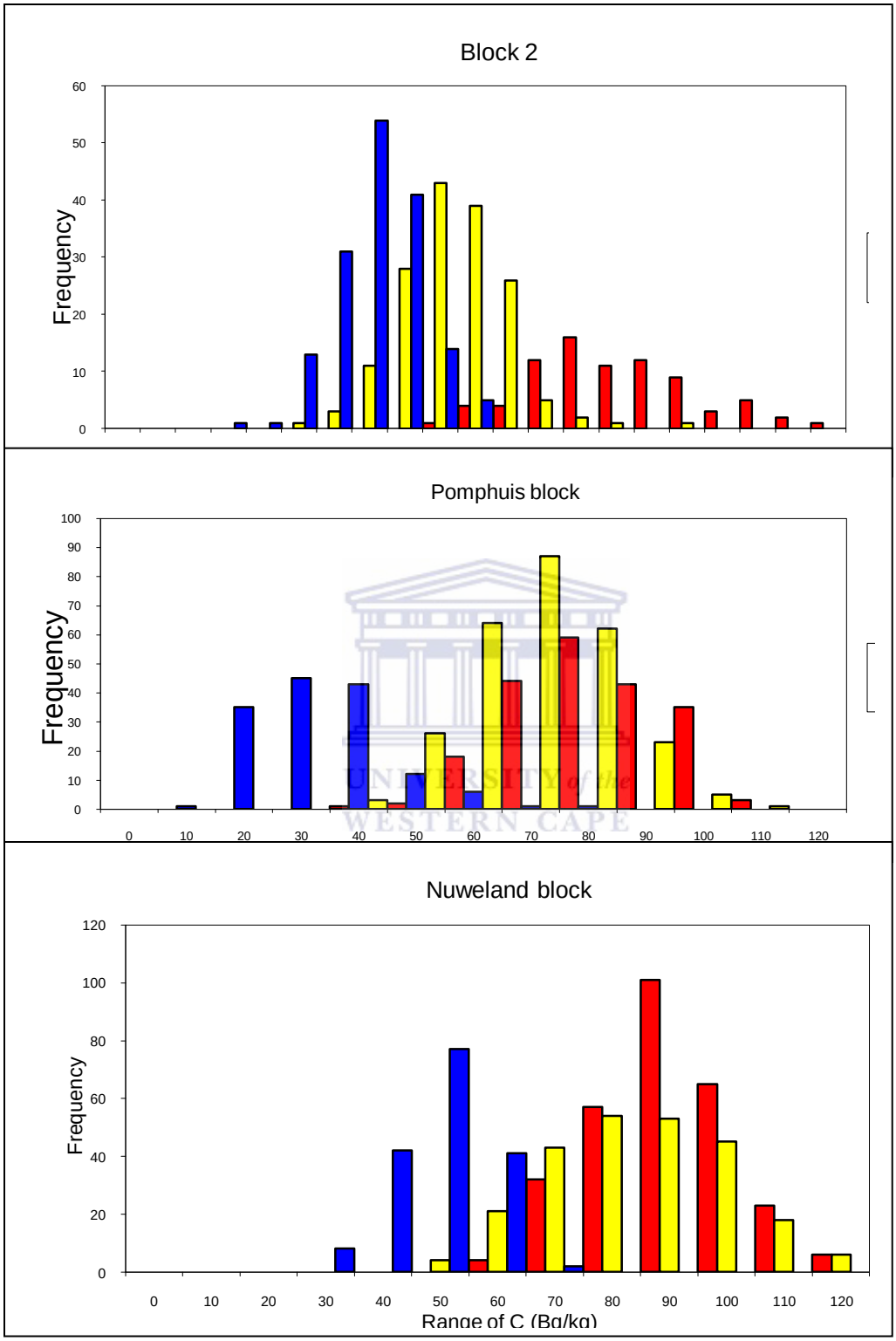

Figure 5-27: *Histograms showing the distribution of C for the sections in the three blocks. C is the linear combination of the U and Th as defined in eq. 5.1*

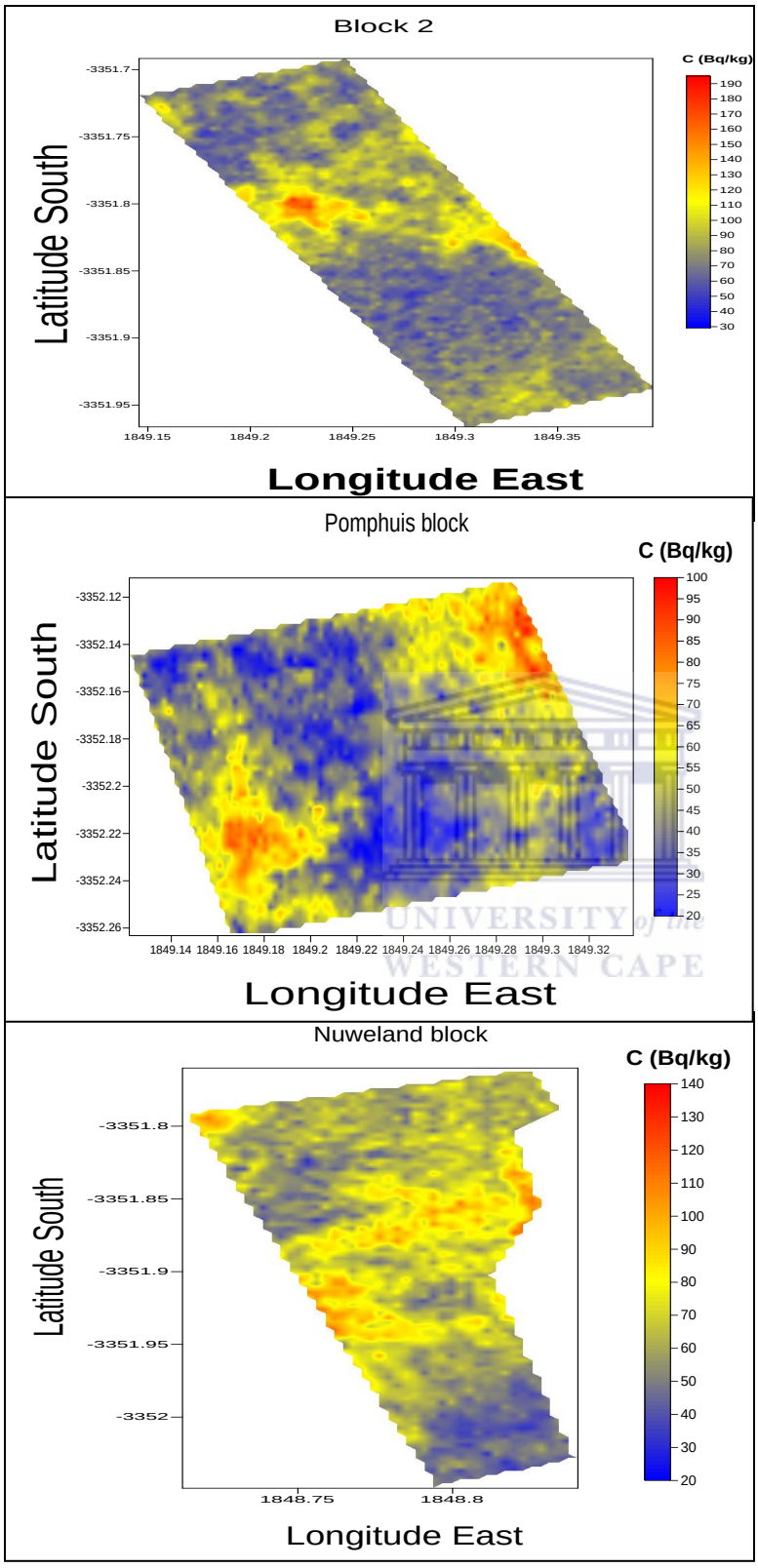

Figure 5-28: *Map showing the distribution of C in the three blocks.*

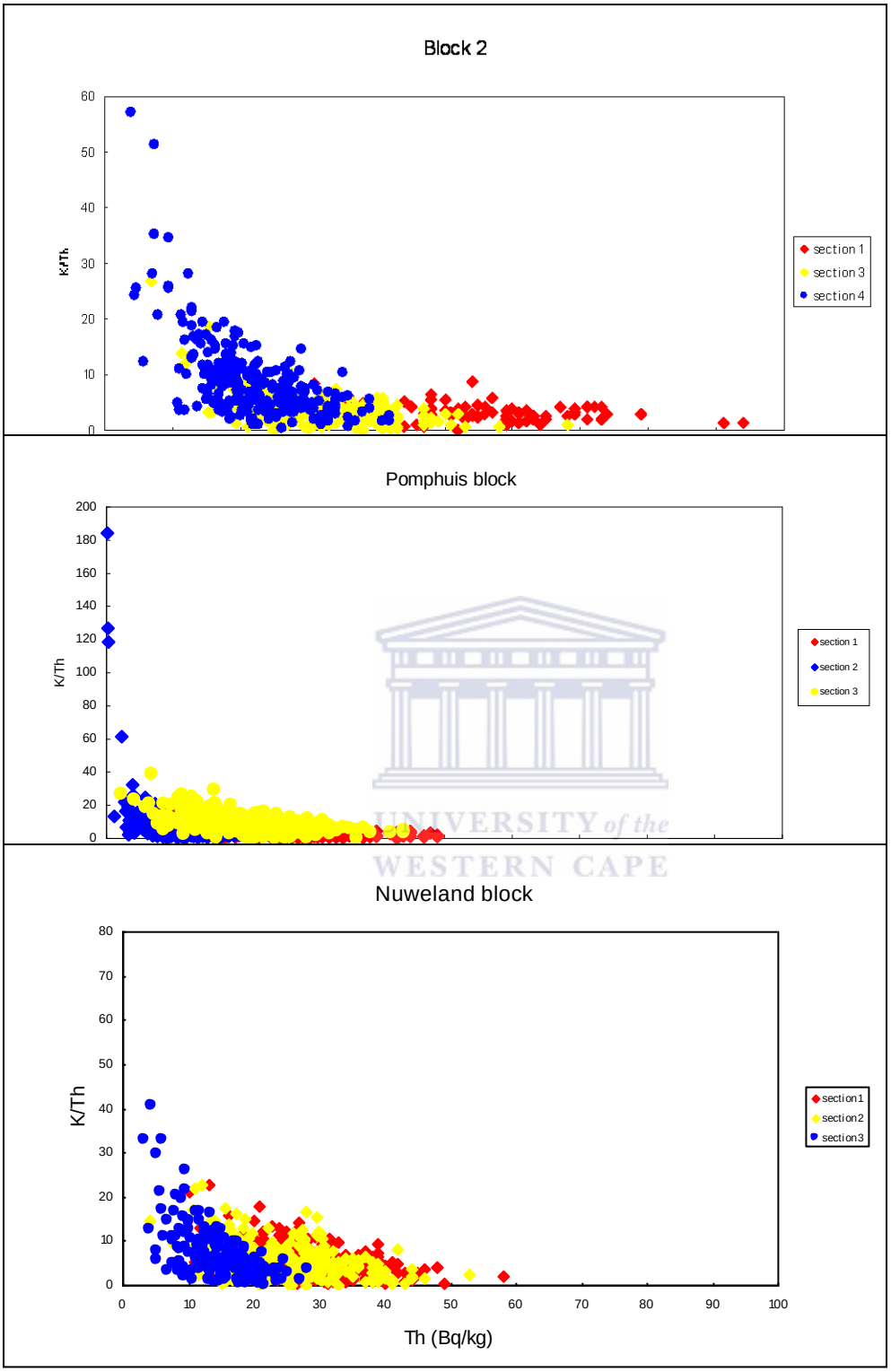

Figure 5-29: *Two dimensional plot of K/Th and Th AC showing the trend and classification of the data for the sections in the three blocks.*

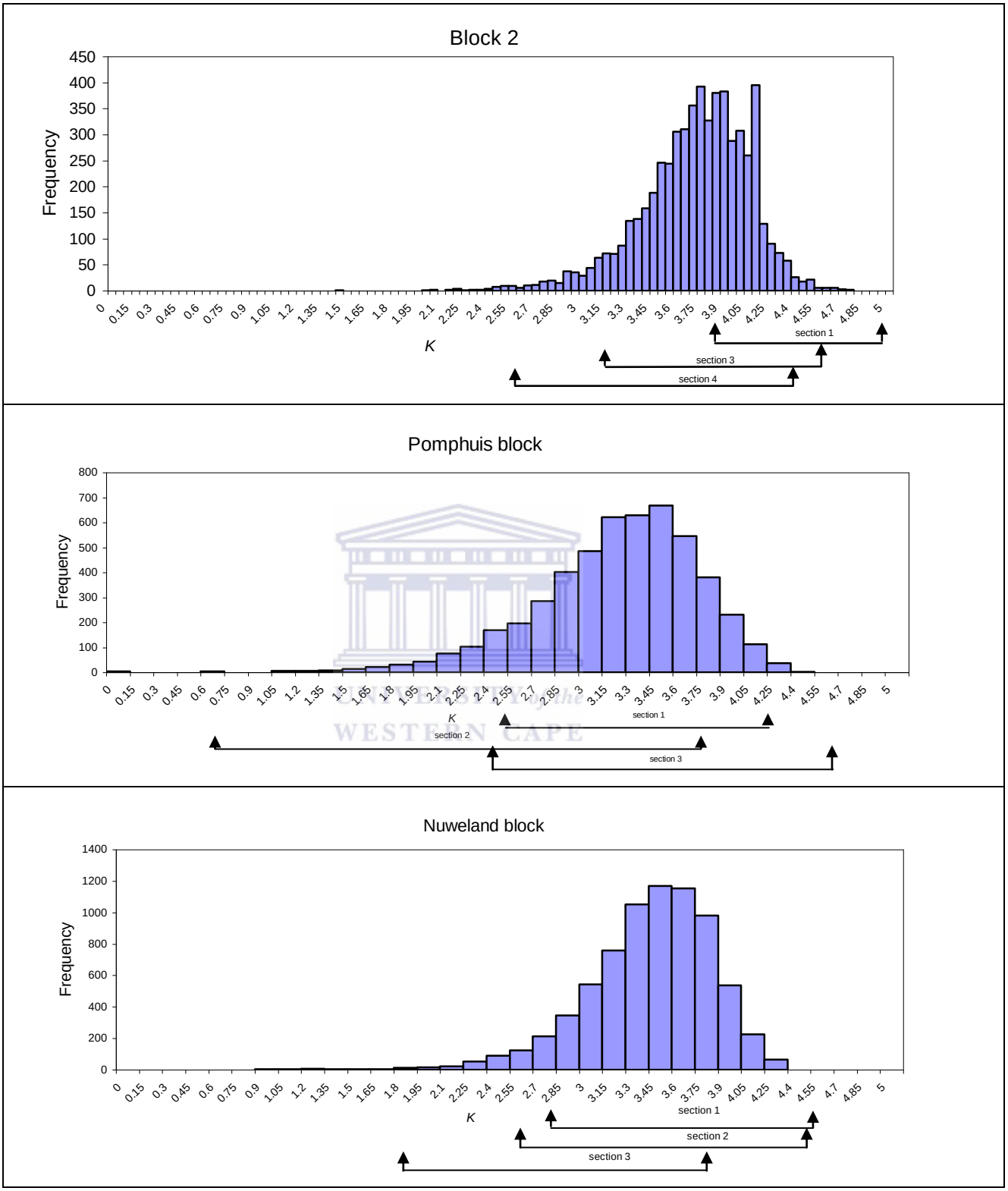

Figure 5-30: *Histogram showing the distribution of k for the entire block data. k is a constant for the combined distributions of the K and Th as defined in eq. 5.2.*

Since the maps showing the distribution of *C* for the three blocks in Figure 5-28 indicate large correspondence with the ^{232}Th AC, the ^{232}Th AC maps for the blocks were produced in the same scale and compared. Figure 5-31 shows the ^{232}Th AC maps in accordance to their location as described in Chapter 2, section 2.1. From the maps, it is clear that the blocks Pomphuis and Nuweland are composed of one sediment group (W_1) whereas Block 2 is composed of another group (W_2) in agreement with the sample results.

The analyses of the combined block sections shown in Figures 5-26 and 5-29 with their respective eqs. (5.1) and (5.2) are useful in identifying the number of sediment groups and assessing their distributions in the entire blocks as shown in Figure 5-28 and confirmed by Figure 5-31.

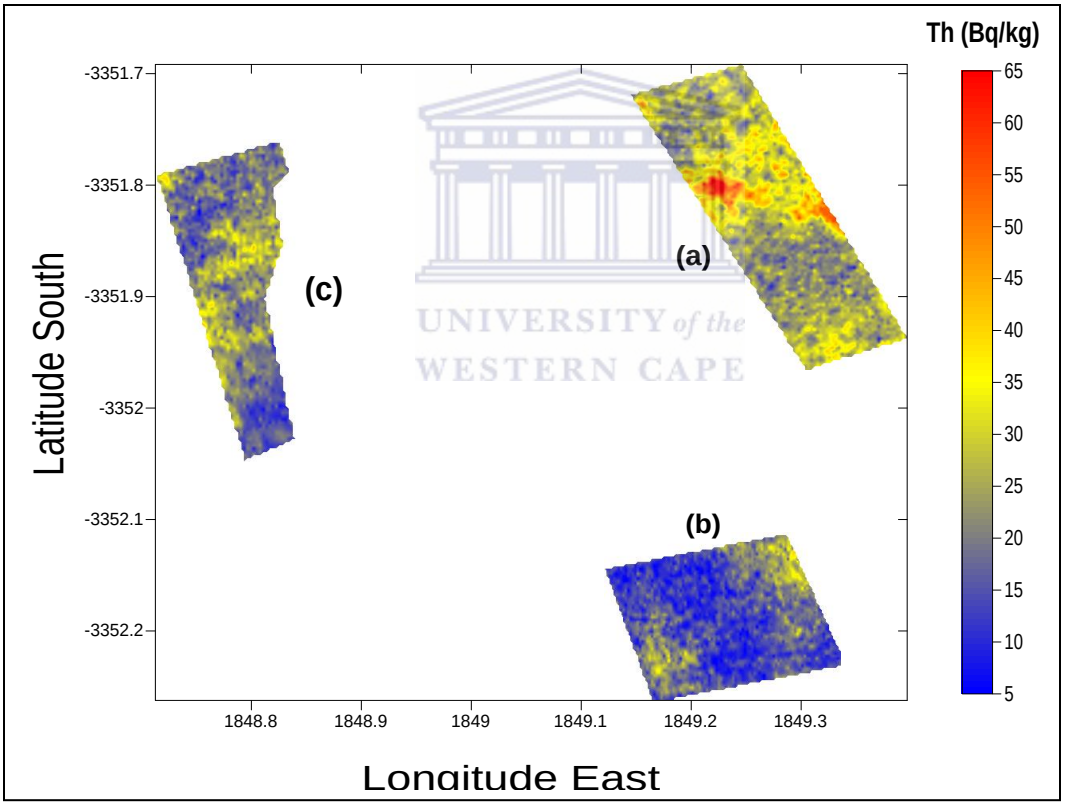

Figure 5-31: *^{232}Th AC maps for (a) Block 2 (b) Pomphuis block and (c) Nuweland block.*

5.5 Radiometric projections of physico-chemical data

In this section an approach to determine the intensity distributions of physico-chemical data in the three blocks is described. The approach involves projecting *in-situ* radiometric data onto physico-chemical data which were found to significantly correlate with radiometry as presented in Chapter 4, section 4.3.4.

To determine the physico-chemical data in a particular location of the block, the radiometric *W*-vector of the MEDUSA data has to first be calculated. In this work, the MEDUSA *W* values were determined by eqs. (4.1) and (4.4) with their respective fit parameters as presented in Chapter 4, section 4.1. The physico-chemical data of the blocks were then calculated from the relations of the correlation and best fits between W-radiometric and physico-chemical vectors presented in the Figures 4.13 to 4.16 (Chapter 4, section 4.3.4).

To assess the accuracy of the data projection method, projected-intensity maps of chemical data were used to determine concentrations at locations where samples were analyzed in the laboratory. Concentration value of chemical data at each location in the intensity map is determined from a mean value of ten points at that location. Tables 5-3 and 5-4 compare the concentrations of chemical data from the projected-field data and laboratory analyses. From the tables, results agree to within 50%, 55% and 35% for major elements, trace elements and exchangeable cations, respectively. Figure 5-32 shows the correlation between projected soil physico-chemical data and the measured samples. The results imply that the radiometric approach has a reasonable predictive power especially for exchangeable cations.

5.6 Summary

In this chapter, radiometric maps from data acquired in 2007 have been presented and compared to the re-analyzed data acquired earlier in 2002/2003. Investigation on the radionuclide distributions and correlations in the three blocks has been discussed in this chapter. Furthermore, the comparison of the trend and distribution of radionuclide ACs between field and laboratory-sample data presented in Chapter 4 has been discussed. The approach to assess the number of sediment groups using *in-situ* radiometric data has been described. The approach involves categorizing the blocks into sections based on high and

low ACs for ^{232}Th and ^{40}K. The analysis results have shown that the soils are basically composed of two sediment groups with their mixing component, consistent with the sample data presented in Chapter 4, section 4.1. The approach to project *in-situ* radiometric data onto soil physico-chemical data by using radiometric-laboratory results presented in chapter 4 has also been described in this chapter.

Table 5-3: Concentrations of projected chemical data (major elements, W^m and trace elements, W^t) from the interpolated maps and compared to soil samples from the corresponding locations and measured by XRF and ICP-MS.

	W^m (%)		W^t (mg/kg)	
Sampling point	XRF	Projected results	ICP-MS	Projected results
P18	8.5±1.9	10.3±0.3	290±54	448±9
P19C	3.3±1.6	6.5±0.3	243±53	339±7
P20	20±3	13.1±0.2	867±80	527±7
P21	20±3	16.7±0.5	643±67	629±13
P22C	3.2±1.7	6.5±0.2	157±52	339±6
P23	5.8±1.8	7.4±0.4	323±58	366±12
P24	3.7±1.7	6.6±0.2	220±55	344±4
P25	5.9±1.8	9.5±0.5	368±57	426±13
N17	18±3	13.1±0.2	937±94	528±6
N18	23±3	13.6±0.7	940±96	542±19
N19	14±2	13.77±0.12	613±72	425±8
N20	9.7±1.9	7.16±0.10	435±61	359±5
N21	12±2	8.7±0.3	544±66	402±8
N22	10.1±1.9	14.0±0.3	390±64	551±7
N23	11±2	10.9±0.8	515±64	464±22
N24	9.6±1.9	9.1±0.2	568±69	412±6

Table 5-4: Concentrations of projected chemical data (exchangeable cations, W^e) from the interpolated intensity maps and compared to soil samples from the corresponding locations and measured by ICP-OES.

Sampling point	ICP-OES (cmol(+)/kg)	Projected results
P1	15.0±1.1	11.9±0.3
P2	3.7±0.5	4.43±0.08
P4	6.4±0.6	5.83±0.09
P8	3.8±0.6	5.18±0.15
P11	6.1±0.6	7.7±0.5
P13	4.1±0.6	5.25±0.12
P16	4.3±0.6	6.52±0.14
P17	8.2±0.7	6.61±0.17
N1	11.7±0.8	10.1±0.3
N2	9.9±0.8	9.46±0.18
N5	5.6±0.6	4.91±0.04
N7	5.1±0.6	6.9±0.2
N8	9.1±0.7	9.2±0.3
N10	5.9±0.6	8.2±0.3
N13	6.5±0.6	7.45±0.18
N16	6.3±0.6	9.3±0.4

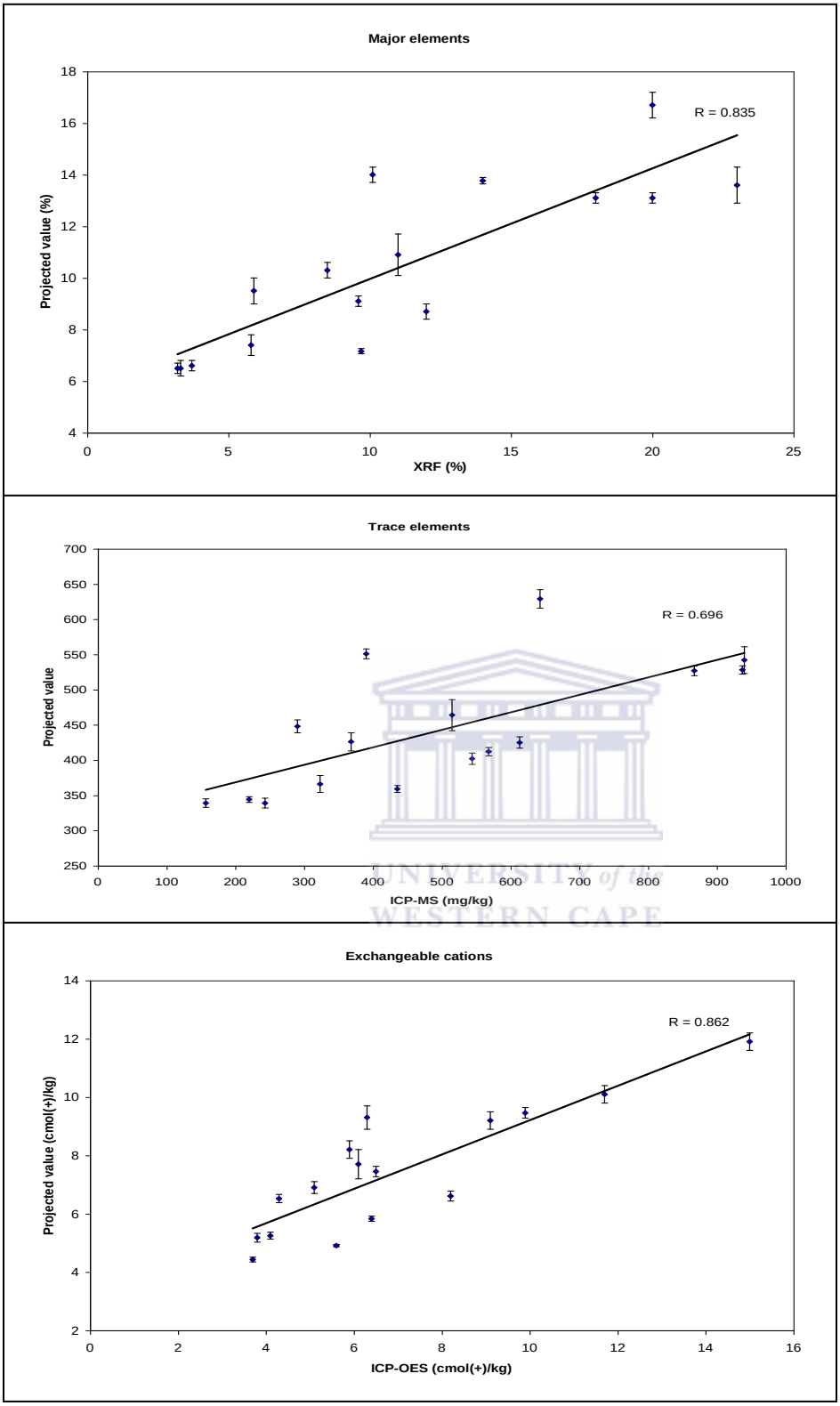

Figure 5-32: *Correlations between projected soil chemical data and measured soil samples. The major and trace elements are given in Table 5-3, whereas exchangeable cations are given in Table 5-4.*

CHAPTER 6 CONCLUSION

In this chapter a summary of the work done for this study is presented firstly. This is followed by the synopsis of important findings and results from this study. To conclude the chapter, suggestions for future further work are presented.

6.1 Summary of work done

As it was stated in Chapter 1, this study was motivated by the previous preliminary study on the search for correlations between soil natural radionuclide activity concentrations and vine growth potential [Mod05]. There is a worldwide growing interest in using *in-situ* radiometric techniques (which are rapid and cost effective of large areas) as alternatives to traditional methods of measurements in the fields of agriculture [Van08], geology, mining, environment etc. This study emerged with a specific focus on investigating the feasibility of using the radiometric technique (in particular γ-ray spectrometry) to determine soil physico-chemical parameters important for the vine growth and ultimately wine production. The aims and objectives of this study are stated in Chapter 1, section 1.4.

The radiometric-experimental approaches *via* laboratory-based (HPGe) and *in-situ* measurement (MEDUSA detector) techniques are detailed in Chapter 2, sections 2.2 and 2.4. Moreover, physico-chemical parameters of relevance in this study were analysed using the standard methods in the various laboratories listed in Chapter 2, section 2.4.

To summarize, the following work was carried out for this study:

- to minimize the effect of coincident summing on ^{232}Th and ^{238}U series activity concentrations measured for soil samples, the effect of using different γ-ray lines in the analyses was studied. An optimum set of lines to use for the analyses was established.
- the effect of different soil sample preparation regimes on the measured soil activity concentrations was studied.

- the MEDUSA data of Modisane (Pomphuis and Nuweland blocks) [Mod05] and Joseph (Block 2) [Jos07] were re-analysed using standard spectra and normalization factors obtained specifically for this study.
- for this study all the three blocks were re-mapped using a custom-designed trolley onto which the MEDUSA detector was mounted. (this was necessitated by the dense vine growth that precluded using a 4x4 vehicle).
- the three new MEDUSA data sets acquired were analysed using the same standard spectra used to analyse the Modisane and Joseph data sets. A new set of normalization factors for MEDUSA data was determined (see Chapter 5, section 5.1).
- the MEDUSA maps obtained were used to design a directed soil sampling strategy on the three blocks. The aim of this exercise was to study the correlations between the soil activity concentrations (^{40}K, ^{232}Th and ^{238}U series) and the soil physico-chemical properties. The activity concentrations in soil samples were measured by low-background high resolution γ-ray spectrometry. The soil physico-chemical properties were determined using, amongst others, XRF, XRD, ICP-OES, ICP-MS. The XRF, ICP-OES and ICP-MS analyses were made at laboratories external to iThemba LABS.
- grapes from two areas of Block 2 showing significant differences in soil activity concentrations and physico-chemical parameters, were sampled for chemical analyses and for making wine. The wine was also analysed for chemical content.

6.2 Summary of main outcomes and findings

6.2.1 Radiometric data from the samples

The activity concentrations of ^{40}K, ^{232}Th series radionuclides and ^{238}U series radionuclides for samples in the three blocks were determined. The AC values of ^{40}K, ^{232}Th series and ^{238}U series range from 127 to 227 Bq/kg, 28 to 111 Bq/kg and 28 to 68 Bq/kg for Block 2, respectively. For the Pomphuis block, the values range from 29 to 288 Bq/kg, 11 to 55 Bq/kg and 11 to 68 Bq/kg, for ^{40}K, ^{232}Th series and ^{238}U series, respectively. As for the Nuweland blocks, the values range from 62 to 315 Bq/kg, 14 to 57 Bq/kg and 17 to 47 Bq/kg for ^{40}K, ^{232}Th series and ^{238}U series, respectively.

From these results, various correlations between the ^{40}K, ^{232}Th series and ^{238}U series ACs were investigated, leading to the identification of two sediment groups, Pomphuis/Nuweland (W_1) and Block 2 (W_2). This categorization was based on the fact that the blocks Pomphuis and Nuweland have the same U/Th ratio (see Chapter 4, section 4.1). In each identified sediment group, the ACs of the three radionuclides (^{40}K, ^{232}Th series and ^{238}U series) are determined to be fully dependent, thus were reduced to one new radiometric-eigenvector, W using the models described in Chapter 4 equations (4.1) and (4.4). The W values for the three blocks are presented in Table 4-5 (Chapter 4, section 4.1).

The two sediment groups are characterized by the variable intensity *P* determined from the W values using eqs. 4.5 and 4.6 (see Chapter 4, section 4.2). Before comparing physico-chemical parameters in the groups, the quality of data was investigated, see Chapter 4, section 4.3.1. The comparison of soil physico-chemical parameters within (hot and cold spots) and between the groups (Pomphuis/Nuweland and Block 2) showed significant variations as discussed in Chapter 4, section 4.3.2. The variations observed motivated a detailed correlation analysis to establish the link between radiometry and soil physico-chemical parameters. However, similar comparison for grape and wine samples as presented in Chapter 4, section 4.3.2 did not show any significant differences contrary to the soil results, implying that the chemical composition of the wine is not clearly linked to soil chemical properties. Measurements to link the chemistry of the soil and the radiometric signal to the chemistry of the grapes and wine is inconclusive at this stage due to the limited number of samples studied.

In view of the correlation results, a relation between K_2O% versus ^{40}K was derived from the good qualitative correlation and best fit (K_2O% versus ^{40}K), with a χ_v^2 of 14. It was found that 1% K_2O corresponds to 306 Bq/kg, leading to an absolute deviation of 17% as compared to the theoretical relation (1% K_2O corresponds to 257 Bq/kg). The likely reason for the deviation is systematic effect associated with XRF measurements especially at ^{40}K ACs above 250 Bq/kg as shown in Figure 4-6 (Chapter 4). For radiometry, ^{40}K analysis was validated using the IAEA standard reference soil and was found to agree within a 95% confidence interval (see Chapter 3, section 3.2.1).

The relation of ^{40}K and leachable K was also derived from the correlation and best fit between ^{40}K and leachable K. The amount of plant available potassium was determined to be (7.0±0.3)%. This value is in agreement with the values published in the literature (0-10%) [Mca09, Sch09, Tho09]. This information is very important to the farmers due to its role in the vine growth. The establishment of this relation is a valuable result which can be used to estimate concentrations of K trace element from ^{40}K AC.

The correlation between the radiometric W-vector and physico-chemical parameters were found as presented in Chapter 4, section 4.3.4 and Appendix 2. From the correlations, the chemical data of relevance in this case (presented in Appendix 2) were reduced to determine the chemical W-vector using a similar approach and models to the radiometric-data treatment. Finding significant correlations addresses the key research questions of this study. The correlation between radiometric W-vector versus major elements K and Al is most likely linked with the mineral muscovite, which also shows significant variation with the radiometric W-vector (see Chapter 4, Figures 4-11 and 4-12). K and Al elements are major components of the mineral muscovite comprising 10% and 20% by mass, respectively.

Comparison of the results of the physico-chemical data in the blocks Pomphuis and Nuweland with the previous work by the Department of Agriculture [Nuw03, Pom03] is presented in Appendix 3.

An important result from the sample-analysis results is their application in determining the physico-chemical data in the blocks *via* the correlation fit parameters and *in-situ* MEDUSA data (see section 6.1.2). Since the radiometry results presented in Table 4-1 (Chapter 4) and soil physico-chemical data presented in Tables A2-4 and A2-5 (Appendix 2) do not show significant variations between 0-30 cm and 30-60 cm soil depths, the results from this study are deemed reliable for 0-60 cm soil depth.

6.2.2 Radiometric data from *in-situ* measurements

Radiometric maps (TC, ^{40}K, ^{232}Th series and ^{238}U series) from data acquired in 2002/2003 and 2007 were produced. For the two sets of data, the maps indicate significant variations mainly in the distribution of the Total Count rate (TC) and activity concentration ^{232}Th AC. In addition, the maps indicate the robustness of data-collecting

technology over a period of up to five years as presented in Chapter 5, section 5.2. The two sets of results also imply that the contribution of fertilizers used to radioactivity levels in the vineyard blocks is not significant. The distributions of ^{40}K, ^{232}Th series and ^{238}U series ACs as histograms in the blocks were investigated. It was found that the blocks Pomphuis and Nuweland have an almost similar distribution pattern as opposed to Block 2, leading to the same conclusion reached in sample data, that the two blocks are composed of one sediment group.

To further investigate the sediment groups in the blocks, the block maps were categorized into sections characterized by high and low ACs of ^{232}Th and ^{40}K as presented and discussed in Chapter 5, section 5.4. Again, the combined block-section analyses revealed that Pomphuis and Nuweland blocks are composed of one sediment group in agreement with our earlier results. The combined block-section analyses presented in Figures 5-26 and 5-29 (Chapter 5) show the usefulness of the approach in classifying the number of sediment groups leading to proper identification of dominant soil types, and eventually their distributions in the entire blocks as shown in Figure 5-28. The correlation fit parameters obtained from the derivation of the new radiometric eigenvector (W) in Chapter 4 (section 4.1) are used in projecting *in-situ* radiometric MEDUSA data onto physico-chemical data using correlation fit parameters between the radiometric W-vector and the chemical W-vector. Comparing the results of chemical parameters from the projected-intensity maps and laboratory analyses showed agreement to within 50%, 55% and 35% for major elements, trace elements and exchangeable cations, respectively. This implies that the radiometric approach has a better predictive power for exchangeable cations than for major and trace elements. This can guide farmers as it gives information which is directly applicable to daily vineyard management, since it provides reliable data on how certain important elements are distributed in the vineyards (at 0-60 cm depth) leading to informed management-decisions being made.

As was stated in Chapter 1, the main scope of this study is to investigate whether radiometry can be used as a predictor of soil properties adding to the *terroir* of wines. From this study, significant correlations between radiometric data and exchangeable cations, major and trace elements were found. For both groups

(Pomphuis/Nuweland and Block 2), radiometric data were found to significantly correlate with major elements MgO, TiO and K_2O (see Appendix 2, Table A2-8). As far as trace elements are concerned, radiometric data were found to significantly correlate with Li, K and Se as shown in Table A2-9, Appendix 2, whereas radiometric data correlate significantly with exchangeable cations Na and Mg for both groups. On the other hand, radiometric data were also found to significantly and positively correlate with clay while correlate negatively with sand (see Appendix 2, Table A2-10).

Based on the aims of this study as stated in Chapter 1, the following conclusions are drawn:

- optimum set of γ-ray lines associated with ^{232}Th and ^{238}U series are established and used in the analysis presented in this study. Details of the lines are as presented in Chapter 3, section 3.2.2 and Appendix 1, section A1.5.
- The potential systematic effects associated with soil-sample preparation methods are investigated (Appendix 1, section A1.3). Sample drying and sealing are found to be potential sources of systematic effects associated with soil sample preparations. The effect of sample drying to the activity concentration of ^{40}K, ^{232}Th series and ^{238}U are 13%, 13% and 12%, respectively. Sample sealing is found to significantly affect ^{238}U series activity concentration by 18%.
- the radiometric data indicate large differences within the blocks and between the blocks. This led to the conclusion that the vineyard soils in the three blocks are composed of two radiometric sediment groups (Pomphuis/Nuweland and Block 2) with a mixing component.
- there are significant correlations between radiometric data and some soil physico-chemical properties as presented in Appendix 2, Tables A2-8 to A2-10.
- soil primordial activity concentrations (for a depth of 30 cm) in the three blocks over a period of about five years do not indicate significant variation. Furthermore, the blocks show a similar distribution pattern of activity concentrations.

- The preliminary assessment to link the observed differences in soil physico-chemical properties with grapes and wine is inconclusive due to the limited number of samples analysed.

6.3 Suggested future work

This study has shown that the radiometric signal can be used to characterize vineyard soil. To expand this work, the link found between the correlation of radiometric data and soil physico-chemical parameters can be investigated. Since the assessment of grape yield and quality is inconclusive in this study, the characterization of soil presented in this thesis can be studied further to look for links with yield and quality.

Further investigation on the normalization factors is recommended to improve the interpolated MEDUSA results as presented in Appendix 1, section A1.6. This will improve the results since the normalization factors at hotspots are mostly found to significantly deviate.

APPENDICES

APPENDIX 1

Radiometric measurements and analysis

A1.1 HPGe spectrum

Figure A1-1 shows the HPGe γ-ray spectrum for soil sample (P19) which was used for the calibration of the MEDUSA detector trolley set-up as described in Chapter 2, section 2.2.3. From the spectra, the numbers 1 to 18 refer to prominent γ-ray lines detected (see Table A1-1 below).

Table A1-1: Prominent γ-ray lines [Fir96] detected in the HPGe spectra of soil sample (see Figure A1-1).

Series/radionuclide	Identification number	Energy (MeV)
^{238}U		
	1	0.186
	3	0.295
	5	0.352
	7	0.609
	12	1.001
	13	1.120
	14	1.238
	15	1.378
	17	1.764
	18	2.204
^{232}Th		
	2	0.238
	4	0.338
	6	0.583
	8	0.727
	9	0.860
	10	0.911
	11	0.969
^{40}K	16	1.461

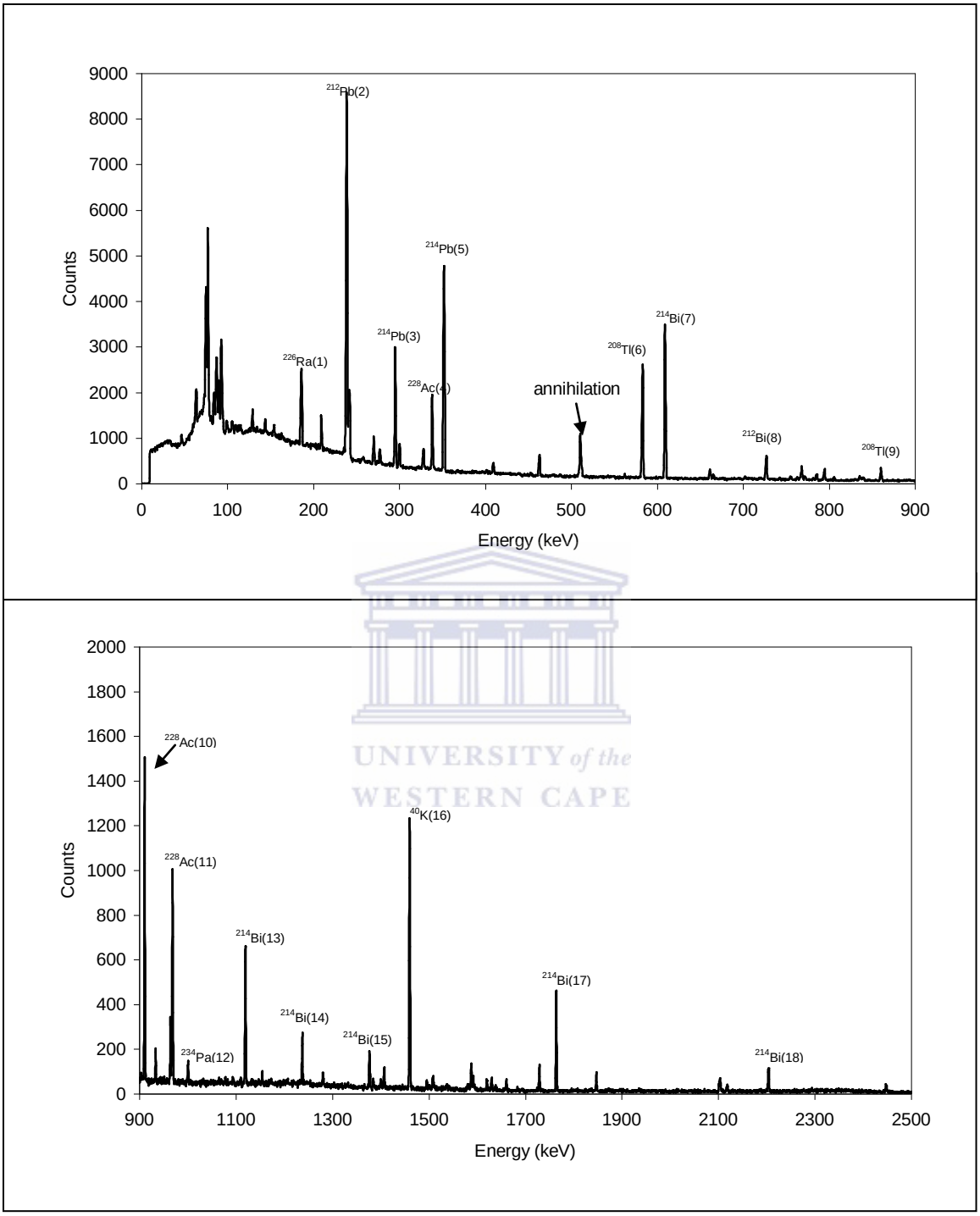

Figure A1-1: *The ERL HPGe spectrum (0-2500 keV) of soil a sample (P19) showing γ-ray energy peaks associated with the decay of ^{40}K and the ^{232}Th and ^{238}U series radionuclides. The spectrum was acquired over 20 hours.*

A1.2 Normalization factors

The normalization factors (see Chapter 2, section 2.2.3) used for producing radiometric maps from data acquired in 2002/2003 were obtained from the calibration measurements using the 4×4 set-up configuration shown in Figure 2-4a (Chapter 2, section 2.2.3). In this case, four accessible points of the iThemba LABS ground with approximate flat-bed geometry were used for the calibration measurements. The calibration spots at this site with their coordinates are presented in Table 1A-1. As for the calibration measurements with the trolley set-up, five soil samples were taken at 0-30 cm depth from each location directly beneath the detector for HPGe measurements as per sampling plan shown in Figure 2-7 (Chapter 2). Table A1-2 presents the normalization factors used for producing radiometric maps from data acquired in 2002/2003 by using the FSA method. An example of the FSA fit is shown in Figure A1-2 below. From the table, the large χ_v^2 values indicate that there is significant variation of the value from one spot to the other. The most likely reason is local variations due to factors like soil moisture, organic matter, grass coverage, depth profiles, stones and rocks and radon exhalation. Further investigation is needed on the normalization factors.

Table 1A-2: Normalization factors (NF) for ^{40}K, ^{232}Th series and ^{238}U series radionuclides obtained from the FSA method. The quoted uncertainties are the external uncertainties.

Calibration spot	Coordinates		Normalization factors		
	Latitude (South)	Longitude (East)	^{40}K	^{232}Th	^{238}U
CS1	34˚01.436’	18˚43.036’	0.203±0.003	0.221±0.004	0.168±0.006
CS2	34˚01.509’	18˚43.150’	0.266±0.003	0.279±0.004	0.272±0.004
CS3	34˚01.418’	18˚43.068’	0.241±0.006	0.265±0.008	0.23±0.03
CS4	34˚01.430’	18˚42.980’	0.220±0.003	0.295±0.004	0.184±0.004
Weighted Av. (A_w)			**0.230±0.015**	**0.266±0.018**	**0.22±0.03**
χ_v^2			77	63	116

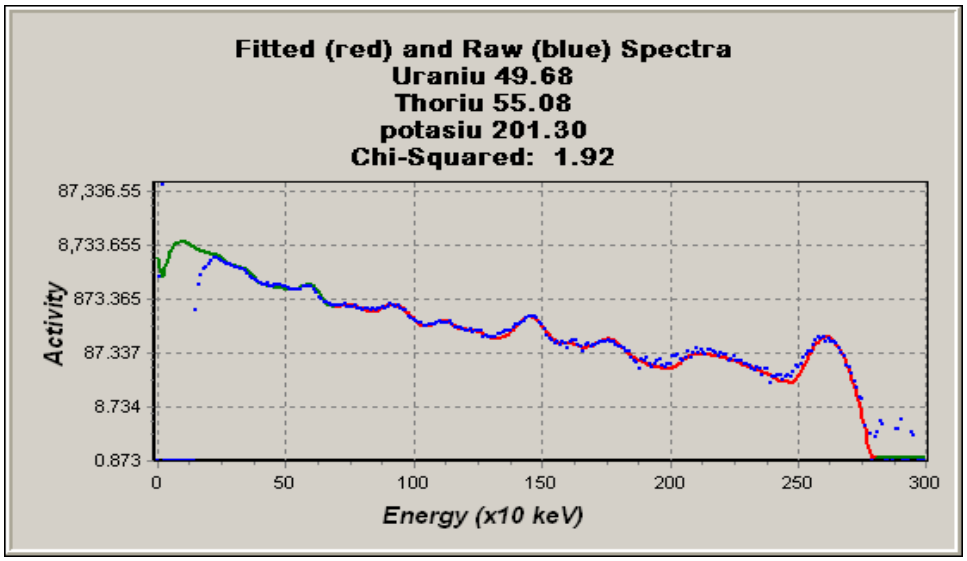

Figure A1-2: *FSA fit for the calibration spot CS1(see Table A1-1) obtained from the procedure described in Chapter 3, section 3.1.2.*

A1.3 Systematic effects associated with sample preparations

To investigate the systematic effects associated with the soil sample preparation, a sample collected at B2 (ground and sieved) was used to investigate the effects of sealing, drying and coning and quartering. Figure A1-3 shows the effects associated with each of the preparation procedures. From the Figure, ^{238}U activity concentration in the sealed sample is determined to be higher than the unsealed one by 12 %. The activity concentrations of ^{40}K, ^{232}Th series and ^{238}U series in the dried sample (sealed) are found to be higher than undried sample (sealed) by 13%, 13% and 18%, respectively. The ^{238}U series activity concentration in the coned and quartered sample (sealed) was found to be higher than the sample which was not coned and quartered (sealed) by 2%, whereas no significant difference was observed for ^{40}K and ^{232}Th ACs.

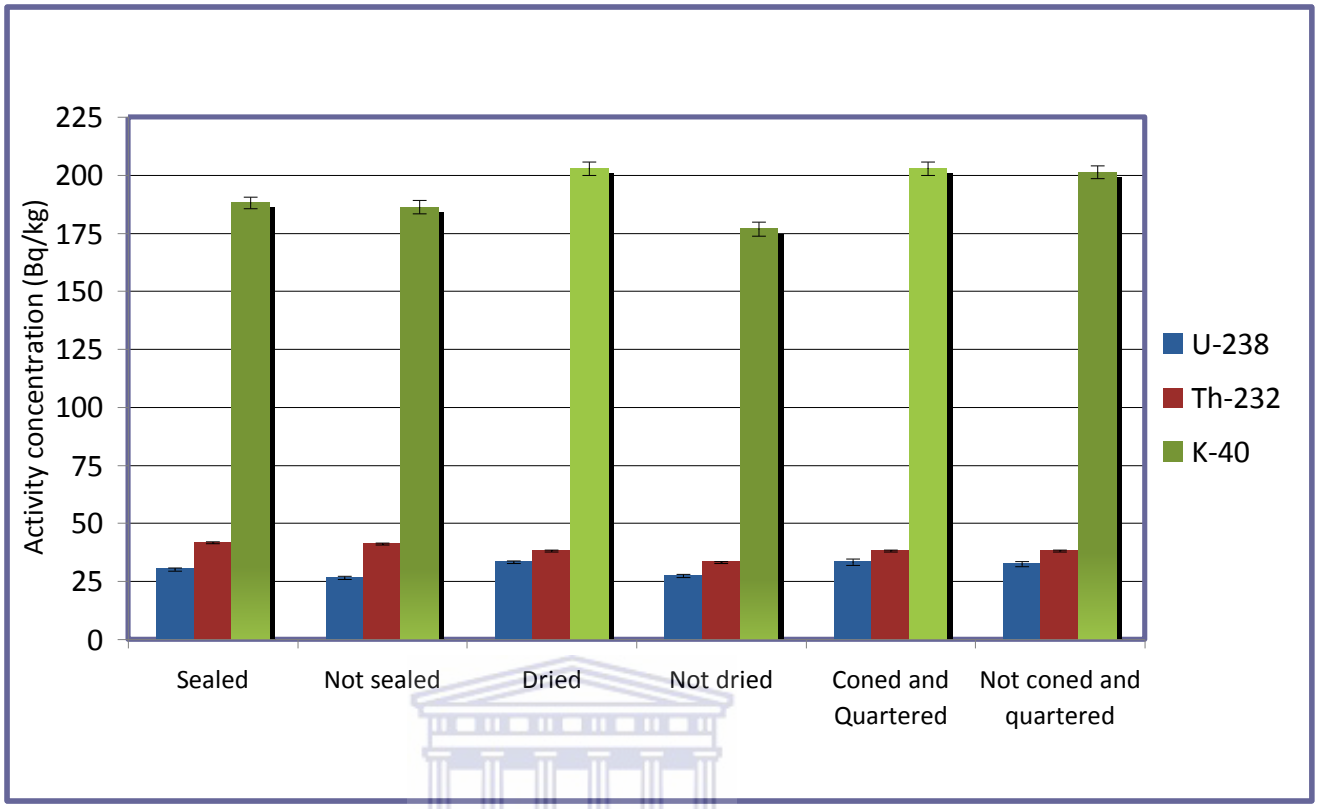

Figure A1-3: *Effects of sample drying, sealing, coning and quartering on the activity concentration determination. The sample (B2) used was collected from Block 2 (see Chapter 2, Figure 2-11).*

A silicone sealant (Bostik Bath type) was used to seal the Marinelli beakers to prevent the escape of radon (generated by ^{226}Ra present in the soil). The contribution of the sealant to the background was studied. To investigate the silicone sealant, three separate measurements were carried out starting with an empty plastic container (100 cm^3 medium sample vial), followed by tap water and finally silicone sealant using the same geometry at a preset time of 24 hours for each measurement. Figure A1-4 compares the superimposed spectra for plastic container, tap water and silicone sealant. From the figure, one notices that silicone sealant has no noticeable radioactivity contribution relative to the background spectrum.

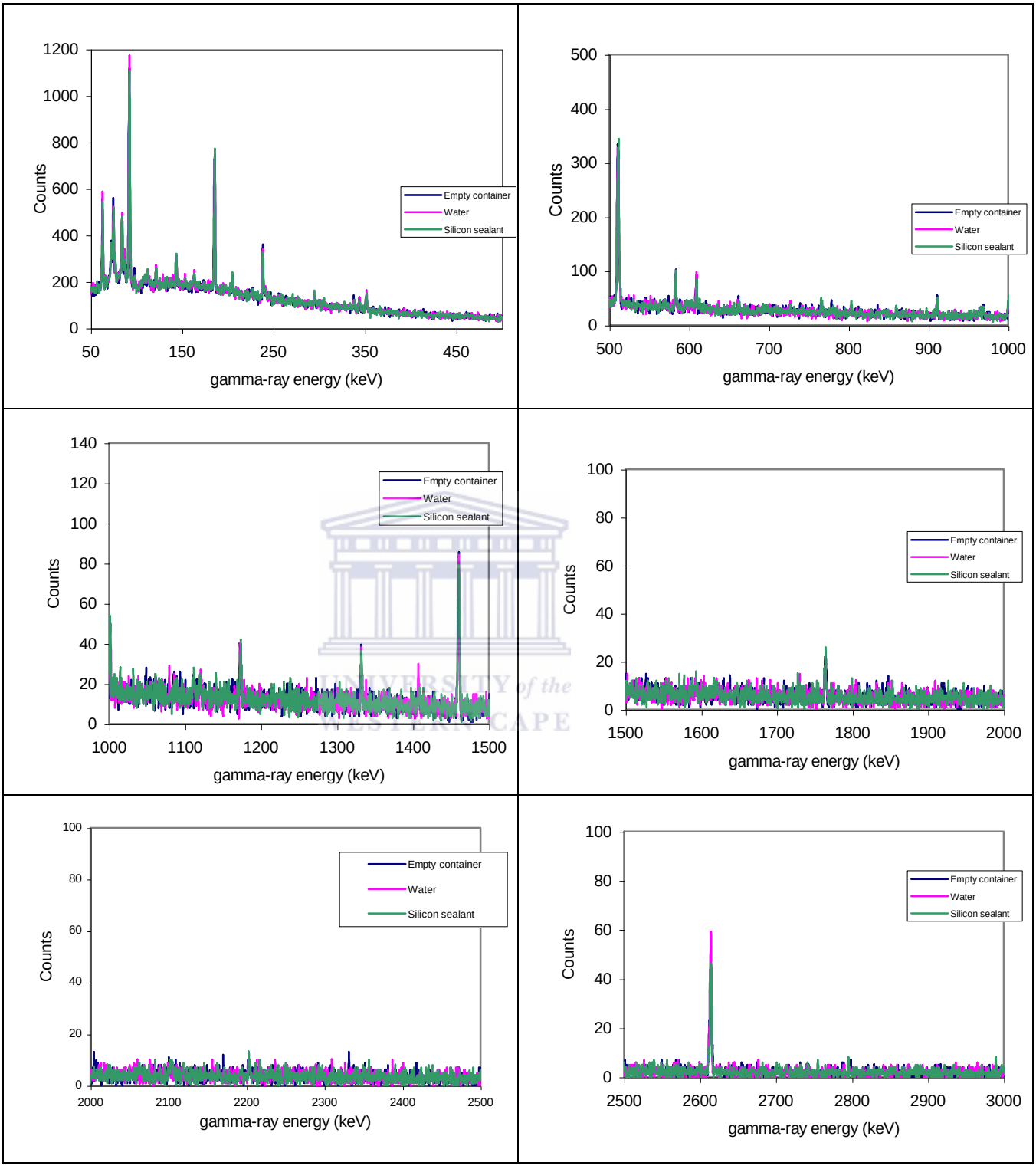

Figure A1-4: *Superimposed HPGe spectra for an empty plastic container (sample vial), container filled with 100 cm^3 water and container filled with silicone sealant. The measurement time associated with each spectrum was 24 hours.*

A1.4 Radon buildup

To verify the in-growth period and that radioactive secular equilibrium between ^{226}Ra and its daughters is achieved for soil samples, a sample N13 was investigated. Eight measurements were performed after every three days starting immediately after sealing. The measurement time was between 48 097s and 235 487s.

Gamma-ray lines of ^{214}Pb and ^{214}Bi (daughter products of ^{222}Rn) presented in Chapter 3, Table 3-2, were used to determine the average activity concentration of ^{214}Pb and ^{214}Bi. Figure A1-5 indicates the in-growth of radon daughters (^{214}Pb and ^{214}Bi). The concentrations increase with time until they become equal at around the 19th day, implying achievement of secular equilibrium. As expected, the activity concentration of ^{226}Ra (29±3 Bq/kg) was found to be consistent with the result of the 8th measurement.

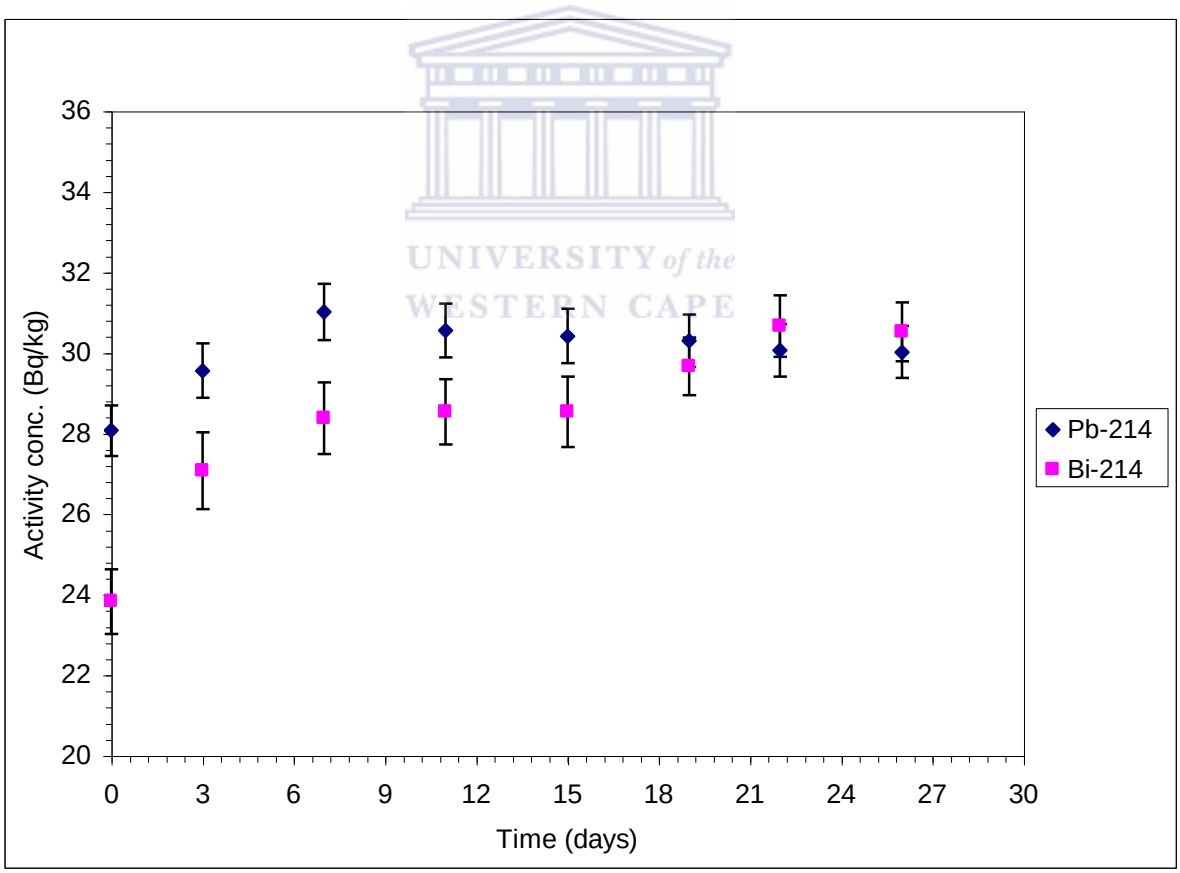

Figure A1-5: *In-growth of radon daughters (^{214}Pb and ^{214}Bi) for soil sample N13. The time (x-axis) refers to the time after sealing.*

A1.5 Spectral lines selection for the analysis

To select energy lines for spectral analysis, a sensitivity analysis of prominent γ-lines was first carried out. Figure A1-6 shows significant deviation of some prominent lines from the mean activity concentrations. From the figure, the numbers 1 to 18 refer to γ-ray energies as indicated in Table A1-3.

The prominent lines such as 0.609, 1.120 MeV (^{238}U series) and 0.583, 0.727, 0.795 MeV (^{232}Th series) were found to significantly deviate from the mean value due to coincident summing [Jos07, New08].

Table A1-3: Prominent γ-ray lines used for sensitivity analysis to select specific lines for spectral analysis (see Figure A1-6).

Series/radionuclide	Identification number	Energy (MeV)
^{238}U		
	13	0.295
	14	0.352
	15	0.609
	16	0.934
	9	1.001
	17	1.120
	18	1.238
	10	1.378
	11	1.764
	12	2.204
^{232}Th		
	1	0.238
	2	0.338
	3	0.583
	4	0.727
	5	0.795
	6	0.860
	7	0.911
	8	0.969

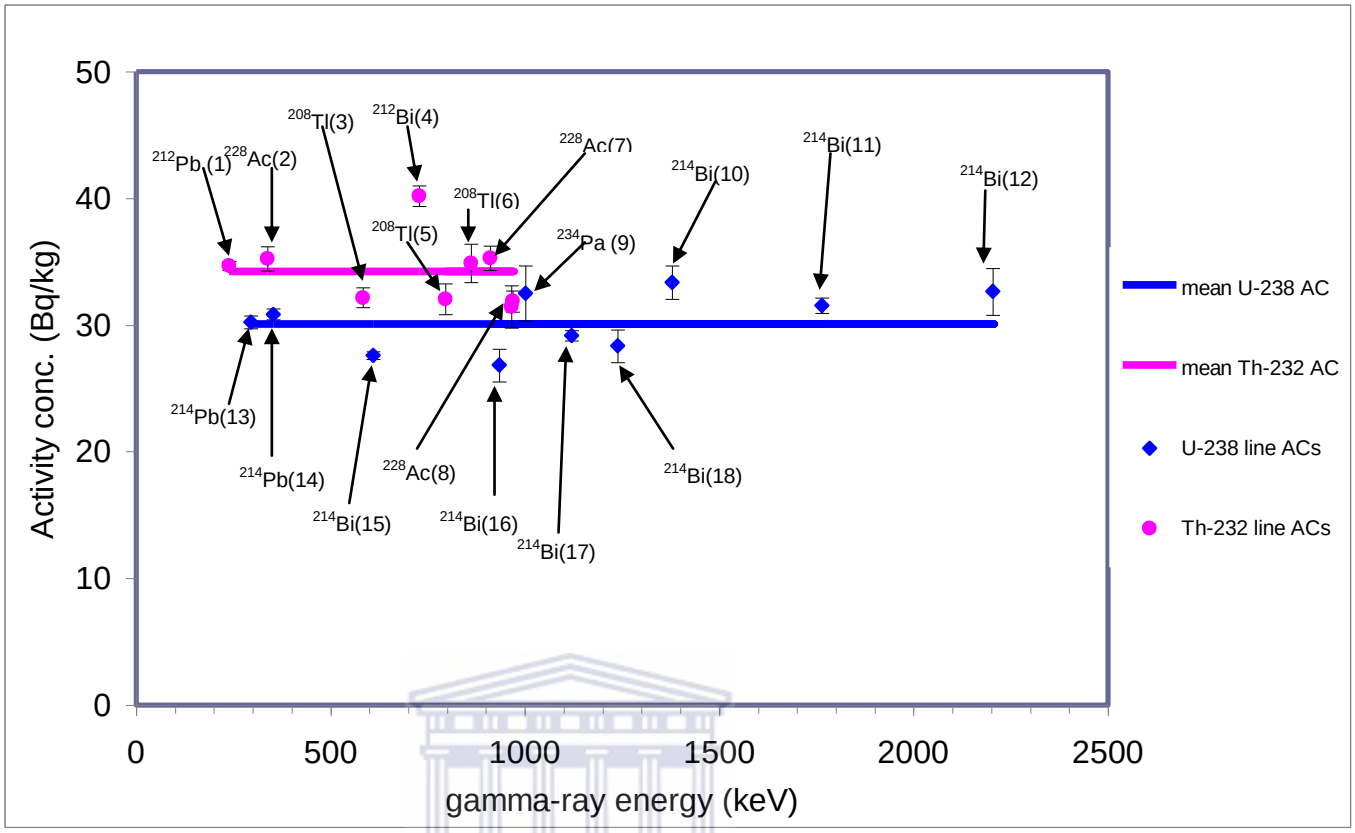

Figure A1-6: *Sensitivity analysis showing significant deviation of 609.3 keV, 583.2 keV and 727.3 keV lines from the mean activity concentration of soil sample N13.*

A1.6 Assessment of the interpolation technique

To assess the representativeness of the interpolations, the maps were used to determine ACs at locations where samples were analyzed in the laboratory (see Chapter 2, Figure 2-12). Activity concentrations from the interpolated MEDUSA maps at the locations of samples are determined from mean values of ten points at each location. The results obtained are given in Table A1-4 and presented in Figure A1-7. From the table, the results agree very well in the case of ^{40}K (< 5 %) and reasonably well for the ^{232}Th series and ^{238}U series.

Table A1-4: The activity concentrations (Bq/kg) of natural radionuclides in vineyard soil samples measured by HPGe detector and compared to interpolated activity concentrations determined from MEDUSA measurements at corresponding locations.

Sampling location	HPGe ACs (Bq/kg)			MEDUSA ACs (Bq/kg)		
	^{40}K	^{232}Th	^{238}U	^{40}K	^{232}Th	^{238}U
B1	168±3	32.6±0.5	33.0±1.1	160±40	25±3	26±5
B4	221±3	110.0±1.2	62±2	230±30	70±10	41±6
B6	139±2	44.6±0.5	35.2±0.9	143±12	45±7	33±4
B8	161±2	37.5±0.5	35.0±1.3	160±20	28±5	32±4

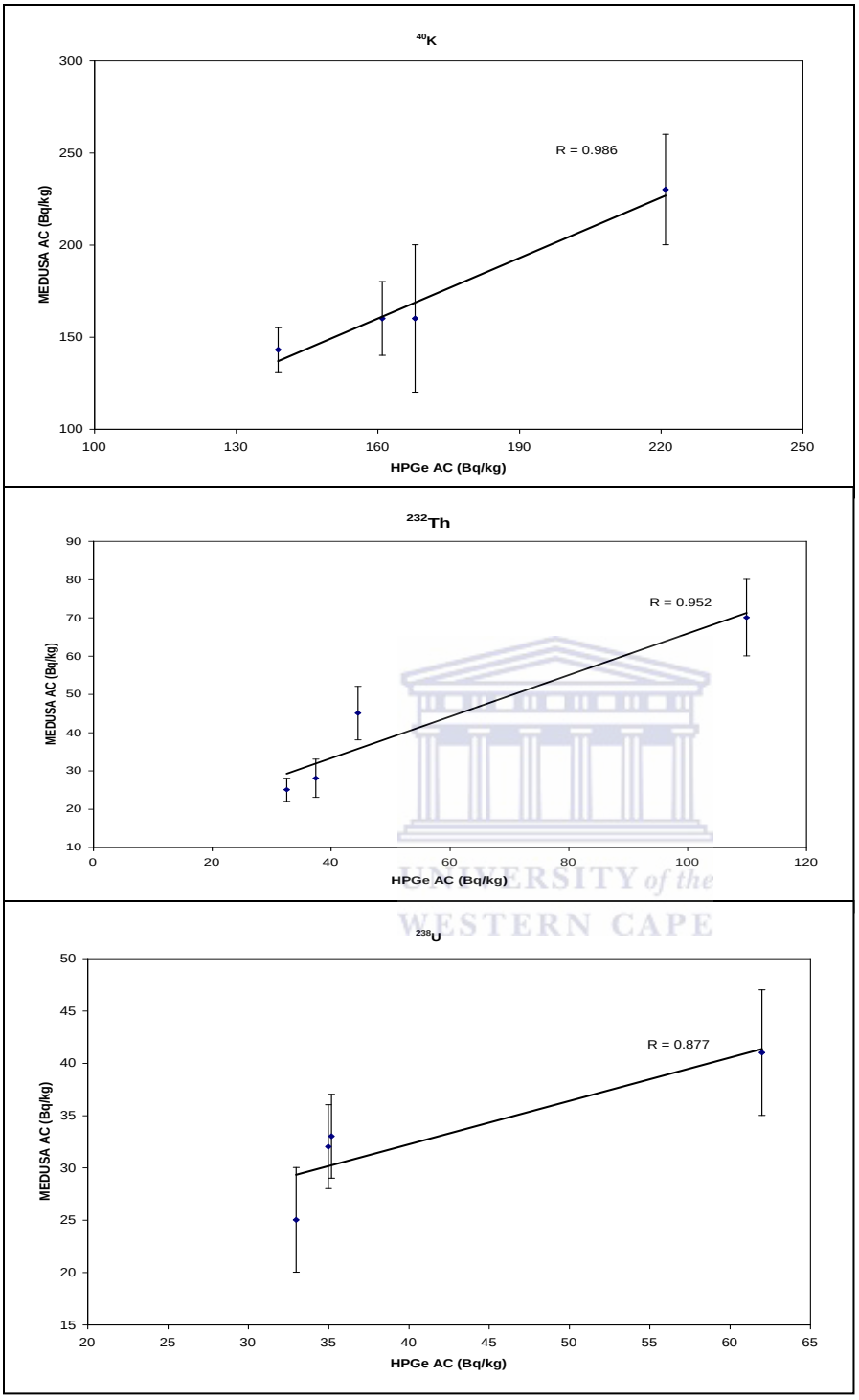

Figure A1-7: *Correlation between MEDUSA and HPGe ACs for ^{40}K, ^{232}Th and ^{238}U series radionuclides. The data are given in Table A1-4.*

A1.7 Calculation of the weighted average

For the variable data x_i with uncertainties σ_{xi}, the weighted average (A_w) is given by [Deb01];

$$A_W = \sum_{i=1}^{N}\left(\frac{x_i}{\sigma_{xi}^2}\right) \Big/ \sum_{i=1}^{N}\left(\frac{1}{\sigma_{xi}^2}\right) \tag{A1.1}$$

The internal uncertainty (S_{int}) in the weighted average is determined by:

$$S_{\text{int}} = \frac{1}{\sqrt{\sum_{i=1}^{N}\frac{1}{\sigma_{xi}^2}}} \tag{A1.2}$$

The external uncertainty (S_{ext}) in the weighted average is given by:

$$S_{ext} = \sqrt{\chi_\nu^2}.S_{\text{int}} \tag{A1.3}$$

A1.8 MEDUSA detector response to temperature variation

To test the temperature stability of the MEDUSA crystal (CsI(Na)), the detector was mounted on the trolley as shown in Chapter 2, Figure 2-4(b). The system was placed at one location (34˚01.484' S and 18˚42.959' E) of the iThemba LABS grounds and measurements were performed at 30-minute intervals starting at 10:40 am and ending at 07:10 am. During the measurements, the crystal temperature ranged from approximately 28˚C to 48˚C.

To determine the soil activity concentrations of ^{40}K, ^{232}Th series and ^{238}U series for each set of measurements acquired at a range of temperature, a similar approach to the one described in Chapter 3, section 3.1 was used. Figure A1-8 shows the control chart for total counts (TC). Similar control charts for ^{40}K, ^{232}Th and ^{238}U series ACs are presented in Figure A1-9. From the figures, all the results are found to be within 95% confidence limit implying reliability of the approach used for the field measurements.

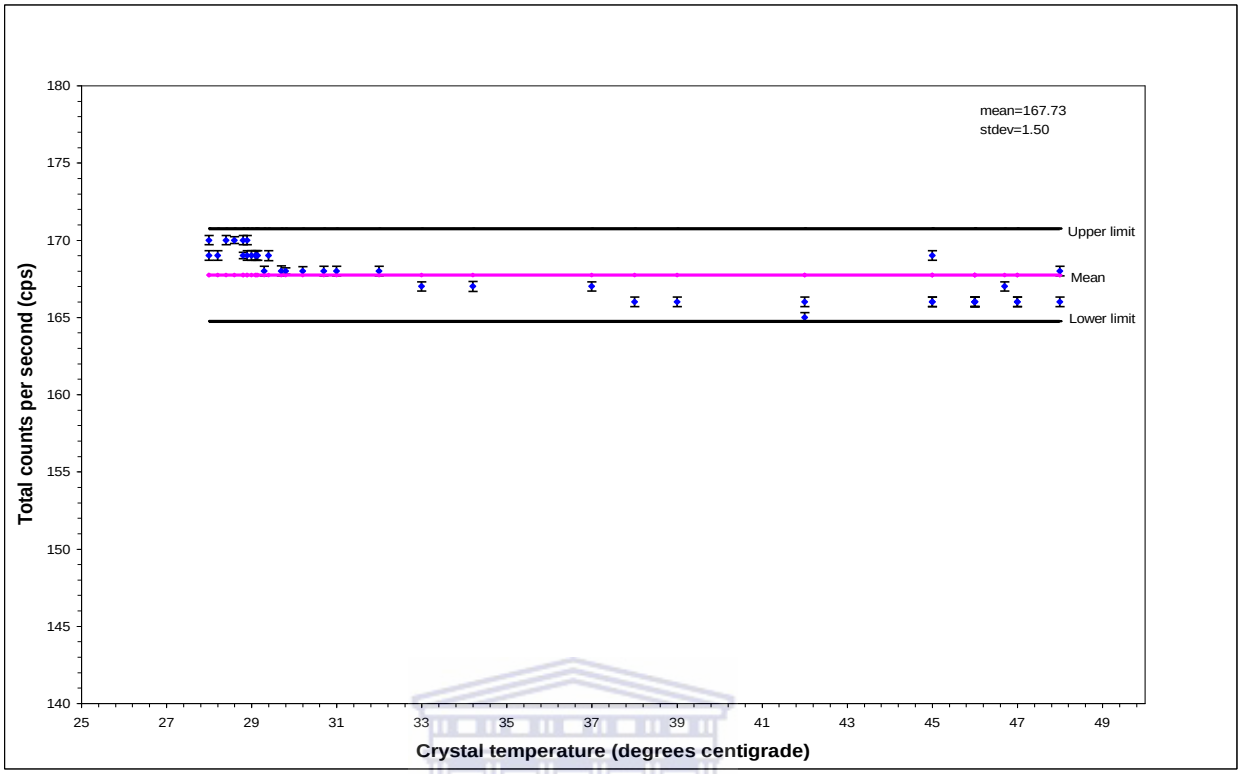

Figure A1-8: *TC over a range of crystal temperatures for the 30-minute measurement intervals. The upper and lower limits are determined from 2σ.*

Figure A1-9: *Activity concentrations of ^{40}K (top), ^{232}Th series (middle) and ^{238}U series (bottom) over a range of crystal temperatures for the 30-minute measurement intervals. The upper and lower limits are determined from 2σ.*

APPENDIX 2

Physico-chemical data

Table A2-1: Concentrations (%) by mass of soil major elements for group W_1 (Pomphuis/Nuweland) by XRF. The quoted uncertainties are at the 1 σ level determined from the standard deviation of ten sub-samples of one sample.

Sampling point	SiO_2 (±0.5)	Al_2O_3 (±0.10)	MgO (±0.02)	CaO (±0.009)	Fe_2O_3 (±0.4)	MnO (±0.0012)	TiO_2 (±0.007)	Cr_2O_3 (±0.009)	Na_2O (±0.08)	K_2O (±0.009)	P_2O_5 (±0.006)	LOI**	Total
P18	83.5	3.95	0.12	0.083	8.2	0.0142	0.373	0.042	0.17	0.221	0.096	3.26	100.10
P19	92.3	1.96	0.06	0.070	3.3	0.0111	0.221	0.048	BDL*	0.116	0.057	1.97	100.14
P20	80.2	9.75	0.34	0.179	2.5	0.0125	0.404	0.031	0.12	0.812	0.066	5.85	100.22
P21	76.9	9.89	0.31	0.136	5.9	0.0133	0.432	0.023	0.14	0.787	0.065	5.67	100.30
P22	94.1	1.89	0.10	0.064	1.9	0.0132	0.174	0.028	0.30	0.128	0.039	1.34	100.07
P23	87.8	3.00	0.12	0.111	5.5	0.0123	0.259	0.044	0.20	0.176	0.083	2.81	100.14
P24	91.9	1.94	0.13	0.114	3.0	0.0122	0.181	0.041	0.29	0.139	0.073	2.30	100.15
P25	87.3	3.26	0.11	0.089	5.4	0.0143	0.244	0.033	0.33	0.207	0.088	3.08	100.14
N17	69.3	9.95	0.24	0.174	13.2	0.0194	0.447	0.042	0.16	0.524	0.062	6.03	100.19
N18	68.3	11.49	0.31	0.151	11.7	0.0467	0.538	0.044	0.35	0.703	0.052	6.68	100.32
N19	69.4	7.40	0.21	0.118	9.4	0.0132	0.412	0.037	0.24	0.411	0.061	13.90	101.65
N20	86.6	4.79	0.11	0.121	4.5	0.0123	0.394	0.026	0.24	0.264	0.051	3.12	100.17
N21	86.5	5.36	0.14	0.216	2.6	0.0142	0.473	0.024	0.09	0.335	0.057	4.12	99.95
N22	79.6	5.68	0.14	0.107	9.7	0.0171	0.335	0.019	0.06	0.267	0.049	4.25	100.21
N23	88.3	4.37	0.15	0.152	2.6	0.0150	0.458	0.022	0.42	0.360	0.053	3.23	100.20
N24	88.1	4.30	0.13	0.204	3.6	0.0143	0.415	0.018	0.09	0.255	0.063	2.97	100.14

Table A2-2: Concentrations (%) by mass of soil major elements for group W_2 (Block 2) by XRF. The concentration quoted uncertainties are at the 1 σ level determined from the standard deviation of ten sub-samples of one sample.

Sampling point	SiO_2 (±0.5)	Al_2O_3 (±0.10)	MgO (±0.02)	CaO (±0.009)	Fe_2O_3 (±0.4)	MnO (±0.0012)	TiO_2 (±0.007)	Cr_2O_3 (±0.009)	Na_2O (±0.08)	K_2O (±0.009)	P_2O_5 (±0.006)	LOI**	Total
B1	83.2	5.51	0.17	0.113	6.4	0.0230	0.553	BDL*	0.02	0.592	0.070	3.45	100.08
B2	85.7	6.62	0.21	0.111	2.2	0.0260	0.585	BDL*	BDL*	0.696	0.041	3.97	100.15
B3	74.3	7.27	0.18	0.090	12.9	0.0200	0.507	0.026	0.03	0.488	0.087	4.27	100.16
B4	81.0	8.50	0.24	0.152	3.0	0.0210	0.601	0.018	BDL*	0.657	0.086	5.95	100.25
B5	77.6	10.50	0.22	0.098	3.6	0.0200	0.679	BDL*	BDL*	0.751	0.077	6.70	100.19
B6	67.4	8.51	0.18	0.090	17.4	0.0180	0.525	0.027	0.06	0.487	0.104	5.31	100.10
B7	65.7	9.33	0.24	0.087	17.7	0.0270	0.568	0.064	BDL*	0.567	0.107	5.81	100.18
B8	84.7	5.81	0.20	0.134	4.0	0.0270	0.595	BDL*	0.01	0.586	0.075	4.05	100.18
B9	82.5	7.18	0.20	0.086	4.5	0.0240	0.632	0.033	BDL*	0.659	0.071	4.33	100.15
B10	80.5	7.43	0.19	0.173	5.5	0.0220	0.619	0.003	BDL*	0.587	0.081	5.02	100.10

*: Below detection limit

**: Loss on ignition

Table A2-3: Concentrations (mg/kg) of soil trace elements for group W_1 (Pomphuis/Nuweland) by ICP-MS. The concentration quoted uncertainties are at the 1 σ level determined from the standard deviation of ten sub-samples of one sample.

Sampling point	Li (±0.05)	Be (±0.006)	B (±0.06)	K (±20)	V (±3)	Cr (±3)	Co (±0.04)	Ni (±0.16)	Cu (±0.7)	Zn (±1.9)	As (±1.5)	Se (±0.012)	Sr (±0.3)	Mo (±0.007)	Cd (±0.008)	Ba (±1.2)
P18	0.86	0.144	0.41	185.50	40	30	0.25	1.05	9.4	13	25.0	0.333	3.2	0.256	0.037	10.0
P19	0.55	0.043	0.44	132.80	9	4	0.21	0.54	12.1	12	9.8	0.148	4.3	0.102	0.019	25.3
P20	2.51	0.179	1.03	430.10	13	9	0.54	1.07	14.7	22	8.6	0.812	12.3	0.092	0.038	82.8
P21	1.69	0.168	0.69	302.90	15	13	0.96	1.36	10.2	9	13.0	0.533	11.5	0.081	0.030	121.5
P22	0.47	0.071	0.46	84.10	22	7	0.30	0.49	7.6	6	13.3	0.137	2.3	0.192	0.014	8.0
P23	0.76	0.053	0.69	141.00	13	6	0.26	0.82	11.0	9	8.7	0.245	5.4	0.162	0.028	14.4
P24	0.36	0.042	0.65	91.20	9	6	0.21	0.68	13.4	24	6.4	0.105	3.9	0.123	0.017	6.2
P25	1.30	0.145	0.60	212.50	13	10	1.08	1.10	14.3	12	10.5	0.263	4.7	0.138	0.030	12.3
N17	4.74	0.770	1.43	474.50	42	59	6.72	6.18	9.6	11	25.4	1.050	9.5	0.192	0.046	86.3
N18	6.63	1.133	1.64	546.10	54	61	29.09	9.01	8.2	6	31.1	1.641	11.2	0.185	0.058	185.6
N19	1.90	0.496	1.00	313.00	21	21	2.29	4.95	5.8	5	19.9	0.618	7.0	0.096	0.018	38.4
N20	1.64	0.117	0.76	227.30	14	9	0.59	1.53	4.1	4	9.1	0.333	5.7	0.133	0.013	12.0
N21	1.31	0.111	0.87	261.90	19	10	1.31	1.52	10.0	11	9.2	0.416	8.1	0.127	0.052	21.3
N22	1.14	0.373	0.77	153.20	45	23	1.87	2.05	4.8	9	20.1	0.459	6.4	0.151	0.023	43.2
N23	1.58	0.157	0.96	272.50	13	15	0.78	1.53	6.6	7	10.3	0.300	6.2	0.137	0.028	18.3
N24	1.47	0.236	0.89	253.50	39	25	0.67	1.46	8.0	9	21.6	0.550	8.8	0.151	0.045	12.2

Table A2-4: Concentrations (mg/kg) of soil trace elements for group W_2 (Block 2) by ICP-MS. The concentration quoted uncertainties are at the 1 σ level determined from the standard deviation of ten sub-samples of one sample.

Sampling point	Li (±0.05)	Be (±0.006)	Si (±20)	K (±20)	Ti (±1.01)	V (±3)	Cr (±3)	Mn (±0.7)	Co (±0.04)	Ni (±0.16)	Cu (±0.7)	Zn (±1.9)	As (±1.5)	Se (±0.012)	Sr (±0.3)	Mo (±0.007)	Cd (±0.008)	Ba (±1.2)	Pb (±0.02)
B16	3.26	0.557	342	348	24.76	29	24	18.5	0.61	3.16	10.7	7.9	22.3	0.478	4.1	0.224	0.036	22.4	8.72
B17	2.61	0.227	587	439	26.31	12	7	55.1	0.84	2.17	8.0	6.6	11.2	0.487	3.4	0.105	0.029	20.3	6.43
B18	3.55	0.393	340	551	17.40	17	7	28.3	1.09	3.58	11.7	7.5	17.6	0.771	2.8	0.632	0.020	26.7	7.99
B18*	3.82	0.509	380	486	25.22	23	11	24.3	0.91	4.37	8.3	5.4	27.7	0.951	1.8	0.115	0.015	30.2	11.41
B19	2.53	0.252	490	419	24.91	12	8	103.3	1.22	2.29	14.6	9.4	14.3	0.581	3.6	0.297	0.024	23.9	6.61
B19*	2.76	0.303	492	423	25.35	13	10	96.5	1.30	2.57	10.4	5.5	14.7	0.572	3.2	0.329	0.019	25.9	7.06
B20	2.01	0.252	455	275	25.21	16	11	12.9	0.47	1.85	7.8	4.2	12.0	0.363	4.2	0.070	0.013	17.4	4.32
B20*	2.18	0.396	535	238	22.83	20	13	9.5	0.65	2.34	7.3	3.6	13.9	0.430	3.8	0.149	0.017	22.3	5.08
B21	1.47	0.156	526	269	23.18	10	8	29.3	0.37	1.21	15.2	8.3	12.4	0.294	5.5	0.074	0.020	13.0	3.84
B21*	1.60	0.176	524	202	23.07	13	14	7.4	0.21	1.14	4.0	3.1	16.3	0.269	3.1	0.342	0.016	12.0	6.42
B22	1.23	0.171	496	239	23.42	16	13	20.4	0.20	1.27	12.4	5.7	16.6	0.344	3.6	0.127	0.015	13.6	4.23
B22*	1.51	0.192	495	234	19.48	14	10	14.3	0.21	1.36	6.8	3.2	14.1	0.354	3.4	0.067	0.010	45.1	3.77
B23	2.77	0.425	478	396	33.27	18	15	22.1	0.44	2.23	13.6	8.6	16.3	0.541	30.3	0.307	0.027	29.1	6.29
B23*	2.92	0.478	493	316	29.93	20	16	15.1	0.47	2.61	7.7	6.8	18.7	0.630	12.5	0.411	0.028	30.9	7.30

Notes:

* Refers to results of 30-60 cm soil sampling depths. Results of other points are based on 0-30 cm soil depths.

Table A2-5: Results of soil physico-chemical parameters for group W_1 (Pomphuis/Nuweland). Exchangeable cations and trace elements are determined by ICP-OES. The uncertainties quoted are at the 1 σ level determined from the standard deviation of ten sub-samples of one sample.

Sampling point	pH (KCl)	Resist.(Ohm) (±200)	Exchangeable cations (cmol(+)/kg)				Extractable elements (mg/kg)					C (±0.03) %	Clay (±0.3) %	Silt (±0.6) %	Sand (±0.8) %
			Na (±0.007)	K (±0.03)	Ca (±0.19)	Mg (±0.04)	P (±2)	Cu (±0.18)	Zn (±0.06)	Mn (±0.3)	B (±0.11)				
P1	6.8	270	0.920	0.36	6.94	3.74	82	2.91	8.10	14.6	0.58	0.79	14.6	30.6	54.8
P2	5.8	3090	0.040	0.21	1.59	0.43	58	3.24	3.60	6.4	0.2	0.28	1.0	6.8	92.2
P4	6.5	610	0.090	0.39	3.49	1.07	42	3.04	7.20	17.9	0.37	0.71	7.2	10.2	82.6
P5	6.8	180	0.870	1.06	6.23	3.75	326	2.13	23.00	22.8	0.81	1.25	10.0	17.0	73.0
P6	6	2330	0.030	0.11	1.01	0.40	42	3.74	4.80	6.0	0.18	0.43	2.8	2.0	95.2
P7	6.5	1380	0.060	0.31	2.33	0.80	102	3.47	6.60	13.5	0.36	0.63	0.8	6.2	93.0
P8	5.8	1310	0.040	0.19	1.6	0.50	37	3.57	4.90	9.4	0.28	0.26	1.6	4.6	93.8
P9	6.8	310	0.780	0.31	5.51	2.82	87	3.04	10.40	12.8	0.59	1.24	6.0	22.0	72.0
P10	6.2	1290	0.040	0.13	1.77	0.47	60	3.11	5.10	9.5	0.31	0.18	2.0	5.8	92.2
P11	5.9	800	0.100	0.22	2.84	1.46	23	6.12	15.90	9.0	0.23	0.44	0.8	15.0	84.2
P12	6.5	440	0.090	0.45	3.29	0.96	99	3.69	6.50	15.9	0.43	0.63	1.2	13.4	85.4
P13	5.8	1110	0.070	0.28	1.61	0.70	90	3.01	6.60	7.6	0.2	0.52	2.2	7.0	90.8
P14	6.5	570	0.180	0.43	1.73	0.67	98	2.19	5.30	7.7	0.28	0.35	3.0	8.4	88.6
P15	6.5	840	0.170	0.19	2.16	0.81	67	2.21	3.60	9.3	0.27	0.48	1.8	6.2	92.0
P16	5.8	1030	0.090	0.72	1.74	0.66	84	1.71	4.90	7.0	0.35	0.43	5.8	9.6	84.6
P17	6.5	690	0.330	0.32	3.68	1.97	76	1.86	4.80	10.6	0.39	0.27	7.0	8.0	85.0
N1	6.6	540	0.520	0.17	6.13	2.48	46	2.20	7.00	14.7	0.35	1.04	3.4	18.2	78.4
N2	6.9	530	0.340	0.23	5.11	2.29	14	1.11	7.30	12.5	0.58	0.38	2.6	15.4	82.0
N4	6.8	1090	0.100	0.2	3.96	0.68	43	1.56	2.60	7.0	0.25	0.54	3.0	14.2	82.8
N5	6.2	500	0.070	0.17	3.26	0.51	43	1.64	3.40	5.4	0.24	0.31	2.8	14.4	82.8
N6	6.8	1090	0.130	0.09	2.63	0.55	30	1.56	3.40	5.1	0.19	0.38	7.8	21.4	70.8
N7	6.7	1370	0.070	0.17	2.75	0.51	31	1.49	2.30	5.3	0.23	0.32	11.6	27.6	60.8
N8	7.2	870	0.290	0.16	5.3	1.35	11	0.81	4.10	13.3	0.22	0.53	1.6	12.7	86.0
N9	6.9	800	0.390	0.15	6.13	2.04	31	1.79	11.20	19.4	0.32	0.84	1.8	14.0	84.2
N10	6.4	1220	0.140	0.1	3.02	0.87	21	1.42	4.80	12.2	0.24	0.48	10.8	13.4	75.8
N11	6.5	1660	0.200	0.08	3.47	1.29	25	1.34	5.30	7.2	0.29	0.35	11.6	18.4	70.0
N12	7.2	540	0.340	0.17	5.25	2.49	8	1.15	2.30	15.3	0.62	0.12	23.0	19.8	57.2
N13	6.7	920	0.170	0.22	3.39	0.98	12	1.06	2.50	6.8	0.42	0.26	13.2	13.8	73.0
N14	6.8	1030	0.140	0.28	3.09	0.70	29	1.24	4.00	7.8	0.29	0.45	9.0	10.2	80.8
N15	6.5	1170	0.090	0.16	2.72	0.76	21	1.41	4.10	8.6	0.38	0.62	8.2	11.4	80.4
N16	7.4	1160	0.100	0.19	3.78	0.65	9	1.32	3.30	16.4	0.32	0.49	7.8	10.0	82.2

Table A2-6: Results of soil physico-chemical parameters for group W_2 (Block 2). Exchangeable cations and trace elements are determined by ICP-OES. The uncertainties quoted are at the 1 σ level determined from the standard deviation of ten sub-samples of one sample.

Sampling	pH	H+	Exchangeable cations (cmol(+)/kg)				Extractable elements (mg/kg)					C (±0.03)	Clay (±0.3)	Silt (±0.6)	Sand (±0.8)
point	(KCl)	(±0.04)	Na (±0.007)	K (±0.03)	Ca (±0.19)	Mg (±0.04)	P (±2)	Cu (±0.18)	Zn (±0.06)	Mn (±0.3)	B (±0.11)	%	%	%	%
B1	6.1	0.29	0.050	0.16	2.53	0.44	19	2.81	1.70	6.5	0.14	0.48	8.4	15.6	76.0
B2	5.5	0.43	0.050	0.29	2.98	0.71	10	3.04	1.80	7.7	0.19	0.60	15.8	17.4	66.8
B3	5.5	0.46	0.040	0.20	2.22	0.53	14	2.69	1.20	5.9	0.16	0.51	7.4	14.6	78.0
B4	5.1	0.72	0.125	0.30	3.88	1.22	14	5.24	2.10	7.9	0.27	0.84	18.8	14.8	66.4
B5	10.0	0.74	0.160	0.48	3.73	1.21	12	2.50	1.30	1.9	0.54	0.83	16.0	7.6	76.4
B6	5.7	0.43	0.045	0.19	2.51	0.52	10	6.36	1.85	6.6	0.19	0.59	8.0	9.6	82.4
B7	5.7	0.46	0.045	0.34	2.75	0.94	8	3.80	1.30	6.5	0.28	0.63	12.2	11.6	76.2
B8	5.5	0.48	0.045	0.29	3.35	0.49	26	4.45	4.28	11.6	0.23	0.61	8.6	13.8	77.6
B9	5.0	0.60	0.050	0.41	2.17	0.70	12	2.74	1.50	5.5	0.24	0.58	15.4	13.6	71.0
B10	5.5	0.53	0.050	0.45	4.55	0.67	23	4.47	3.40	9.9	0.39	0.94	12.4	12.0	75.6
B11	6.2	BDL	0.080	0.53	4.38	1.25	29	5.23	5.00	15.0	0.61	1.03	6.2	14.6	79.2
B12	5.7	0.60	0.070	0.57	4.58	0.93	27	3.11	6.60	17.2	0.83	1.00	3.8	14.4	81.8
B13	4.8	1.01	0.060	0.53	2.84	0.54	21	3.73	4.90	9.0	0.28	1.05	3.8	15.6	80.6
B14	5.5	0.66	0.100	0.63	4.05	1.31	20	3.35	4.00	7.1	0.40	0.87	4.6	16.2	79.2
B15	6.6	BDL	0.070	0.37	3.18	0.87	15	3.93	3.60	14.4	0.39	0.54	9.4	14.6	76.0
B16	4.8	0.91	0.055	0.51	2.75	0.98	7	2.00	0.90	1.8	0.27	0.67	18.6	14.0	67.4
B17	5.7	0.35	0.060	0.28	2.87	0.54	20	1.79	1.70	5.0	0.23	0.48	12.0	9.0	79.0
B18	5.8	0.25	0.050	0.64	3.76	0.72	5	1.25	0.90	3.4	0.72	0.40	22.0	8.0	70.0
B18*	5.8	0.25	0.040	0.45	2.37	0.82	0	0.73	0.30	1.4	0.96	0.25	24.4	8.4	67.2
B19	5.8	0.25	0.190	0.26	2.55	0.85	6	4.25	2.00	7.1	0.33	0.38	12.4	9.0	78.6
B19*	5.8	0.25	0.200	0.25	2.31	0.92	4	2.66	1.00	5.2	0.35	0.35	18.0	9.0	73.0
B20	5.8	0.25	0.040	0.20	2.71	0.41	3	2.02	0.70	1.9	0.17	0.37	16.4	8.0	75.6
B20*	5.7	0.35	0.060	0.14	2.74	0.59	0	0.88	0.30	0.9	0.28	0.32	8.4	8.0	83.6
B21	5.4	0.45	0.040	0.23	3.42	0.62	22	3.39	2.60	3.9	0.20	0.74	5.2	10.8	84.0
B21*	5.2	0.40	0.050	0.10	1.94	0.44	7	0.80	0.40	0.9	0.22	0.22	7.6	7.6	84.8
B22	5.8	0.30	0.020	0.14	2.42	0.43	12	3.60	1.10	3.3	0.24	0.46	5.2	10.0	84.8
B22*	5.5	0.35	0.050	0.10	1.76	0.40	8	1.55	0.50	1.5	0.16	0.31	10.0	8.0	82.0
B23	6.5	BDL	0.050	0.38	7.30	0.63	22	0.93	1.90	5.9	0.35	1.20	12.0	12.0	76.0
B23*	6.2	BDL	0.060	0.20	4.68	0.55	13	1.79	1.50	4.1	0.22	0.50	15.2	8.0	76.8

Notes:

* Refers to results of 30-60 cm soil sampling depths. Results of other points are based on 0-30 cm soil depths.

Table A2-7: Critical values of (r) for the Pearson correlation coefficient [Fis74]. For *n* samples, and *m* variables, the critical values are determined at *n-m*. *m* = 2 in most of the work in this thesis.

n-m	P=0.05	P=0.01	*n-m*	P=0.05	P=0.01
1	0.997	0.999	21	0.4133	0.526
2	0.950	0.990	22	0.404	0.515
3	0.878	0.959	23	0.396	0.505
4	0.811	0.917	24	0.388	0.496
5	0.754	0.874	25	0.381	0.487
6	0.707	0.834	26	0.374	0.479
7	0.666	0.798	27	0.367	0.471
8	0.632	0.765	28	0.361	0.463
9	0.602	0.735	29	0.355	0.456
10	0.576	0.708	30	0.349	0.449
11	0.553	0.684	35	0.325	0.412
12	0.532	0.661	40	0.304	0.393
13	0.514	0.641	45	0.288	0.372
14	0.497	0.623	50	0.273	0.354
15	0.482	0.606	60	0.250	0.325
16	0.468	0.590	70	0.232	0.302
17	0.456	0.575	80	0.217	0.283
18	0.444	0.561	90	0.205	0.267
19	0.433	0.549	100	0.195	0.254
20	0.423	0.537			

Table A2-8: Correlation coefficient (r) between major elements and variable *W* for the two groups. Statistical significance was determined at both 0.05 and 0.01 levels giving a significant correlation coefficient of r $\geq$ +/-0.497 and r $\geq$ +/-0.623, respectively, for W_1 (16 samples) and r $\geq$ +/-0.632 and r $\geq$ +/-0.765, respectively, for W_2 (10 samples). The statistically significant correlations are highlighted in bold.

Parameters/variables	Pomphuis/Nuweland blocks (W_1)	Block 2 (W_2)
	(r)	(r)
SiO_2 vs *W*	-0.113	0.261
Al_2O_3 vs *W*	**0.911****	0.539
MgO vs *W*	**0.964****	**0.704***
CaO vs *W*	0.433	0.205
Fe_2O_3 vs *W*	0.295	-0.569
MnO vs *W*	NS[a]	0.096
TiO vs *W*	**0.627****	**0.701***
Cr_2O_3 vs *W*	-0.073	-0.236
NaO vs *W*	0.192	BDL[+]
K_2O vs *W*	**0.988****	**0.842****
P_2O_5 vs *W*	-0.056	-0.251

Table A2-9: Correlation coefficient (r) between trace elements and variable *W* for the two groups. Statistical significance was determined at both 0.05 and 0.01 levels giving a significant correlation coefficient of r $\geq$ +/-0.497 and r $\geq$ +/-0.623, respectively, for W_1 (16 samples) and r $\geq$ +/-0.532 and r $\geq$ +/-0.661, respectively, for W_2 (14 samples).

Parameters/variables	Pomphuis and Nuweland blocks (W_1)	Block 2 (W_2)
	(r)	(r)
Li vs *W*	**0.594***	**0.855****
Be vs *W*	0.449	**0.943****
B vs *W*	**0.554***	-
K vs *W*	**0.781****	**0.543***
V vs *W*	0.134	**0.743****
Cr vs *W*	NS[a]	0.415
Co vs *W*	0.373	0.364
Ni vs *W*	0.431	**0.834****
Cu vs *W*	0.150	0.014
Zn vs *W*	0.082	0.244
As vs *W*	0.227	**0.700****
Se vs *W*	**0.673****	**0.793****
Sr vs *W*	**0.882****	NS[a]
Mo vs *W*	0.331	0.493
Cd vs *W*	0.439	NS[a]
Ba vs *W*	**0.818****	0.512
Si vs *W*	-	**-0.624***
Pb vs *W*	-	**0.744****

** Correlation is significant at 0.01 level; * Correlation is significant at 0.05 level

[+] Most samples are below detection limit;

[a] Variation between sediment group and base sediment not significant

Table A2-10: Correlation coefficient (r) between physico-chemical parameters and variable *W* for the two groups. Statistical significance was determined at both 0.05 and 0.01 levels giving a significant correlation coefficient of r $\geq$ +/-0.367 and r $\geq$ +/-0.471, respectively, for W_1 (31 samples) and r $\geq$ +/-0.381 and r $\geq$ +/-0.487, respectively, for W_2 (27 samples).

Parameters/variables	Pomphuis and Nuweland blocks (W_1)	Block 2 (W_2)
	(r)	(r)
P vs *W*	0.024	-0.278
Na vs *W*	**0.733****	**0.594****
K vs *W*	0.039	**0.386***
Ca vs *W*	**0.840****	0.354
Mg vs *W*	**0.815****	**0.516****
Cu vs *W*	-0.261	-0.242
Zn vs *W*	0.247	-0.215
Mn vs *W*	**0.483****	0.257
B vs *W*	**0.628****	0.307
C vs *W*	0.336	0.173
Clay vs *W*	**0.597****	**0.648****
Silt vs *W*	**0.679****	0.055
pH vs *W*	NS[a]	0.341
Sand vs *W*	**-0.724****	**-0.644****
Resistance vs *W*	**-0.433***	0.220

** Correlation is significant at 0.01 level

* Correlation is significant at 0.05 level

[a] Variation between sediment group and base sediment not significant

APPENDIX 3

Comparison of physico-chemical data

Soil physico-chemical data from the present study and results from the Department of Agriculture (Western Cape) presented in the reports [Nuw3, Pom03], and used by Modisane [Mod05] were compared. Table A3-1 compares the result ranges of soil physico-chemical data. From the table, elements Zn, B, Ca, Mg and pH show comparable ranges for both blocks despite the limited number of sampling points and interval of sampling (~ 5 years). Element Zn shows comparable range for the Pomphuis block whereas Cu and C indicate comparable range for the Nuweland block.

Table A3-1: Comparison of physico-chemical data at 0-30 cm soil depth between the present study and the previous work by the Department of Agriculture [Nuw3, Pom03] for Pomphuis and Nuweland blocks.

Physico-chemical data	Pomphuis block		Nuweland block	
	Present study (16 sample points)	Dept. of Agriculture (11 sample points)	Present study (15 sample points)	Dept. of Agriculture (6 sample points)
Cu (mg/kg)	1.9-6.1	1.2-14.4	0.8-2.2	1.1-2.7
Zn (mg/kg)	3.6-23	2.4-17.6	2.3-11.2	0.9-2.9
Mn (mg/kg)	6-22.8	4.5-45.8	5.1-19.4	3.7-35.5
B (mg/kg)	0.2-0.8	0.1-0.5	0.2-0.6	0.3-0.6
Ca (cmol(+)/kg)	1.0-6.9	1.0-6.5	2.6-6.1	1.4-5.7
Mg (cmol(+)/kg)	0.4-3.7	0.3-1.6	0.6-2.5	0.5-1.5
C (%)	0.2-0.8	-	0.1-1.0	0.3-0.6
pH	5.8-6.8	5.2-6.2	6.4-7.4	4.8-6.4
Resistance (ohm)	180-3090	630-1560	500-1660	1680-4350

Comparing the correlations found between radiometric data and physico-chemical data (see Appendix 2, Tables A2-8 to A2-A2-10) with the results from the previous study [Mod05] as discussed in Chapter 1 (section 1.3), similar significant correlations between radiometric data and K, Na, B, and Mg are found.

REFERENCES

[Ame93] American Nuclear Systems. (1993-1997). *Oxford Win-MCA and Assayer software,* Version 3.80. User`s manual.

[Bol79] Bolt, G.M., 1979. *Soil Chemistry. B. Physico-Chemical Models*. Elsevier, Amsterdam.

[Bon02] Bonnardot, V. *et al*., 2002. *Diurnal wind, relative humidity and temperature variation in the Stellenbosch-Groot Drakenstein Wine Growing Area*. S. Afr. J. Enol. Vitic. 23, 62-71.

[Bra74] Brady N.C., 1974. *The nature and properties of soils.* 8th Edition. Macmillan Publishing Co. Inc. New York.

[Bru03] Bruker., 2003. *Advanced X-Ray solutions*. User`s Manual DIFFRAC^{plus}, 2003.

[Cat06] Catarino, S. *et al.,* 2006. *Measurements of contaminant elements of wines by inductively coupled plasma-mass spectrometry: A comparison of two calibration approaches.* Talanta 70, 1073-1080.

[Chu94] Chuma, J.L., 1994. *Physica© Reference Manual*. TRIUMF, 4004 Wesbrook Mall, Vancouver, B.C., Canada V6T 2A3.

[Cou84] Courtney F.M., Trudgill S.T., 1984. *An Introduction to Soil study*, 2nd edition Spottiswoode Ballantyme Ltd, Colchester and London.

[Coz08] Cozzolino, D. *et al.,* 2008. *Analysis of elements in wine using near infrared spectroscopy and partial least squares regression*. Talanta 74, 711-716.

[Cro99] Croft, S., Hutchinson, I.G., 1999. *The measurement of U, Th and K concentrations in building materials*. Applied Radiation and Isotopes, 51(5), 483-492.

[Dam05] Damon, R.W., 2005. *Determination of the photopeak detection efficiency of a HPGe detector, for volume sources, via Monte Carlo simulations*. Unpublished Masters Thesis, University of the Western Cape. Available online at: http://etd.uwc.ac.za/.

[Dan06] Daniels, W.L., Haering, K.C., 2006. *Concepts of basic soil science*. The Mid-Atlantic nutrient management handbook. Department of crop and soil environmental sciences, Virginia Tech. MAWP 06-02.

[Deb01] Debertin, K., Helmer. R.G., 2001. *Gamma and X-Ray spectrometry with semiconductor detectors*. 3rd impression. Elsevier B.V, Amsterdam, The Netherlands, 2001.

[deM97] de Meijer, R. J. *et al*., 1997. *Improved and New Uses of Natural Radioactivity in Mineral Exploration and Processing*. Explor. Mining Geol. 6(1), 105-117.

[deM02] de Meijer, R.J. *et al*., 2002. *Natural Radioactivity in Monitoring Waste Disposal*. Physica Scripta. T97, 139-147.

[deM09] de Meijer, R.J., 2009. Department of Physics, University of the Western Cape, South Africa and Stichting EARTH, The Netherlands. Private communication.

[Dym95] Dymott, T.C., 1995. *ICP-OES Techniques in Environmental QC*. VCH, Weinheim, New York.

[Edg88] Edgell, K., 1988. *USEPA Method Study 37-SW-846, Method 3050 Acid Digestion of Sediments, Sludges, and Soils*. EPA Contract No. 68-03-3254.

[EPA06] Environmental Protection Agency (USA)., 2006. *Radiation Protection Program*, USA.

[Esc88] Eschnauer, H., Neeb, R., 1988. *Micro element analysis in wine and grapes* in: modern methods of plant analysis. In: Linskens H.I, Jackson J.F, Springer-Verlag, 67-91.

[Eur98] European Patent Office., 1998. *System for determining a composition of radionuclides*, Patent Number US5744804. Available online http://v3.espacenet.com/textdoc DB=EPODOC&IDX=US6057542&F=0.

[Fer08] Ferreira, S.L.C. *et al.,* 2008. *Direct determination of iron and manganese in wine using the reference element technique and fast sequential multi-element flame atomic absorption spectrometry.* Talanta 74, 699-702.

[Fir96] Firestone, R.B., *et al.,* 1996. *Table of Isotopes*. In: Shirley, V.S. (Ed.). John Wiley and Sons, New York.

[Fir98] Firestone, R.B., 1998. *Table of Isotopes*. 8th edition, John Wiley & Sons, Inc. New York.

[Fis74] Fisher, R.A., Yates F., 1974. *Biological, Agricultural and Medical Research*, Longman Group Ltd, London.

[Fit86] FitzPatrick., 1986. *An introduction to soil science*. 2nd Edition. John Wiley and Sons Ltd, New York.

[Fra08] Frazenburg, M., 2008. Department of Geology, University of Stellenbosch, South Africa. Private communication.

[Gal02] Galani-Nikolakaki, S. *et al.,* Kallithrakas-Kontos, N., Katsanos, A.A., 2002. *Trace element analysis of Cretan wines and wine products*. The science of the Total Environment, 285, 155-163.

[Gar01] Garcia-Talavera, M. et al., 2001. *Coincidence summing corrections for the natural decay series in γ-ray spectrometry.* J. Rad. Isot. 54(5), 769-776.

[Gol02] Golden Software, Inc., 2002. *Surfer8 User`s Guide, Contouring and 3D Surface Mapping for Scientist and Engineers*, Colorado, USA.

[Hen01] Hendriks, P.H.G.M. *et al*., 2001. *Full-spectrum analysis of natural γ-ray spectra*, J. Env. Radioactivity, 53 (3), 365 – 380.
[Hen02] Hendriks, P. H. G. M. *et al*., 2002. *MCNP modelling of scintillation-detector γ-ray spectra from natural radionuclides*. Appl. Radiat. Isot. 57, 449 – 457.

[Hla07] Hlatshwayo, I.N., 2007. *In-situ Gamma-Ray Mapping of Environmental Radioactivity at iThemba LABS and Associated risk assessment*. MSc. Thesis, unpublished, University of Zululand, South Africa.

[ICRU94] International Commission on Radiation Units and Measurements, 1994. *Gamma ray Spectrometry in the Environment.* ICRU Report 53, Bethesda, USA.

[Jar92] Jarvis *et al*., 1992. *Handbook of Inductively Coupled Plasma Mass Spectrometry*. Chapman and Hall: New York.

[Jon94] Jones, D.G., 1994. *Towed Seabed Gamma Ray Spectrometer: "Eel" is radiometric instrument for wide range of offshore mineral exploitation, environmental survey applications.* Sea Technology, 89-93.

[Jos07] Joseph, A. D., 2007. *Radiometric Study of Soil: The Systematic Effects*. Unpublished Master's thesis. Bellville: University of the Western Cape. Available online at http://etd.uwc.ac.za/.

[Jos98] Josten, N. E. & Gehrke, R., 1998. *In-situ Radiation Mapping for Assessment of Distributed Radioactive contamination*.
http://tech.inel.gov/documents/teb/calcium_fluoride_detector_array/insitu_mapping_spectrum98.pdf.

[Kab01] Kabata-Pendias, A., Pendias, H., 2001. *Trace elements in soils and plants,* 3rd ed. CRC Press, Boca Raton, FL.

[Kab04] Kabata-Pendias, A., 2004. *Soil-plant transfer of trace elements, an environmental issue.* Geoderma 122, 143-149.

[Kas05] Kastlander J., Bargholtz. C., 2005. *Efficient in–situ method to determine Radionuclide Concentration in Soil.* Nuclear Instruments and Methods in Physics Research A 547, 2-3, 400-410.

[Ken83] Kench, J., Hands P., Hughes D., 1983. *The complete book of South African Wine*. C. Struik Publishers, Cape Town.

[Kme05] Kment, P. *et al.*, 2005. *Differentiation of Czech wines using multielement composition-A comparison with vineyard soil*. Food Chemistry 91, 157-165.

[Kno99] Knoll G.F., 1999. *Radiation Detection and Measurements*, 3rd Edition. John Wiley and Sons Ltd, New York.

[Lar05] Lara, R. *et al.*, 2005. *Trace element determination of Argentine wines using ETAAS and USN-ICP-OES*. Food and Chemical Toxicology, 43, 293-297.

[Leo87] Leo, W.R., 1987. *Techniques for Nuclear and Particle Physics Experiments.* New York: Springer-Verlag.

[Lil01] Lilley, J.S., 2001. *Nuclear Physics Principles and Applications.* John Wiley & Son Ltd, England.

[Limb00] Limburg, J., de Meijer, R.J., 2000. The Nuclear Geophysics Division at KVI in Groningen: *Past, present and future*. FKPE 5th Workshop "Bohrlochgeophysik und Gesteinsphysik", Hannover, October 7-8 1999Sonderband III/2000: 52-55.

[Mal01] Maleka P.P., 2001. *Calibration of Germanium Detectors for Applications of Radiometric Methods in South Africa*, Unpublished M.Sc. Thesis, University of the Western Cape, South Africa.

[Mal07] Maleka P.P., 2007. Department of Physics, University of the Western Cape, South Africa. Private communication.

[Mar93] Martin R.C., 1993. *Soil sampling and methods of analysis*. Lewis Publishers, Boca Raton.

[Mar99] Martin, G.J. *et al.*, 1999. *Characterization of the Geographic Origin of Bordeaux Wines by a Combined Use of Isotopic and Trace Element Measurements*. Am. J. Enol. Vitic. 50:4:409-417.

[Mca09] McAfee, J., 2009. *Potassium, A Key Nutrient for Plant Growth.* http://jimmcafee.tamu.edu/files/potassium%20a%20key%20nutrient%20for%20plant%20gro (referenced on 17 May 09).

[Mil77] Miller, J. M. *et al.*, 1977. *A towed sea-bed gamma-ray spectrometer for continental shelf surveys*. Nuclear Techniques and Mineral Resources, Proceedings of an International Sysmposium, IAEA, Vienna, 465-498

[Mod05] Modisane T. J., 2005. *Correlation between natural radionuclide concentrations in soils and vine-growth potential*. Unpublished M.Sc Thesis, North West University, Mafikeng, South Africa.

[New04b] Newman, R.T. *et al.*, 2004. *Report on in-situ gamma-ray mapping of Paarl*, Report no.: ERL/04/UWC/02. Environmental Radioactivity Lab, Physics Group, iThemba LABS.

[New08] Newman, R.T. *et al.*, 2008. *Determination of soil, sand and ore primordial radionuclides concentrations by full-spectrum analyses of high-purity germanium detector spectra.* Appl. Rad. Isot. 66, 855-859.

[New96] Newman, A. 1996. *Elements of ICPMS*. Analytical Chemistry. 68(Jan 1): 46A-51A.

[Nuw03] Nuweland., 2003. *Report by the Department of Agriculture*, no: Stb0041, Elsenburg, Western Cape, July.

[Oxf97] Oxford Instruments Inc, 1977. *Instructional Manual PCA3*, Third Generation Personal Computer Analyser, PPCA 300F010197, USA.

[Poh07] Pohl, P., 2007. *What do metals tell us about wine?* Trends in Analytical Chemistry, 26 (9), 941-949.

[Pom03] Pomphuis., 2003. *Report by the Department of Agriculture*, no: Stb0041, Elsenburg, Western Cape, July.

[Pre92] Press, W. H. *et al*., 1992. *Numerical recipes in Fortran: The art of scientific computing*. 2nd edition. Press Syndicate of the University of Cambridge. New York.

[Ree92] Ree, B.C., 1992. *Linear least-squares fits with errors in both coordinates. II: Comments on parameter variances*. Am. Journal of Phy. 60 (1), 59-62.

[Roh86] Rohrbough, W.G. *et al*., 1986. *Reagent Chemicals, American Chemical Society Specifications*, 7th ed.; American Chemical Society: Washington, DC.

[Saa92] Saayman, D., 1992. *Natural influences and wine quality*. Part 2: the role of soil. WineLand, August, 49-51.

[Sch09] Schulte, E.E., Kelling, K.A., 2009. *Plant Nutrients*. Soils and Applied Potassium (A2521). learningstore.uwex.edu/pdf/A2521.pdf.

[Sha97] Sharshar, T. *et al*., 1997. *Efficiency Calibration of HPGe Detectors for Volume-source Geometries.* App. Radiat. Isot. 48 (5), 695-697.

[Soi99] *Soil analysis handbook of reference methods*, 1999. Soil and Plant Analysis Council, CRC Press, Boca Raton.

[Spa95] Sparks, D.L., 1995. *Environmental Soil Chemistry Academic Press*, San Diego.

[Tal09] Talha, A.S., 2009. *Measurements and Applications of Radon in South African Aquifer and River Waters.* PhD Thesis, University of the Western Cape, South Africa. Available online at: http://etd.uwc.ac.za/.

[Tan98] Tan, K.H., 1998. *Principles of Soil Chemistry*, 3rd ed. Marcel Dekker, New York.

[Tho09] Thompson, B., 2009. *Efficient fertilizer use-Potassium*. http://rainbowplantfood.com/agronomics/efu/potassium.pdf.

[Tyk95] Tykva R., Sabol J., 1995. *Low-level environmental Radioactivity sources and evaluation*, Technomic Publishing Company, Lancaster, Pennsylvania.

[Van08] Van Egmond F.M. *et al*., 2008. *Gamma-ray sensor for topsoil mapping; the mole.* In: Proc. High Resolution Digital Soil Sensing and Mapping in Sydney, Australia. Available online at: http://soilcompany.nl/uk/index.htm.

[Van66] Van Der Watt, H.V.H., 1966. *Improved tables and a simplified procedure for soil particle size analyses by the hydrometer method*. S. Afr. J. Agric. Sci. 9, 911-916.

[Wil93] Wild, A., 1993. *Soils and the environment: An introduction.* 1st edition. Cambridge University press. New York, USA.

[Wil98] Wilson, J.E., 1998. *Terroir: The role of geology, climate and culture in the making of French wines.* University of California Press, Berkeley, California. Vienna, 465.

[Www01] http://en.wikipedia.org/wiki/terroir (referenced on 20 October 08).

[Www02] http://soils.usda.gov/education/resources/K_12/lessons/profile/ (referenced on 24 March 09).

[Www03] http://www.vitiwise.com.au/a_balanced_approach.htm (referenced on 4 May 09).

[Www04] http://www.safarinow.com/destinations/Western-Cape/maps.aspx (referenced on 20 October 08).